Experimental study of the hydrodynamic loads generated by breaking wave impacts on floating offshore wind turbines

Florian Hulin

COLLEGES SCIENCES
BRETAGNE POUR L'INGENIEUR
LOIRE ET LE NUMERIQUE

ENSTA BRETAGNE

THÈSE DE DOCTORAT DE

L'ÉCOLE NATIONALE SUPÉRIEURE
DE TECHNIQUES AVANCÉES BRETAGNE

ÉCOLE DOCTORALE N° 648
Sciences pour l'Ingénieur et le Numérique
Spécialité : *Physique et Sciences de l'Ingénieur*

Par

Florian Hulin

Experimental study of the hydrodynamic loads generated by breaking wave impacts on floating offshore wind turbines

Thèse présentée et soutenue à Brest, le 10 avril 2024
Unité de recherche : Institut de Recherche Dupuy de Lôme (IRDL) - UMR CNRS 6027

Rapporteurs avant soutenance :

Guillaume Ducrozet	Professeur des Universités, Centrale Nantes
Laurent David	Professeur des Universités, Université de Poitiers

Composition du Jury :

Président :	Grégory Pinon	Professeur des Universités, Université Le Havre Normandie
Examinateurs :	Grégory Pinon	Professeur des Universités, Université Le Havre Normandie
	Deborah Greaves	Professor, University of Plymouth
Dir. de thèse :	Nicolas Jacques	Maître de Conférences HDR, ENSTA Bretagne
Encadrant :	Alan Tassin	Chercheur, Ifremer
Encadrant :	Jean-François Filipot	Directeur scientifique, France Énergies Marines

Acknowledgement

J'aimerais commencer par remercier Alan, Jean-François et Nicolas pour leur grande implication dans mon travail de thèse, leurs suggestions toujours pertinentes et leur disponibilité.

Viennent ensuite les collègues de l'Ifremer et de France Énergies Marines, impliqués de près ou de loin dans le projet DIMPACT et les essais. Merci à Julien, Seb, Alex, Thomas et Matthieu pour leur soutien technique avant et pendant les essais. Les échanges réguliers avec les collègues de France Énergies Marines et du projet DIMPACT ont été riches et ont contribué à la réussite de cette thèse. Merci à Paul, Marc B., Marc P., Rui, Fabien, Jeffrey, Maria et Christophe. Merci aussi à Stephan de m'avoir laissé utiliser intensivement son code potentiel.

Du côté des collègues doctorants et autres précaires, j'ai une pensée pour Saïd, Camil, Agathe, Simon, Sacha, Romain, Laure, Robin, Louis, Gauthier, Alban, Andres, Pierre. Merci pour ces nombreuses discussions autour d'un café. Je n'oublie pas les stagiaires qu'ont été Baptiste et Alexandre et qui ont fait commencer cette thèse sur les chapeaux de roues ! Merci aussi aux fidèles du Rak !

C'est grâce aux nombreuses personnes que j'ai rencontrées à Brest que ces trois années ont été si riches et agréables. Je pense d'abord à mes colocataires et apparentés. Il y a là Estelle, Alexandre, Robin, Guillaume, Marie, Théophile, Mélina, Nico, Cécile, Francis, Emma, Paul, Noémie, Gwen et Alex. Vient ensuite l'équipe de choc que forment Simon, Sam, Romain et Morgane. Dans le désordre, mes pensées vont aussi aux P'tyrochs, aux grimpeurs de l'ASCIG, aux voileux du dimanche matin, au Ty Kall, à Karine, Marie, Christophe, Thierry, Luca, Thomas, Coline, Noémie, Pierre, Raquel, Gaspard, Tristan, Maxence, Alix, Véro, Kenza, Hugo, Lisa, Robin, Édouard, Seb, Maixent, et j'en oublie certainement. Enfin, un grand merci à Joana.

Table of Contents

NOMENCLATURE

Acronyms

PDF Probability density function

CFD Computational fluid dynamics

EMD Empirical mode decomposition

FEA Finite element analysis

FEM France Énergies Marines

FOWT Floating offshore wind turbine

IEPE Integrated electronics piezo-electric

NWT Numerical wave tank

RTE Réseau de Transport d'Électricité

SWL Still water level

VOF Volume of fluid

Mathematical symbols

α_i Coefficient of the compensation methodology associated to the i^{th} accelerometer

δ Distance between the breaking location and the front face of the cylinder

δ_r Distance between $x = 21$ m and the front face of the cylinder

η_b Heigth of a breaking crest

γ Peak enhancement factor

γ_i Acceleration recorded by the i^{th} accelerometer

$\mathbf{W}$ Square matrix allowing to write the γ_j as a linear combination of the $\ddot{a}_i$

$\mathcal{D}$ Material domain of a solid

ϕ Velocity potential

ρ Density of water

τ Time constant in Goda's formula

θ Pitch angle

$\vec{F}_{hyd}$ Hydrodynamic force

$\vec{f}_{hyd}$ Hydrodynamic force per surface unit

$\vec{F}_{meas}$ Force measured by a load cell

$\vec{n}_j$ Direction of the j^{th} accelerometer

$\vec{T}$ Displacement function

$\vec{w}_i(x, y, z)$ Modal shape of the i^{th} mode

$\vec{X}_i$ Position of the i^{th} accelerometer

$\vec{\Gamma}$ Vector of the accelerations γ_i

$\vec{m}_i$ Vector of the modal masses of the i^{th} mode

$\vec{U}(x, y, z, t)$ Velocity of the material point (x, y, z) at the instant t

A_i Accelerometer number i

a_i Modal coordinate of the i$^{\text{th}}$ mode

c Crest speed of a wave

C_S Slamming coefficient

D Diameter of a cylinder

f_c^i Cut-off frequency used for the compensation methodology on section S_i

F_D Drag force

F_I Inertia force

F_S Slamming force

f_S Slamming force per unit length

F_{SWL} Sum of the compensated forces acting on the three upper sections

g	Acceleration of gravity
H_S	Significant wave height
L	Characteristic wavelength
M	Material point of a solid
m_s	Mass of a skin element
N	Order of the compensation methodology
R	Radius of a cylinder
S_i	Section number i
t_1	Start of the coefficient identification time interval
t_2	End of the coefficient identification time interval
T_p	Peak period
u	Horizontal fluid velocity
F_{ham}	Force measured by the instrumented hammer
$\mathbf{M}$	Modal mass matrix

Chapter 1

Introduction

This doctoral dissertation presents an experimental study of the hydrodynamic loads generated by breaking wave impacts on an idealized SPAR-type floating wind turbine. The influence of several parameters of the breaking waves and of the cylinder on the impact loads are studied. This work is the experimental part of the DIMPACT (Design of floating wind turbines and impacts of energetic steep and breaking waves) project led by France Énergies Marines (FEM). The project aims to better characterise the loads generated by breaking wave impacts on floating offshore wind turbines (FOWT) in order to provide improved design guidelines to the industry. The supervision of the thesis was shared between France Énergies Marines, Ifremer and ENSTA Bretagne.

1.1 Motivation for the current work

1.1.1 The development of floating offshore wind turbines

France aims to achieve net zero carbon emissions by 2050. This implies to dramatically decrease the consumption of fossil fuels. A report detailing the different possibilities to attain this objective was recently published by RTE (Réseau de Transport d'Électricité), the operator in charge of the French electricity transmission system (RTE 2021). The report highlights that even in the case of a decrease of 40 % of the French final energy consumption, reaching net zero carbon emissions requires to increase the production of electricity (of 35 % in the reference scenario). Different scenarios for the evolution of the French power sector are investigated in the report. All of them consider a strong development of offshore wind energy. The scenario with the largest contribution of offshore wind energy relies on the installation of 62 GW of offshore wind turbines. Even the scenario with the largest contribution of nuclear power relies on the installation of 22 GW of offshore wind energy. Today, about one GW of offshore wind has been installed in France. This makes the gap to reach any of these objectives important.

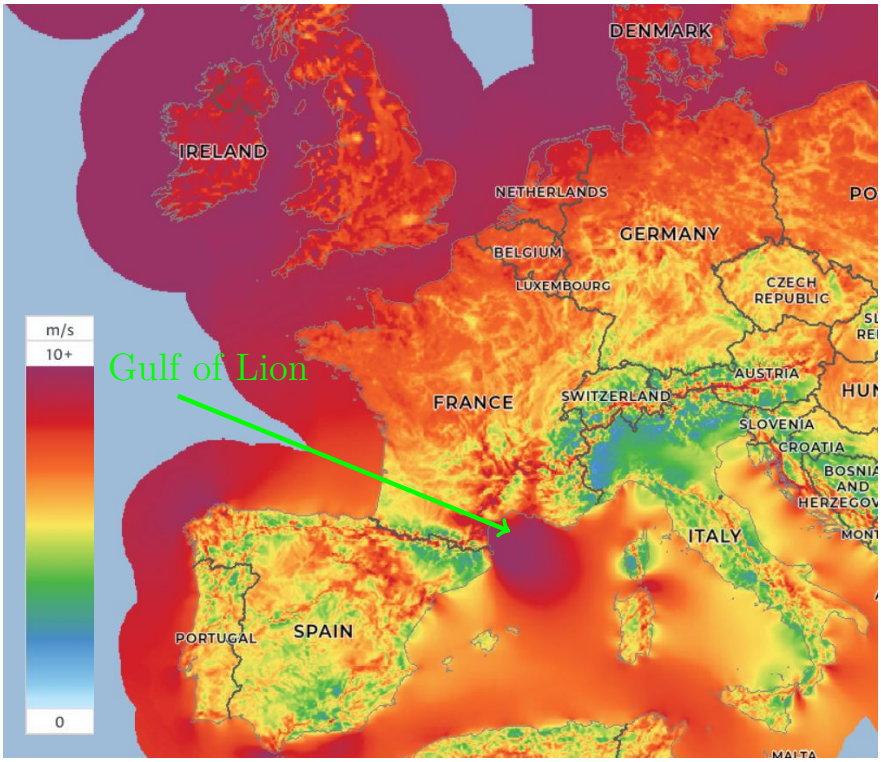

Figure 1.1 – Mean wind velocity at 100 m. Screenshot from the Global wind atlas.

In order to address this challenge, it will be necessary to exploit wind fields with important technical constraints, such as deep waters. The first french wind farms, located in Saint-Nazaire and Saint-Brieuc, are composed of bottom fixed wind turbines. The turbines of the Saint-Nazaire farm, implanted at depths ranging from 10 to 20 m, are seated on monopiles. The deeper waters of the Saint-Brieuc bay, over 30 m, required to install the wind turbines on jacket structures. Jacket structures are limited to a water depth of around 50 m (Sánchez et al. 2019). Therefore, they are not suitable for the Gulf of Lion, in the Mediterranean sea, where the water depth increases rapidly with the distance from the coast. As it is shown on the wind resource map depicted in figure 1.1, the Gulf of Lion has an important wind potential. More generally, the map shows that the more energetic wind fields are located further away off the coast. The bathymetric map of figure 1.2 shows that further offshore waters are often deeper. The only possibility to exploit these fields is to rely on FOWT, which can be installed at depths exceeding 50 m.

The development of floating wind farms is recent. The world first floating wind farm, Hywind Scotland, was commissioned in 2017 at a depth of about 100 m. During its 5

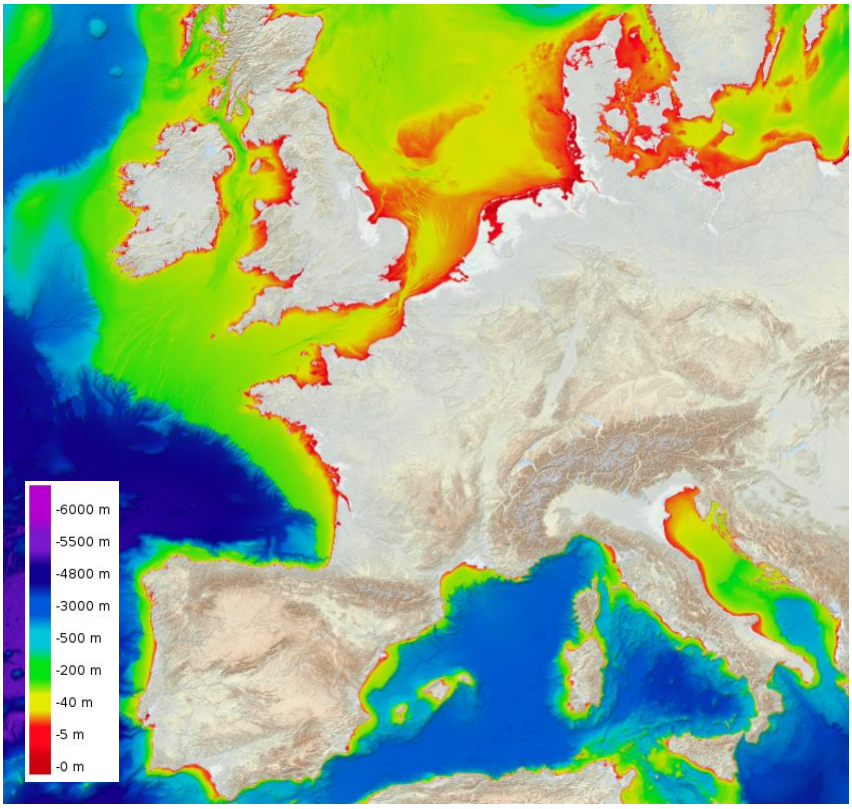

Figure 1.2 – Water depth distribution. Screenshot from the European Marine Observation and Data Network.

Figure 1.3 – The 2.3 MW SPAR-type prototype Zefyros. Source: Metcentre.

first years of operation, it reached a capacity factor as high as 54% and became the best performing wind farm in history (Biogradlija 2022). A picture of the SPAR-type wind turbine Zefyros, the prototype of the Hywind Scotland wind turbines, is depicted in figure 1.3. Other FOWT technologies have already been developed and installed. The most common designs are described in figure 1.4. In France, the FOWTs of the pilot farm Provence Grand Large, installed in 2023 off the coast of Marseille, are fixed on tension-leg platforms. Two other pilot farms, using the semi-submersible platform of Principle Power and the barge of Ideol, should be installed in 2024 in the Gulf of Lion. Three 250 MW floating wind farms, two in the Mediterranean sea and one in South Brittany, are considered for commissioning by 2030. Besides the possibility of exploiting deeper wind fields, other advantages of the floating technologies are often cited. Installing the turbines further offshore limits the risk of conflicts with the fishing industry. It also reduces the visual impacts of the farms and the opposition from the public. Finally, the assembly of the turbines can be done in the harbor. Compared to bottom fixed wind turbines which are assembled on-site, this may reduce the impacts on marine life as only the anchors are fixed on-site.

1.1.2 Breaking wave impacts on wind turbines

FOWTs installed far from the coast and exposed to energetic winds face harsh meteorological conditions. During storms, the loads generated by breaking wave impacts may be responsible for an important part of the total loads. Wave impact, also called wave

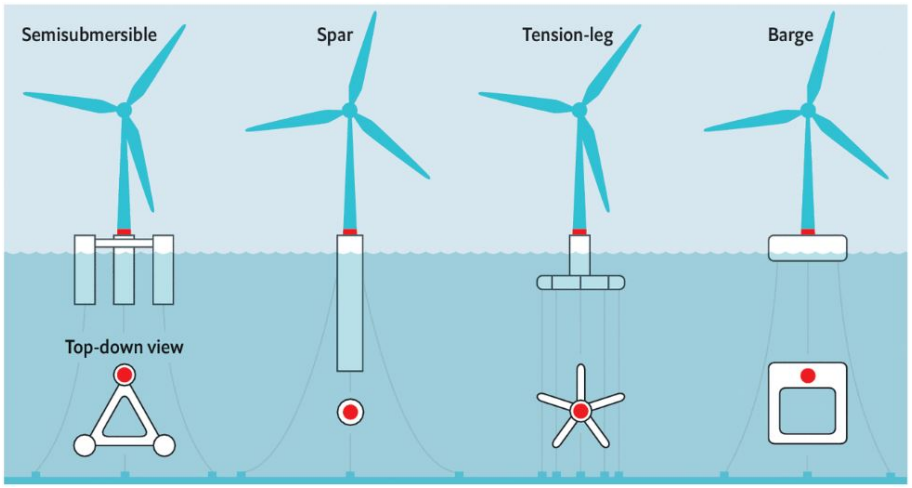

Figure 1.4 – Common floating wind platforms (Mei et al. 2021)

Figure 1.5 – Images of a breaking wave impacting the La Jument lighthouse, situated at the South-West of Ushant ©Air Vide et Eau

slamming, is the process during which a wave with a steep front encounters a solid structure. This may lead to a sudden rise of the load generated by the wave on the structure. This process is illustrated in figure 1.5, where a picture of the La Jument lighthouse hit by a breaking wave is depicted. Laboratory studies (Kjeldsen et al. 1986; Basco et al. 1989; Paulsen et al. 2019) have reported that the loads generated by breaking wave impacts on vertical cylinders can be up to two times the loads generated by non-breaking waves of similar wavelength and height. In the oil and gas industry, some incidents are attributed to wave slamming. For instance, in December 2015, a fatal incident due to wave slamming on vertical members is reported for the semi-submersible drilling unit COSLInnovator (Viste-Ollestad 2016). It caused important damages to the unit and led to one fatality and four injuries. As highlighted in the review of breaking wave force on the bridge pear by Wei et al. 2022, breaking waves may also be a threat for bridges which are often situated in breaking zones. In addition to their large magnitude, the loads generated by breaking wave impacts are impulsive. Their duration is short and therefore they may excite

the structure over a large frequency band. If the natural frequencies of the structure lie within this band, a dynamic amplification of the load may occur and increase the risk of failure of the structure. The dynamic response of a reduced scale wind turbine subjected to breaking wave impacts is investigated by Suja-Thauvin et al. 2017.

As a consequence, wave impact loads should be considered in the design of offshore wind turbines. Considering wave impacts is however challenging in several aspects. One of these aspects is to determine the design sea state for breaking wave impacts. Indeed, this sea state may be different from the design sea state for non-breaking wave loads. For instance, the incident reported by Viste-Ollestad 2016 occurred during a relatively moderate sea state milder than the design sea state. Such conditions were already experienced and withstood by the unit. Moreover, in a given sea state, it has been reported that the waves leading to slamming do not necessarily correspond to the highest waves (Paulsen et al. 2019; Guo et al. 2020). Determining a design sea state and a design wave for breaking wave loads remains challenging. Another challenge consists in determining the magnitude of the load that will be generated by a particular breaking wave on the turbine and the time evolution of the load. This can either be done using analytical, numerical or experimental approaches. The advantages and disadvantages of these approaches are discussed later in sections 1.2 and 1.3.

1.1.3 Taking into account breaking wave impacts

Certification organisations (*e.g.* DNV GL, Bureau Veritas) give some guidance to account for breaking wave impacts during the design of offshore wind turbines, but these recommendations are sometimes vague and often conservative. For instance, in the *British Standards Document BS EN IEC 61400-1 for wind energy generation systems* 2019, no information is given concerning the type and size of the waves that may generate hydrodynamic impacts. The slamming coefficient, which is an important non-dimensional force coefficient of slamming load models (see section 1.2.1), is reported to lay between 3 and 7. This can lead to variations of a factor of more than 2 on the impact loads. The formula proposed to model wave impacts are based on the work of Wienke et al. 2005. Paulsen et al. 2019 reported that this formula is highly conservative. Also note that the current recommendations are made for bottom fixed wind turbines, but FOWTs have specificities that may influence the breaking loads. For instance, the turbine may be inclined or moving during an impact. No guidance is given to account for these effects and the literature on the subject is scarce.

The lack of guidance to take breaking wave impacts into account leads the developers of FOWTs to be conservative during the design phase. This increases the cost of the structures and thus slows down the development of offshore wind power. The DIMPACT project aims to get more insights into the loads generated by breaking wave impacts on FOWTs. The final goal is to provide the industry with improved certification guidelines and an appropriate engineering tool to account for breaking wave loads. The work presented here is the experimental part of the DIMPACT project.

1.2 Modelling breaking wave impact loads

In this section, we review the analytical and numerical approaches that may be used to model breaking wave impacts. Analytical approaches are addressed in section 1.2.1 and numerical approaches in section 1.2.2. In the rest of the current work, we define the breaking location of a wave as the point where the free surface first presents a vertical slope. The instant of breaking corresponds to the instant at which the vertical slope appears.

1.2.1 Analytical approaches

Analytical approaches are widely used to compute the forces induced by breaking wave impacts on vertical or nearly vertical cylinders. The load is separated into two parts: a Morison-type load, which is predicted using the Morison model, and an impact load, which may be modelled using various approaches. Most of these approaches rely on the early impact models proposed by Karman 1929 and Wagner 1932. Based on this decomposition, the force acting on the cylinder is expressed as:

$$F = F_D + F_I + F_S, \tag{1.1}$$

where F_D and F_I are respectively the drag and inertia terms of the Morison model and F_S is the slamming force term. We will present here the main approaches that are used to analytically model the slamming term F_S during breaking wave impacts. Most of the actual analytical wave impact models rely on the early work of Goda et al. 1966. In this model, the upper part of the wave front is supposed to be vertical, as described in figure 1.6. The percentage of the wave crest which is vertical is called the curling factor λ. The impact occurs in the region of the cylinder which is hit by the vertical part of the wave

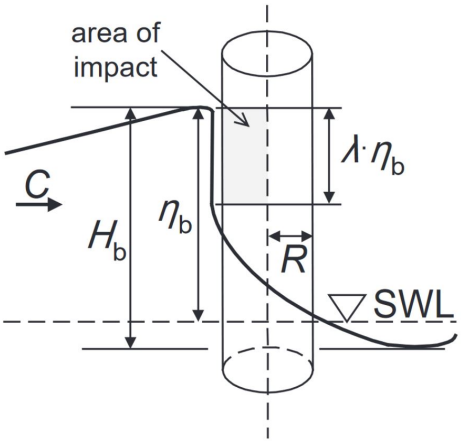

Figure 1.6 – Schematic representation of a breaking wave impacting a cylinder (Wienke et al. 2005)

crest. The vertical part extends over a height $\lambda\eta_b$, where η_b is the height of the crest. The time evolution of the breaking wave impact force per unit length on a vertical cylinder is given by the following relation:

$$f_S(t) = \frac{1}{2} C_S \rho u^2 D \left(1 - \frac{t}{\tau}\right), \tag{1.2}$$

where ρ is the density of the fluid, u is the horizontal fluid velocity and D is the diameter of the pile. Following von Karman's approach, the slamming coefficient C_S is equal to π. The duration of the impact is $\tau = D/2c$. Parameter c is the celerity of the wave. To obtain the total load acting on the cylinder, this formula is integrated over the height $\lambda\eta_b$. The fluid velocity u is assumed uniform and equal to the wave celerity c over this height. The total slamming load is thus:

$$F_S(t) = \frac{1}{2} C_S \rho c^2 D \left(1 - \frac{t}{\tau}\right) \lambda\eta_b. \tag{1.3}$$

A summary of Goda's theory, which was originally published in Japanese, can be found in Sawaragi et al. 1984.

Several improvements to the model of Goda have been proposed. In particular, modifications have been proposed for the time evolution of the force, the value of the slamming coefficient C_S and the value of the curling factor λ. For instance, Wienke et al. 2005 proposed to account for the pile-up effect as described in Wagner's theory. This leads to an increase in the maximum impact force as the slamming coefficient C_S is increased to

2π, and to a reduction of the impact duration. The details of the analytical development, which are not given in Wienke et al. 2005, can be found in Wienke 2001. More recently, another modification of this approach was proposed by Paulsen et al. 2019. The changes are based on experimental results and numerical simulations. The temporal development of the force is supposed to follow a squared sine function and a multiplying factor is added to account for the non-uniform spatial distribution of the load. A new formulation for the curling factor λ based on the vertical pressure distribution during impact is also proposed. Paulsen et al. 2019 carried out wave basin experiments with irregular sea states to derive the wave parameters generating an impact load close to the 100 % non-exceedance probability of the considered sea state. However, the proposed formula does not account for the sea-state steepness, even though it is a parameter controlling the occurrence of breaking. They observed that the shape of a breaking wave is weakly linked to the magnitude of the induced impact force. The explanation proposed by Paulsen et al. 2019 is that the magnitude of the impact force is highly dependent on the distance between the structure and the breaking location, which was not taken into account.

It should be noted that these models are based on the strong assumption that the wave impact takes place at the same time over the height $\lambda\eta_b$. Over this height, the fluid velocity is supposed to be constant and equal to the phase speed of the wave. As it is visible in figure 1.7, the percentage of the crest over which the fluid velocity in the crest of a breaking wave is close to the wave celerity is much smaller than the commonly found values for the curling factor. Moreover, there is no consensus on how to determine the curling factor of a breaking wave. Wienke et al. 2005 consider the curling factor as a calibration parameter. It is adjusted so that the maximum measured impact force matches the predicted maximum impact force. Renaud et al. 2023b took a curling factor equal to 0.4 as it is a commonly used value. Paulsen et al. 2019 proposed a definition of the curling factor based on the measured pressure distribution.

In summary, the different load models presented here all have the following structure:

$$F_S(t) = \beta\nu(t)\rho\eta_b D c^2. \tag{1.4}$$

Function ν is a non-dimensional function describing the time evolution of the force. Its maximum value is equal to one. The parameter β is also non-dimensional and accounts for various effects such as the slamming coefficient, the wave shape through the curling factor and the spatial distribution of the load.

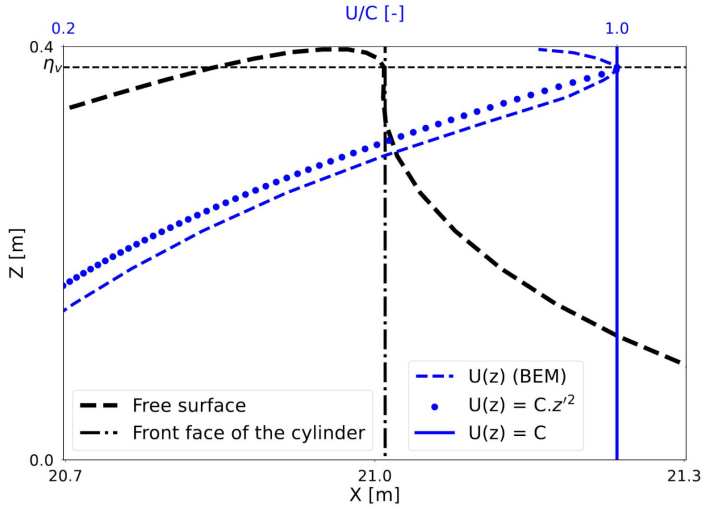

Figure 1.7 – Horizontal fluid velocity in a breaking wave. The black dashed line corresponds to the free-surface elevation, the blue dashed line to the horizontal fluid velocity at the free surface, the blue dotted line to an exponential fit of the horizontal fluid velocity and the blue vertical line corresponds to a fluid velocity U equal to the crest speed C. Extracted from Renaud et al. 2023a.

Another family of analytical models is based on the so-called strip-theory approach. It consists in dividing the cylinder into small horizontal strips. The load is computed independently for each strip based on the free-surface geometry and the fluid kinematics. The three-dimensional effects, *i.e.* the vertical development of the flow, are neglected. These models, compared to the previously presented models, rely on a more accurate description of the impacting wave. This approach makes it possible to account for the vertical distribution of the horizontal fluid velocity and the progressive immersion of the cylinder. The total force acting on the cylinder corresponds to the sum of the forces acting on the different strips. Nestegard et al. 2004 used the free-surface elevation measured at the location of the cylinder to derive the velocity of the impacting fluid. A Wheeler stretching method is applied to the measurements to compute the fluid velocity. Hansen et al. 2017 also used the free-surface elevation measured at the location of the cylinder. They determined if the impact load in a given strip should be considered based on the rate of change of the measured free-surface elevation at the strip. For each strip, the measured free-surface elevation allows to account for the impact load at the instant at which the strip is immersed. One thus obtains a more realistic time evolution of the impact load. The fluid velocity is supposed constant over the height of impact and equal to 80 % of the linear wave celerity at the spectral peak frequency. Other strip-theory approaches such as

the one proposed in Renaud et al. 2023a and Renaud et al. 2023b rely on a fully non-linear modelling of the impacting wave. In each strip, the horizontal fluid velocity u is extracted from a fully non-linear simulation, in which the presence of the cylinder is not taken into account.

One should note that an alternative to the previously described analytical models, called pressure impulse theory, was recently developed by Ghadirian et al. 2019. The pressure impulse theory was initially proposed by Cooker et al. 1995. The pressure impulse is the time integral of the pressure over a period of time. It satisfies Laplace's equation and mixed boundary conditions at the free surface and on the body. An analytical expression of the pressure impulse over the body is obtained through separation of variables and Fourier series analysis. In Ghadirian et al. 2019, the pressure impulse is computed based on an idealized configuration in which the fluid velocity is uniform over the wave height. This methodology allows to obtain pressure impulse distributions on the structure which are consistent with computational fluid dynamics (CFD) results. The pressure impulse model has been used in Ghadirian et al. 2023 to estimate slamming loads on monopiles. It has been coupled to the fully non-linear potential solver OceanWave3D (Engsig-Karup et al. 2009) to compute the loads generated by breaking waves on a vertical cylinder. The probability and peak slamming load obtained using the model were compared to the probability and to the magnitude of the slamming force obtained from long-term experiments. Although the tail of the distribution is not reproduced by the pressure impulse approach, an overall good agreement is obtained between the observed and modelled distributions.

1.2.2 Numerical approaches

A variety of numerical approaches have been employed to model breaking wave impacts. We first present the approaches relying on the potential flow assumption in section 1.2.2.1. The presence of the structure is not accounted for and impact loads are modelled using an *ad hoc* model, for instance one of the semi-analytical models presented in the previous section. Then we present the approaches using Navier-Stokes solvers in section 1.2.2.2. These models are able to account for the presence of the structure.

1.2.2.1 Potential flow solvers

Non-linear potential flow solvers are widely used to model the flow in a wave tank. In these approaches, the fully non-linear boundary conditions are taken into account at

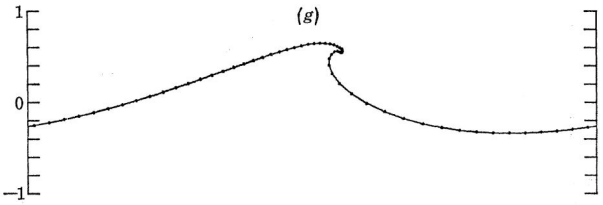

Figure 1.8 – Free-surface profile of a breaking wave obtained with the first proposed boundary element method by Longuet-Higgins et al. 1976

the free surface. Different methods, such as the boundary element method (BEM) (see *e.g.* Longuet-Higgins et al. 1976; Grilli et al. 1989, 1996) or the finite-difference method (Engsig-Karup et al. 2009) have been employed. Highly non-linear methods such as the high order spectral (HOS) method (Ducrozet et al. 2012) are also used. These approaches being non-dissipative, they allow an accurate propagation of the waves. Depending on the model, crest overturning may or not be modelled. For instance the Lagrangian approach used by Grilli et al. 1989 allows to model wave overturning up to the instant at which the wave tongue reconnects with the free surface. Other Eulerian approaches, which rely on a description of the free surface with a single-valued function, do not allow to model a multi-valued free surface. In these types of approaches, wave breaking must be prevented by adding a dissipation term to reproduce the loss of energy induced by breaking (see Seiffert et al. 2018; Mohanlal et al. 2023 for instance). An example of the free-surface profile of a breaking wave obtained using a BEM is depicted in figure 1.8. The velocity distribution along the water column can be computed around the instant of breaking. Such a velocity distribution has been used as an input to the semi-analytical impact model proposed by Renaud et al. 2023a. However, the presence of the cylinder, which modifies the fluid kinematics within the impacting wave, is not taken into account in the method.

1.2.2.2 Navier-Stokes solvers

High fidelity numerical solvers based on the Navier-Stokes equations are also used to model the impact of breaking waves on cylinders (Paulsen et al. 2014; Batlle Martin et al. 2023). In Paulsen et al. 2014 and Batlle Martin et al. 2023, a volume of fluid (VOF) approach is used to track the air-water interface. This approach is able to model wave overturning, viscous effects and the modification of the flow induced by the presence of a structure. Compared to potential flow approaches, the computational cost is several

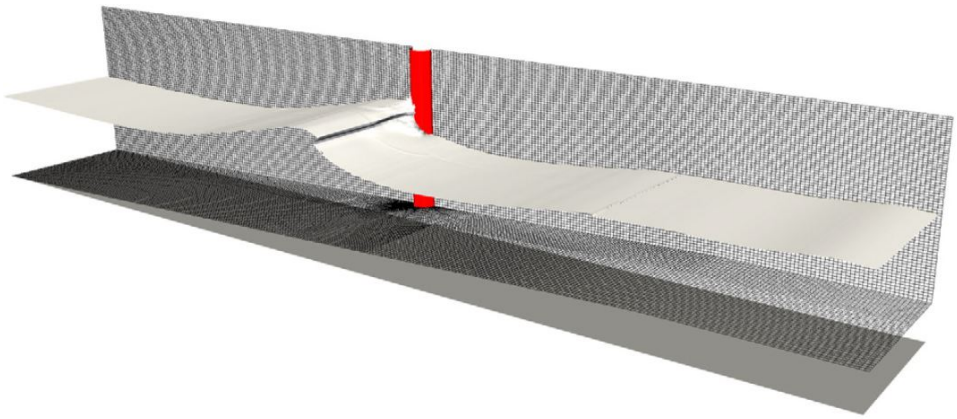

Figure 1.9 – Snapshot of a simulation of a breaking wave impacting a vertical cylinder from Paulsen et al. 2014

orders of magnitude larger. Moreover, the presence of numerical dissipation reduces the ability of the model to accurately propagate waves over a long distance. For this reason, Paulsen et al. 2014 decomposed the domain into an outer part and an inner part. In the outer part, in which the wave propagates, the flow is modelled using the fully non-linear potential flow (FNPF) solver OceanWave3D. In the inner part around the cylinder, in which the interactions with the cylinder take place, the flow is computed using a Navier-Stokes solver. A snapshot of a simulation of a breaking wave impacting a vertical cylinder presented by Paulsen et al. 2014 is depicted in figure 1.9. This model has been further used by Veic et al. 2016 to reproduce the impact of a breaking wave on a vertical cylinder in a wave tank. A comparison between the experimentally measured and modelled forces is shown in figure 1.10. It appears that the time evolution and the magnitude of the load are accurately reproduced by the numerical model. Recently, this model has been used by Paulsen et al. 2019 to investigate the pressure distribution during a breaking wave impact. The new analytical breaking wave impact model proposed in this study was derived according to the results of the numerical simulations.

1.3 Measuring breaking wave impact loads

In this section, we review the different physical measurements of breaking wave impact forces and pressures. We first present in-situ measurements in section 1.3.1. Laboratory experiments, which is the approach adopted in the current thesis, are presented in more details in section 1.3.2. A particular attention is given to the difficulties associated to the

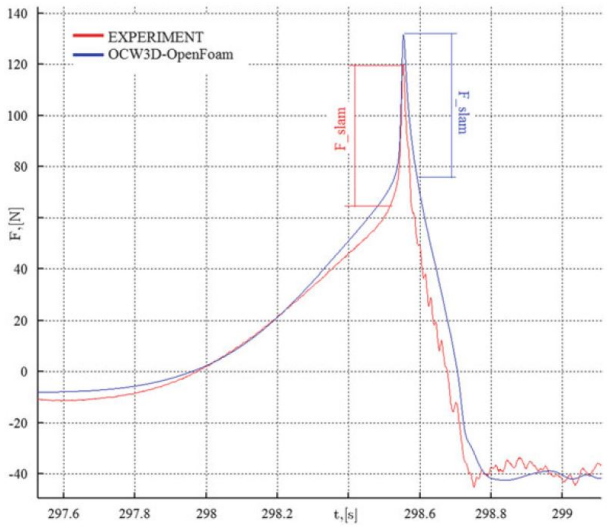

Figure 1.10 – Comparison between the force on a vertical pile modelled using the approach of Paulsen et al. 2014 and of the force measured during experimental tests. Extracted from Veic et al. 2016.

measurement of an impact force on a structure. Impact forces being impulsive, they tend to excite the structure and to induce oscillations on the measured force. In section 1.3.3, the difficulty of isolating the slamming term of the force from the measured hydrodynamic force is discussed.

1.3.1 In-situ measurements

Measuring breaking wave impact loads at sea is a complicated task. To the author's knowledge, the only in-situ measurement of the load induced by breaking waves on a full scale wind turbine reported in the literature was carried out at the Blyth offshore wind farm and is reported by Hallowell et al. 2016. In this study, the mast of a 2 MW bottom fixed wind turbine was equipped with strain gauges. This allowed to indirectly measure the bending moment at different locations of the turbine. Oscillations, which are due to the dynamic response of the structure, are visible on the measured moment. Simultaneously, the free-surface elevation was measured 1.8 m away from the turbine using a wave radar. The radar was used together with the bending moment measurement to detect breaking wave impacts. The measurements at the Blyth wind turbine showed that the highest wave loadings were obtained during breaking wave impacts. They also showed that within a sea state, the waves leading to the strongest impacts are not necessarily the largest or the

steepest waves.

Indirect measurements of the loads acting on offshore structures during wave impacts have also been performed. For example, Antonini et al. 2021 inferred the force acting on the Wolf Rock lighthouse during wave impacts from accelerometers located at different heights on the structure. The main dynamic parameters and mode shapes of the structure were obtained using a shaker placed in the lighthouse and by recording the acceleration at several heights. During a wave impact, the excited mode was identified and the force acting on the structure was reconstructed using an inverse transform. Important uncertainties concerning the magnitude of the force peak are still present. Unfortunately, Antonini et al. 2021 could not link the properties of the impacting waves to the impact loads, as the waves were not recorded during the hurricane. This methodology is promising and could be applied to other structures such as wind turbines. Antonini et al. 2021 advised to record the incoming waves when measuring the loads on offshore structures. This kind of measurements could be obtained with a stereo-video wave acquisition system, which is a promising tool to obtain a spatial measurement of the impacting wave profile. Filipot et al. 2019 successfully measured the profile of a strong breaking wave that impacted the La Jument lighthouse. The simultaneous measurement of the acceleration of the tower showed that the wave induced a dynamic response of the structure. However, no reconstruction of the force was proposed.

Pressure transducers are sometimes also considered to gain more insights into the wave impact loads. For instance the Artha breakwater, located at the entrance of the bay of Saint-Jean de Luz, France, has been equipped with pressure transducers to study the pressure peaks generated by different waves impacting the breakwater (Poncet et al. 2022). Two classes of pressure signals were identified. They correspond to the impact of different types of waves. However, this approach does not allow to obtain the global force acting on the structure.

1.3.2 Wave basin experiments

On-site measurements are scarce and strongly influenced by various phenomena. As the loads are not measured directly but inferred from the measurements of other physical quantities such as acceleration or strain, the results present uncertainties which are difficult to quantify. Finally, the harsh environment complicates the deployment of the sensors and increases the cost of the campaigns. For these reasons, experiments in a controlled environment, such as a wave basin, are very common to study the impact of breaking waves.

Laboratory experiments also play an important role in the validation of the theoretical models presented in section 1.2.

In the following sections, we will present the different experimental approaches used to measure breaking wave impact loads. Note that different challenges arise when one wants to conduct such experiments. To begin with, one needs to generate controlled breaking waves. This aspect is reviewed in section 1.3.2.1. The different methods allowing to measure the generated waves are described in section 1.3.2.2. Another key aspect is the measurement of the induced loads. The different approaches used for this purpose are listed in section 1.3.2.3. The intrinsic low repeatability of the breaking wave impact phenomenon is discussed in section 1.3.2.4. Finally, the frequently encountered issue of force oscillations induced by the vibrations of the mockup is discussed in section 1.3.2.5. Different methodologies that were proposed to tackle this issue will be reviewed.

1.3.2.1 Generation of breaking waves

The first step to experimentally study breaking wave impact loads is to generate breaking waves. They are three main approaches to generate breaking waves: energy focusing, shoaling or generation of an irregular breaking sea state.

The energy focusing method, also called dispersive focusing or focalisation, was described by Rapp et al. 1990. It relies on the fact that waves of different wavelengths propagate with different velocities. It is possible to choose the phases of the different components so that all the components of the spectrum are in phase at a given time and location. If the free-surface elevation at the focus point is high enough, the wave breaks. Phase-focused breaking waves have been used by several authors to investigate the loads generated by breaking wave impacts on vertical cylinders (Kjeldsen et al. 1986; Zhou et al. 1991; Wienke et al. 2005; Manjula et al. 2013; Ha et al. 2020).

Wave shoaling is the process during which a wave propagates over a seabed displaying a decreasing water depth. This leads to a gradual deformation of the wave during its propagation. In particular, the wave height increases up to a point at which the wave breaks. This process can be reproduced in a wave tank using a constant slope, as in the experiments by Antonini et al. 2021 (see figure 1.11), or a bar, as in the experiments of Paulsen et al. 2019 (see figure 1.12). Wave breaking can be obtained through the shoaling of regular, irregular or solitary waves. Other studies making use of this methodology can be found in Sawaragi et al. 1984 and Ma et al. 2020.

Finally, breaking waves can be generated in a steep irregular sea state. In infinite

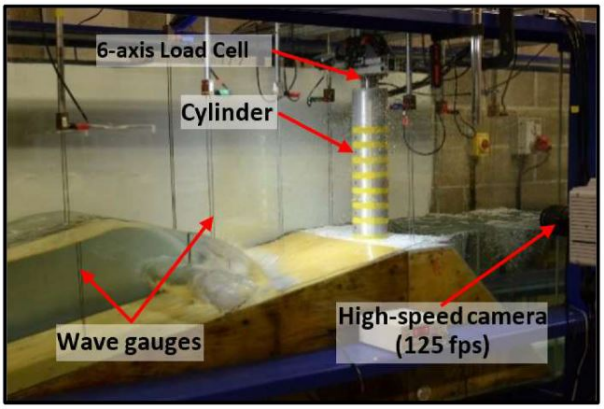

Figure 1.11 – A wave shoaling over a constant slope (Antonini et al. 2021)

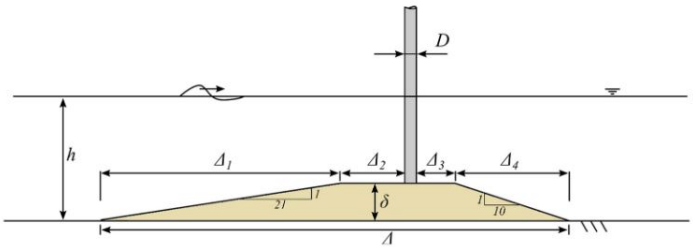

Figure 1.12 – Scheme of the bar over which the waves break in the experiments of Paulsen et al. 2019

depth, this method is more representative of the processes taking place at sea. First, a wave spectrum representative of the wave conditions for a particular site is selected. The spectrum determines the amplitudes of the different wave components and the phases are chosen randomly. Studies relying on this approach are reported by Paulsen et al. 2014; Lian 2018 and Guo et al. 2020. A bar, such as the one shown in figure 1.12, may be used to increase the probability of breaking. This bar was used by Paulsen et al. 2019 to model the effect of a sand bar.

These three approaches have different advantages and are representative of the conditions of different sites. For instance, wave shoaling occurs in shallow waters in which the water depth decreases. It is thus more likely to happen in bottom fixed wind farms than in floating wind farms. Dispersive focusing allows to obtain a single breaking event. The fact that there is no breaking event before the breaking event of interest allows to model the flow with a potential solver such as the one proposed by Grilli et al. 1989. This solver is able to model the crest overturning, but will stop when the wave tongue impacts the free surface. On the contrary, this kind of model is not able to model a breaking irregular sea state. Indeed, the model will stop after the first breaking wave, which will probably not break at the structure. The use of a potential flow solver allows to precisely determine the characteristics of the breaking waves. Thus, the geometry of the wave and its breaking strength can be linked to the measured impact load.

On the other hand, it is difficult to link a breaking wave obtained through dispersive focusing to a breaking sea state. It is thus not clear if a phase-focused breaking wave can be used to represent a wave impact occurring at sea. For instance, in Paulsen et al. 2019, the non-representativity of phase-focused waves is advanced as a possible explanation for the discrepancies observed between their experiments and the theory proposed by Wienke et al. 2005. In the studies relying on steep irregular sea states, statistical data on the occurrence of slamming may be directly derived from long term experiments. As an example, the non-exceedance probability of the magnitude of impact loads obtained by Paulsen et al. 2019 is depicted in figure 1.13. The data for different sea-beds are plotted. The slamming events being rare, the experiments have to be run during a long time to obtain statistically reliable data. As a consequence, the presence of wave reflection or wave diffraction by the cylinder may affect the results. It has also been observed by Canard et al. 2022 that, even if the measured spectrum corresponds to the target spectrum, the number of extreme events may differ from its corresponding number at sea. This is due to the fact that the waves only propagate over a short distance in a wave basin, which does

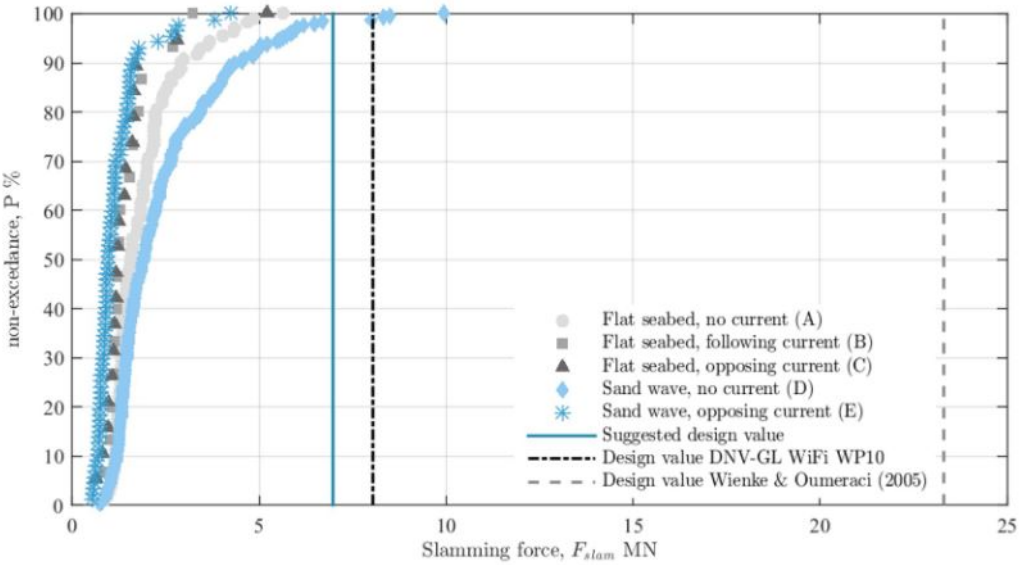

Figure 1.13 – Non-exceedance probability of the magnitude of slamming on a vertical pile for different sea-beds (Paulsen et al. 2019)

not allow the non-linear effects to fully develop. This could lead to an underestimation of the number of breaking events.

In summary, focused breaking waves are useful if one wants to precisely relate the parameters of a breaking wave to the load it will generate. However, if one is more interested in directly determining the probability of wave impact in a given sea state, irregular sea states should be used.

1.3.2.2 Measurement of breaking waves

In order to study the influence of the wave parameters on the impact loads, it is important to precisely characterise the waves. The free-surface elevation of a wave is usually measured using standard wave gauges which measure the water elevation locally. However, wave gauges do not allow to measure the slope of the wave front and the speed of the crest, which are critical parameters in the slamming process. To overcome this limitation, it is possible to use several gauges located in a region of interest. The number of gauges is nevertheless limited by their size and their cost. Swan et al. 2015 obtained more measurement points by generating the same waves several times and by changing the position of the gauges at each repeat. This technique is very time consuming and relies on the assumption that the wave field is perfectly repeatable. Baldock et al. 1994

proposed to use a point measurement and a double Fourier series expansion in space and time to reconstruct the fluid kinematics in a region around the point of measurement. The measured free-surface elevation is taken into account in a least-square minimization which determines the amplitude of the components of the Fourier series. A promising approach to directly measure the wave surface is stereo-video. The current methods rely either on seeding the flume, or on a sophisticated laser lightning (Savelyev et al. 2018). Le Page et al. 2023 are currently working on a simpler set-up that would allow stereo-video reconstruction in a wave basin.

For two-dimensional waves, it is possible to measure the evolution of the interface between the air and the water at the wall of the flume using a video camera. The most common methodology consists in filming the interface between the air and the water through a glass wall. This methodology has been applied successfully by several authors (Kimmoun et al. 2010; Hernández et al. 2018; Ma et al. 2020). Different techniques are used to detect the interface on the image. Ma et al. 2020 converted the gray-scale images into binary images out of which the contour, which corresponds to the free-surface elevation, is extracted. Hernández et al. 2018 computed the free-surface elevation through the use of the percentage of black pixels in an area of the binary image expanding vertically. The camera is positioned on the side of the flume. The use of a glass wall allows to place the camera perpendicularly to the wall, so that the plane of the camera sensor is parallel to the plane of the wall. This avoids geometric distortions of the images. It is thus possible to use an object of known dimensions to determine the position of a point located in the plane of the glass wall. These techniques require to set the camera perfectly perpendicular to the glass wall. If this is not the case, a geometric distortion is induced and the "real world" size of a pixel will be dependent on the pixel position on the sensor.

To the best of the author's knowledge, only one attempt of measuring the free-surface elevation in a flume with non-transparent walls is reported in the literature (Dorfman et al. 2007). In this experiment, the interface between the wall and the flume is filmed from above. Filming the interface from above may be an advantage: when the free surface is filmed perpendicularly through a glass wall, the intersection between the opposite wall of the flume and the free surface is also visible on the images and is very close to the intersection between the glass wall and the free surface. The contour detection algorithm may thus detect the rear intersection, which would falsify the measurements. However, when filming from above, the "real world" size of a pixel is pixel dependent and an external calibration procedure of the video camera is required. Dorfman et al. 2007 did

the calibration using a square pattern placed on the wall of the flume. The coordinates corresponding to the interface are detected using a contour detection algorithm and by assuming that the interface on a given image is close to the interface on the previous image. The distortion induced by the camera was neglected.

1.3.2.3 Measurement of the hydrodynamic loads

The different experiments that were carried out to measure breaking wave impact loads on a vertical cylinder display very different set-ups. One common approach consists in measuring the total force at the base of the cylinder (Hansen et al. 2017; Suja-Thauvin et al. 2017; Shi et al. 2023). The cylinder is mounted on a load cell which is attached to the bottom of the flume. This approach allows to model the dynamic response of a bottom fixed wind turbine subjected to breaking wave impacts, as it is done in Suja-Thauvin et al. 2017. An alternative consists in measuring the total load at the top of the cylinder (Esandi et al. 2020; Ma et al. 2020; Antonini et al. 2021) or at both ends (Wienke et al. 2005; Paulsen et al. 2019). Measuring the load at both ends allows to stiffen the mockup and to increase its natural frequencies. However, with this kind of set-up, it is not possible to obtain the distribution of the load along the cylinder and to separate the impact load, which acts on the upper part of the cylinder, from the rest of the hydrodynamic load. In some studies (Paulsen et al. 2019), pressure sensors were added along the cylinder to obtain the vertical pressure distribution. They allow to obtain a spatial distribution of the load. For instance, Paulsen et al. 2019 used the pressure sensors to determine the curling factor. Other studies (Zhou et al. 1991; Manjula et al. 2013) only focused on the pressure distribution and the total force resulting from the pressure distribution was not measured. Both studies investigated the effect of the distance between the cylinder and the breaking location. Even though pressure measurements provide some interesting insights on the wave impact phenomenon, the lack of a global force measurement makes it less attractive from a structural point of view. Pressure measurements are also very sensitive to the experimental conditions. It has been reported by Van Nuffel et al. 2011 that a special care must be given to the mounting of the sensors to avoid measurements artefacts. In particular, the membrane of the sensor needs to be perfectly flush with the surface of the mockup. A bad mounting could lead to air trapping or turbulence that would falsify the pressure measurements. Van Nuffel et al. 2011 also explained that the pressure sensors may be sensitive to the temperature shock occurring at the instant of impact. They recommend to dry the sensors between the repeats in order to increase the

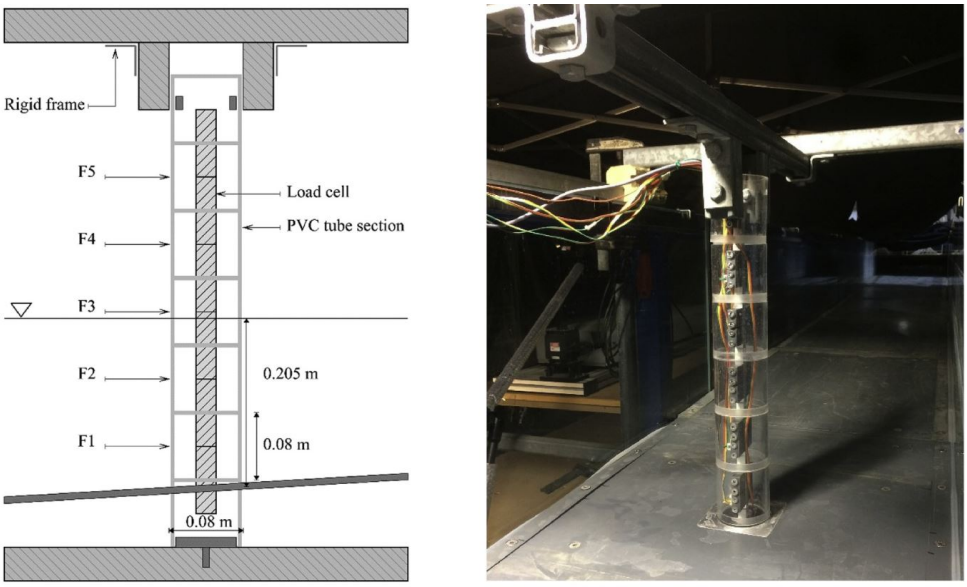

Figure 1.14 – Sketch and image of the segmented mockup used during the experiments presented in Vested et al. 2020

repeatability of the measurements. Indeed, they observed an important difference in the mean values of the measured impact pressure between the case of a dry mockup and of a wet mockup.

A compromise between global force measurements and pressure measurements is to measure the force acting on a portion of the model. The most common design is the so-called "segmented model". In this kind of approach, the mockup is divided into cylindrical sections and the force is measured on each section. This approach was used in several studies (Sawaragi et al. 1984; Kjeldsen et al. 1986; Vested et al. 2020). An example of a segmented model is depicted in figure 1.14. This mockup, which was used in the experiments reported by Vested et al. 2020, consisted in five cylindrical sections mounted on an inner beam through force sensors. The load is thus independently measured on each section. In some experiments, the vertical extent of the sections is much smaller and a finer vertical load distribution can be obtained. For instance, in the experiments of Kjeldsen et al. 1986, the cylinder was divided into 26 load cells with various heights (see figure 1.15a). In total, the instrumented part of the cylinder was 2.40 m high. At the expected location of impact, the cells were 5 cm high. The load distributions obtained during the impact of a plunging wave and of a non-breaking wave are depicted in figure 1.15b. The non-breaking wave is higher and has a longer wavelength than the breaking wave. Nevertheless, the force generated by the breaking wave is much larger than the

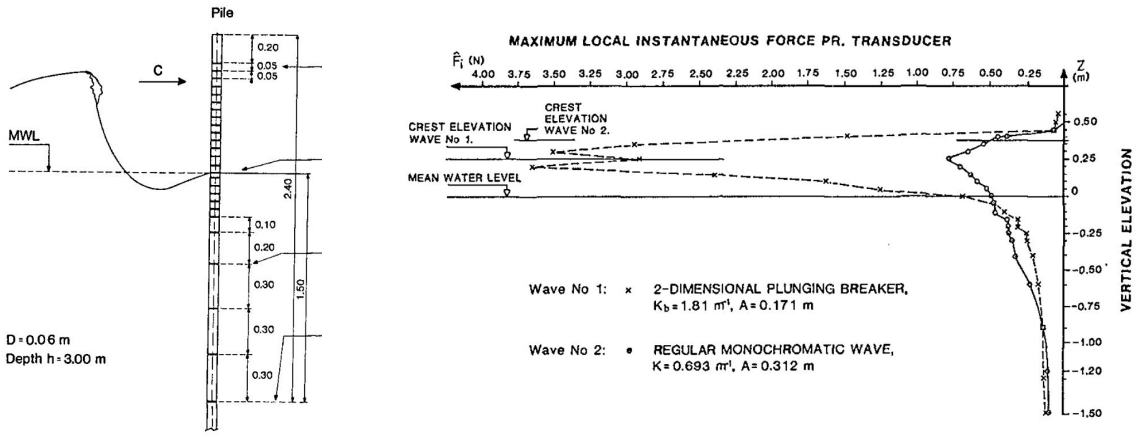

(a) (b)

Figure 1.15 – (a) Illustration of the mockup used in the experiments of Kjeldsen et al. 1986. (b) Comparison between the horizontal force profiles measured during the impact of a plunging breaker and of a regular monochromatic wave. (K is the wave number and A is the wave amplitude.)

force generated by the non-breaking wave. In particular, large loads are observed above the still water level (SWL), in the area over which the wave front impacts the cylinder. The magnitude of the force acting in this area is increased by a factor of four.

Another design which may be encountered consists in using square load cells that allow to measure the vertical and radial load distribution on a cylinder. A picture of such a mockup (Lian 2018) is depicted in figure 1.16. This design requires a large number of load cells, which are rather expensive components. In the experiments reported in Lian 2018, the cells did not cover the entire mockup. Square load cells were also used in the experiments of Ha et al. 2020.

Compared to pressure measurements, the use of a segmented model allows to be less sensitive to the experimental conditions and to increase the repeatability of the measurements. Compared to total load measurements, a finer distribution of the load is obtained. A segmented model allows to study the load acting on a reduced region, for instance the part of the cylinder above the SWL on which impact occurs. Finally, the natural frequencies of the segments of a segmented mockup are higher than the natural frequencies of a model with total force measurement. Indeed, the parts which are fixed on a load cell being lighter and smaller, they have higher natural frequencies. This eases the process of removing the dynamic response of the model from the load measurements.

Figure 1.16 – Description of the cylinder used in the experiments of Lian 2018. From left to right, the pictures display the cylinder fixed in the basin, the force transducers numbering and the force transducers and steel plates.

1.3.2.4 Repeatability of breaking wave impact load measurements

When studying breaking wave impacts, a low repeatability of the experiments is often reported. For instance, Maes et al. 2018 reported that "the variation in the wave elevation, wave pressure, and therefore the wave impact load observed for different experiments with the same input parameters is very large and often even larger than the variation between experiments with different input parameters." In the study of Ha et al. 2020, the same breaking wave impact experiment was repeated 20 times to study its repeatability. The resulting force histories are depicted in figure 1.17. It appears that the time at which the force starts to increase and its magnitude are not repeatable. The low repeatability of the incoming waves is often mentioned as a source of discrepancies between the different repeats of the same experiment. Scharnke et al. 2019 observed that from one repeat of a wave to the other, the measured free-surface profile may vary significantly. To increase the repeatability of the incoming wave profile, Kimmoun et al. 2010 recommended to remove the high-frequency content from the wave paddle motion, to wait for a long time between each repeat in order to ensure that the flume is at rest, and, if possible, to do all the experiments on the same day so as to minimize the water depth variations induced by evaporation. Even slight variations in the wave profile are reported to induce important variations on the measured impact loads. Indeed, it is known that a small variation in the relative angle between the free surface and the body has a strong effect on the impact force. This is highlighted in the experiments of Campbell et al. 1980, in which the force applying on a horizontal and a nearly horizontal cylinder entering calm

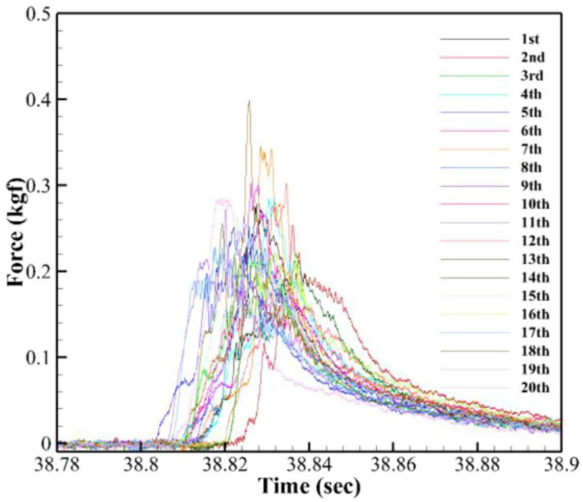

Figure 1.17 – Time histories of the force measured during 20 repetitions of a spilling wave impact (Ha et al. 2020). The load is measured on force panels that do not cover the entire surface of the cylinder.

water was measured. It appeared that an angle of 1° reduces the slamming force by a factor of two with respect to the horizontal cylinder.

1.3.2.5 Force signal oscillations induced by the vibrations of the structure

Another commonly encountered issue when measuring impact loads is the emergence of signal oscillations induced by structural vibrations. As it can be observed in figure 1.10, impact loads are rather impulsive. The slamming part of the load, F_S, which acts on the upper part of the cylinder, contains frequencies much higher than the load acting on the bottom part of the cylinder. The load acting on the bottom is closer to the load generated by an oscillatory flow. The load cell, as well as the mockup, are elastic bodies. Wave impacts may trigger different modes of vibration of the structure. As a consequence, the measured load can be affected by the dynamic response of the structure and not correspond to the hydrodynamic load acting on the structure. The oscillations induced by the response of the structure may be removed by low-pass filtering the force signal. However, this would also remove the high frequency content of the impact force.

To overcome this issue, the first option consists in designing a mockup as stiff and light as possible in order to increase its natural frequencies, so that they are above the frequency content of the impact load. For instance, the half-ring force transducers used by Sawaragi et al. 1984 displayed a fundamental frequency of 2000 Hz. This is high enough to be out

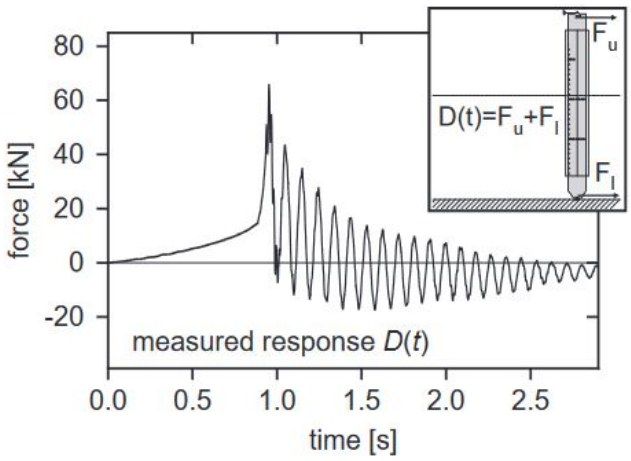

Figure 1.18 – Load measured during a breaking wave impact on a vertical cylinder. Extracted from Wienke et al. 2005.

of the slamming load frequency range. However, they give no information concerning the fundamental frequency of the whole set-up. This frequency is probably lower than the natural frequency of the half rings and its vibration may affect the force measurement.

In total force measurement approaches, the force signal oscillations are often due to the global response of the structure. In the case of an elongated cylinder, the response of the structure is dominated by the bending mode. Unfortunately, even with very lightweight composite materials, it is in general not possible to increase the natural frequency of the bending mode so that it is higher than the upper bound of the spectrum of the impact force. Indeed, for very lightweight structures, the added mass becomes preponderant so that a reduction of the mass of the structure only has a small effect on the natural frequencies. The difficulty of obtaining a high enough response frequency of the force transducer was already highlighted in the early work of Campbell et al. 1980, who studied the impact force acting on a horizontal cylinder slamming into calm water. The same issue is visible in the breaking wave impact force measurement on a vertical cylinder of Wienke et al. 2005 depicted in figure 1.18. The cylinder was fixed with load cells at both ends, which increases its natural frequencies. Wienke et al. 2005 isolated the slamming part of the hydrodynamic force by subtracting the force measured during the impact of a similar non-breaking wave. To remove the effect of the dynamic response of the structure, they applied a deconvolution technique on the slamming part of the force. In their approach, the time evolution of the force is assumed to correspond to the time evolution of the force acting on a horizontal cylinder impacting on calm water. The curling factor λ, *i.e.* the

length over which the force applies, is chosen so as to obtain a good agreement between the measured force and the convolution between the assumed time history and the response function of the structure. More elaborated inverse techniques have since been proposed by Maes et al. 2018 and Antonini et al. 2021. Both methods rely on the knowledge of the dynamic properties of the structure. Note that rather strong assumptions concerning the spatial load distribution over the cylinder are made. In the inverse Bayesian approach proposed by Antonini et al. 2021, one has to select an *a priori* for the force time evolution. Both approaches rely on rather complex theories that complicate their understanding and application.

The empirical mode decomposition (EMD) has been used by some authors to remove the effect of dynamic amplification. Choi et al. 2015 applied the EMD to remove the force oscillations induced by the dynamic response of a pile during breaking wave impacts. This technique was improved later by Spinosa et al. 2022. They applied it to remove oscillations induced by the carriage and the servo-actuator during the experimental modelling of aircraft ditching. Their technique, known as ensemble empirical mode decomposition (EEMD), allows to reduce the variability of the decomposition from one test to the other. Similarly to filtering, EMD methodologies are purely numerical and are not based on the physics of the problem.

1.3.3 Identifying the slamming force in the measured hydrodynamic force

We saw in section 1.2.1 that most analytical approaches rely on the assumption that the hydrodynamic force can be decomposed into a slamming term F_S and two Morison terms F_I and F_D. An important number of studies are devoted to the improvement of the prediction of the slamming term F_S. However, if one carries out experimental force measurements or numerical simulations, the obtained force is the sum of both components. To study the slamming term F_S, it must be separated from the total hydrodynamic force. Unfortunately, this separation is merely theoretical, and there is no consensus on the method that should be used to separate the impact force from the total hydrodynamic force. Ghadirian et al. 2023 compared several methods to separate the impact force from the regular force in experimental force measurements. In figure 1.19, the results obtained with the six different methodologies considered by Ghadirian et al. 2023 are depicted. The shaded area corresponds to the part of the force which is identified as the slamming

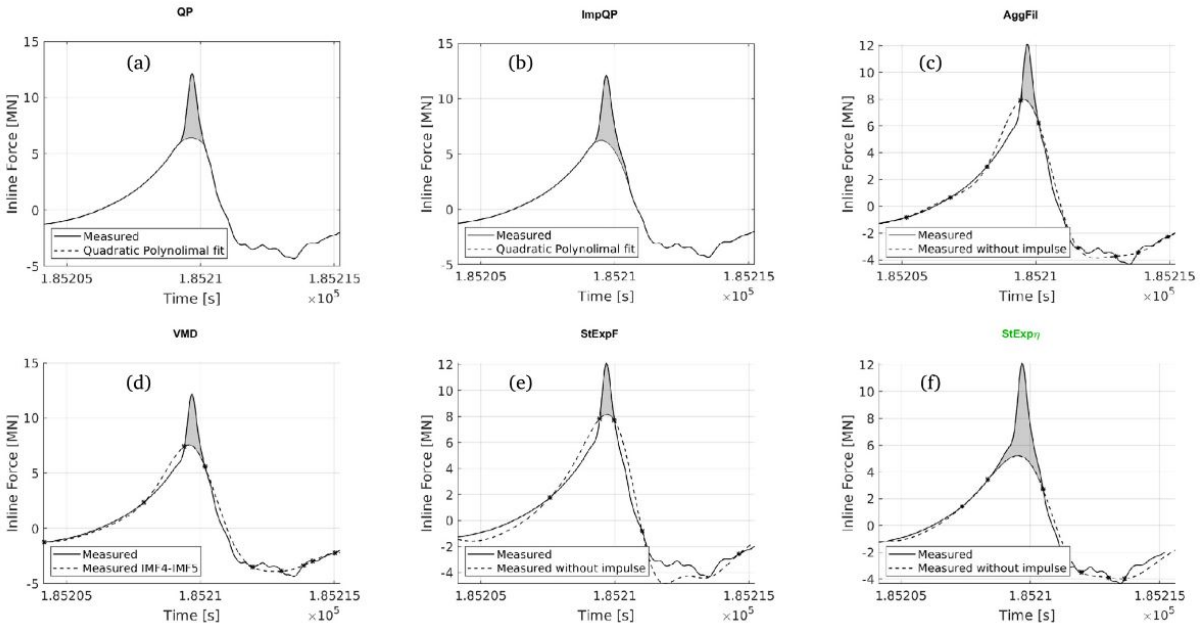

Figure 1.19 – Application of different methodologies to isolate the slamming term F_S from the measured hydrodynamic force. Extracted from Ghadirian et al. 2023.

term F_S. It appears that the different methodologies yield different slamming forces. Also note that the considered criteria are based on numerical thresholds, such as the presence of an inflection point in the force measurement, and not on physical considerations. The application of these methodologies may be more complicated if one tries to apply them to experimental measurements displaying more perturbations, for instance oscillations induced by the structural response of the mockup. If the signal is oscillatory, it will display several inflection points. The implementation of these methods by Ghadirian et al. 2023 was likely eased by the fact that the force measurements were low-pass filtered at 3 Hz.

Wienke et al. 2005 computed the slamming force by subtracting from the total force measurement the force measured when the wave is breaking after the cylinder. The subtracted force is expected to correspond to the force that is generated by an "equivalent" non-breaking wave. However, as it has been pointed out by Wienke et al. 2005 themselves, the wave shape evolves from one case to the other, thus limiting the validity of the approach. Paulsen et al. 2019 did not try to isolate the impact force from the measured hydrodynamic force. They used the depth integrated force, *i.e.* the total force measured on the cylinder. They observed that, during a slamming event, the magnitude of the impulsive part of the force was of the order of the non-impulsive part of the force. Slamming

events were thus identified when the depth-integrated force rapidly exceeded three times the standard deviation of the force. Sawaragi et al. 1984, who used a segmented mockup, computed the impact force as the sum of the forces measured on the sections above the SWL. In their approach, a part of the non-impulsive force is contained in the impact force. However, this definition has the advantage of being unambiguous and simple.

1.4 The different parameters affecting breaking wave impact loads

In this section, we review the parameters which are known to influence the loads generated by breaking wave impacts on a cylinder. The different parameters identified in the literature are listed in section 1.4.1. The effect of the distance between the breaking location and the structure is discussed in section 1.4.2. The diffraction of the wave by the structure is addressed in section 1.4.3. Finally, two parameters specific to FOWTs are reviewed. The influence of the pitch angle of the cylinder is addressed in section 1.4.4 and the influence of the horizontal velocity of the cylinder in section 1.4.5.

1.4.1 Wave parameters affecting breaking wave impact loads

Several parameters of a breaking wave are known to influence the impact load. In the analytical formulas presented in section 1.2.1, the maximum force generated by a breaking wave impact is assumed to be proportional to the square of the fluid velocity. In many analytical formulas, the velocity of the fluid is approached by the celerity of the crest c_b. In analytical approaches, the impact force is often obtained by integrating the force per unit length f_s over the height over which impact is assumed to occur. This height is $\lambda\eta_b$, where η_b is the height of the crest of the wave and λ is the curling factor, which corresponds to the percentage of the wave crest height over which impact is assumed to occur. The curling factor is linked to the breaking strength of the impacting wave. Indeed, Goda et al. 1966 reported that plunging breakers display a curling factor of 0.4 while spilling breakers display a curling factor of 0.1. Unfortunately, as mentioned in section 1.2.1, there is no widely accepted definition of the curling factor. The range of curling factors reported in the literature is very wide: Sawaragi et al. 1984 reported curling factors ranging from 0 to 0.9 and Paulsen et al. 2019 from 0.1 to 0.7.

A measure of the breaking strength of a wave, denoted by Γ, was recently introduced

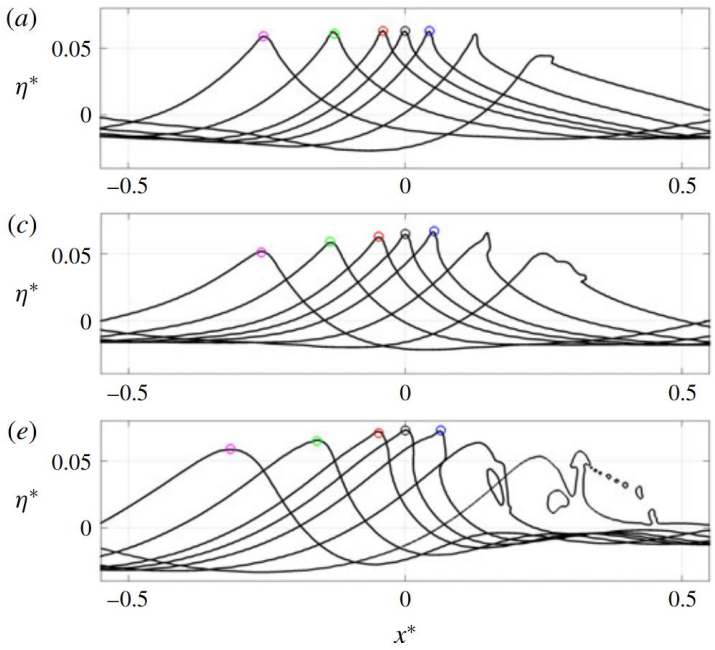

Figure 1.20 – Free-surface profiles of breaking waves showing different breaking strengths Γ. Derakhti et al. 2018 reported that the first wave (a) has a Γ value of 0.45, the second wave (c) of 0.83 and the third wave (e) of 1.44.

by Derakhti et al. 2018 based on the breaking inception criterion of Barthelemy et al. 2018. Derakhti et al. 2018 showed that the energy dissipated during a breaking event is correlated to the Γ parameter. In figure 1.20, the free-surface profiles of breaking waves displaying different values of Γ are depicted. Visually, it appears that the higher the breaking strength Γ is, the more important the percentage λ of the front which is vertical at breaking is. The parameter Γ, which definition is unique, may thus be a good candidate to account for the breaking strength during breaking wave impacts. Note that the computation of the Γ parameter requires to have access to the fluid kinematics at the crest of the wave.

1.4.2 Distance between the breaking location and the structure

In the current work, the breaking location of a wave is defined as the point at which the free surface presents a vertical slope for the first time. The instant of breaking corresponds to the instant at which a vertical slope appears. The distance between the breaking location and the front face of the cylinder influences the impact load. This distance, denoted by δ in the following, is illustrated in figure 1.21. It appears that the shape of the

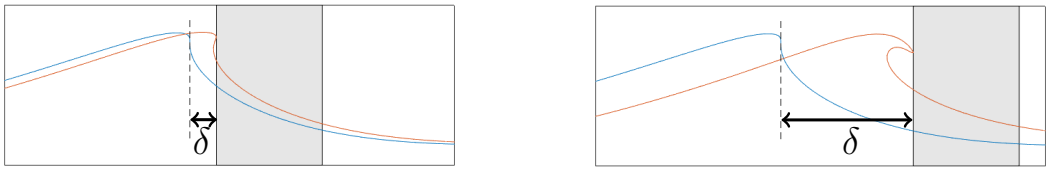

(a) (b)

Figure 1.21 – Illustration of the δ parameter. The blue free-surface profiles correspond to the profile at the instant of breaking, *i.e.* when the free surface has a vertical slope for the first time, and the orange one to the profile at the instant at which the wave impacts the cylinder. The shaded area represents the cylinder.

wave at impact strongly evolves for different values of δ. Different authors have shown that to obtain impact loads, *i.e.* loads showing an impulsive increase, the δ parameter must lie within a given range. For instance, Zhou et al. 1991 reported that impact pressures are only obtained if δ is smaller than 10 % of the characteristic wavelength. They also reported that within this region, the breaking loads can vary significantly. Chan et al. 1995 found that impact pressures are obtained if δ is smaller than 20 % of the characteristic wavelength. A few studies investigated the influence of the δ parameter by systematically varying its value (Sawaragi et al. 1984; Ma et al. 2020; Zhu et al. 2022). Sawaragi et al. 1984, whose results are depicted in figure 1.22, showed that the strongest impact loads are observed when the impacting wave already started overturning ($\delta > 0$). In figure 1.22, the non-dimensional maximum impact force $F^*_{lp} = F/(0.5\pi\rho c_b^2 D\eta_b)$ is plotted as a function of x_b/L for waves displaying different breaking strengths. The force F corresponds to the sum of the forces acting on the sections located above the SWL, the distance x_b to the distance δ and the length L to the characteristic wavelength. Note that the definition of the breaking location adopted in the different studies does not always correspond to the definition adopted in the present work. Similarly, the definition of the characteristic wavelength depends on the study and is not always clearly defined. More recently, Ma et al. 2020, whose results are depicted in figure 1.23, showed that the maximum impact load is obtained when the front face of the cylinder is at a point located between the breaking location and the impingement point. The impingement point is the point at which the tongue of the breaking wave touches the water surface. Note that the non-dimensionalization adopted by Ma et al. 2020 does not correspond to the one used by Sawaragi et al. 1984.

In spite of the significant effect of the δ parameter on the impact load, to the best of

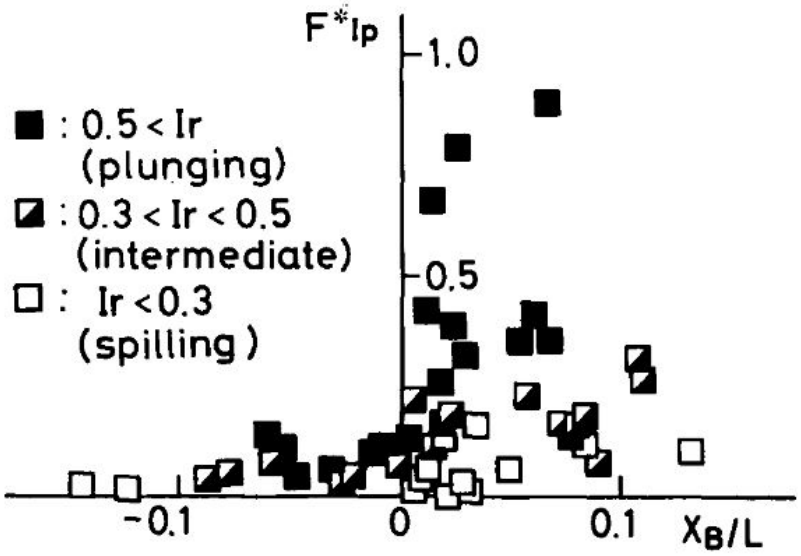

Figure 1.22 – Relation between the non-dimensional impact force and x_B/L, where $x_B = \delta$ is the distance between the breaking location and the cylinder and L is the characteristic wavelength. Extracted from Sawaragi et al. 1984.

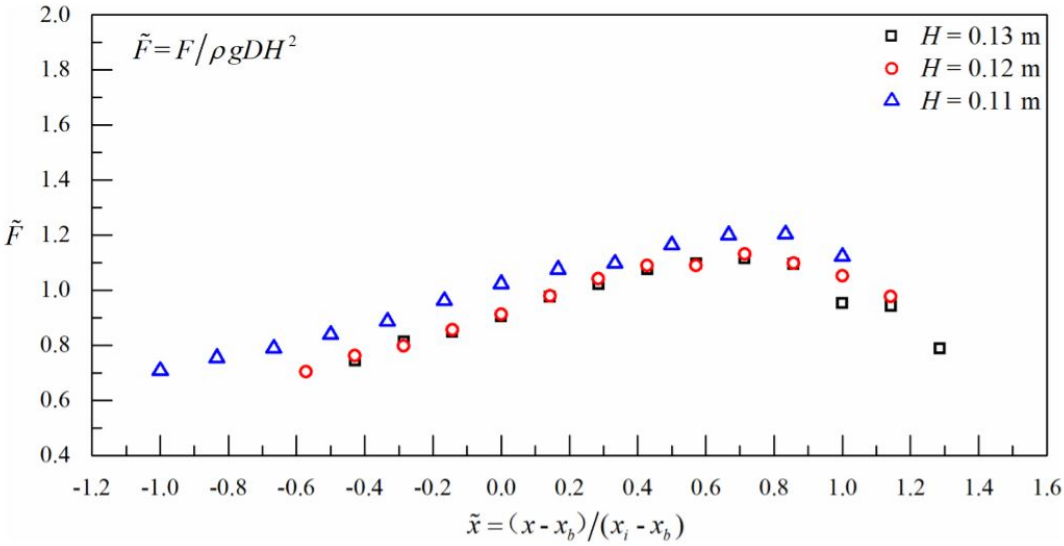

Figure 1.23 – Relation between the non-dimensional impact force and the non-dimensional distance to breaking obtained by Ma et al. 2020. Parameter H corresponds to the height of the shoaling waves. The impact force is non-dimensionalized by $\rho g D H^2$. The distance $x - x_b$, which corresponds to δ, is non-dimensionalized by the distance between the impingement point and the breaking location. The impingement point is the point at which the tongue of the breaking wave touches the water surface.

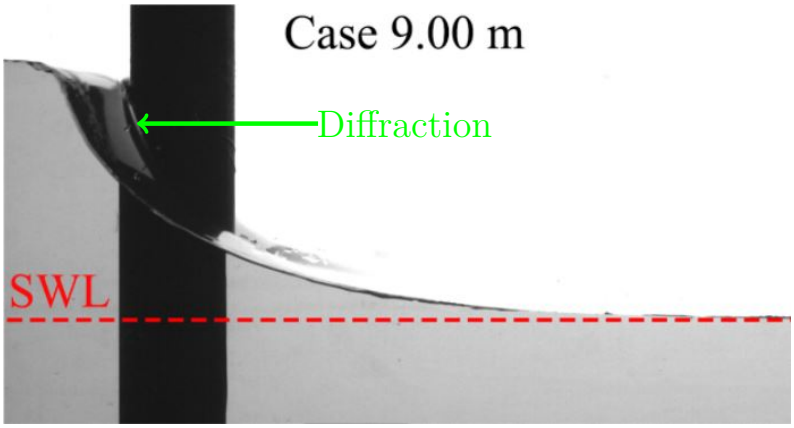

Figure 1.24 – Picture of a breaking wave impacting a vertical cylinder (Ma et al. 2020). The green arrow shows the diffraction of the wave by the cylinder.

the author's knowledge, no attempt to include δ into the analytical load formulations has been undertaken so far. We think that this may explain the lack of correlation between the characteristics of a given breaking wave and the magnitude of the generated impact force observed by some authors (Paulsen et al. 2019; Guo et al. 2020). Indeed, since the slamming load is highly dependent on δ, a strong breaking wave may induce a smaller peak force than a mild breaking wave. Moreover, in some studies (Wienke et al. 2005; Ghadirian et al. 2023), the curling factor is adjusted so that a good agreement is obtained between the measured force and the proposed model. With such an approach, the same wave impacting at different values of δ may display different curling factors.

1.4.3 Influence of the diffraction of the incident wave by the cylinder

When a wave approaches a fixed vertical cylinder, the presence of the cylinder may modify the shape of the free surface. This phenomenon, which we call "diffraction " in the following, may generate run-up. This is highlighted by figure 1.24, where the modification of the free surface induced by the cylinder is visible. This modification may distort the front of the breaking wave and affect the impact load. It has been reported by Ha et al. 2020 and Renaud et al. 2023b that the diffraction may mitigate the severity of the impact load. Renaud et al. 2023b even reported that for some gentle breaking waves, the diffraction may prevent the load to impulsively increase. Batlle Martin et al. 2023

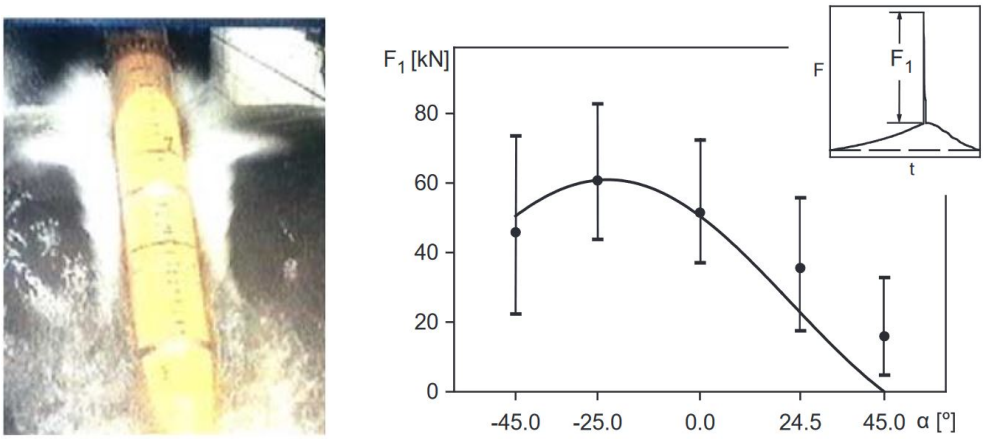

(a) (b)

Figure 1.25 – (a) Picture of a breaking wave impacting a cylinder with a 45° pitch angle. (b) Evolution of the maximum of the impact force as a function of the pitch angle. Extracted from Wienke et al. 2005.

compared the wave profiles distorted by the cylinder to the undisturbed wave profiles. They also concluded that diffraction mitigates the severity of impact.

1.4.4 Pitch angle of the cylinder

During a breaking wave impact, a FOWT may be inclined. This inclination, characterised by the pitch angle θ, has been studied by Tanimoto et al. 1987, Irschik et al. 2004 and Wienke et al. 2005. In the two last studies, five configurations with angles in the range [-45; 45]° were tested. Five configurations in the range [-30; 30]° were investigated in the study by Tanimoto et al. 1987. A picture of a breaking wave impacting a cylinder with a 45° pitch angle captured during the experimental campaign reported by Wienke et al. 2005 is depicted in figure 1.25a. The evolution of the magnitude of the impact force as a function of the pitch angle measured by Wienke et al. 2005 is depicted in figure 1.25b. It appears that up to an angle of approximately 25°, a pile inclined towards the wave maker experiences a higher impact load than a vertical pile. Lower loads occur when the cylinder is inclined in the opposite direction. However, such large angles are not encountered by FOWTs. It is thus of importance to investigate the influence of smaller pitch angles that are representative of the inclination of a FOWT during breaking wave impacts. To the best of the author's knowledge, the influence of smaller angles on the impact force has not been investigated yet.

It is worth noticing that in the study by Wienke et al. 2005, the rotation of the cylinder is made around the point located at the intersection between the axis of the cylinder and the bottom of the flume. Given the geometry of the set-up, a rotation of 45 ° induces a horizontal shift of 5 m of the impact area of the cylinder. The wavelength L of the impacting wave being around 22 m, the inclination induces a variation of δ/L close to 0.25. Following the results of Sawaragi et al. 1984 depicted in figure 1.22, such a variation of δ/L may induce a significant variation of the maximum impact force. It is thus to be expected that the variations observed by Wienke et al. 2005 when the pitch angle of the cylinder is varied are strongly affected by the horizontal shift of the impact location. The same rotation point is used in the study by Irschik et al. 2004. In the study by Tanimoto et al. 1987, the rotation point corresponds to the intersection between the SWL and the axis of the cylinder. This reduces the shift in δ at the height of impact. It corresponds to a shift in δ/L of 0.02 for the longest waves and of 0.05 for the shortest one. Even if this shift is reduced compared to the work of Wienke et al. 2005, it is high enough to influence the impact load.

1.4.5 Horizontal velocity of the cylinder

A FOWT may be moving during a breaking wave impact. It is expected that a motion in the wave propagation direction decreases the impact load while a motion against the wave propagation increases the impact load. So far, very few results on the subject are available. To the best of the author's knowledge, the only breaking wave impact experiments on a moving cylinder were reported by Saincher et al. 2022 who aimed to study the simultaneous loading of breaking waves and current on a monopile. The mockup was towed in the direction opposite to the wave propagation direction.

However, it has been shown by Guo et al. 2020, who analyzed the displacements of a reduced-scale semi-submersible offshore platform in a breaking sea state, that a floating structure tends to be following the waves when a breaking wave impact occurs. During the strongest wave impacts recorded by Guo et al. 2020, the platform was always moving in the wave propagation direction. This naturally mitigates the severity of the breaking wave impacts. Similar conclusions were drawn in an unpublished preliminary work of the DIMPACT project during which the motion of different FOWT designs in a breaking sea-state where simulated (Peyrard et al. 2021). For FOWTs, it is thus more relevant to study the effect of the structure motion in the wave propagation direction than in the opposite direction.

1.5 Objectives and outline of the thesis

1.5.1 Conclusions on the literature review

Even if breaking wave impacts are already taken into account during the design of FOWTs, it appeared that significant progress is required to predict with confidence the impact loads that may be encountered by a FOWT during its lifetime. Even in controlled experimental environments, measuring the impact load generated by a breaking wave is challenging: the experiments suffer from a low repeatability and the impulsive nature of the impact force may induce a dynamic response of the set-up which complicates the interpretation of the results. The distance δ between the breaking point and the front of the cylinder and the diffraction of the wave, which seem to significantly influence the impact load, are not taken into account in current analytical impact formulas. Moreover, the link between the breaking strength of the wave and the curling factor λ is not clear. In addition, there is no consensus on the definition of the curling factor, and in some approaches, the same wave impacting at different distances δ may be associated to different values of δ. Finally, the effect of the motion and inclination of the turbine at impact, which is important in the case of FOWTs, has barely been studied until now.

1.5.2 Objectives of the thesis

The present PhD work aims to experimentally assess the influence of the different parameters that may affect the impact force generated by a breaking wave on a FOWT. The final goal is to include these parameters into the FOWT design formulas for the assessment of slamming loads. The case study selected for this investigation is a vertical circular cylinder. This geometry represents an idealized SPAR-type FOWT. The parameters that have been studied are the breaking strength Γ of the impacting wave, the distance δ between the breaking location and the front face of the cylinder, the inclination θ of the cylinder and its horizontal velocity V. We aim to quantitatively assess the importance of these different parameters. For this reason, it is necessary to accurately characterise the breaking waves and to precisely control the position and motion of the cylinder. We also investigated the effect of the diffraction of the wave by the cylinder, which appeared to strongly influence the measured forces. An important effort has been dedicated to the compensation of the vibration induced oscillations of the force measurements.

1.5.3 Outline of the thesis

In this section, we present the outline of the thesis. Besides the introduction, the thesis consists in three chapters and a conclusion.

In chapter 2, the experimental approach is described. The experiments were carried out in the wave flume of Ifremer, Brest. A segmented circular cylindrical mockup was used to measure the forces generated by breaking wave impacts. A novel methodology was developed to compensate for the force oscillations induced by the vibrations of the mockup, which are caused by the impulsive nature of the impacts. The method relies on the use of accelerometers.

In chapter 3, we detail the breaking wave generation, measurement and characterisation. The breaking waves, which display various breaking strengths, were generated through focalisation. An important effort was devoted to the characterisation of the breaking waves in terms of geometry, crest speed and breaking strength. They were measured using a high-speed video camera and modelled with a FNPF solver. The parameters of the breaking waves were determined numerically using the FNPF solver. The breaking strength was characterised through the Γ parameter proposed by Derakhti et al. 2018. The breaking wave simulations were also used to validate a linear equivalent to the breaking threshold proposed by Barthelemy et al. 2018.

The experimental results are presented in chapter 4. The influence of several parameters on the impact load is investigated. These parameters are the breaking strength Γ of the impacting waves, the distance δ between the breaking location and the front face of the cylinder, the tilt angle of the cylinder and the horizontal velocity of the cylinder during impact. The influence of the breaking strength is quantitatively characterised, and a clear correlation between the breaking strength Γ and the magnitude of the impact force is observed. The effect of the distance δ is also highlighted and an empirical formula is proposed to take it into account. This formula could be used to refine the slamming load assessment in the design process of FOWTs. The diffraction of the wave by the cylinder, which appears to influence the breaking wave loads, is also investigated.

Conclusions and perspectives are drawn in chapter 5.

Chapter 2

Experimental set-up and impact force measurement methodology

In this chapter, we present the experimental set-up used for the experimental campaigns. Two experimental campaigns were run during the thesis. A first two-weeks campaign was run in July 2022. A second campaign extended from January 2023 to April 2023. Based on the objectives of the thesis and on the literature review presented in the introduction, we present the design choices that were made for the experiments in section 2.1. The experimental set-up and the experimental facility are presented in section 2.2. Following the first campaign, it appeared that important oscillations were present in the load measurements. Contrary to what we expected, the load oscillations were mainly due to the dynamic response of the skin elements and not only to the elasticity of the load cell and of the backbone. This is highlighted in section 2.3 where some load measurements of the first experimental campaign are presented. This oscillatory behavior complicates the analysis of the experimental data. For this reason, we developed a novel methodology to compensate for the load oscillations. The methodology and its implementation are presented in section 2.4. The methodology was applied throughout the second experimental campaign.

2.1 Design choices for the experiments

In this section, we present the choices that were made to design the mockup based on the objectives presented in section 1.5.2. As all FOWTs include circular cylindrical parts (see figure 1.4), and in order to obtain widely applicable results, we decided to limit the study to the impact of breaking waves on a vertical or nearly vertical circular cylinder. Moreover, during the DIMPACT project, it was initially planned to equip the SPAR-type prototype Zefyros depicted in figure 1.3 with pressure sensors. This also motivated the choice of a circular cylinder which is close to the SPAR design. The diameter of 40 cm of

the cylinder was chosen so that the mockup is representative of the mast of a SPAR-type FOWT with a diameter of 10 m at a scale 1:25. In order to access the vertical distribution of the load, we opted for a segmented mockup. The mockup is composed of 4 instrumented sections, labelled S_1 to S_4, as described in figure 2.1. The force acting on each section is measured independently. The intersection between the sections S_3 and S_4 is situated at

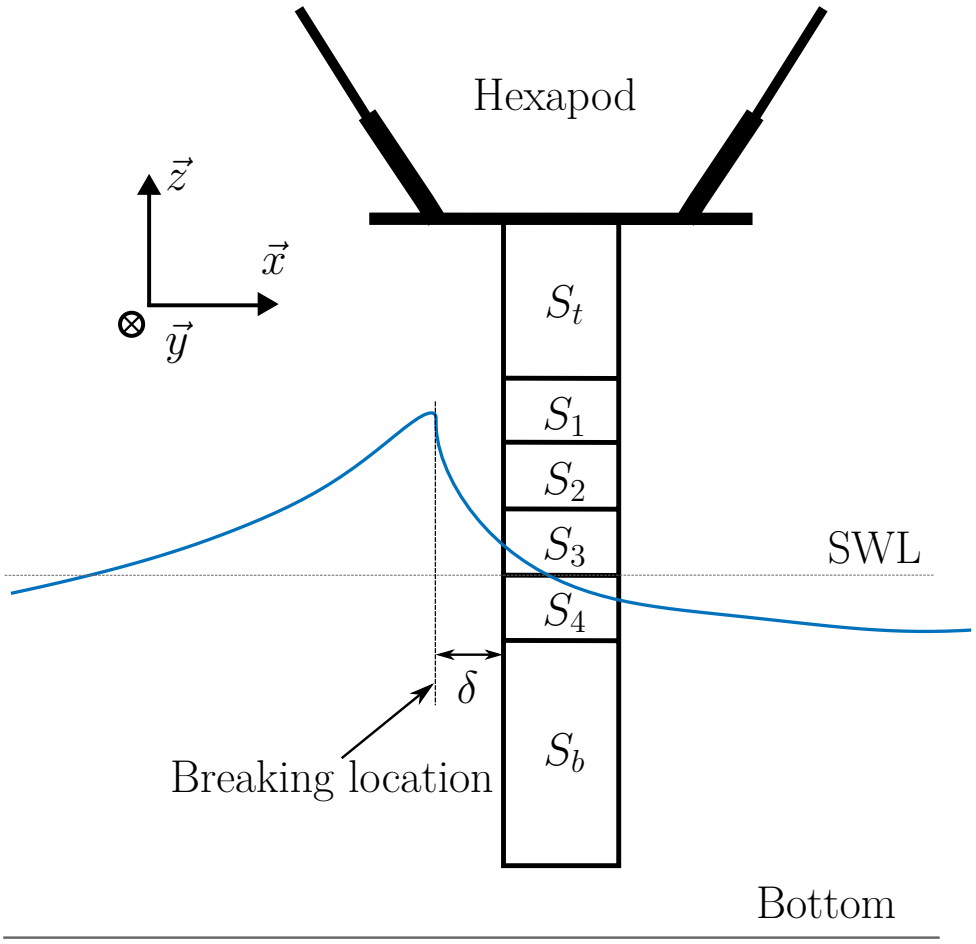

Figure 2.1 – Description of a breaking wave impacting the mockup in the flume. Parameter δ corresponds to the distance between the breaking location and the front face of the cylinder. The origin of the flume frame of reference takes is located at the intersection between the SWL and the wave paddle at its neutral position.

the SWL, so that we can measure the load acting above the SWL independently. In order to be able to easily change the distance δ depicted in figure 2.1, we fixed the mockup to a six degree-of-freedom motion generator, called the "hexapod". The hexapod allows to precisely modify δ, and also to incline the mockup and to dynamically control its position

to study the influence of a horizontal motion. High-speed video cameras were used to visualize the evolution of the flow at impact. A grid pattern was drawn on the mockup to qualitatively follow the wetted surface during the impacts. Note that the design of the mockup and the technical drawings were done mainly by Alan Tassin and Matthieu Laurent from Ifremer.

The breaking waves were obtained through focalisation. Waves of different breaking strengths were generated. As there is no breaking event before the main breaking wave, we could use the FNPF solver proposed by Grilli et al. 1989 to model each wave and to precisely determine its characteristics. For each wave, the breaking location, the crest height, the breaking strength and the crest speed were determined numerically. Experimental measurements of the free-surface profiles of the waves were also carried out and compared to the numerical free-surface profiles.

2.2 Experimental set-up

2.2.1 Description of the wave flume

The experiments were carried out in Ifremer's wave flume. A global view of the flume is depicted in figure 2.2 and a schematic description is presented in figure 2.3. The flume is equipped with a piston-type wave generator composed of 8 segments. It is 40.5 m long from the generator to the damping beach, 2 m deep at the centre of the wave generator and 4 m wide. The bottom of the flume presents a slope of -0.5 % in the longitudinal and transversal directions. An absorbing beach is present at one end of the flume.

2.2.2 Description of the segmented model

2.2.2.1 Design of the mockup

A sketch of the mockup is depicted in figure 2.1. It is a segmented circular cylinder with diameter of 40 cm. The mockup is mounted on the hexapod, a six degree-of-freedom motion generator. The hexapod itself is supported by a rather stiff steel structure which is fixed to the rails on both sides of the flume with pressure screws. A global overview of the mockup mounted over the flume is depicted in figure 2.4.

The mockup is divided into 6 sections, out of which 4 are instrumented to measure the force exerted on the mockup during a wave impact (see 2.1). The upper section, labelled

Figure 2.2 – Picture of Ifremer's wave flume

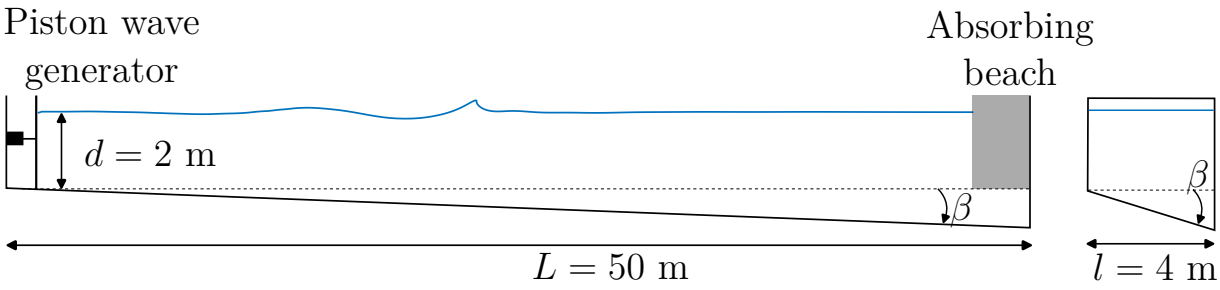

Figure 2.3 – Description of Ifremer's wave flume with a cross-sectional view on the right. The flume displays a slope $\tan\beta \approx -0.5\%$ in the longitudinal and transversal directions.

Figure 2.4 – Overview of the mockup mounted over the flume

S_t, allows to fix the mockup on the motion generator. The lowest section, labelled S_b, is not instrumented. It allows the flow to develop around the cylinder as it would do around a non-truncated cylinder. The four instrumented sections are labelled S_1 to S_4. The sections above the SWL are visible in figure 2.5. Each instrumented section consists in a shell of aluminum named "skin" hereafter and an inner part made out of stainless steel named "backbone element". The skin and the backbone elements are depicted in figures 2.6a and 2.6b. The inner parts are screwed on top of each other and to the upper and lower sections. They form the so-called "backbone" of the mockup and were designed to be as stiff as possible. On each of the inner sections, a skin element is fixed through a force sensor. A

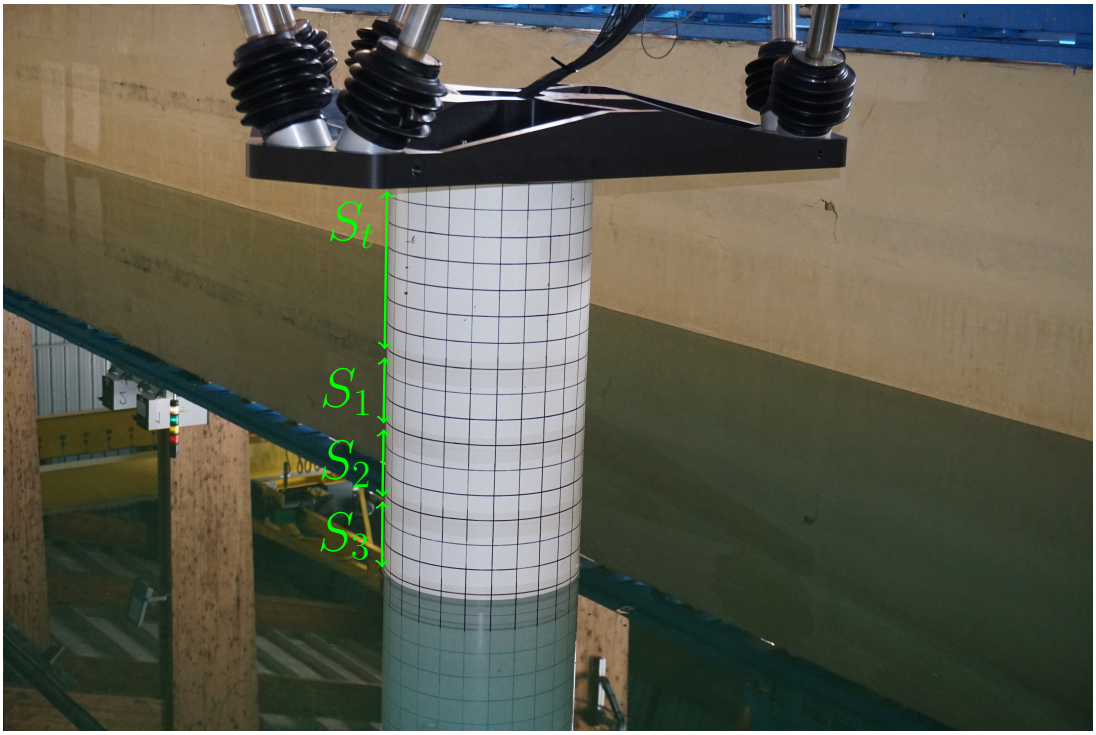

Figure 2.5 – Picture of the mockup mounted on the hexapod. The upper section S_t and the three instrumented sections located above the SWL S_1, S_2 and S_3 are indicated.

technical drawing of the mockup is depicted in figure 2.7a along with an exploded view of two instrumented sections in figure 2.7b. This design allows to independently measure the forces acting on each section.

The height of each instrumented section is 147 mm. There is a 3 mm gap between each section. This gap was sealed with tape. During the first experimental campaign, two layers of tape were superimposed. Figure 2.8 depicts the gap between the sections and the two layers of tape. A first layer of surgical tape was applied to ensure the waterproofness of the mockup (Opsite Flexifix, produced by Smith&Nephew). A second layer of stiffer and stronger white vinyl tape was applied (Scapa 2721 White) to protect the surgical tape. The vinyl tape is 0.16 mm thick. The thickness of the surgical tape is not known. It is thinner and softer than the vinyl tape. The tape is visible in figure 2.5 between the sections. However, it appeared during the preparation of the second experimental campaign that the upper layer of tape modifies the dynamic response of the structure so that the compensation methodology presented in section 2.4 could not be applied. We thus removed this layer between sections S_t and S_1, S_1 and S_2, and S_2 and S_3 for the second

(a) (b)

Figure 2.6 – (*a*) Skin and (*b*) backbone element of a section. The load cell is mounted on the inner part of the section.

experimental campaign. The surgical tape withstood the whole second experimental campaign. As can be seen in figure 2.5, a grid pattern was drawn on the sections to locate the intersection between the free surface and the cylinder. The horizontal lines of the grid are placed every 5 cm and the vertical lines are separated with an arc of length 5 cm. The detailed dimensions of the grid are given in figure 2.9.

2.2.2.2 Positioning of the mockup

The mockup was fixed to a Mistral-type hexapod manufactured by Symétrie. The hexapod is visible in figure 2.4. The use of the hexapod allows an accurate positioning of the mockup. The mockup was placed so as to be perfectly perpendicular to the still water surface. Its vertical axis coincides with the middle of the flume. The vertical position of the mockup was adjusted such that the limit between the third and fourth sections coincides with the still water level. The grid drawn on the mockup was used to precisely set the vertical position. The distance between the front face of the cylinder and the wave maker is equal to 21.46 m when the hexapod is at its "zero" position. This distance was measured using a laser telemeter. The hexapod allows to easily modify the longitudinal position of the mockup. Similarly, the horizontal velocity and the inclination of the mockup were enforced using the hexapod.

2.2.2.3 Expected dynamic response of the mockup

It has been highlighted in section 1.3.2.5 that the dynamic response of the mockup may influence the measurement of the force. If a natural frequency of the mockup is within

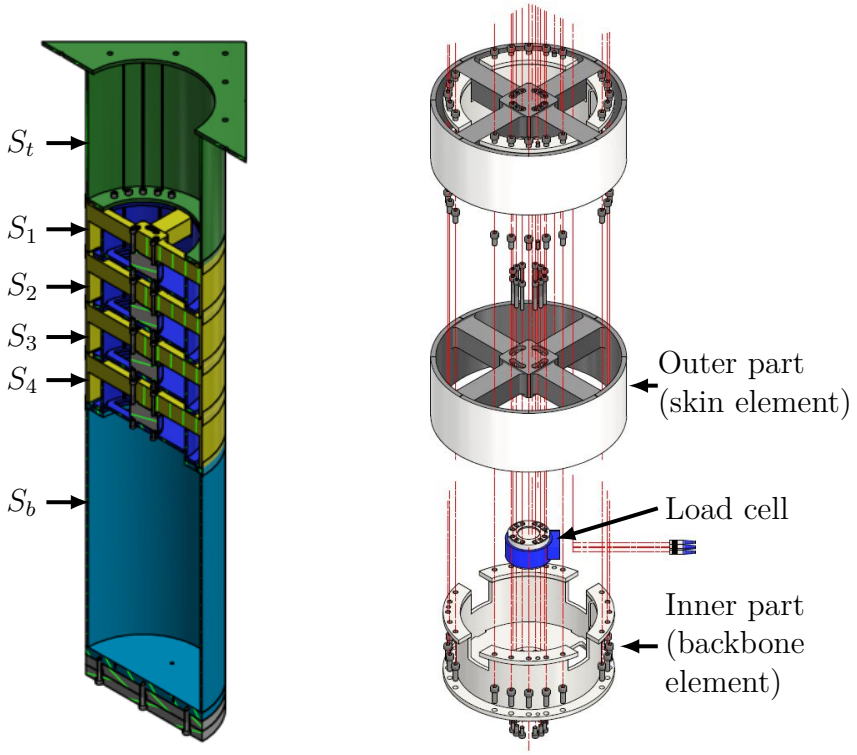

(a) Cross-sectional view of the mockup

(b) Exploded view of two instrumented sections

Figure 2.7 – Description of the mockup

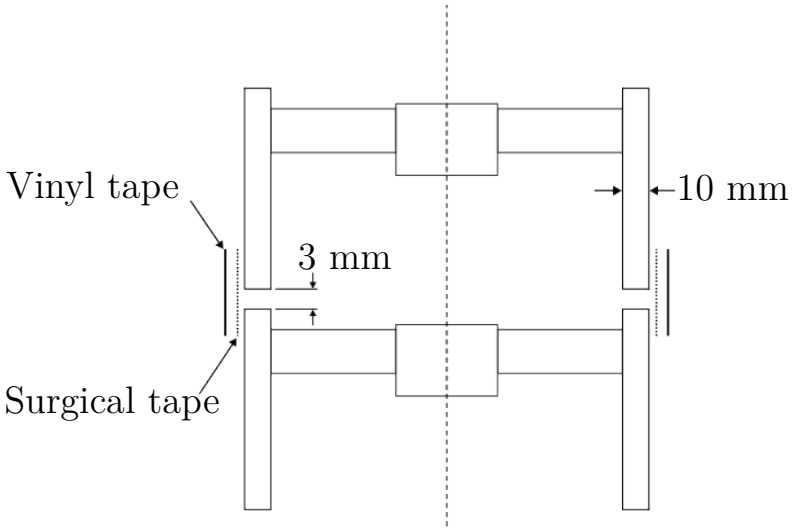

Figure 2.8 – Scheme of the tape sealing between two sections. During the second experimental campaign, we removed the vinyl tape layer between sections S_t and S_1, S_1 and S_2, and S_2 and S_3.

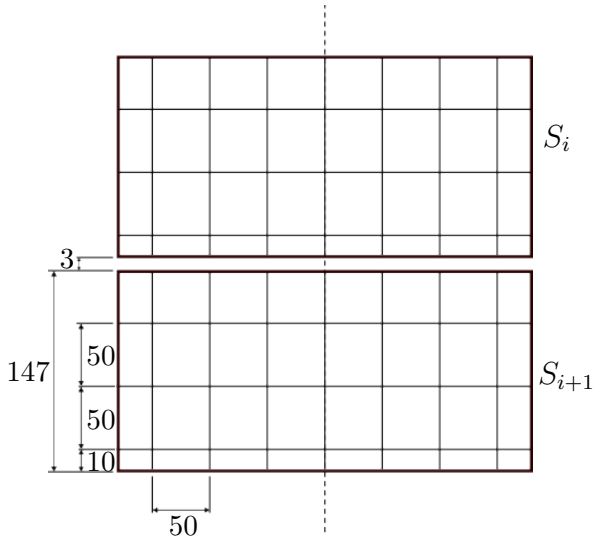

Figure 2.9 – Scheme of the marking on the sections. The dimensions are given in mm.

the frequency range of the wave impact force, the corresponding mode may be excited and may induce oscillations of the force signals. During the design of the mockup, we aimed to obtain natural frequencies which are above 20 times the frequency associated to the duration of a breaking wave impact. Following Goda's approach, the duration of a breaking wave impact corresponds to the time it takes for the crest of a wave to move from the front face of the cylinder to its axis. The characteristic time thus writes $\tau = D/2c = 60$ ms, where $D = 0.4$ m is the diameter of the cylinder and $c = 3.3$ m/s is the phase speed of a 2.25 s period wave. This value is representative of the phase speed of the waves that were used during the experiments. The frequency associated to this characteristic time is $1/\tau = 16.7$ Hz. We thus aimed to obtain natural frequencies of the mockup higher than 300 Hz. In particular, we aimed to obtain a natural frequency associated to the rigid body motion of the skin elements higher than 300 Hz. This motion is induced by the elasticity of the load cells. In order to increase the rigid body oscillations frequency, the mass of the skin elements was optimized to be as low as possible. We obtained a skin element mass of $m_s = 9.85$ kg. Given the characteristics of the load cells, which are given in table 2.1, the natural frequency associated to the rigid body motion of the skin writes:

$$f = \frac{1}{2\pi}\sqrt{\frac{k_i}{m_m + m_s + m_a}} = 384 \text{ Hz}, \tag{2.1}$$

where k_i is the elasticity of the load cell, m_m is the mass of the moving part of the load cell and $m_a = \pi\rho h_s R^2/2 = 9.4$ kg is the added mass of the section predicted by Wagner's theory when the cylinder is fully wet. The height of the section is $h_s = 0.15$ m. The oscillations of the force induced by the rigid body motion being above 300 Hz, we should be able to filter them without impacting the force measurements. However, such a high frequency is out of reach for the first mode of the beam part constituting the "backbone" of the mockup.

In order to verify the feasibility of filtering the dynamic response in the force measurements and to assess the importance of the beam oscillations, we numerically modelled the structural response of the mockup to a breaking wave impact. This work is reported in the DIMPACT report on the definition of the wave tank experiments (Tassin et al. 2022). The model is described in figure 2.10. The backbone of the model has been modelled with beam elements having different stiffnesses EI depending on the position of the element. The skin elements are represented by a punctual mass m to which the added mass was added. The sensors are represented by an equivalent linear spring with a stiffness corre-

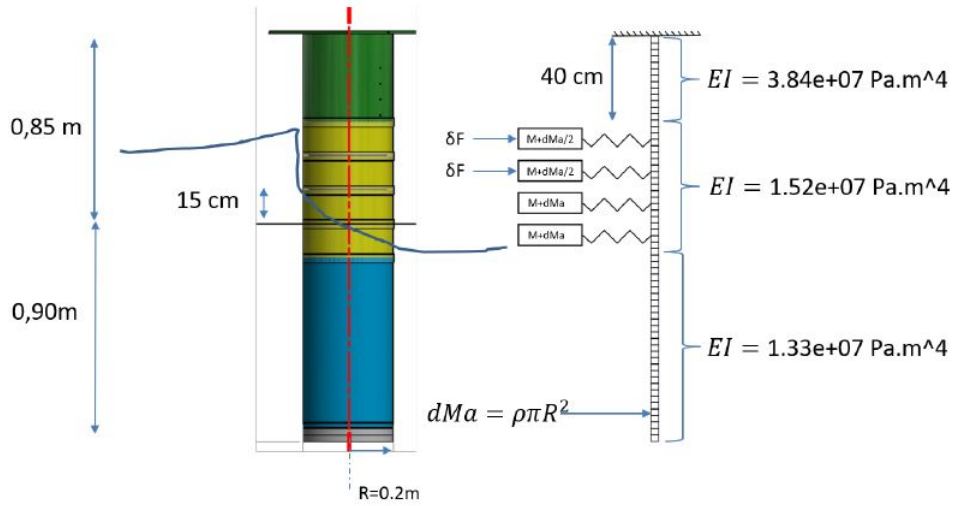

Figure 2.10 – Numerical modelling of a breaking wave impacting the segmented model. Extracted from Tassin et al. 2022.

sponding to the stiffness of the load cells. A force δF induced by the impact of a breaking wave acts on the different sections. The added mass of a cylinder was added to the mass of the two lower instrumented sections and of the bottom section which are fully immersed. Only half of the added mass was added to the mass of the upper sections which are not fully immersed during an impact. The dynamic structural problem was solved following the so-called finite element method under the assumptions of the Euler-beam model (see Korobkin et al. 2006) and an implicit second-order conservative Newmark time-integration scheme. Note that the structural model was implemented by Alan Tassin at an early stage of the project.

The load applying on the cylinder during a breaking wave impact was estimated using a strip-theory approach based on the fluid kinematics in a breaking wave. The fluid kinematics were obtained with the FNPF solver that will be presented in section 3.1.1. The force applying on the cylinder is depicted in figure 2.11 with bold dashed lines for the different sections. The simulation of the measured forces, which are proportional to the deformation of the springs, correspond to the thin solid lines. The oscillations are due to the dynamic excitation of the model. The bold solid lines correspond to the measured force filtered at 250 Hz. The high frequency oscillations are removed by the filtering. Some low frequency oscillations, likely induced by the beam-like response of the backbone, are present. Their amplitude is low and they do not hinder the understanding of the results. Consequently, the dynamic response of the mockup was deemed acceptable.

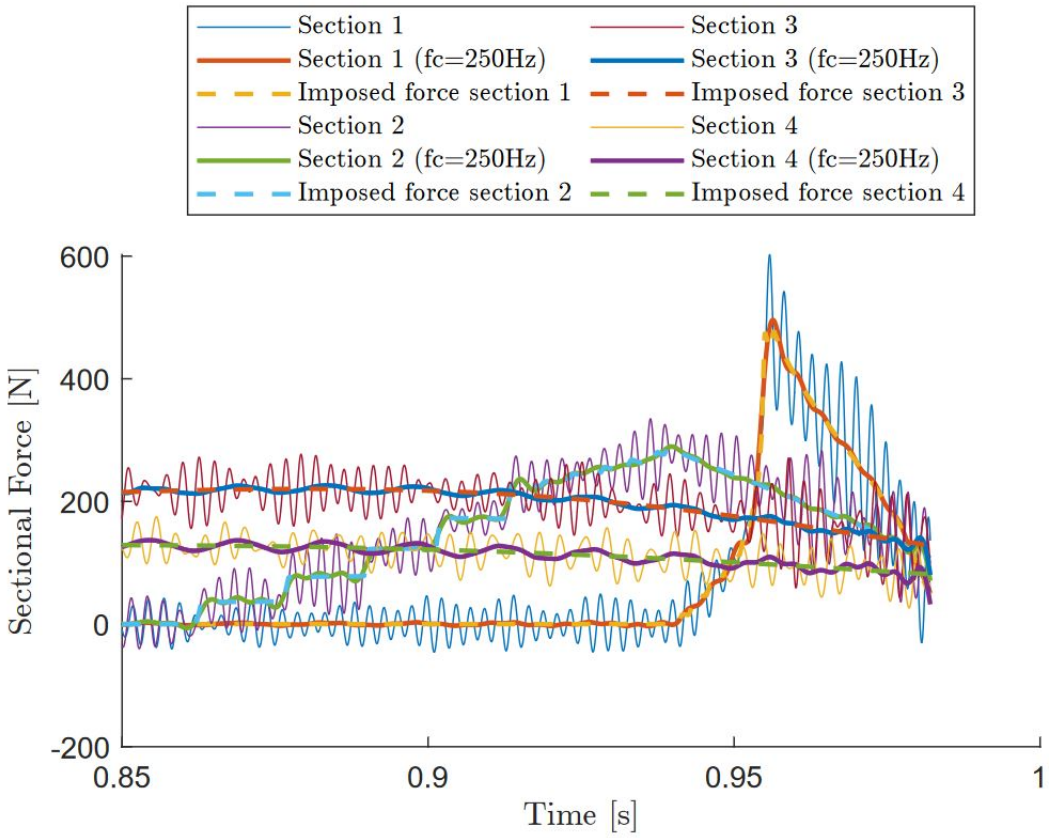

Figure 2.11 – Imposed, measured and filtered forces obtained with the structural model. Extracted from Tassin et al. 2022.

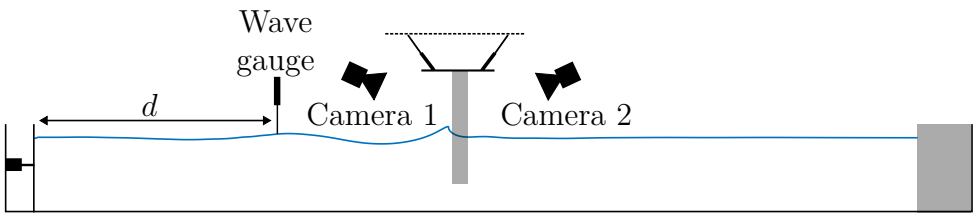

Figure 2.12 – Scheme of wave flume with the wave gauge, the mockup and the high-speed video cameras. The distance between the wave gauge and the wave generator is $d = 11.895$ m.

2.2.3 Instrumentation

This section presents the data acquisition system and the different sensors used during the experiments.

2.2.3.1 Data acquisition system

The measurements were performed using a GEN7 HBM recorder equipped with three input racks of type GN1640B and GN840B. It can work with a sampling frequency up to 500 kSample/s. The recorder allows to work with two different sampling frequencies during the same experiment. The second sampling frequency can be started upon a trigger. For the DIMPACT experiments, the sampling frequency is increased to $f_{high} = 250$ kHz during the impact stage. The sampling frequency is increased during 10 s starting from the instant at which the free-surface elevation measured by the wave gauge (see figure 2.12) exceeds a threshold value. This threshold was chosen so that the wave impact takes place during the 10 s having the highest sampling rate. During the rest of the experiment, a sampling frequency of 10 kHz was used. At the start of the paddle motion, a trigger is sent by the wave generator and recorded by the recorder. This allows to synchronize the measurements with the paddle motion. Note that the position of the wave paddles was also recorded in order to check the synchronization.

2.2.3.2 Free-surface elevation measurements

During the experiments, the free-surface elevation was measured at a single location using a non-intrusive servo-controlled wave gauge. The tip of the gauge precisely follows the free surface. There is a distance of 11.895 m between the wave gauge and the wave generator (see figure 2.12).

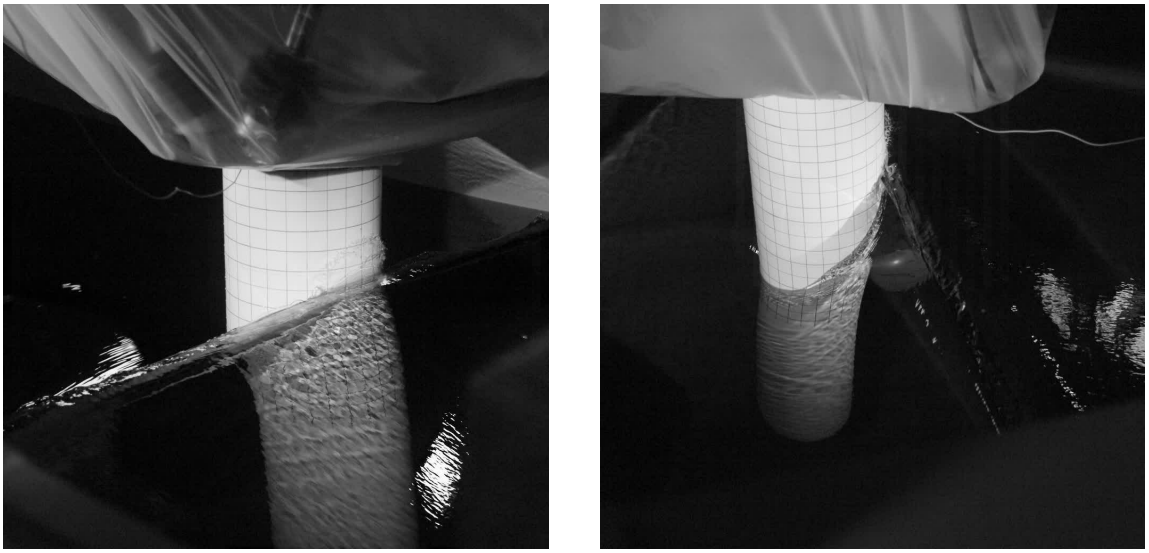

(a) (b)

Figure 2.13 – Images recorded by the high-speed video camera 1 (a) and 2 (b) at the instant at which the measured impact load is maximum

2.2.3.3 High-speed video cameras

Two synchronized high-speed video cameras of type Photron FASTCAM Mini AX200 were used to film the evolution of the wave impacting the mockup (see figures 2.12 and 2.14). Camera 1 filmed the front face of the mockup, *i.e.* the face directed towards the wave paddle, and camera 2 filmed the rear face of the mockup. Two Dedolight spots were added to lighten the mockup. Two pictures of a wave impact captured by the video cameras are depicted in figure 2.13. The images were taken at the instant at which the measured force is maximum. The cameras recorded 1000 frames per second. The images contain 1024x1024 pixels. The recording of the video cameras was started upon the trigger at which the data acquisition system switched from the low to the high acquisition frequency. The grid pattern drawn on the mockup allowed to qualitatively track the intersection between the mockup and the free surface.

2.2.3.4 Position of the wave paddle

The position of the wave generator was recorded using a draw-wire sensor. The wire was fixed to one of the wave paddles. The paddle position was measured to verify that the wave paddles are following the setpoints. Note that during the measurements of the free-surface profile of the different breaking waves presented in section 3.2, the trigger sent by

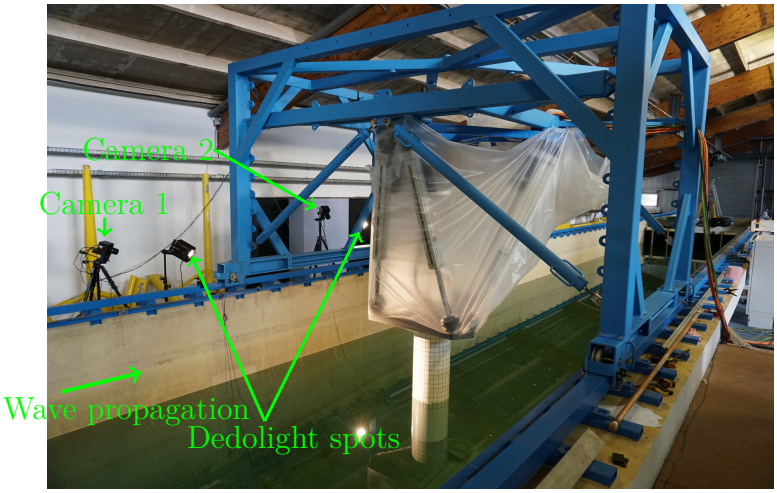

Figure 2.14 – Mockup mounted on the hanging frame and high-speed video cameras.

the wave paddle at the start of the wave generation was not recorded. The time at which the wave generation starts was thus identified from the paddle position measurement.

2.2.3.5 Force measurements

The load cells linking the skin elements to the backbone elements are HBM load cells of type MCS10-025 and MCS10-010. The MCS-025 sensors are used for sections 1 to 3 and the MCS10-010 sensor is used on section 4. The forces and the torques along the x- and y-axis were measured (see figure 2.1 for the axis definition). The characteristics of the load cells are given in table 2.1.

The choice of the nominal force of the load cells is based on the estimation of the force using the strip-theory approach briefly presented in section 2.2.2.3. The dynamic amplification of the force is taken into account.

2.2.3.6 Acceleration measurements

In the configuration of the first experimental campaign, an integrated electronics piezo-electric (IEPE) accelerometer of type Kistler-8640A5 was fixed at the center of each skin element. The accelerometers aimed to measure the rigid body oscillations induced by the elasticity of the load cells and the deformation of the backbone. A picture of an accelerometer mounted on one section is depicted in figure 2.15. They measured the acceleration along the x-direction. They have a nominal range of 5 g. Accelerations higher

	MCS10-010	MCS10-025
M [kg]	1.0	1.8
k_x, k_y [kN/mm]	54	117
k_z [kN/mm]	471	993
c_x, c_y [kN.m/°]	3.75	7.93
c_z [kN.m/°]	2.14	4.59
f_n [kHz]	1.7	1.9
m_m [kg]	0.473	0.821
F_{nom} [kN]	2	5

Table 2.1 – Characteristics of the MCS10-010 and-025 force sensors. M is the mass of the sensor, k_x and k_y its stiffness in the horizontal direction, k_z its stiffness in the vertical direction, c_x and c_y its bending stiffness, c_z its torsional stiffness, f_n its lower natural frequency when no structure is mounted, m_m the mass of the moving part of the sensor and F_{nom} its nominal force. The full datasheet is available at http://spectromas.ro/wp-content/uploads/2017/12/Fisa-tehnica-MCS10.pdf.

than 5 g were observed for the strongest impacts and during hammer tests. This led to the saturation of the signals. In addition, we observed that an important part of the force signal oscillations originated from the elastic deformation of the skin elements. In order to compensate for the strong oscillations of the force that were observed during breaking waves impacts, more accelerometers were added on the skin elements during the second experimental campaign. The location of the accelerometers and the origin of the oscillations are detailed in sections 2.3 and 2.4 (see figure 2.26 for the layout of the accelerometers during the second campaign). The full datasheet of the accelerometers can be consulted on the following link: https://www.kistler.com/files/document/000-842e.pdf.

Figure 2.15 – Accelerometer mounted on the skin element of the second section.

2.3 Structural response of the model

In this section, we investigate the structural response of the mockup. First, the response of the mockup to hammer tests carried out prior to the wave impact experiments is presented in section 2.3.1. In section 2.3.2, we present the results obtained from numerical eigenmode calculations. In section 2.3.3, we present the response of the structure to breaking wave impacts.

2.3.1 Vibratory response of the mockup to a hammer test

Prior to the first experimental campaign, hammer tests were carried out on the four instrumented sections to determine the frequency response of the structure. During the hammer tests, the mockup was mounted on the hexapod. It was set in high position so that all sections were in air. Each section was impacted with a plastic mallet in the x-direction (*i.e.* the wave propagation direction). The response spectra to hammer tests done on the 4 sections are depicted in figure 2.16. The different curves are normalized by there integral so that the hammer impacts on the different sections, which have different magnitudes, are comparable. It appears that several peaks are visible at frequencies higher than the expected rigid body oscillation frequency. Indeed, three important peaks are observed around 480 Hz, 900 Hz and 1230 Hz. The natural frequency in air of the rigid body motion in translation of the section due to the elasticity of the load cell can be computed

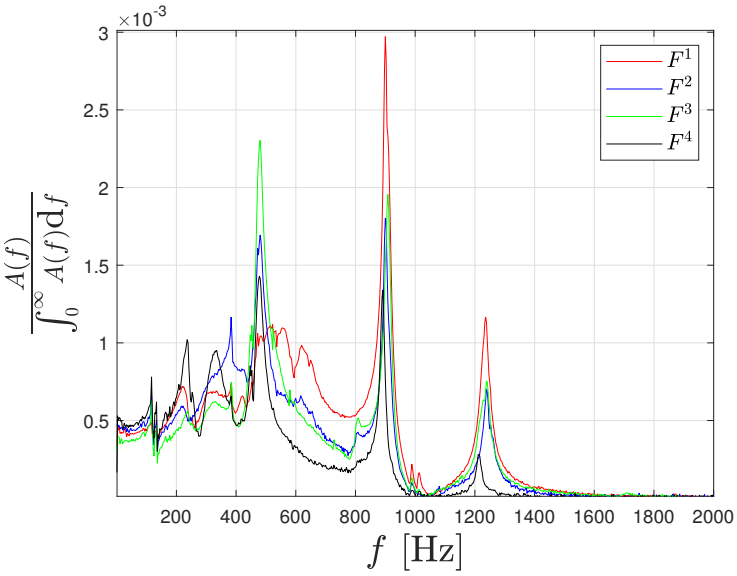

Figure 2.16 – Normalized frequency response of hammer tests performed on the middle of the four sections. Note that a gentler impact was applied on the last section as the nominal force of the sensor is of 2 kN.

as:

$$f_i = \frac{1}{2\pi}\sqrt{\frac{k_i}{m_m + m_s}}, \tag{2.2}$$

where k_i, m_m and m_s are respectively the stiffness of the i^{th} load cell, its moving mass and the mass of the section. Parameters k_i and m_m are given in table 2.1. The section mass is $m_s = 9.85$ kg. For sections 1 to 3, one obtains a theoretical natural frequency in air $f_i = 527$ Hz. The natural frequency of section 4, which is less stiff, is $f_4 = 364$ Hz in air. As the peaks in figure 2.16 occur at similar frequencies for the different sections and are above the predicted frequency for the rigid body modes, it is likely that they correspond to elastic deformations of the skin elements. To investigate the vibratory response of the skin elements, a numerical study of the eigenmodes of a skin element is presented in the following section.

2.3.2 Computation of the section eigenmodes and frequencies

To gain more insights into the dynamic response of the structure, a finite element analysis (FEA) of a skin element was carried out using Abaqus. Note that the simulations were carried out by Nicolas Jacques. The mode shapes resulting from the analysis are

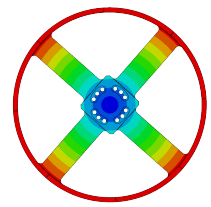

(a) mode 1, $f_1 = 156$ Hz

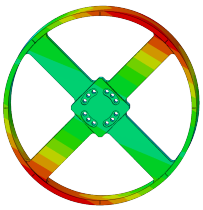

(b) mode 2, $f_2 = 241$ Hz

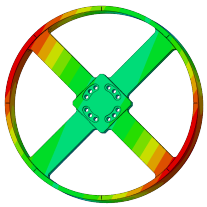

(c) mode 3, $f_3 = 241$ Hz

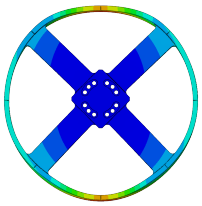

(d) mode 4, $f_4 = 454$ Hz

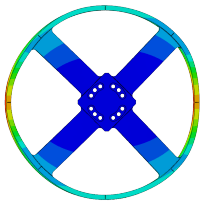

(e) mode 5, $f_5 = 454$ Hz

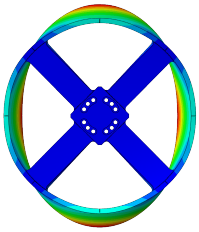

(f) mode 6, $f_6 = 531$ Hz

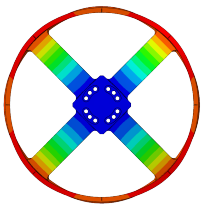

(g) mode 7, $f_7 = 663$ Hz

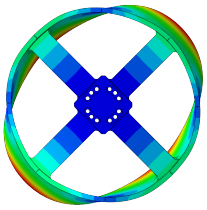

(h) mode 8, $f_8 = 703$ Hz

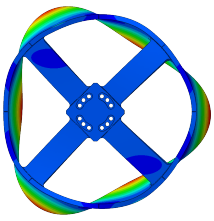

(i) mode 9, $f_9 = 920$ Hz

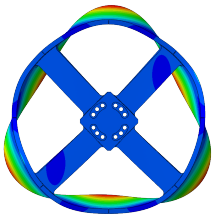

(j) mode 10, $f_{10} = 920$ Hz

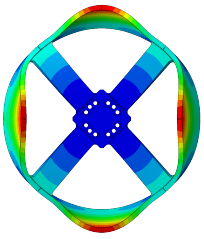

(k) mode 11, $f_{11} = 940$ Hz

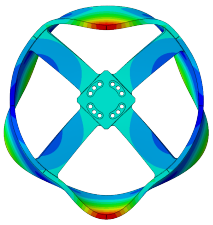

(l) mode 12, $f_{12} = 1299$ Hz

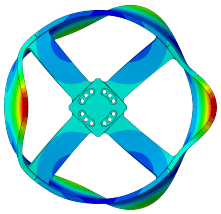

(m) mode 13, $f_{13} = 1299$ Hz

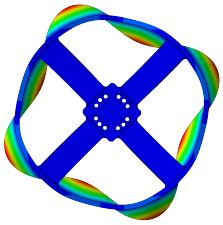

(n) mode 14, $f_{14} = 1323$ Hz

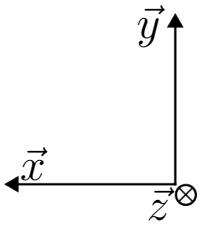

(o) Axis definition

Figure 2.17 – Top-view of the shape of the 14 first modes of the skin element mounted on the MCS10-025 load cell obtained with Abaqus. The load cell is represented by a spring. Its characteristics are given in table 2.1. The definition of the coordinate system is given in the last cell.

No	Freq. [Hz]	M_x^t [kg]	M_y^t [kg]	M_z^t [kg]	M_x^r [T.mm^2]	M_y^r [T.mm^2]	M_z^r [T.mm^2]
1	156	7.60×10^{-9}	6.88×10^{-8}	2.44×10^{-10}	6.13×10^{-9}	2.45×10^{-6}	243,95
2	241	0.25	0.78	1.25×10^{-9}	67.11	21.09	2.76×10^{-8}
3	241	0.78	0.25	2.43×10^{-8}	21.10	67.10	6.47×10^{-6}
4	454	9.05×10^{-2}	8.14	2.65×10^{-8}	68.93	0.77	1.34×10^{-6}
5	454	8.14	9.05×10^{-2}	7.64×10^{-8}	0.77	68.4	1.99×10^{-7}
6	531	7.72×10^{-8}	1.13×10^{-8}	1.51×10^{-7}	9.56×10^{-7}	2.09×10^{-6}	1.87×10^{-8}
7	663	1.46×10^{-8}	2.48×10^{-8}	7.74	3.21×10^{-7}	1.01×10^{-6}	2.56×10^{-9}
8	703	8.43×10^{-10}	4.87×10^{-7}	1.24×10^{-8}	3.13×10^{-6}	8.11×10^{-8}	5.31×10^{-8}
9	920	0.23	3.46×10^{-3}	8.88×10^{-8}	2.49×10^{-2}	1.65	1.33×10^{-9}
10	920	3.46×10^{-3}	0.23	8.52×10^{-9}	1.65	2.50×10^{-2}	7.16×10^{-10}
11	940	2.21×10^{-7}	2.27×10^{-7}	3.50×10^{-9}	2.59×10^{-6}	2.65×10^{-10}	6.00×10^{-9}
12	1299	1.61×10^{-4}	0.26	3.11×10^{-9}	1.96	1.22×10^{-3}	2.95×10^{-8}
13	1299	0.26	1.61×10^{-4}	2.67×10^{-8}	1.22×10^{-3}	1.96	2.52×10^{-9}
14	1323	3.52×10^{-8}	1.28×10^{-8}	3.06×10^{-10}	9.70×10^{-8}	2.94×10^{-7}	7.88×10^{-3}

Table 2.2 – Modal masses of the different modes of a skin element mounted on the MCS10-025 load cell. Parameters M_i^t correspond to the modal mass of the mode in translation along the i-axis and M_i^r corresponds to the modal moment of inertia about the i-axis. In translation, the modal masses are normalized so that the sum of the modal masses equals the mass of the section. In rotation, the sum of the modal moments of inertia equals the rigid body moment of inertia of the skin element about the considered axis.

depicted in figure 2.17. In the FEA analysis, the x-direction corresponds to the direction of wave propagation. The coordinate system is defined in the last cell of figure 2.17. The simulation assumes that the skin element is fixed to a linear spring with stiffnesses corresponding to the MCS10-025 load cell (see table 2.1). This is the load cell used on the three upper sections. The natural frequencies of the different modes are given in the caption. The modal masses in rotation M^r and the modal moments of inertia M^t of the different modes are given in table 2.2. If a mode displays a modal mass in translation M_x^t close to zero, it will not induce oscillations of the force measured along the x-axis. This is for instance the case of modes 1, 6, 7, 11 and 14. Figure 2.16 shows that several modes of the sections are likely excited during a hammer test. This will be further confirmed in section 2.4 through the analysis of acceleration signals recorded at different locations on a skin element. We will also link the different frequency peaks to the modes that induced the different peaks.

2.3.3 Vibratory response of the mockup to a wave impact

In this section, we present the force measured on the different sections during a breaking wave impact and we highlight its oscillatory behavior. The considered wave impact was carried out during the first experimental campaign. It is the impact number 124 in the list of wave impacts performed during the first campaign. This list is given in appendix A.1 along with the experimental conditions. The total load, *i.e.* the sum of the longitudinal forces measured on the 4 sections, is depicted in figure 2.18a. A zoomed-in view at the instant of impact is depicted in figure 2.18b. The raw data are plotted along with the 1500 Hz Fourier low-pass filtered data. The data were filtered to remove the very high frequency content of the signal. In the rest of the section, only the 1500 Hz low-pass filtered forces are shown. It appears that just after the load increase, force oscillations with an amplitude similar to the magnitude of the first force peak are present. In figure 2.19, the forces measured on the different sections during wave impact 124 are shown separately. A rather important level of oscillations is visible on the two upper sections. It also appears that the oscillations are composed of several frequencies. The Fourier transforms of the forces exerted on the four sections are depicted in figure 2.20. The different peaks visible on the Fourier transforms confirm that the oscillations are composed of several frequencies. This strengthen the hypothesis that the oscillations are due to the excitation of different modes of the structure. These oscillations, which are more important and occur over a wider frequency band than expected during the design phase of the mockup, are

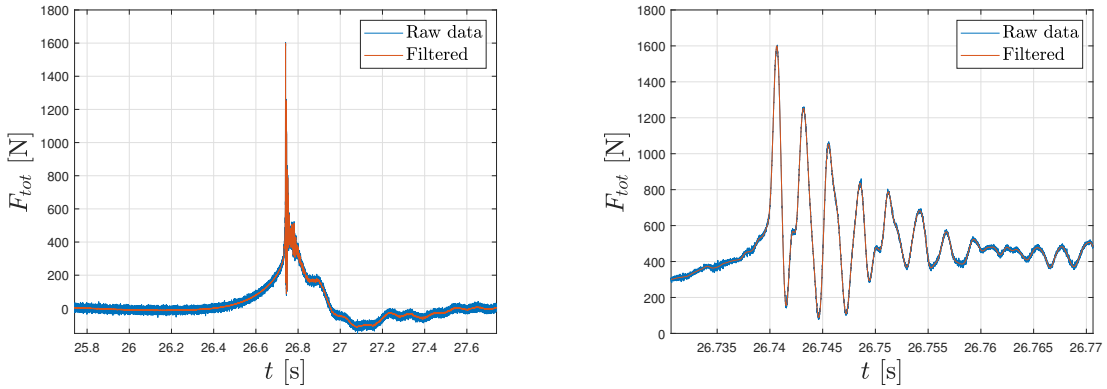

(a) (b)

Figure 2.18 – (*a*) Sum of the forces measured on the different sections during impact case number 124. The force measured on each section was low-pass filtered using a cut-off frequency $f_c = 1500$ Hz. (*b*) Zoomed-in view at the instant of impact.

likely to complicate the interpretation of the force measurements. In order to compensate these oscillations and ease the interpretation of the force measurements, we developed a new methodology presented in section 2.4.

2.4 Implementation of a new method to reduce the effect of the structural vibrations on the force measurements

In order to address the issue of the oscillations observed on the force measurements, we developed a new methodology to compensate for the vibratory response of the model. It consists in recording the structural response with accelerometers fixed to the structure and removing from the force measurements the inertia terms induced by the elastic deformations. The methodology was first tested on the case of a hydrofoil entering calm water and displaying beam-like oscillations in the longitudinal direction (Tassin et al. 2023). Within the current doctoral work, the methodology has been extended to a body displaying three-dimensional elastic deformations, namely the skin elements of the model. The theoretical background of the methodology is presented in section 2.4.1. The choice of the position of the accelerometers is detailed in section 2.4.2. In section 2.4.3, the methodology is applied to compensate the force oscillations during a hammer impact. The case of

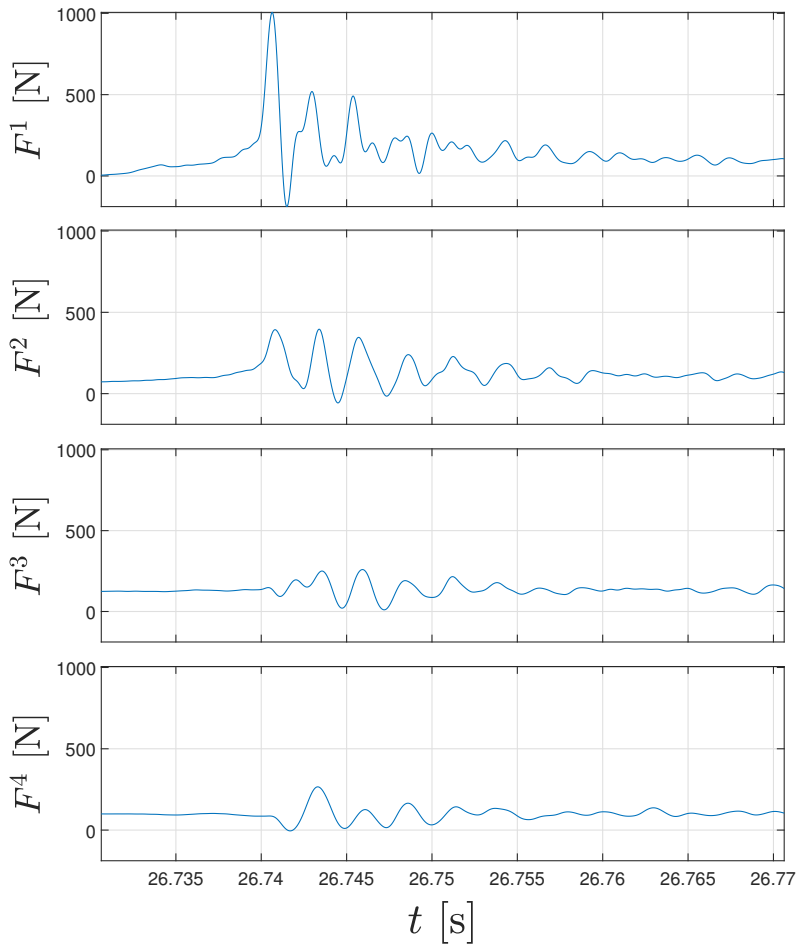

Figure 2.19 – Longitudinal forces measured on the four sections during impact case number 124 (see table A.1 for the experimental conditions)

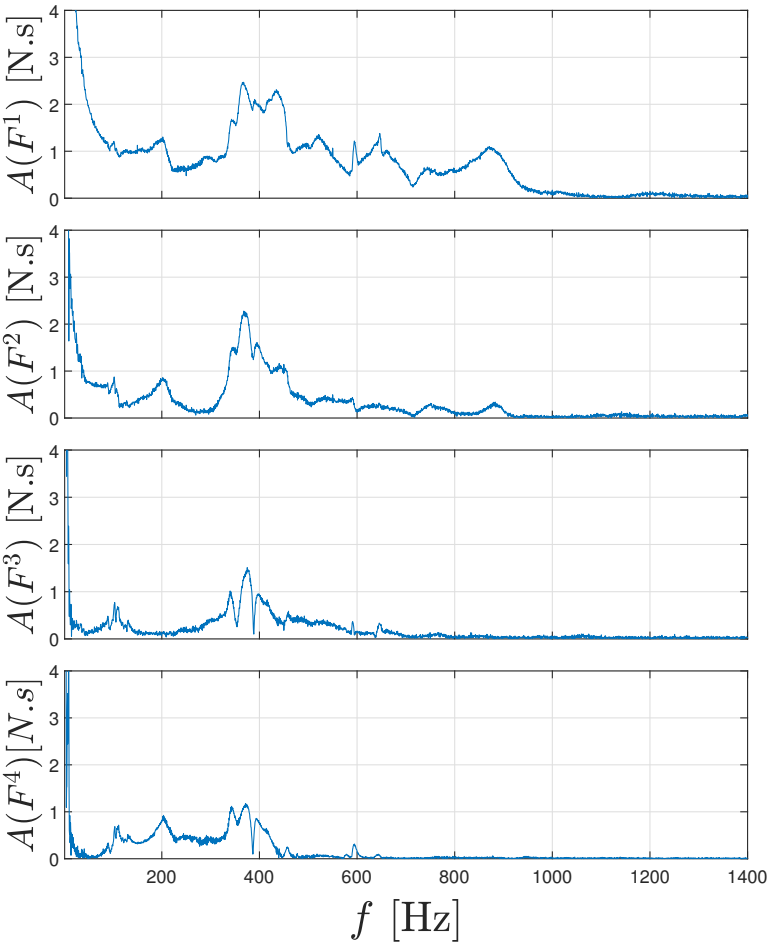

Figure 2.20 – Fourier transforms of the forces measured on the four sections during impact case number 124 (see table A.1 for the experimental conditions)

a breaking wave is addressed in section 2.4.5.

2.4.1 Description of the methodology

Let us consider the elastic three-dimensional body depicted in figure 2.21. A distributed

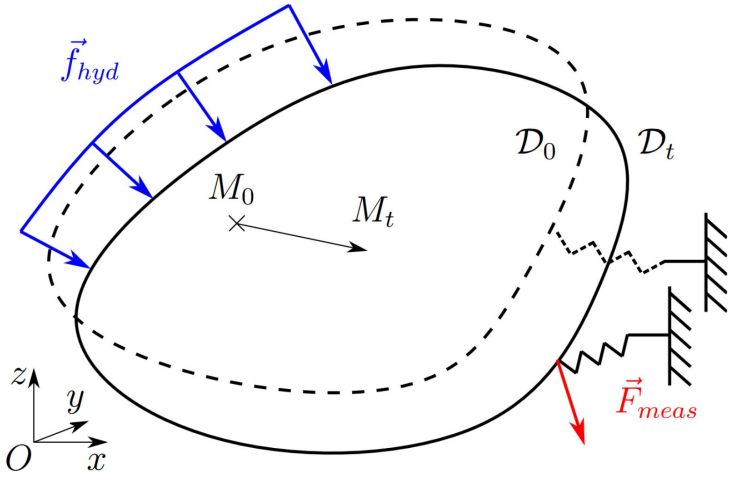

Figure 2.21 – Description of a three-dimensional body fixed on a load cell vibrating under the action of a distributed external load $\vec{f}_{hyd}$. The load cell may be connected to a fixed or moving body. Extracted from Tassin et al. 2023.

external load $\vec{f}_{hyd}$ with a resultant $\vec{F}_{hyd}$ acts on the body. The body is linked to another structure, potentially moving as well, through a load cell. The load cell, typically a six-axis load cell, is represented by a linear spring. It applies a reaction force $-\vec{F}_{meas}$ on the body. At the initial time, the body occupies the material domain $\mathcal{D}_0$. At the instant t, the distorted body occupies the material domain $\mathcal{D}_t$. A material point M_0 with coordinates (x_0, y_0, z_0) at the initial instant is displaced to the point M_t of coordinates (x, y, z) at the instant t. The function $\vec{T}$ describes the displacement of the material point M in space. It is such that $\vec{M}_t = \vec{M}_0 + \vec{T}(M_0, t)$. Applying the principle of momentum conservation to the elastic body at an instant t, we obtain:

$$\vec{F}_{hyd} - \vec{F}_{meas} = \frac{\mathrm{d}}{\mathrm{d}t}\left(\iiint_{\mathcal{D}_t} \rho(x,y,z,t)\vec{U}(x,y,z,t)\mathrm{d}x\mathrm{d}y\mathrm{d}z\right), \tag{2.3}$$

where $\vec{U}(x, y, z, t)$ is the velocity of a material point M_t and $\rho(x, y, z, t)$ is the local density. The mass conservation states that $\rho(x, y, z, t)\mathrm{d}x\mathrm{d}y\mathrm{d}z = \rho_0(x_0, y_0, z_0)\mathrm{d}x_0\mathrm{d}y_0\mathrm{d}z_0$. Using the

mass conservation and making the change of variables $(x, y, z) = (x_0, y_0, z_0) + \vec{T}(M_0, t)$, the preceding equation can be rewritten as:

$$\vec{F}_{hyd} - \vec{F}_{meas} = \frac{\mathrm{d}}{\mathrm{d}t}\left(\iiint_{\mathcal{D}_0} \rho_0(x_0, y_0, z_0) \frac{\partial}{\partial t}\vec{T}(x_0, y_0, z_0, t)\mathrm{d}x_0\mathrm{d}y_0\mathrm{d}z_0 \right). \tag{2.4}$$

This allows to interchange the order of integration and differentiation in equation 2.4 and to write:

$$\vec{F}_{hyd} - \vec{F}_{meas} = \iiint_{\mathcal{D}_0} \rho_0(x_0, y_0, z_0) \frac{\partial^2}{\partial t^2}\vec{T}(x_0, y_0, z_0, t)\mathrm{d}x_0\mathrm{d}y_0\mathrm{d}z_0. \tag{2.5}$$

Let us assume that the body deforms preferentially along its N first modes of vibration. Function $\vec{T}$ can be approximated by:

$$\vec{T}(x_0, y_0, z_0, t) \approx \sum_{i=1}^{N} a_i(t)\vec{w}_i(x_0, y_0, z_0), \tag{2.6}$$

where functions $a_i(t)$ are the modal coordinates and functions $\vec{w}_i(x_0, y_0, z_0)$ the modal shapes. By substituting equation 2.6 into equation 2.5, one obtains:

$$\vec{F}_{hyd} - \vec{F}_{meas} \approx \sum_{i=1}^{N} \ddot{a}_i(t) \underbrace{\iiint_{\mathcal{D}_0} \rho_0(x_0, y_0, z_0)\vec{w}_i(x_0, y_0, z_0)\mathrm{d}x_0\mathrm{d}y_0\mathrm{d}z_0}_{\vec{m}_i}, \tag{2.7}$$

where $\vec{m}_i$ is the modal-mass vector of the i^{th} mode. It is now possible to express the hydrodynamic force $\vec{F}_{hyd}$ as a sum of the measured force $\vec{F}_{meas}$ and a term involving the modal accelerations:

$$\vec{F}_{hyd}(t) \approx \vec{F}_{meas}(t) + \sum_{i=1}^{N} \ddot{a}_i(t)\vec{m}_i. \tag{2.8}$$

Let us now consider that N accelerometers are placed on the solid at the locations $\vec{X}_j$. Each accelerometer records an acceleration γ_j in the direction $\vec{n}_j$. The acceleration γ_j corresponds to the sum of the accelerations generated by the different modes at the position $\vec{X}_j$:

$$\gamma_j(t) = \sum_{i=1}^{N} \vec{w}_i(\vec{X}_j) \cdot \vec{n}_j \; \ddot{a}_i(t). \tag{2.9}$$

Using matrix notations, the previous equations can be written as:

$$\underbrace{\begin{bmatrix}\gamma_1(t)\\ \vdots \\ \gamma_N(t)\end{bmatrix}}_{\vec{\Gamma}(t)} = \underbrace{\begin{bmatrix}\vec{w}_1(\vec{X_1})\cdot\vec{n}_1 & \cdots & \vec{w}_N(\vec{X_1})\cdot\vec{n}_1 \\ \vdots & \vdots & \vdots \\ \vec{w}_1(\vec{X_N})\cdot\vec{n}_N & \cdots & \vec{w}_N(\vec{X_N})\cdot\vec{n}_N\end{bmatrix}}_{\mathbf{W}} \begin{bmatrix}\ddot{a}_1(t)\\ \vdots \\ \ddot{a}_N(t)\end{bmatrix}. \tag{2.10}$$

Assuming that matrix $\mathbf{W}$ is invertible, the second time derivatives of the modal coordinates can be expressed as linear combinations of the recorded accelerations γ_j. Substituting equation 2.10 into equation 2.8, we obtain:

$$\vec{F}_{hyd}(t) \approx \vec{F}_{meas}(t) + \mathbf{M}\mathbf{W}^{-\mathbf{1}}\vec{\Gamma}(t), \tag{2.11}$$

where $\mathbf{M}$ is the modal-mass matrix defined as:

$$\mathbf{M} = \begin{bmatrix}\vec{m}_1\cdot\vec{e}_x & \ldots & \vec{m}_N\cdot\vec{e}_x \\ \vec{m}_1\cdot\vec{e}_y & \ldots & \vec{m}_N\cdot\vec{e}_y \\ \vec{m}_1\cdot\vec{e}_z & \ldots & \vec{m}_N\cdot\vec{e}_z\end{bmatrix}. \tag{2.12}$$

Equation 2.11 can be projected along a particular axis, for instance the x-axis. This allows to write the x-component of the hydrodynamic force as a linear combination of the x-component of the measured force and acceleration signals as:

$$F^x_{hyd}(t) \approx F^x_{meas}(t) + \sum_{i=1}^{N}\alpha^x_i\gamma_i(t), \tag{2.13}$$

where the upper script x refers to the x-component of the terms. For simplicity, the upper script will be omitted in the following and non-vector component implicitly refer to the x-component as we will focus on this component. Equation 2.13 allows to express the hydrodynamic force as a function of the measured force and accelerations. The computation of the α_i coefficients would require to know the modes of the structure, which is not the case in practice (it would require a very detailed structural model of the mockup). As an alternative, we suggest to experimentally identify the α_i coefficients. The identification of the α_i coefficients may be carried out over a time interval $[t_1, t_2]$ during which the evolution of the hydrodynamic force is known. This is the case during a hammer test with an instrumented hammer, which measures the excitation force applied by the hammer.

During this time interval, the force and acceleration signals satisfy the following equation:

$$F_{meas}(t) + \sum_{i=1}^{N} \alpha_i \gamma_i(t) = F_{ham}(t), \quad t \in [t_1, t_2], \tag{2.14}$$

where $F_{ham}(t)$ is the force measured by the instrumented hammer. If the hammer is not instrumented, it is possible to select a period during which the external force is equal to zero and the mockup freely vibrates. For instance, just after the hammer impact, the external force is zero while the structure is still vibrating. The coefficients are chosen so as to minimize the following quantity:

$$\epsilon = \sum_{k=1}^{n} \left(F_{meas}(t^k) - F_{ham}(t^k) + \sum_{i=1}^{N} \alpha_i \gamma_i(t^k) \right)^2, \tag{2.15}$$

where $t^k \in [t_1, t_2]$. The accuracy of the method will depend on the number of accelerometers placed on the structure, but it will also depend on the location of the accelerometers on the structure. This point is discussed in the following section.

2.4.2 Position of the accelerometers on the skin element

Several layouts of accelerometers have been tested in the process of developing the compensation methodology. Initially, we did not expect that the layout of accelerometers would be so influential because, in theory, the only condition is that matrix $\mathbf{W}$ is invertible. This means that there must not be two accelerometers k and l located at $\vec{X}_k$ and $\vec{X}_l$ and oriented along $\vec{n}_k$ and $\vec{n}_l$ such that for all the modes i, $\vec{w}_i(\vec{X}_k) \cdot \vec{n}_k = \vec{w}_i(\vec{X}_l) \cdot \vec{n}_l$. Given that the mode shapes depicted in figure 2.17 are rather different, it seems unlikely that a configuration of accelerometers does not respect this criterion. However, as it will be shown in the following section, with a rather limited number of accelerometers and an important number of modes to compensate for, the location of the accelerometers affects the efficiency of the methodology. We first present in section 2.4.2.1 an early configuration of accelerometers tested on a simplified set-up. This configuration allowed to draw some conclusions concerning the optimal layout. The selected layout is presented in section 2.4.2.2.

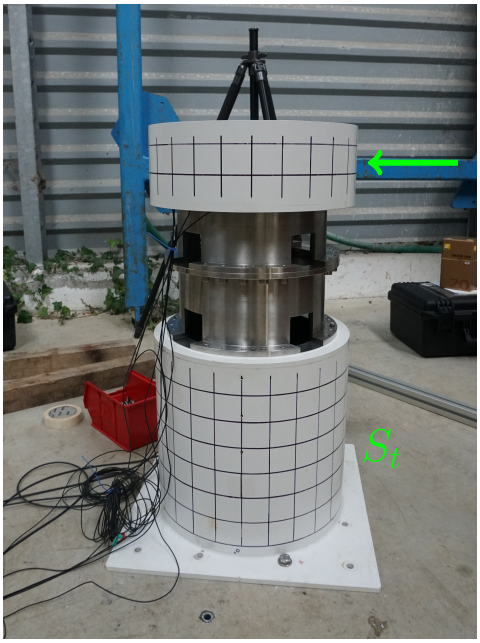

Figure 2.22 – Picture of the set-up used to determine the locations of the accelerometers on the skin element. The green arrow indicates the position at which the skin element was impacted.

2.4.2.1 First accelerometers configuration used to determine the optimal layout

To validate the methodology described in section 2.4.1 and to determine the appropriate accelerometers locations, we first carried out some tests with a simplified set-up illustrated in figure 2.22. This set-up consisted in an instrumented section mounted over the top section S_t (see figure 2.7a). The top section was screwed to the ground. An impulsive force was applied on the section using a hammer along the direction of wave propagation, which corresponds to the green arrow. We used a plastic mallet as we had not access to an instrumented hammer at that time. Several accelerometers were placed on the skin element. We tested different configurations of the accelerometers. For brevity, we will only analyze the acceleration measurements obtained with the configuration described in figures 2.23a and 2.23b. Six accelerometers, labelled A_1 to A_6, were placed on the skin element. Due to budget considerations, space limitations and to the number of channels of the recorder, we limited the number of accelerometers on the section to 6. The accelerometers labelled A_1 to A_5 are piezoelectric charge accelerometers of types Brüel and Kjær 4370-V and 4381-V. They were plugged to charge amplifiers of types Kistler

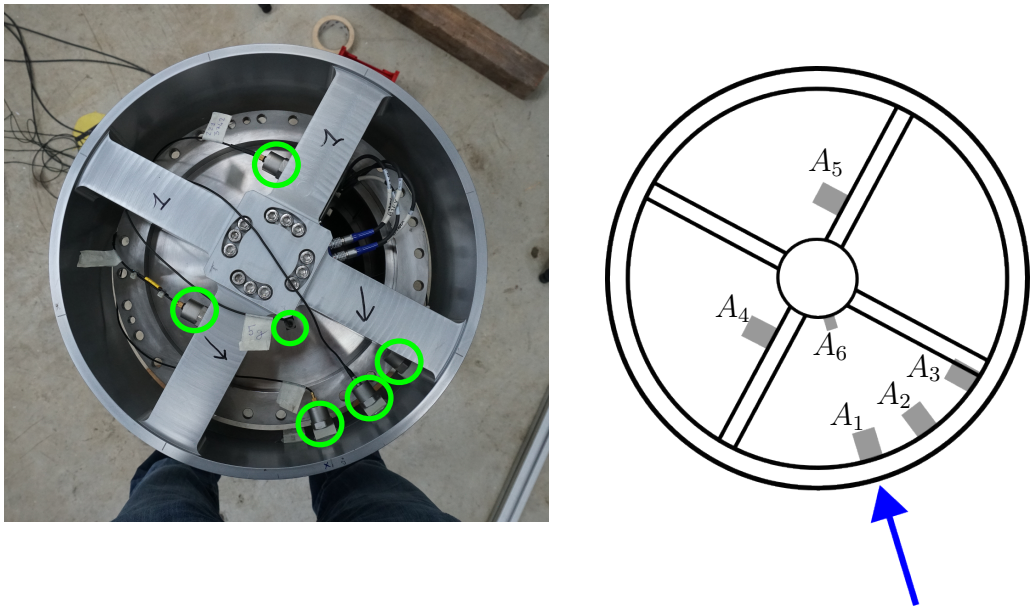

(a) (b)

Figure 2.23 – First accelerometers configuration. (a) Picture of the accelerometers placed on the skin element. (b) Scheme of the positions of the accelerometers. The blue arrow corresponds to the direction of the impact force.

5167A and 5165A. The selected amplification range allowed to measure accelerations up to 200 g. Accelerometer A_6 is an integrated electronics piezo-electric (IEPE) sensor of type Kistler 8640A50 with a nominal range of 50 g. The accelerometers were glued to the mockup using epoxy and cyanoacrylate adhesives.

The Fourier transforms of the accelerometer signals and measured forces along the x- and y-axis during a hammer impact are depicted in figure 2.24. Several peaks corresponding to different modes are visible on the spectra. For each peak, the natural frequency f_i of the inferred corresponding mode i is printed next to the peak. The first important peak at 35 Hz is likely due to the response of the supporting section S_t because of the non-perfect boundary conditions. A zoomed-in view of the first, second and third vibration peaks is depicted in figure 2.25a. The double peak identified as f_{2+3} is likely due to the bending modes 2 and 3. Indeed, these modes display a non-negligible mass along the x- and y-axis (see table 2.2). The double peak may be due to the fact that the mass of the accelerometers is spread unevenly on the skin, thus affecting differently the frequency of each mode. The reason why the fundamental frequencies of these modes are at 147 Hz instead of the 241 Hz predicted by the FEA is unknown. It could be related to the fact

the elasticity of the backbone and of the supporting section is not taken into account by the FE model. In the final configuration, in which the moments along the x- and y-axis were also recorded, an important peak appears at 147 Hz in the Fourier transforms of the moment along the y-axis (see figure 2.27). This supports the idea that the peak at 147 Hz corresponds to the bending modes 2 and 3. The frequency of mode 1 is identified at 152 Hz. This is close to the 156 Hz frequency predicted by the FEA. As the only non-zero modal mass of mode 1 is the modal moment of inertia along $\vec{z}$ (see table 2.2), this mode is a torsion mode. Consequently, it is visible only on accelerometers A_4 and A_5, which are not in the radial direction. Note that the first mode has no effect on the x-component of the force.

Modes 4 and 5 are identified at 388 and 381 Hz, respectively. Mode 4 is visible on the force along the y-direction while mode 5 is visible on the force along the x-direction. Similarly to modes 2 and 3, the frequency shift between the two modes is likely due to the uneven distribution of the mass of the accelerometers or to the manufacturing of the model. We think that the peak at 516 Hz corresponds to mode 6. A zoomed-in view around this peak is depicted in figure 2.25b. It appears that accelerometer A_1, which is the closest to an anti-node of mode 6, displays the highest 516 Hz peak. Accelerometer A_3, which is closer to a node, displays a smaller peak. The peak of accelerometer A_2 is between the peaks of A_1 and A_3. Accelerometers A_4, A_5 and A_6, which are not directly on the skin, display much lower peaks. However, the forces display a non-zero peak, even though the modal masses along the x- and y-directions are close to zero (see table 2.2). This is probably due to the uneven distribution of the accelerometers. We have no explanation concerning the lower peak around 560 Hz. This peak disappears in the final configuration of accelerometers (see figure 2.27). The peak at 688 Hz, visible on the acceleration spectra (see figure 2.24), corresponds to mode 8. The modal masses of the mode along the x- and y-directions are close to zero, which explains why the recorded forces do not display a peak at 688 Hz. The two accelerometers displaying a peak are A_2 and A_3. The peak of A_3 is higher, which corresponds to the fact that A_3 is placed closer to an anti-node of mode 8. The peaks at at 876, 888 and 924 Hz are attributed respectively to modes 9, 10 and 11. A zoomed-in view for this frequency range is shown in figure 2.25c. The frequency shift between modes 9 and 10 is likely due to the distribution of the accelerometers. The closer an accelerometer is to an anti-node, the higher its peak is. This is also the case for mode 11. Only a small peak is visible in the Fourier transforms of F_x at 924 Hz. As the modal mass associated to mode 11 is low, this peak may be due to the uneven distribution

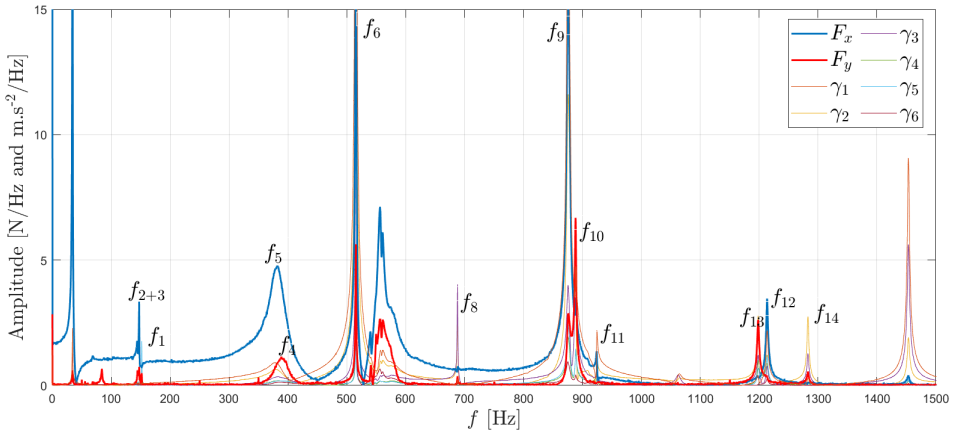

Figure 2.24 – Fourier transforms of the forces along the x- and y-axis and of the accelerations measured during a hammer impact

of accelerometers. A zoomed-in view on the peaks induced by the modes 12, 13 and 14 is depicted in figure 2.25d. In accordance with the computed modal masses in table 2.2, mode 13 generates a peak on the force along the y-direction while mode 12 generates a peak on the force along the x-direction. Mode 14 generates a peak on accelerometers A_2 and A_3, but not on the force in the x-direction. It generates a small peak on the force in the y-direction.

2.4.2.2 Selected layout for the accelerometers on the skin elements

Two main conclusions can be drawn from the previous layout of accelerometers and from the finite element analysis. First, to avoid polluting the force measurements with accelerations induced by the torsion mode (mode 1), the accelerometers have to be placed in the radial direction. As we have access to 6 accelerometers per section and as the modes 1 and 7 do not appear on the force measurements, the 6 accelerometers should allow to compensate for modes 2, 3, 4, 5, 6 and 8. It appears from figure 2.17 that the nodes and anti-nodes of these 6 modes are placed every 45 °. We decided to place 5 accelerometers on the skin at angles corresponding to multiples of 45°. The sixth accelerometer was placed in the central part of the skin element with the idea to record principally the rigid body motion.

The final layout for the accelerometers on the four sections is described in figure 2.26. Accelerometers A_3 and A_4 are of type Kistler 8640A5 with a nominal range of 5 g. As it has been observed during the first experimental campaign (see section 2.3.3), the oscillations

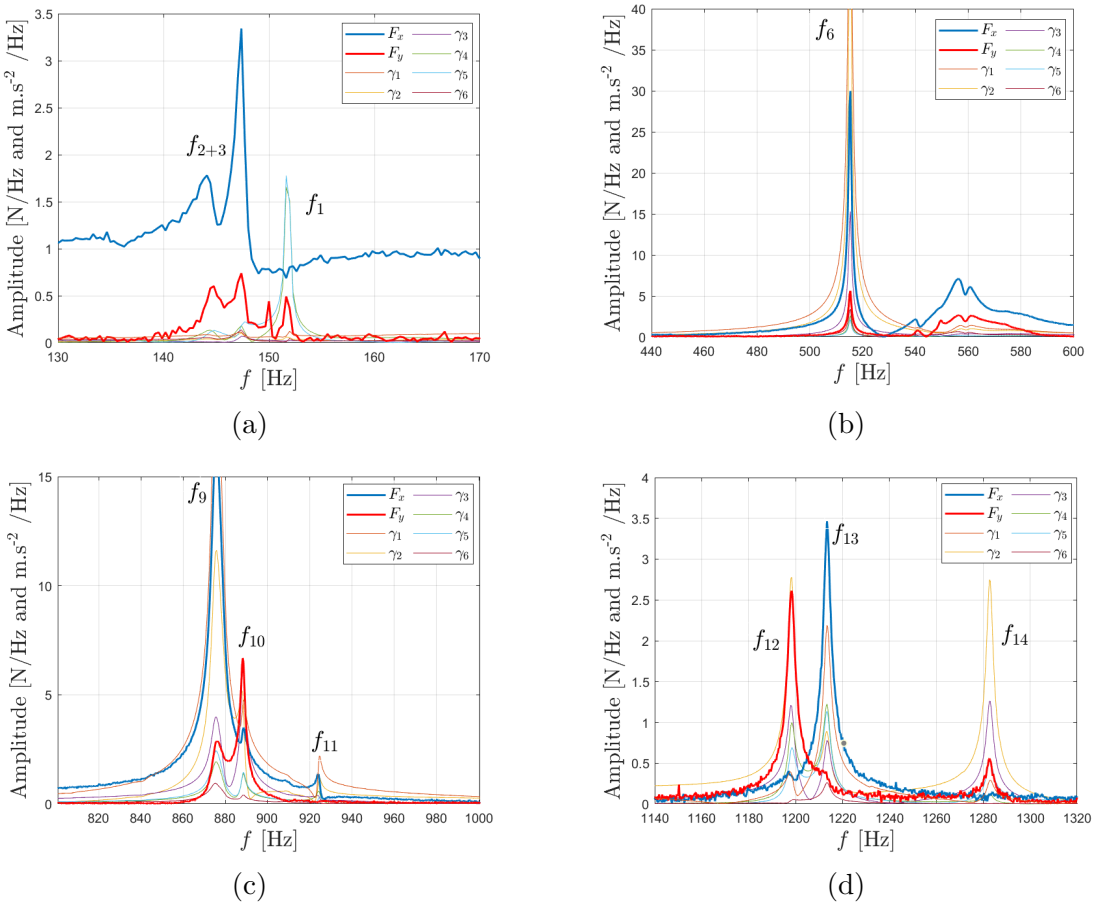

Figure 2.25 – Zoomed-in views of figure 2.24 on different frequency ranges

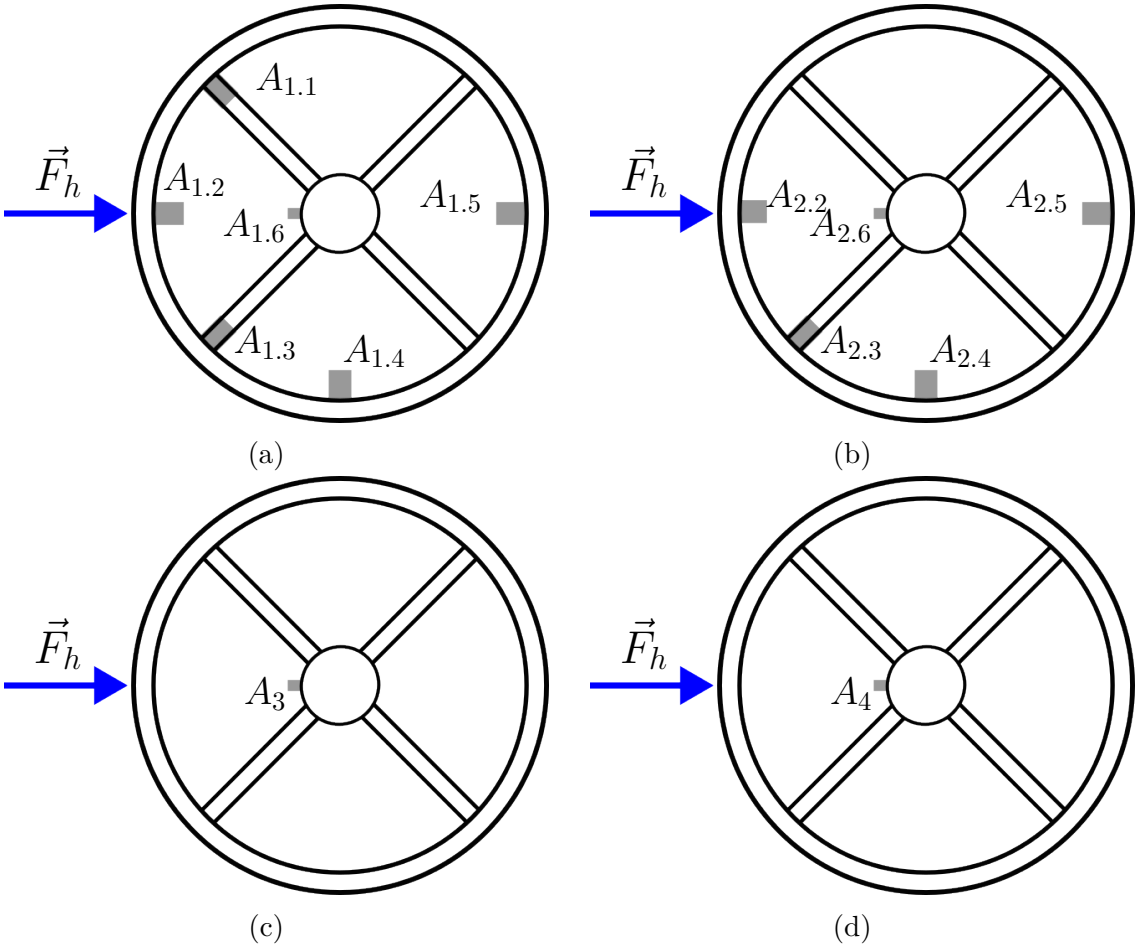

Figure 2.26 – Accelerometer configuration for the complete set-up: top view of the skin elements for sections S_1 (a), S_2 (b), S_3 (c) and S_4 (d).

are mainly present on the two upper sections. Consequently, only the two upper sections were equipped with six accelerometers. On section S_2, there is no accelerometer at the location of $A_{1.1}$. An accelerometer was initially placed at this location, but it fall down during impact tests at the start of the experimental campaign. Because of time constraints, the risks of damaging the set-up during the disassembling and reassembling process, and given the reasonably good results obtained with the missing accelerometer, it was decided to perform the experiments without the accelerometer. Hammer tests were carried out to investigate the dynamic properties of the fully assembled set-up. The tests were carried out with an instrumented hammer impact of type Kistler 9724A5000. This hammer was bought for the second experimental campaign. During the hammer tests, the mockup was mounted on the hexapod in the configuration of the experiments. The Fourier transforms

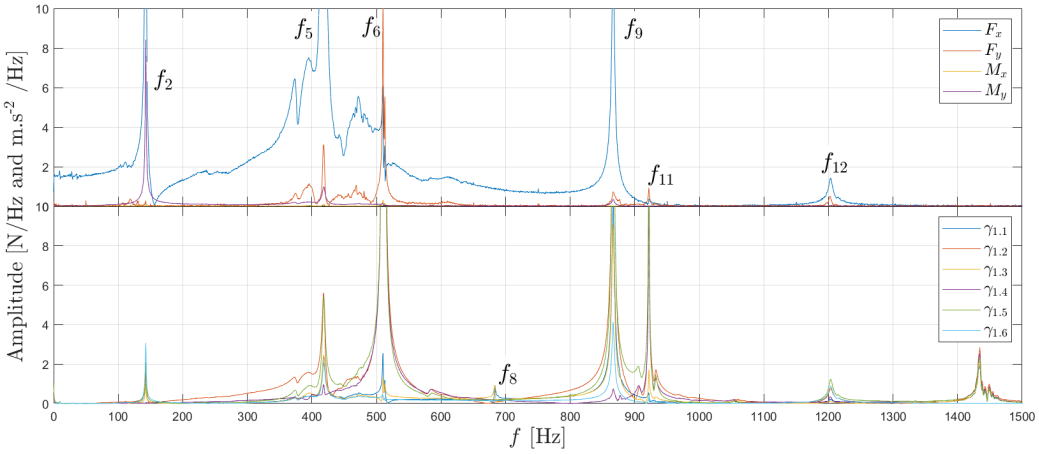

Figure 2.27 – Fourier transforms of the forces along the x- and y-axis and of the accelerations measured during a hammer impact. The Fourier transforms of the moment along the x- and y-axis are also plotted.

of the accelerometers, of the loads and of the moment along the x- and y-axis recorded during the hammer impacts are depicted in figure 2.27. Similarly to the previous layout, we identified the different modes. Using the new accelerometers distribution, the first mode (the torsion mode) does not appear on the Fourier transforms. At 143 Hz, there is now a single peak. No peak is observed on the force along the y-direction and on the moment around the x-axis. An important peak is observed on the x-component of the force and on the moment around the y-axis. However, no peak is visible on the Fourier transform of the y-component of the force and on the moment around the x-axis. This peak likely corresponds to a mix of the bending modes 2 and 3 which induces bending around the y-axis. Note that modes 2 and 3 are not around the x- and y-axis, but rather around axes rotated by 45°. The fact that there is now a single peak may be due to the more even distribution of accelerometers in the final layout. An important peak appears at 418 Hz with the new configuration. We have no explanation concerning the fact that it does not appear on the previous configuration. It is close to the peaks corresponding to modes 4 and 5 that were identified at 388 and 381 Hz in the previous configuration.

The peak at 510 Hz is attributed to mode 6. The peak induced on the x-component of the force is reduced compared to the previous configuration. This may also be due to the more even distribution of the accelerometers. The peak at 683 Hz corresponds to mode 8 and the peaks at 867 Hz and 922 Hz to modes 9 and 11, respectively. It seems that mode 10 is not excited. At 1203 Hz, only one peak corresponding to mode 12 appears.

2.4.3 Identification of the reconstruction coefficients during hammer tests

As explained in section 2.4.1, the α_i coefficients can be obtained by performing hammer tests on the sections and through the least-square minimization presented in equation 2.15. The start of the identification interval t_1 is taken 3 ms before the maximum of the force recorded by the hammer. Its end t_2 is taken 0.1s after the maximum of the force. It appears that the quality of the reconstruction does not vary much with the value of t_1 and t_2 if the interval is long enough. All the signals are low-pass filtered using a Butterworth filter of order 6 to remove the measurement noise and the high-frequency oscillations. The filter is applied to the data in the forward and reverse directions so that it does not modify the phases. The cut-off frequency f_c depends on the considered section. As the number of accelerometers varies between the sections, the number of modes that may be compensated for also varies. It is thus necessary to adapt the cut-off frequency so as to remove the modes that cannot be compensated for.

2.4.3.1 Identification of the reconstruction coefficients for the first section

For the first section, the cut-off frequency is taken as $f_c^1 = 1000$ Hz. The compensation coefficients that were identified are:

$$\begin{aligned} \alpha_{1.1} &= -2.07 \text{ kg} \\ \alpha_{1.2} &= -1.53 \text{ kg} \\ \alpha_{1.3} &= 0.39 \text{ kg} \\ \alpha_{1.4} &= -0.81 \text{ kg} \\ \alpha_{1.5} &= 0.76 \text{ kg} \\ \alpha_{1.6} &= -9.30 \text{ kg}. \end{aligned} \tag{2.16}$$

The time histories of the force measured by the impact hammer, of the force measured by the load cell and of the compensated force are depicted in figure 2.28a. The solid vertical line corresponds to the start t_1 of the identification interval and the dashed vertical line to its end t_2. A zoomed-in view of this figure is depicted in figure 2.28b. A nearly perfect agreement is obtained between the compensated force and the measured force close to the instant of impact. Indeed, the overshoot and the delay of the measured force with respect to the hammer signal are corrected very accurately. After the impact,

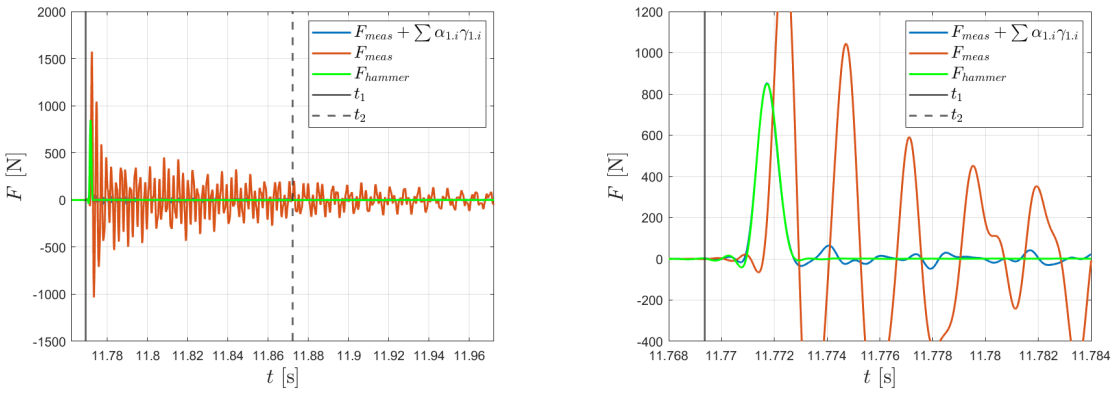

(a) (b)

Figure 2.28 – (a) Reconstruction of the force along the x-direction during a hammer impact on the first section. (b) Zoomed-in view at the instant of impact.

residual oscillations are present on the compensated force. The Fourier transforms of the measured and reconstructed forces are shown in figure 2.29. It appears that the main peaks are compensated for. Some residual peaks are present. In particular, a peak that is not present on the force measurement appears at 684 Hz. It corresponds to mode 8. Indeed, one can observe in the Fourier transforms depicted in figure 2.27 that this peak appears on accelerometers $A_{1.1}$ and $A_{1.3}$, but not on the force measured by the load cell. Similarly, a peak due to mode 11, which is barely present on the force measurement, appears at 921 Hz. In figure 2.27, this mode is visible on accelerometers $A_{1.2}$, $A_{1.4}$ and $A_{1.5}$.

2.4.3.2 Identification of the reconstruction coefficients for the second section

A similar identification is made for the second section, S_2. As explained earlier, accelerometer $A_{2.1}$ was missing as it fell down during a hammer test. We found out that a better accordance between the compensated force and the force measured on the hammer was obtained when accelerometer $A_{2.3}$ was not used in the reconstruction. Indeed, as mode 8 is visible on $A_{2.3}$ but not on the force and on the other acceleration measurements, adding $A_{2.3}$ pollutes the force reconstruction. Furthermore, when $A_{2.3}$ is used, a slightly better compensation of the high frequencies is obtained at the expense of the compensation of the lower frequencies. As the lower frequencies are present for more wave impact conditions than the high frequencies, we decided not to use accelerometer $A_{2.3}$. Thus, we only used four accelerometers for the compensation. Consequently, it is not possible to

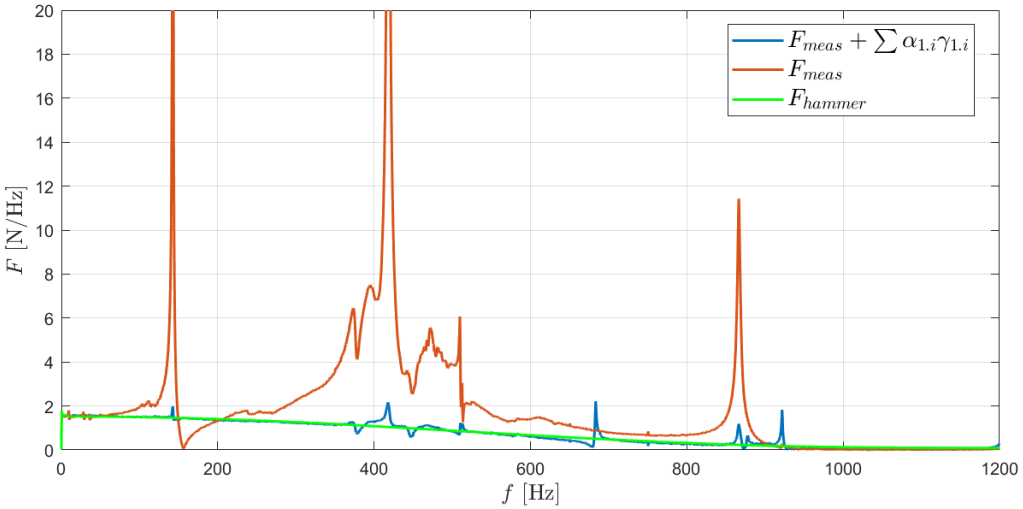

Figure 2.29 – Fourier transforms of the measured and reconstructed forces during a hammer impact on section S_1

compensate for the same number of modes as for section S_1. All the signals were filtered at a lower frequency $f_c^2 = 700$ Hz. The compensation coefficients obtained during the identification are:

$$\begin{aligned} \alpha_{2.2} &= 0.02 \text{ kg} \\ \alpha_{2.4} &= 2.43 \text{ kg} \\ \alpha_{2.5} &= 2.30 \text{ kg} \\ \alpha_{2.6} &= -10.03 \text{ kg}. \end{aligned} \tag{2.17}$$

We do not show the signals that allowed to carry out the identification. Instead, we will detail the application of the compensation methodology to another hammer impact on section S_2 in section 2.4.4.2.

2.4.3.3 Identification of the reconstruction coefficient for the third section

We observed in section 2.3.3 that during a wave impact, the force oscillations are mainly present on the first and second sections. For this reason, only one accelerometer, named A_3, was installed on section S_3. Its location is given in figure 2.26c. We did not perform hammer tests on section S_3. We thus used the impacts carried out on section S_2 to identify the compensation coefficient on section S_3. During an impact on section S_2, the modes of section S_3 are excited as well. Indeed, it appears in figure 2.30 that the

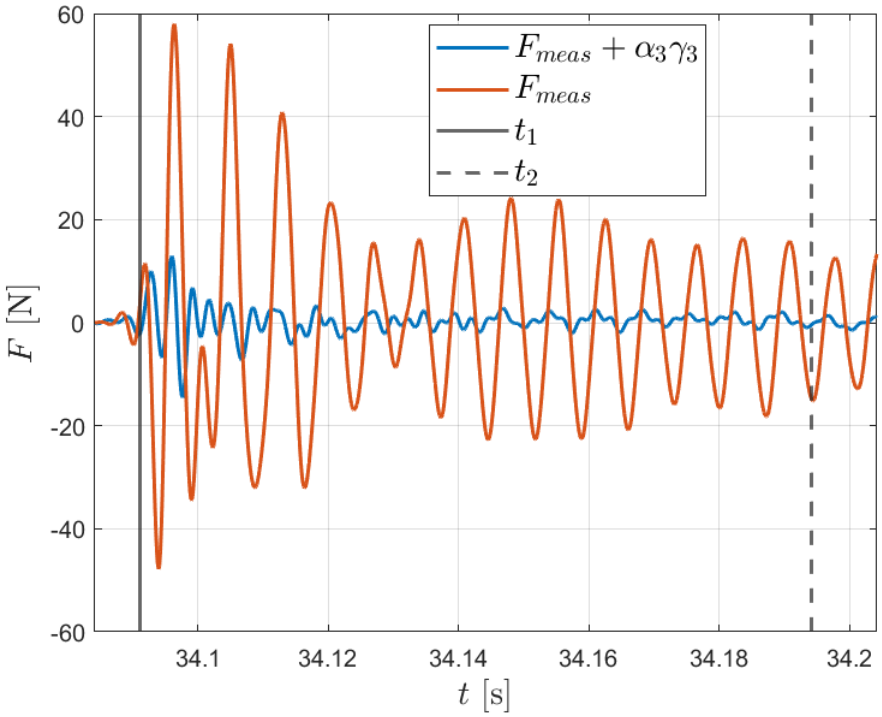

Figure 2.30 – Reconstruction of the load on section S_3 during a hammer impact on the second section S_2. The data are filtered at $f_c^3 = 300$ Hz.

force recorded by the load cell of section S_3 during a hammer impact on section S_2 is oscillatory. It is thus possible to carry out a coefficient identification. It is assumed that the load acting on section S_3 is equal to zero (see equation 2.15). We filtered the data at $f_c^3 = 300$ Hz. The obtained coefficient is:

$$\alpha_3 = -17.28 \text{ kg}. \tag{2.18}$$

The load measured on section S_3 during a hammer impact on section S_2 is depicted in figure 2.30 along with the compensated force. It appears that an important part of the oscillations below 300 Hz are compensated for. The Fourier transforms of these signals are depicted in figure 2.31. All the energy below 300 Hz is removed from the measurements. To highlight the fact that an important part of the frequency content is not taken into account, the Fourier transforms of the raw force measurement and of the low-pass filtered force measurement are depicted.

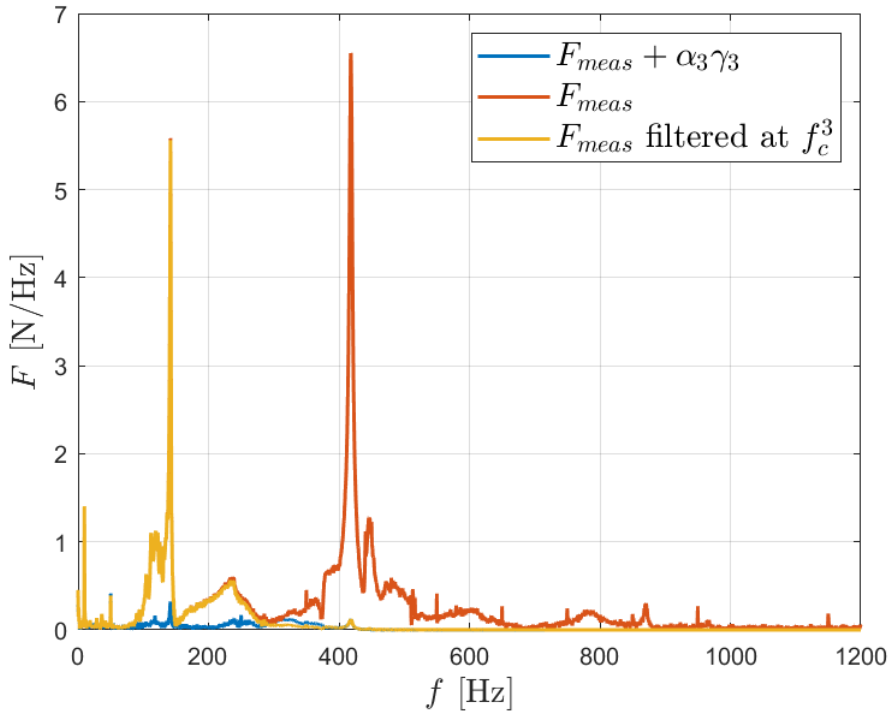

Figure 2.31 – Fourier transforms of the measured and reconstructed forces on section S_3 during a hammer impact on section S_3

2.4.3.4 Identification of the reconstruction coefficient for the fourth section

Similarly to section S_3, one accelerometer, named A_4, was fixed on section S_4. Its location is given in figure 2.26d. As no hammer tests were carried out on section S_4, the coefficient identification was carried out during a hammer test on section S_2. The time histories and Fourier transforms of the forces being very similar to those obtained during the coefficient identification for the third section, they are not shown here. The signals are filtered at $f_c^4 = 300$ Hz. The obtained compensation coefficient is:

$$\alpha_4 = -11.47 \text{ kg}. \tag{2.19}$$

2.4.4 Compensation of the force oscillations during hammer tests

In this section, we highlight the capabilities of the compensation methodology by applying it to the force measured during hammer tests. This allows to compare the compensated force to the force measured by the impact hammer. For these hammer tests, the impact hammer was equipped with a slightly stiffer impactor. It allows to show that even if the frequency content changes, the methodology still performs well.

2.4.4.1 Reconstruction of a hammer impact on the first section

The force reconstructed during a hammer impact on section S_1 is depicted in figure 2.32a along with the forces measured by the hammer and the load cell. A good agreement between the force measured by the hammer and the reconstructed force is obtained. The reconstructed peak force displays an overestimation of 6 %. After the impact, residual oscillations are present. The amplitude of the highest residual oscillation correspond to 7.5 % of the peak force measured by the hammer. It appears that the reconstructed force is much closer to the force measured by the hammer than the 300 Hz low-pass filtered force. The time evolution of the load is well reproduced. In particular, the time delay of the force measured by the load cell compared to the force measured by the hammer during the impact is corrected. The Fourier transforms of the measured and reconstructed forces are shown in figure 2.32b. The frequency content of the compensated force is very close to the frequency content of the force measured by the impact hammer.

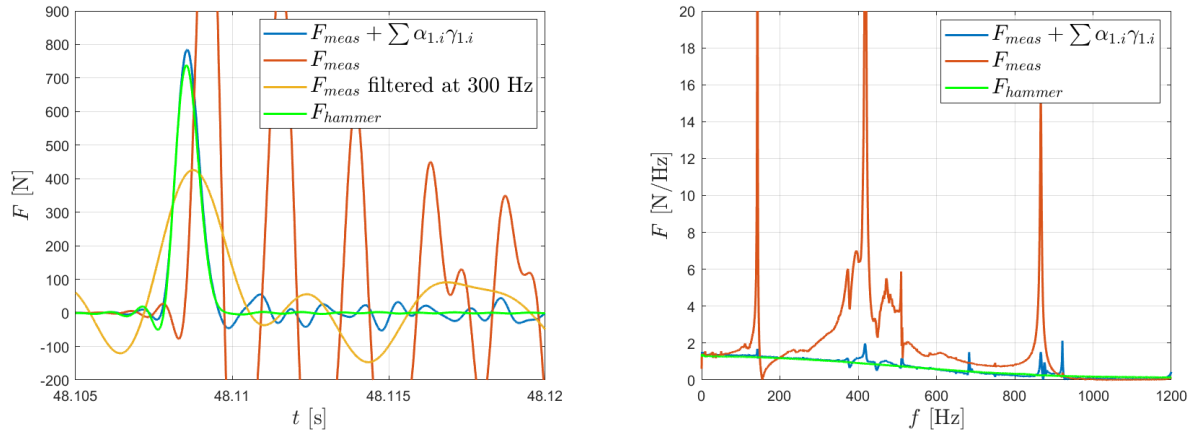

(a) (b)

Figure 2.32 – (a) Compensation of the force along the x-direction during a hammer impact on section S_1. The force measured by the load cell filtered at 300 Hz is plotted for comparison. (b) Fourier transforms of the forces.

2.4.4.2 Reconstruction of a hammer impact on the second section

Similarly to the section one, we present the reconstruction of a hammer impact with a stiffer impactor on section S_2. The measured and reconstructed forces are depicted in figure 2.33a. A more important difference between the measured and compensated forces is observed at the peak. The reconstructed force peak value displays an overestimation of 10 %. Similarly, residual oscillations are present after the impact. The highest residual peak corresponds to 13% of the peak load recorded by the hammer. The troughs present just before and just after the peak on F_{hammer} and on the compensated force are due to the filtering at f_c^2. The Fourier transforms of the different signals are depicted in figure 2.33b. A more important part of the high-frequency content of the impact force is lost for section S_2 compared to section S_1.

2.4.4.3 Reconstruction of the force measured on the third section during a hammer impact on the second section

As no hammer tests were done on section S_3, we reconstructed the force measured on S_3 during a hammer impact on S_2. The time histories of the forces are shown in figure 2.34a and their Fourier transforms in figure 2.34b. Most of the oscillations with a frequency lower than 300 Hz are removed from the measurements.

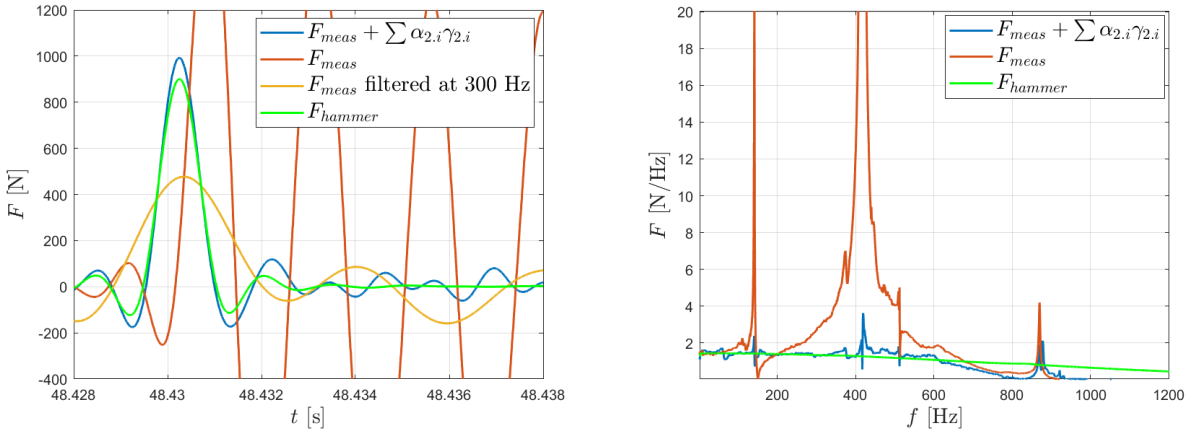

(a) (b)

Figure 2.33 – (a) Compensation of the force along the x-direction during a hammer impact on section S_2. The force measured by the load cell filtered at 300 Hz is plotted for comparison. (b) Fourier transforms of the forces.

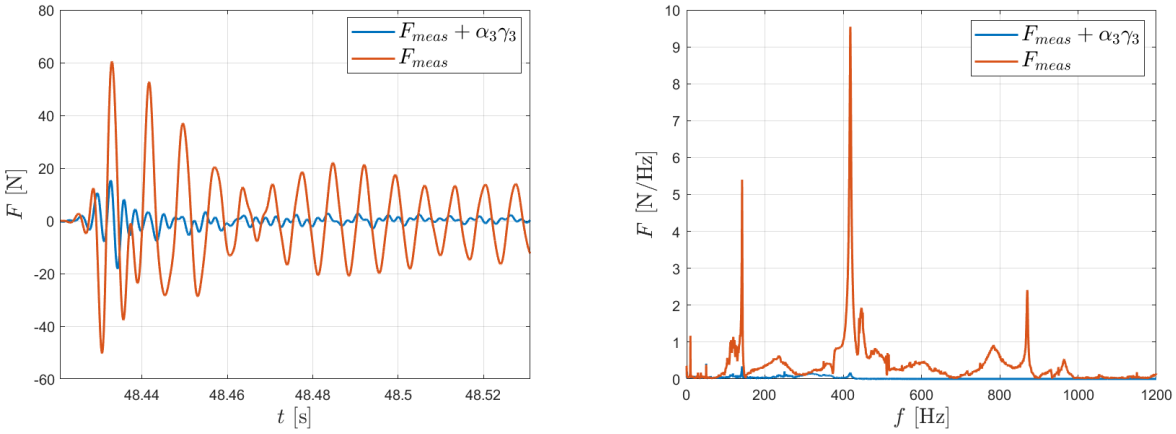

(a) (b)

Figure 2.34 – (a) Compensation of the force measured on S_3 during a hammer impact on S_2. (b) Fourier transforms of the forces.

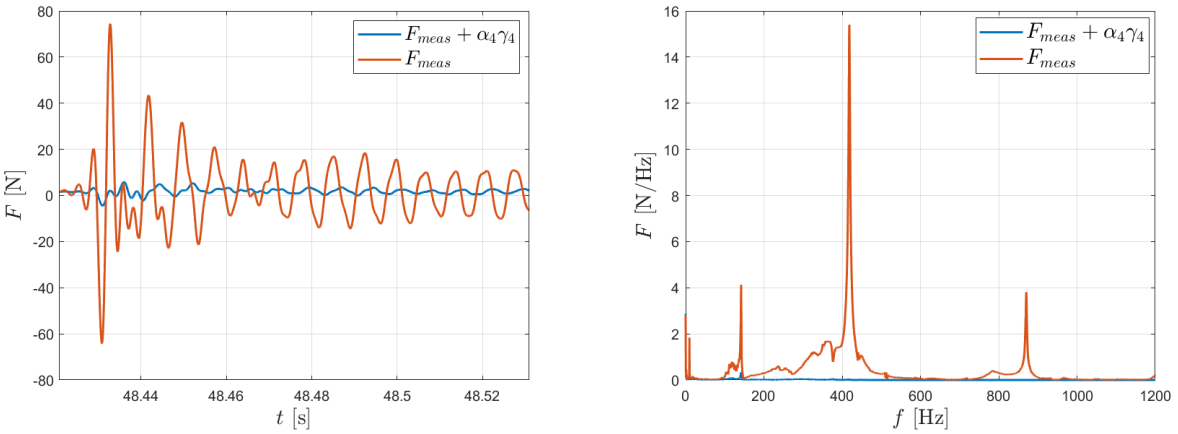

(a) (b)

Figure 2.35 – (a) Compensation of the force measured on S_4 during a hammer impact on S_2. (b) Fourier transforms of the forces.

2.4.4.4 Reconstruction of the force measured on the fourth section during a hammer impact on the second section

Similarly to section S_3, we reconstruct the force measured on S_4 during a hammer impact on S_2. The time histories of the forces are shown in figure 2.35a and their Fourier transforms in figure 2.35b. Most of the oscillations with a frequency lower than 300 Hz are removed as well.

2.4.5 Compensation of the force oscillations during breaking wave impacts

In this section, we present the reconstruction of the force acting on the cylinder during two breaking wave impacts. We first present in section 2.4.5.1 the case of a plunging breaker which induces an important dynamic response of the mockup. In section 2.4.5.2, we present the compensation of the oscillations induced by a gentler breaking wave.

2.4.5.1 Reconstruction of the force during the impact of a plunging breaker

In this section, the impact of a plunging breaker inducing an important dynamic response of the mockup is investigated. We study the impact case 712 (see table A.2), which corresponds to the impact of wave 3 (see table 3.2) on the fixed vertical mockup. The reconstruction of the force is performed with the coefficients obtained in section

2.4.3. The measured and reconstructed force signals are depicted in figure 2.36 for each section. Note that the measured force signal are low-pass filtered at f_c^k, where k is the number of the section. The corresponding Fourier transforms are shown in figure 2.37. For comparison, the Fourier transforms of the raw signals and of the low-pass filtered signals are depicted. For the two upper sections, most of the frequency content is retained in the low-pass filtered signal. For the two lower sections, a significant part of the signal is filtered out. The sum of the forces acting on the three upper sections is compared to the raw force measurement in figure 2.38. As it will be explained in section 4.1.1, this force will be identified as the impact force.

It appears in figures 2.36 and 2.37 that, for all the sections, the amplitude of the oscillations is drastically reduced by the reconstruction method. Similarly to what was observed during the hammer impacts, the maximum of the reconstructed force is reduced and is reached before the maximum of the measured force.

2.4.5.2 Reconstruction of the force during the impact of a gentler breaking wave

In this section, we present the application of the methodology to a gentler breaking wave which induces a lower level of vibrations. We study the impact case 608 (see table A.2), which corresponds to the impact of wave 24 (see table 3.2) on the fixed vertical mockup located at a distance δ higher than in the previously studied impact case. The measured and compensated forces on the different sections are shown in figure 2.39, while the corresponding Fourier transforms are shown in figure 2.40. Most of the oscillations occur on sections S_1 and S_2 and are compensated for. Low frequency oscillations with a low amplitude present on the four sections are compensated for. The sum of the forces measured on the three upper sections is compared to the corresponding compensated force in figure 2.41. Similarly, the amplitude of the oscillations is drastically reduced. It appears in figure 2.41 that the force above the SWL displays a slow increase, followed by a more rapid increase. Then an impulsive increase followed by a decrease occurs. Compared to a filtering approach, the proposed methodology allows to retain these features.

The proposed methodology has several important advantages. First, it allows to compensate for low frequency oscillations. This cannot be achieved through filtering, as it has been done for the first DIMPACT experimental campaign (Hulin et al. 2022). Then, it is not dependent on the level of oscillations: the same coefficients were used for the two presented impact cases. In other methods such as EMD (Choi et al. 2015; Spinosa et al.

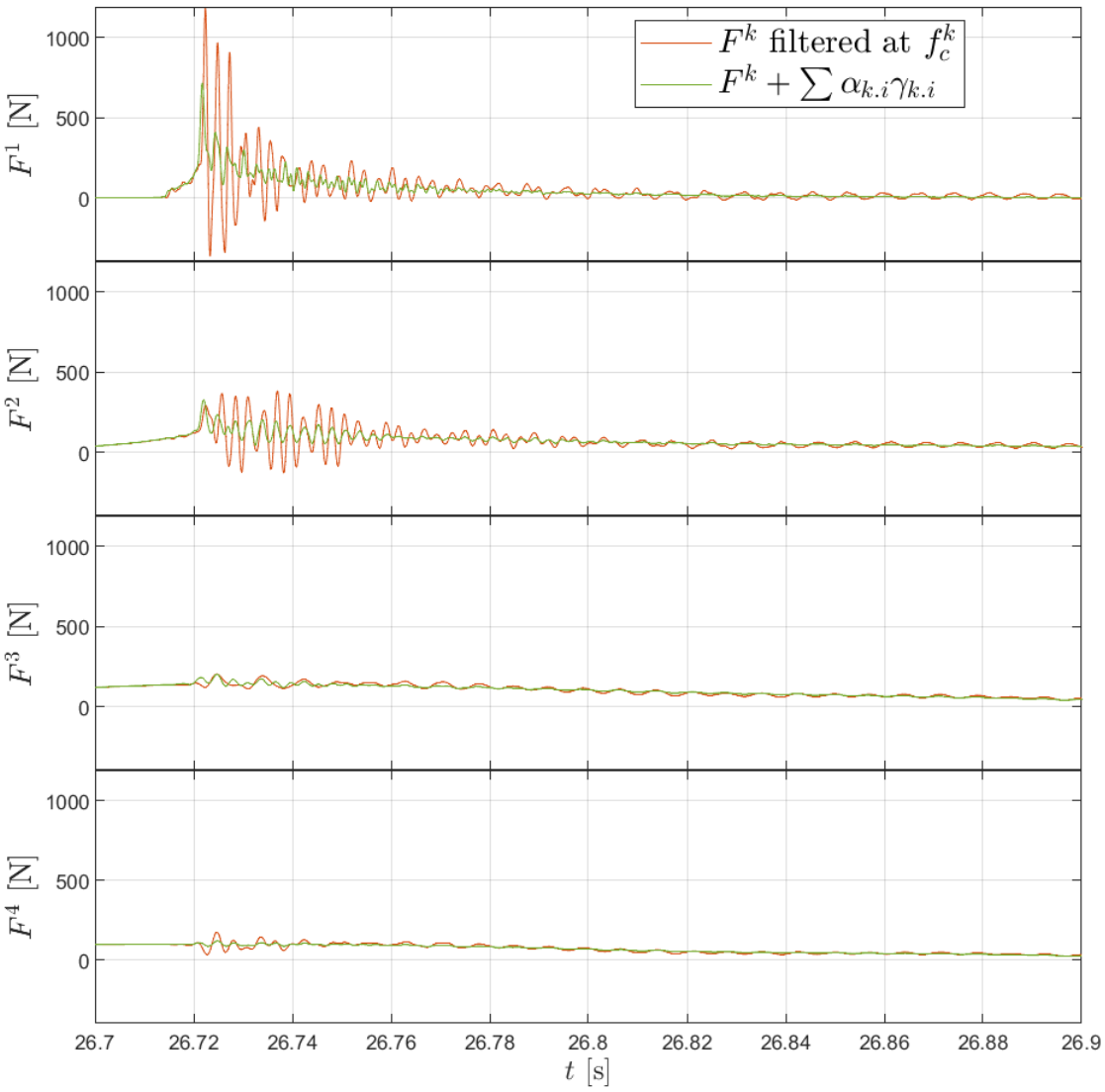

Figure 2.36 – Reconstruction of the forces acting on the different sections during wave impact 712 (wave 3). The orange curves correspond to the force measurements filtered at f_c^k, where k is the section number. The green curves are the reconstructed forces.

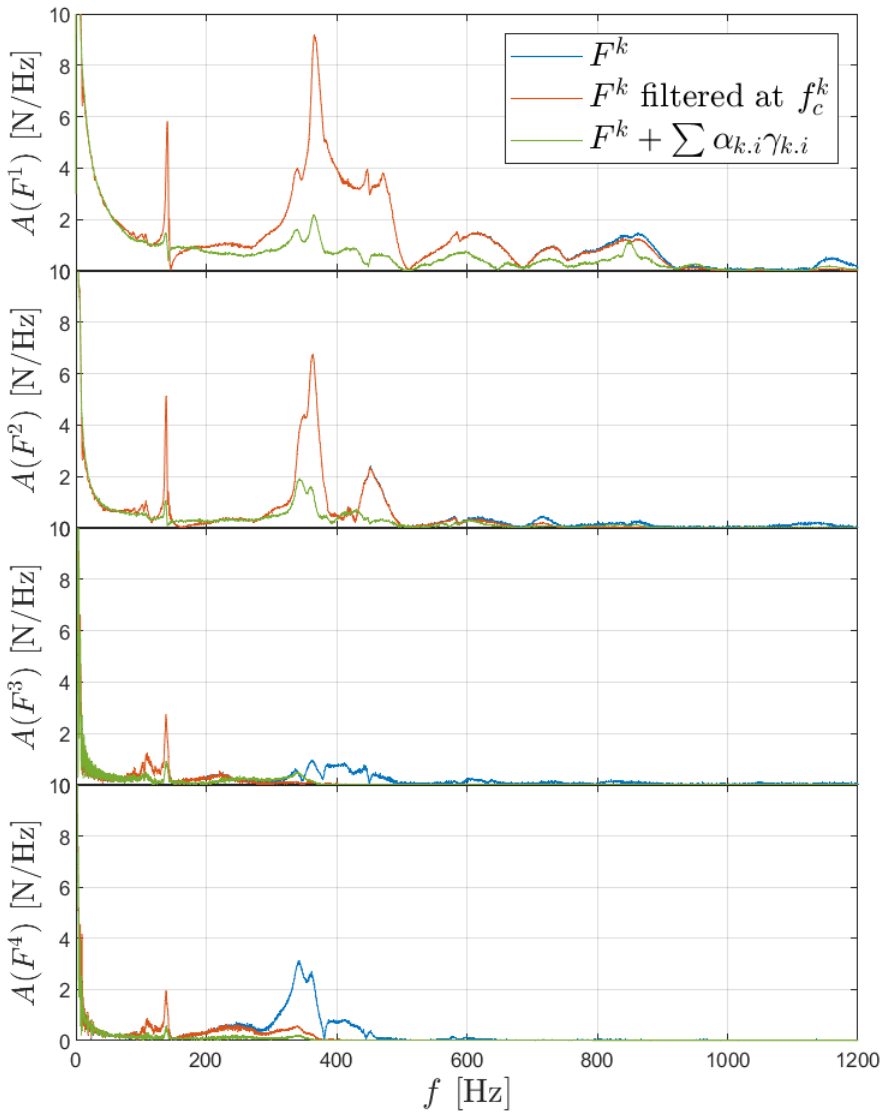

Figure 2.37 – Fourier transforms of the compensated forces (in green) and of the original forces measured on the different sections during wave impact 712. The blue curves correspond to the Fourier transforms of the raw force measurements while the orange curves correspond to the Fourier transforms of the force measurements filtered at f_c^k, where k is the section number.

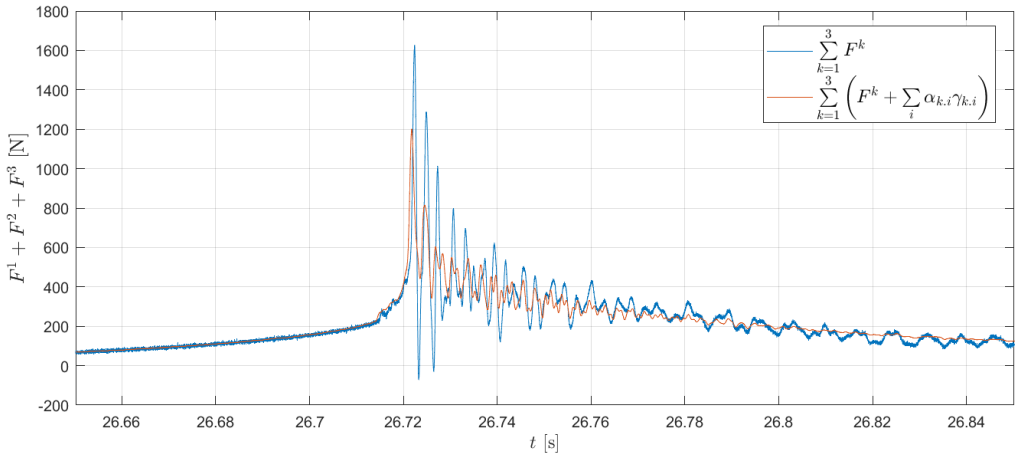

Figure 2.38 – Filtered and compensated forces measured during wave impact 712 (wave 3). The measurements are the sum of the forces measured on the three upper sections.

2022), the number of components that must be kept depends on the level of oscillations, which makes it case dependent (Spinosa et al. 2022). The current methodology is also able to compensate for several modes, which is a first, to the best of the author's knowledge.

As it is observed during the reconstruction of the hammer impacts and of the breaking wave impacts, residual oscillations are present after the peak. These oscillations may be due to the fact that the number of modes affecting the force and acceleration measurements is higher than the number of accelerometers. For breaking wave impacts, the accuracy of the reconstruction may also be reduced by the effect of the added mass. Indeed, the effect of added mass may be different from one mode to the other. It may thus modify the reconstruction coefficients that should be used. Indeed, the added-mass varies during an impact as the cylinder penetrates the wave. It is thus likely that the effect of added-mass is more important at the end of the impact than at the start of the impact. The compensation methodology has been applied to all the results presented in chapter 4. In the following section, we propose a methodology to quantify the level of residual oscillations in the compensated force.

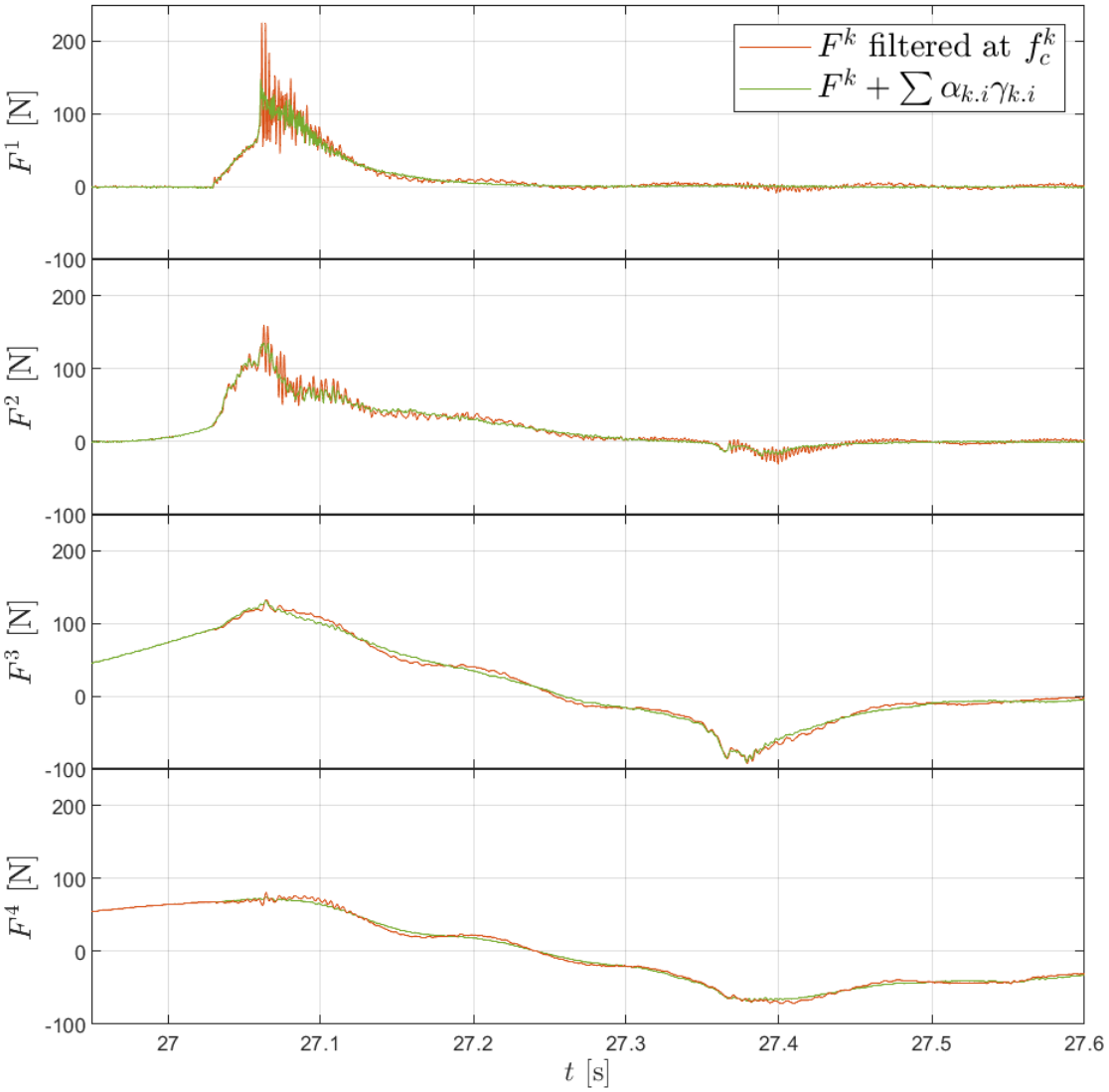

Figure 2.39 – Reconstruction of the forces acting on the different sections during wave impact 608 (wave 24). The orange curves correspond to the force measurements filtered at f_c^k, k being the section number. The green curves are the reconstructed forces.

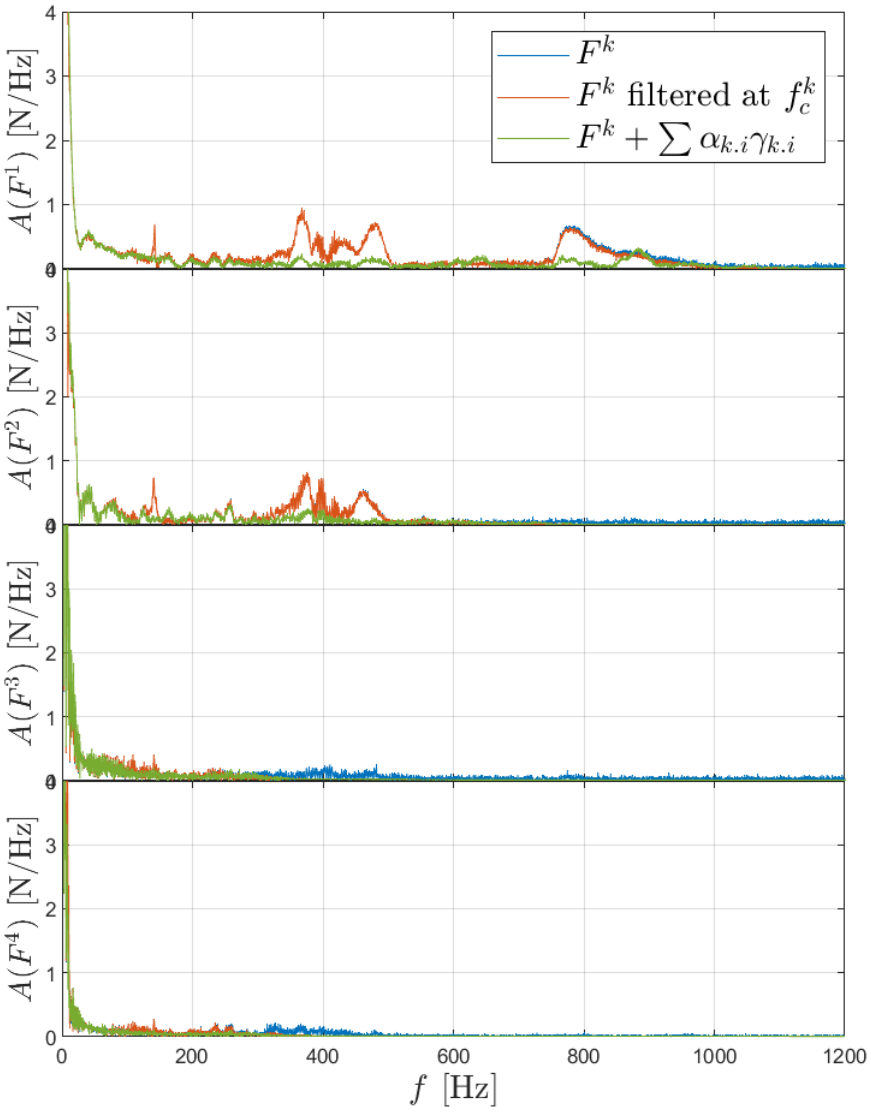

Figure 2.40 – Fourier transforms of the compensated forces (in green) and of the original forces measured on the different sections during wave impact 608. The blue curves correspond to the Fourier transforms of the raw force measurements while the orange curves correspond to the Fourier transforms of the force measurements filtered at f_c^k, where k is the section number.

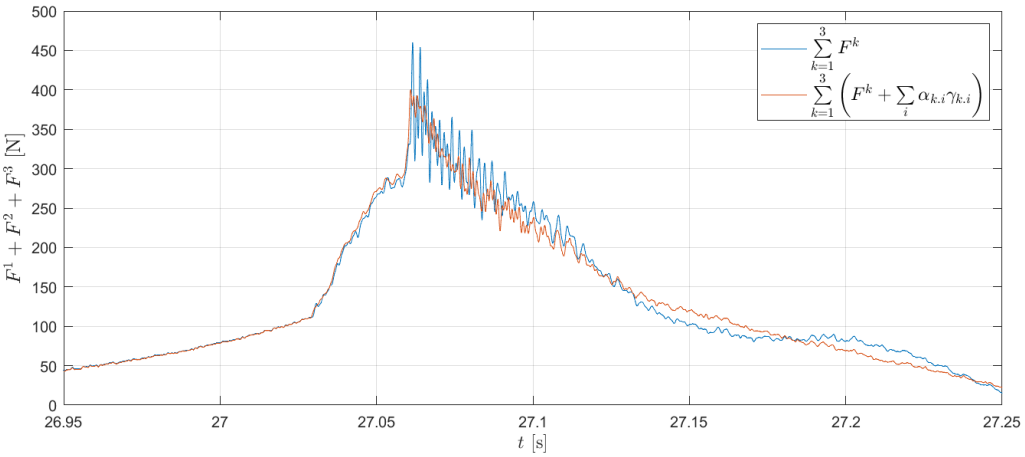

Figure 2.41 – Filtered and compensated force measurements on the three upper sections during wave impact 608 (wave 24).

2.4.6 Estimation of the level of residual oscillations in the compensated force

In spite of our efforts to reduce the effect of the vibrations on the force measurements, some residual oscillations remain in the force signals. It is of interest to characterise the level of residual oscillations, which may vary between two impacts with different experimental conditions. Based on the forces measured during hammer tests, we propose to define a confidence interval for the maximum impact force, which corresponds to the maximum impact force minus the amplitude of the highest residual oscillation. Indeed, we observed during the hammer tests that the amplitude of the highest residual oscillation is higher than the difference between the maximum of the compensated force and the force measured by the hammer. This is highlighted in figure 2.42, where the force measured by the hammer and the compensated force during a hammer test on section S_1 are depicted. The black segment corresponds to two times the amplitude A of the highest residual oscillation. The red segment, of length A, corresponds to the proposed confidence interval. For all the hammer tests, we observed that we overestimated the impact force measured by the hammer and that the difference between the measured force and the compensated force is smaller than the amplitude A of the highest residual oscillation. It is thus plausible that a similar behavior occurs when compensating a breaking wave impact force signal. We applied this estimation to two compensated force signals resulting from two breaking wave impacts displaying different levels of residual oscillations in figure 2.43.

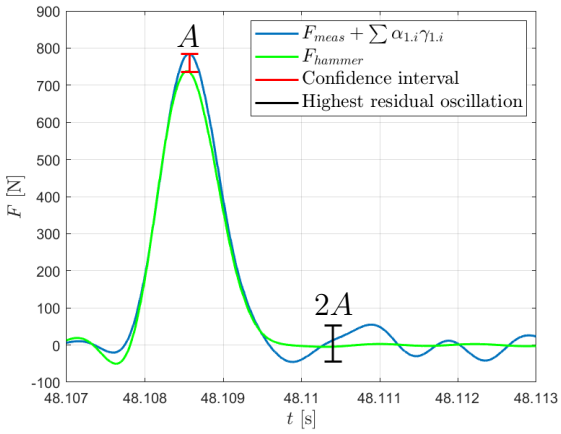

Figure 2.42 – Compensated force and force measured by the hammer during a hammer test on section S_1. The black segment corresponds to the crest to crest amplitude of the highest residual oscillation and the red segment to the proposed confidence interval.

We think that for a wave impact, the ratio between the error on the maximum impact force and the amplitude of the highest residual oscillation will be reduced compared to the ratio obtained during hammer tests. Indeed, at the instant of the maximum force, which corresponds to the start of the impact stage, the wetted surface of the mockup is small. Consequently, the effect of the added mass is smaller than for later instants, at which the wetted surface is larger. This tends to increase the amplitude of the residual oscillations as the coefficients of the compensation methodology were identified during hammer tests in air. Besides, the residual oscillations take place during the decrease of the impact force. As we decided to compute the amplitude of the highest oscillation as the highest difference between a maximum (which must be different from the global maximum) and the following minimum, we tend to overestimate the residual oscillations. This suggests that the magnitude of the highest residual oscillations probably corresponds to an upper bound of the level of residual oscillations, and thus of the error on the maximum value of the impact force.

In chapter 4, which presents the experimental results, we will apply this estimation of the level residual oscillations to breaking wave impacts with different experimental conditions. Note that this estimation is only applicable for the measurements which present a high level of residual oscillations. Indeed, for the measurements for which most of the oscillations are compensated for, there is no maxima and minima after the force peak. This is due to the fact that the oscillations occur during the decrease of the hydrodynamic

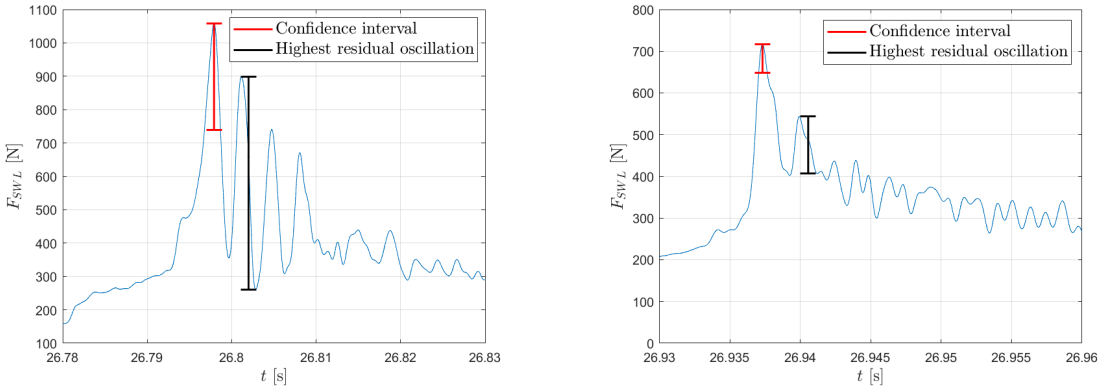

(a) (b)

Figure 2.43 – Impact force during the impact cases (a) 430 and (b) 599 (see table A.2 for the details of the experimental conditions). The black segment corresponds to two times the amplitude of the strongest oscillation. We estimate that the actual maximum of the force is included in the red interval.

force.

2.5 Conclusion

In this chapter, we presented the design choices that were made for the experimental set-up and the instrumentation of the model. We investigated in details the dynamic properties of the mockup. The hammer tests showed that different elastic modes of the instrumented sections may be excited. The shapes and frequencies of these modes were determined using a numerical structural model. The modes are also excited during breaking wave impacts. They induce rather strong oscillations of the force measurements which complicate the interpretation of the results. A new methodology has been implemented in order to compensate for these oscillations. This work has been submitted to the Journal of Sound and Vibrations and is under revision (Tassin et al. 2023). The method compensates for the inertial terms of the measured force using the signals of a set of accelerometers placed on the sections which are excited during breaking wave impacts. We showed that the compensation methodology allows to accurately reconstruct the excitation force during hammer tests. During breaking wave impacts, we were able to compensate an important part of the oscillations. Residual oscillations, which we attribute to the modification of the added-mass during the impact, are still present.

Chapter 3

Generation, measurement and characterisation of the breaking waves

In this chapter, we present the preparatory work dedicated to the generation and characterisation of the breaking waves. The generation of waves breaking at the desired location with different strengths, periods and heights required an extensive numerical investigation before the experimental campaign. After the numerical simulations, the waves were generated in the wave flume prior to the installation of the mockup. The free-surface profile of the waves was measured with a video camera along the wall of the flume. A good accordance was obtained between the modelled and measured profiles. Consequently, we decided to use the numerical simulations to estimate different parameters of the waves, such as the crest height at breaking, the crest velocity at breaking and the breaking strength Γ. Finally, we show that it is possible to differentiate breaking waves from non-breaking waves using a linear wave breaking threshold. We present a validation of a linear breaking threshold which makes use of the wave generation methodology developed for the experimental campaigns. The chapter is organized as follow: section 3.1 describes the numerical model and the wave generation approach, section 3.2 presents the measurements of the free-surface profile of the waves, section 3.3 details the characterisation of the breaking waves and section 3.4 is dedicated to the validation of the linear breaking threshold.

3.1 Modelling and generation of the breaking waves for the experimental campaigns

The breaking waves generated for the experimental campaigns were obtained through the focalisation of a JONSWAP spectrum following the method described by Rapp et al. 1990. A numerical wave tank, which is presented in section 3.1.1, was used to adjust the breaking location before generating the waves in the flume. The generation procedure is detailed in section 3.1.2. The list of the waves that were investigated during the experimental campaigns is given in section 3.1.3 along with the parameters of the breaking waves.

3.1.1 Presentation of the numerical wave tank

All the waves were modelled using the two-dimensional fully non-linear potential flow (FNPF) solver developed by Grilli et al. 1989, 1996 which relies on a boundary element method (BEM). In this section, we recall the main assumptions of the solver and its numerical procedure. More details can be found in Grilli et al. 1989.

3.1.1.1 Governing equations and boundary conditions

The fluid is assumed inviscid and incompressible and the flow irrotational. It makes it possible to describe the flow through the velocity potential $\phi(\mathbf{x}, t)$, where $\mathbf{x} = (x, z)$ is the vector of the two-dimensional coordinates and ϕ is such that the fluid velocity is expressed as $\vec{V} = \vec{\nabla}\phi$. The continuity equation is thus the Laplace equation for the velocity potential:

$$\Delta\phi = 0, \qquad \text{in } \Omega(t), \tag{3.1}$$

where $\Omega(t)$ is the fluid domain with boundary $\partial\Omega(t)$. On the free surface $\partial\Omega_s(t)$, the following kinematic and dynamic boundary conditions are satisfied:

$$\frac{D\mathbf{r}}{Dt} = \boldsymbol{\nabla}\phi, \qquad \text{on } \partial\Omega_s(t), \tag{3.2a}$$

$$\frac{D\phi}{Dt} = \frac{1}{2}(\nabla\phi)^2 - gz - \frac{p_a}{\rho}, \qquad \text{on } \partial\Omega_s(t), \tag{3.2b}$$

where ρ is the fluid density, p_a is the atmospheric pressure, g is the acceleration due to gravity and $\mathbf{r} \in \partial\Omega_s$ is the vector coordinates of a fluid particle located at the free surface. On fixed boundaries $\partial\Omega_f$ such as the bottom and the walls of the basin, the fluid velocity normal to the boundary is equal to zero:

$$\boldsymbol{\nabla}\phi.\mathbf{n} = 0, \qquad \text{on } \partial\Omega_f, \tag{3.3}$$

where $\mathbf{n}$ is the vector normal to the boundary. Along moving boundaries $\partial\Omega_m(t)$ such as the wave generator, the fluid velocity normal to the boundary surface is equal to the normal velocity component of the boundary surface:

$$\boldsymbol{\nabla}\phi.\mathbf{n} = \mathbf{u}_p.\mathbf{n}, \qquad \text{on } \partial\Omega_m(t), \tag{3.4}$$

where $\mathbf{u}_p$ is the velocity of the boundary.

3.1.1.2 Time integration

The position of the free surface $\mathbf{r}(t)$ and the velocity potential at the free surface $\phi(\mathbf{r}(t))$ are updated in time using the following second-order Taylor series expansions:

$$\mathbf{r}(t+\Delta t) = \mathbf{r}(t) + \sum_{k=1}^{2} \frac{(\Delta t)^k}{k!} \frac{\mathrm{D}^k \mathbf{r}}{\mathrm{D}t^k}(t) + \mathcal{O}((\Delta t)^3), \tag{3.5a}$$

$$\phi(\mathbf{r}(t+\Delta t)) = \phi(\mathbf{r}(t)) + \sum_{k=1}^{2} \frac{(\Delta t)^k}{k!} \frac{\mathrm{D}^k \phi(\mathbf{r}(t))}{\mathrm{D}t^k} + \mathcal{O}((\Delta t)^3). \tag{3.5b}$$

The first and second order coefficients in equation 3.5a and 3.5b are obtained through the resolution of two mixed boundary value problems. First, a mixed boundary value problem for the velocity potential is solved. The first order coefficients $\frac{\mathrm{D}\mathbf{r}}{\mathrm{D}t}(t)$ and $\frac{\mathrm{D}\phi(\mathbf{r}(t))}{\mathrm{D}t}$ in equations 3.5a and 3.5b are expressed as a function of the velocity potential through equation 3.2a and 3.2b, respectively. A second mixed boundary value problem for the time derivative of the velocity potential $\frac{\partial\phi}{\partial t}$ is then solved. The second order coefficients $\frac{\mathrm{D}^2\mathbf{r}}{\mathrm{D}t^2}(t)$ and $\frac{\mathrm{D}^2\phi(\mathbf{r}(t))}{\mathrm{D}t^2}$ in equations 3.5a and 3.5b are expressed as a function of the time derivative of the velocity potential by differentiating equations 3.5a and 3.5b. Once these coefficients have been computed, the position of the free surface and the velocity potential are updated in time and they define the boundary conditions of the Laplace problem at $t + \Delta t$.

The Laplace problems for ϕ (and $\frac{\mathrm{d}\phi}{\mathrm{d}t}$) are solved using the boundary element method (BEM). The continuity equation is transformed into a boundary integral equation using Green's third identity and the free-space Green's function $G(\mathbf{x}, \mathbf{x_l})$ as:

$$\alpha(\mathbf{x_l})\varphi(\mathbf{x_l}) = \int_{\partial\Omega(\mathbf{x})} \left(\frac{\partial\varphi}{\partial n}(\mathbf{x}) G(\mathbf{x}, \mathbf{x_l}) - \varphi(\mathbf{x}) \frac{\partial G}{\partial n}(\mathbf{x}, \mathbf{x_l}) \right) \mathrm{d}\partial\Omega(\mathbf{x}), \tag{3.6}$$

where $\alpha(\mathbf{x_l})$ is a geometric coefficient and $\mathbf{x}$ and $\mathbf{x_l}$ are points on the boundary $\partial\Omega$. This boundary integral equation is written for $N_{\partial\Omega}$ collocation points $\mathbf{x_l}$ placed along the boundary $\partial\Omega$. Each integral is discretized and the solution to the problem is obtained by solving the linear problem.

At each time step, the positions of the collocation points $\mathbf{x_l}$ on the free surface are updated in time, so that the distance between two adjacent nodes may vary. In particular, in an overturning wave, the nodes will gather at the crest. The time step Δt is updated automatically so that the Courant number $C = \frac{u\Delta t}{\Delta x}$ is equal to 0.5, where Δx is the distance between the two closest nodes and $u = \sqrt{gh}$ is the fluid velocity.

3.1.1.3 Modelling of Ifremer's wave flume

The FNPF solver was used to model breaking waves in Ifremer's wave flume. The dimensions of the flume were given in section 2.2.1 (see figure 2.3). In the simulations, 774 nodes were distributed along the boundary of the domain. The free surface was discretized with 601 nodes, the fixed wall opposite to the wave generator with 31 nodes, the bottom with 101 nodes and the piston-type wave generator with 41 nodes. The absorbing beach was not modelled and the non-penetration condition 3.3 was applied at the extremity of the flume. The horizontal distance Δx between two adjacent nodes on the free surface at the start of the simulation is depicted in figure 3.1. In a region extending from $x = 19$ to $x = 22$ m, which contains the breaking location, the distance Δx is reduced. The higher density of nodes allows to obtain a more accurate description of the breaking phenomenon and of the wave kinematics. The distance between the nodes is reduced progressively over a three meters region extending on each side of the region with a higher node density.

The errors on the volume and on the energy were computed for a particular wave (wave 3 in table 3.2) to check the accuracy of the simulations. The maximum relative variation of the volume of fluid in the domain was of 0.002 % over the duration of the simulation. The numerical error in terms of energy was analyzed by comparing the change of energy in the fluid ΔE_f with the work W_p done by the paddle. Both quantities are

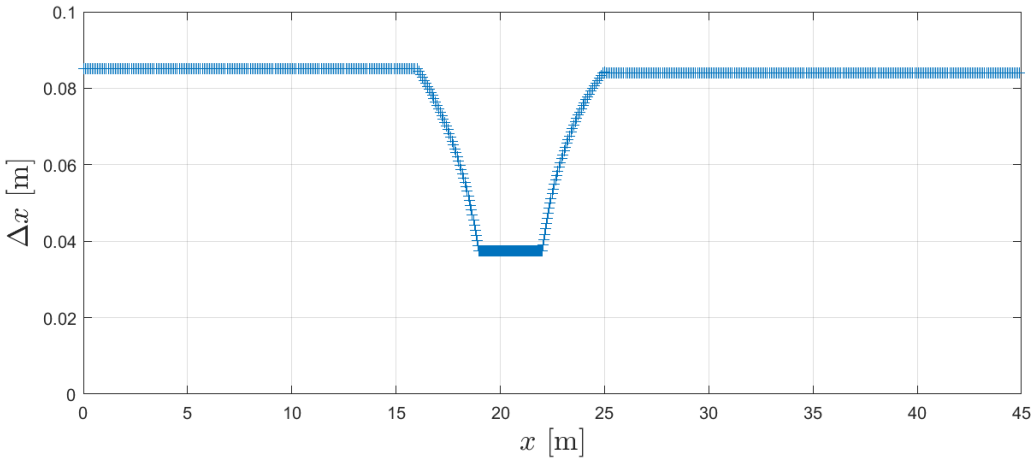

Figure 3.1 – Distance between two adjacent nodes on the free surface at the start of the simulation as a function of the longitudinal position of the nodes in the numerical flume.

depicted in figure 3.2. The variation ΔE_f of the energy of the fluid corresponds to the sum of the kinetic fluid energy (the fluid is initially at rest) and of the difference between the potential energy and the initial potential energy. The work of the paddle W_p corresponds to the work of the pressure force on the paddle. At the end of the simulation, the relative error on the energy, $\frac{\Delta E_f - W_p}{W_p}$, is smaller than one percent.

3.1.2 Breaking wave generation

The technique used to generate the breaking waves relies on a frequency focusing approach (see Rapp et al. 1990 for instance). This method relies on the assumption that the free-surface elevation, η, is the sum of N different components which satisfy the linear dispersion relation:

$$\eta(x,t) = \sum_{n=1}^{N} a_n \cos(k_n x - \omega_n t - \phi_n), \tag{3.7}$$

where the amplitude of the components $a_n = \sqrt{2S(f)\mathrm{d}f}$ are defined by the spectral density, $S(f)$, of the wave spectrum. The angular frequency ω_n and the wavelength k_n are linked through the dispersion relation $\omega_n^2 = g k_n \tanh(k_n h)$, where h is the water depth. The phases ϕ_n of the different components are chosen so that at an instant t_f and at a position x_f, the different components are all in phase:

$$\phi_n = k_n x_f - \omega_n t_f. \tag{3.8}$$

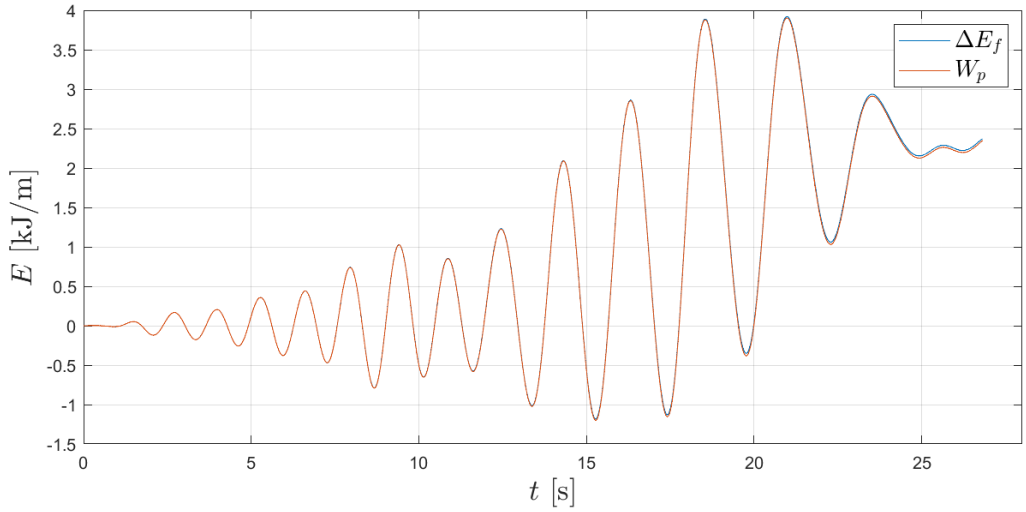

Figure 3.2 – Comparison of the total energy of the fluid E_f and of the work of the paddle W_p

The paddle displacement $x_p(t)$ is obtained using the first-order Biésel transfer function T of the paddle and by applying a phase shift of $\pi/2$ to all the components (Andersen et al. 2014):

$$x_p(t) = \sum_{n=1}^{N} \frac{a_n}{T(\omega_n)} \sin(\omega_n t + \phi_n). \tag{3.9}$$

In the present study, the frequency content of the waves was defined with a JONSWAP spectrum, defined as (see Molin 2002 for instance):

$$S(\omega) = \alpha H_S^2 \omega_p^4 \omega^{-5} e^{-\frac{5}{4}\left(\frac{\omega}{\omega_p}\right)^{-4}} \gamma^a, \tag{3.10}$$

where

$$a = e^{-\frac{(\omega-\omega_p)^2}{2\sigma^2\omega_p^2}}, \tag{3.11}$$

$\sigma = 0.07$ if $\omega < \omega_p$, $\sigma = 0.09$ if $\omega > \omega_p$ and ω_p is the angular frequency of the peak. The coefficient α is chosen so that:

$$H_S^2 = 16 \int_0^\infty S(\omega) \mathrm{d}\omega. \tag{3.12}$$

The peak period T_p and the peak enhancement factor γ were chosen based on a preliminary study carried out by different partners of the DIMPACT project (Peyrard et al. 2021) to

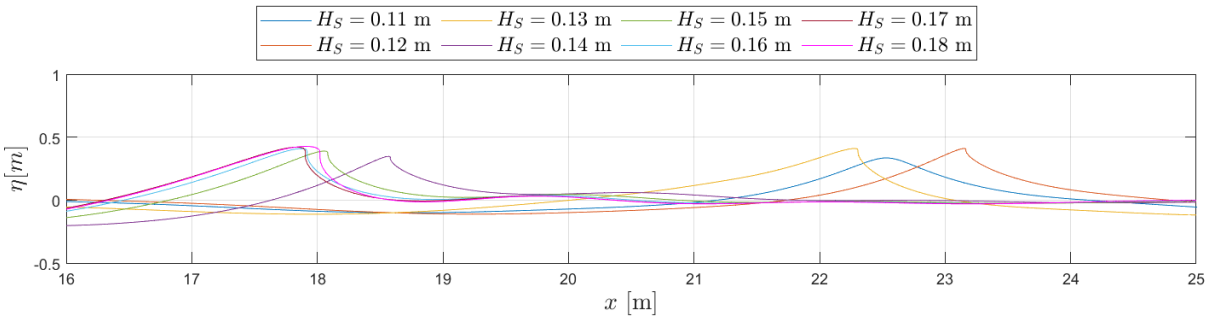

Figure 3.3 – Free-surface profiles of the waves obtained for different values of H_S, $T_p = 2.49$ s and $\gamma = 1.4$. The free-surface profiles are depicted either at the instant of breaking or at the instant at which the free-surface elevation is maximum for the non-breaking waves.

study the statistics of wave breaking events. They are representative of a site in South Brittany. Breaking waves of different height and strength were obtained by varying the significant wave height H_S. Note that, as it will be explained later, the breaking strength is not a monotonic function of H_S. The wave period was varied by changing the peak period T_p of the spectrum. The N components are evenly spaced in the frequency range $[0; f_c]$, where f_c is the upper frequency limit of the spectrum. The components with a frequency above f_c were not included to avoid uncontrollable small breaking events. The frequency resolution is $\Delta f = 0.01$ Hz. An illustration of the free-surface profiles obtained for different values of H_S, but the same values of $T_p = 2.49$ s and $\gamma = 1.4$ is presented in figure 3.3. The upper frequency limit is $f_c = 0.8$ Hz and the focus time and location are $t_f = 30$ s and $x_f = 21$ m, respectively. The profiles are shown either at the instant of breaking for the breaking waves, or at the instant at which the free-surface elevation is maximum for the non-breaking waves. A significant wave height $H_S = 0.11$ m (the blue profile in figure 3.3) leads to a steep non-breaking wave. In this case, the maximum free-surface elevation occurs downstream of the theoretical focusing point at $x = 22.53$ m and at $t = 30.39$ s. An increase of the significant wave height to $H_S = 0.12$ m leads to the breaking of the focused wave. Breaking occurs downstream of the theoretical focusing location and after the focusing time. The location and instant of breaking for the different values of H_S are given in table 3.1. If one further increases the significant wave height to $H_S = 0.13$ m, breaking occurs earlier and more upstream. The part of the wave which is breaking, *i.e.* which is near vertical, is more important for $H_S = 0.13$ m than for $H_S = 0.12$ m. As it can be seen in table 3.1, further increasing H_S to 0.14 m induces an important shift of the breaking location and time. The steepness of the wave preceding

H_S [m]	Breaking	x_f [m]	t_f [s]	x_b [m]	t_b [s]
0.11	No	21	30	22.53	30.39
0.12	Yes	21	30	23.16	30.54
0.13	Yes	21	30	22.31	30.11
0.14	Yes	21	30	18.58	27.01
0.15	Yes	21	30	18.08	26.73
0.16	Yes	21	30	17.92	26.61
0.17	Yes	21	30	17.90	26.55
0.18	Yes	21	30	18.02	26.54

Table 3.1 – Evolution of the breaking time and location for the different significant wave heights. The time and position given for the non-breaking wave correspond to the time and position of the maximum free-surface elevation.

the focused wave has been increased so that this wave is now breaking before focalisation is attained. The breaking wave is therefore only partially focused. Breaking occurs around $x = 18$ m and $t = 27$ s, *i.e.* approximately half a wavelength closer to the wave maker and one wave period earlier. If one continues to increase the significant wave height, the breaking location moves slightly towards the wave maker and breaking occurs slightly earlier. This is true up to $H_S = 0.18$ m. For $H_S = 0.19$ m, which is not shown in figure 3.3, the wave breaks approximately one wavelength ahead of the focusing point and two wave period before the focusing time. For the waves displaying a significant wave height between 0.14 and 0.18 m, the shape of the free-surface profiles suggest that the breaking strength increases when H_S increases. The process of progressively increasing H_S thus allows to obtain breaking waves of different strengths. However, if the increase is too important, the preceding wave will break and the wave may display a smaller breaking strength.

It appears that the different breaking waves break at different locations and times. For the purpose of our experiments, we needed the waves to break at the same location $x_t = 21$ m, where the model was placed. We corrected the breaking location by iteratively modifying the focus point. For the first iteration, the wave simulation is run with the theoretical focus point $x_f = x_t = 21$ m. The waves obtained with this value of x_f are those depicted in figure 3.3. In the following iterations, the focus point x_{foc} is corrected iteratively as follows:

$$x_{foc}^{i+1} = x_{foc}^{i} - (x_b^i - x_t), \tag{3.13}$$

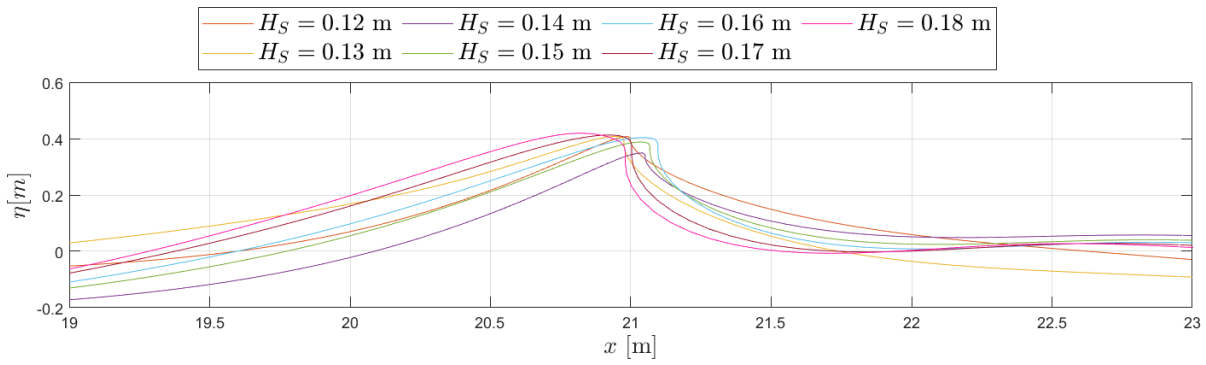

Figure 3.4 – Free-surface profiles of the breaking waves listed in table 3.1 at the instant of breaking. The breaking locations have been iteratively modified.

where x_b^i corresponds to the breaking location obtained at the i^{th} iteration. At each iteration, the phases of the wave components are recomputed using the new focusing position in equation 3.8. For all the investigated cases, 3 to 4 iterations were sufficient to obtain breaking within $\pm$ 10 cm of the target location x_t. Figure 3.4 shows the final free-surface profiles of the breaking waves obtained by applying the iterative procedure to the waves listed in table 3.1. Note that for all the spectra that were used to generate the breaking waves, the strongest plunging breakers were obtained when breaking occurred one period before the focused wave. We were not able to obtain a strong plunging breaker with the focused wave because an increase of H_S led the previous wave to break instead of increasing the breaking strength.

3.1.3 List of the generated breaking waves

Three groups of breaking waves, which are listed in table 3.2, were generated with the methodology described in the previous section. For each group, a peak period T_p, a peak enhancement factor γ and a cut-off frequency f_c were chosen. The significant wave height H_S was varied to obtain waves of different breaking strengths. The focus time is $t_f = 30$ s and the focus location x_f was obtained with the iterative procedure presented in the previous section. The majority of the waves were obtained with a peak period of 2.25 s and 2.49 s. An additional wave obtained with $T_p = 2$ s was also studied to complement the test matrix with a shorter breaking wave.

Wave Number	H_S [m]	T_p [s]	γ [1]	f_c [Hz]	x_f [m]	t_f [s]
1	0.12	2.25	3.3	0.8	18.80	30
2	0.13	2.25	3.3	0.8	22.99	30
23	0.135	2.25	3.3	0.8	23.57	30
24	0.14	2.25	3.3	0.8	23.87	30
3	0.15	2.25	3.3	0.8	24.15	30
4	0.17	2.25	3.3	0.8	27.90	30
5	0.20	2.25	3.3	0.8	27.42	30
6	0.12	2.49	1.4	0.8	18.84	30
7	0.13	2.49	1.4	0.8	19.69	30
8	0.14	2.49	1.4	0.8	23.42	30
9	0.15	2.49	1.4	0.8	23.92	30
10	0.16	2.49	1.4	0.8	24.08	30
11	0.17	2.49	1.4	0.8	23.94	30
12	0.18	2.49	1.4	0.8	23.72	30
15	0.10	2.0	3.3	0.9	23.40	30

Table 3.2 – List of the parameters used to generate the breaking waves for the experimental campaigns. The parameters of the JONSWAP spectrum are the significant wave height H_S, the peak period T_p, the peak enhancement factor γ and the cut-off frequency f_c. Parameters x_f and t_f correspond to the focusing position and to the focusing time, respectively.

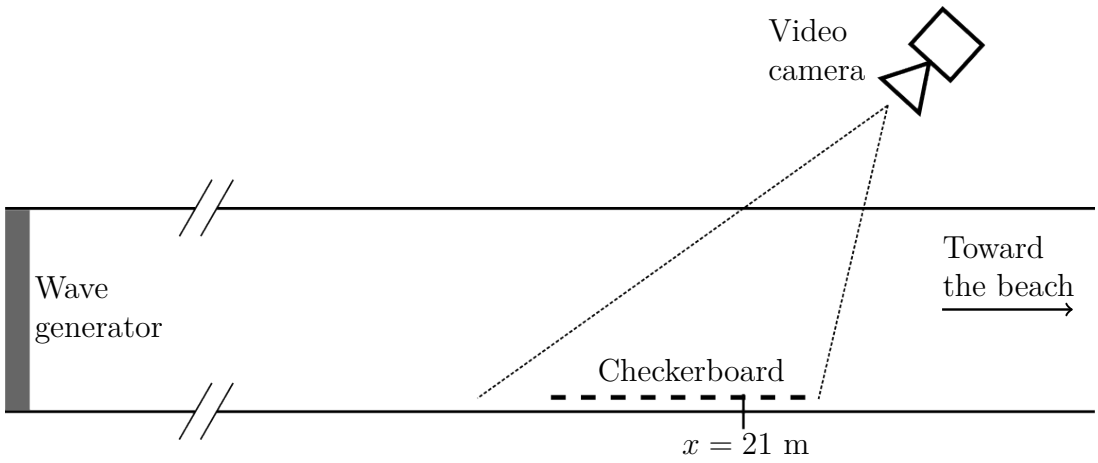

Figure 3.5 – Top view of the experimental set-up used to measure the waves free-surface profiles with a video camera in the flume

3.2 Free-surface profile measurement of the breaking waves

After the numerical simulation presented in section 3.1, the waves listed in table 3.2 were generated in the wave flume prior to the installation of the mockup. The free-surface profiles of the waves were measured by filming the interface between the wall and the free surface with a high-speed video camera, similarly to the method proposed in Dorfman et al. 2007. The experimental set-up is presented in section 3.2.1. The camera calibration method is presented in section 3.2.2 and the detection of the free surface profile in section 3.2.3. Free-surface profile measurements of breaking waves are presented in section 3.2.4. The repeatability of the wave profiles is investigated and the measured free-surface profiles are compared to the numerical free-surface profiles.

3.2.1 Experimental set-up

The experimental set-up is summarized in figure 3.5. A high-speed video camera of type Photron FASTCAM Mini AX200 was placed along the flume to film the interface between the wall of the flume and the water surface. The filmed area was centred around $x = 21$ m. The frame rate is of 2000 frames per second. The lens is of type AF-S NIKKOR 35mm f/1.8G ED and has a focal length of 35 mm. A surface piercing wave gauge is located upstream of the filmed area at 11.895 m from the wave paddle. This wave gauge is used to trigger the high-speed video camera. The trigger is sent when the free-surface elevation

exceeds a certain level, chosen so that it is reached approximately 5 s before the wave breaks. The displacement of the wave paddle was recorded using a draw-wire sensor. As the trigger corresponding to the start of the paddle motion was not recorded, the paddle position was used to precisely determine the instant at which the wave paddle started moving.

3.2.2 Calibration of the video camera

The calibration of a camera measurement device is in general performed in two steps: an intrinsic calibration and an extrinsic calibration. The intrinsic calibration step, which is described in section 3.2.2.1, aims to transform the image coordinates into the video camera coordinates. For this purpose, the parameters of the optical system, such as the distortion and the focal distance, are determined to obtain an idealized pin-hole model. This step is usually performed using a checkerboard calibration plate, or another type of calibration plate, which is displaced in front of the camera. If the lens displays an important distortion, non-linear corrections must be applied to the video camera coordinates to compensate for the distortion. In the present approach, given the low level of distortion of the lens, we neglected the distortion in the calibration process. The extrinsic calibration step, which is described in section 3.2.2.2, consists into determining the transfer matrix between the camera frame of reference and another frame of reference, the frame of reference of the flume in our case. This step was performed by using a 2 m long checkerboard plate placed along the wall of the flume, as depicted in figure 3.7.

If the distortion of the lens is not accounted for, the intrinsic calibration process becomes linear. It is thus possible to simplify the calibration procedure by carrying an implicit calibration, which consists into directly determining the linear transfer function between the checkerboard coordinates and the image coordinates. This process, which is called implicit calibration, is described in section 3.2.2.3.

3.2.2.1 Intrinsic calibration

The intrinsic calibration process is illustrated in figure 3.6. It consists in defining the relation between the image coordinates (X_i, Y_i) of the image of a world point (the blue cross) and the camera coordinates (X_c, Y_c, Z_c) of the point (the red cross). The image coordinates are given in the image frame of reference $(O_i, \vec{x}_i, \vec{y}_i, \vec{z}_i)$, the origin of which is located at the top left corner of the image. The x_i- and y_i-axis are directed along the

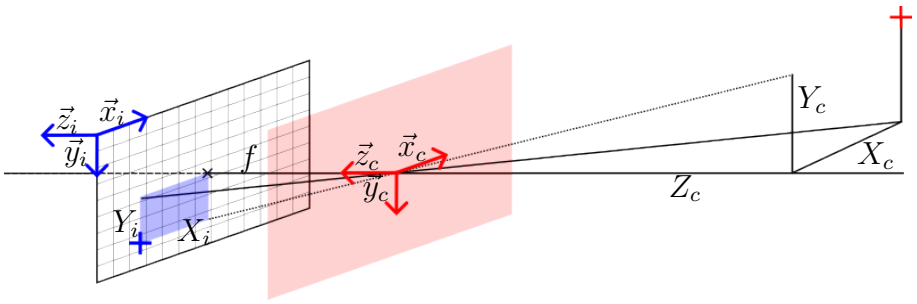

Figure 3.6 – Image and camera frames of reference

horizontal and vertical directions of the images, respectively. The z_i-axis is defined so as to have a direct frame of reference. The camera frame of reference $(O_c, \vec{x_c}, \vec{y_c}, \vec{z_c})$ takes its origin at the camera optical center. Its z_c-axis is collinear to the optical axis of the camera. As we assumed that the camera captor is perfectly perpendicular to the optical axis, the camera z_c-axis $\vec{z_c}$ is collinear to the image z_i-axis $\vec{z_i}$. The x_c- and y_c-axis are collinear to the corresponding axis of the image frame of reference. The distance between the sensor and the focal point, *i.e.* the origin of the camera frame of reference, is the focal length f. The intercept theorem states that the relation between the image coordinates and the camera coordinates is:

$$\begin{aligned} X_i' &= \frac{f}{Z_c} X_c, \\ Y_i' &= \frac{f}{Z_c} Y_c, \end{aligned} \tag{3.14}$$

where (X_i', Y_i') are the picture coordinates in pixels with an origin located on the optical axis of the video camera. Moving the origin to the upper left corner and multiplying by the pixel density allows to write the previous equation as:

$$Z_c \begin{bmatrix} X_i \\ Y_i \end{bmatrix} = F \begin{bmatrix} X_c \\ Y_c \end{bmatrix} + Z_c \begin{bmatrix} c_x \\ c_y \end{bmatrix}, \tag{3.15}$$

where F is the focal length in pixel and (c_x, c_y) are the pixel coordinates of the optical center. This equation can be written in matrix form as:

$$Z_c \begin{bmatrix} X_i \\ Y_i \\ 1 \end{bmatrix} = \underbrace{\begin{bmatrix} F & 0 & c_x \\ 0 & F & c_y \\ 0 & 0 & 1 \end{bmatrix}}_{K} \begin{bmatrix} X_c \\ Y_c \\ Z_c \end{bmatrix}. \tag{3.16}$$

Matrix K is called the intrinsic matrix of the video camera.

3.2.2.2 Extrinsic calibration

The extrinsic calibration of a video camera consists in finding the rotation matrix R and the translation vector $\mathbf{t}$ which relate the video camera coordinates of a point to its checkerboard coordinates (X_b, Y_b, Z_b). The checkerboard used in the present experiments is depicted in figure 3.7. The checkerboard frame of reference $(O_b, \vec{x_b}, \vec{y_b}, \vec{z_b})$ takes its origin at the top left intersection point of the checkerboard. Its x_b-axis is directed along the longitudinal direction of the checkerboard and its y_b-axis along the vertical direction of the checkerboard. The vectors $\vec{x_b}$ and $\vec{y_b}$ of the checkerboard reference frame are shown in figure 3.9. The z_b-axis is defined so as to have a direct coordinate system. The relation between the camera coordinates and the checkerboard coordinates writes:

$$\begin{bmatrix} X_c \\ Y_c \\ Z_c \end{bmatrix} = \begin{bmatrix} R & \mathbf{t} \end{bmatrix} \begin{bmatrix} X_b \\ Y_b \\ Z_b \\ 1 \end{bmatrix}, \tag{3.17}$$

where R is a rotation matrix and $\mathbf{t}$ a translation vector. Measuring the position of a point with a single camera only allows to obtain two coordinates. The third coordinates, Z_b, is assumed to be zero. This corresponds to the fact that the measured points are in the plane of the checkerboard, *i.e.* in the plane of the wall of the flume. The previous equation can be rewritten as:

$$\begin{bmatrix} X_c \\ Y_c \\ Z_c \end{bmatrix} = \begin{bmatrix} R_1 & R_2 & \mathbf{t} \end{bmatrix} \begin{bmatrix} X_b \\ Y_b \\ 1 \end{bmatrix}, \tag{3.18}$$

where R_1 and R_2 denote the first and second columns of the rotation matrix R.

3.2.2.3 Implicit calibration

Combining equations 3.16 and 3.18, the relation between the image coordinates of a point and its checkerboard coordinates writes:

$$Z_c \begin{bmatrix} X_i \\ Y_i \\ 1 \end{bmatrix} = \underbrace{K \begin{bmatrix} R_1 & R_2 & \mathbf{t} \end{bmatrix}}_{\mathbf{B}} \begin{bmatrix} X_b \\ Y_b \\ 1 \end{bmatrix}. \tag{3.19}$$

The implicit calibration consists in determining the coefficients B_{ij} of matrix $\mathbf{B}$ and the value of Z_c, so that the image coordinates (X_i, Y_i) of a point can be transformed into its checkerboard coordinates (X_b, Y_b). The third line of the previous equation allows to express the third camera coordinate Z_c as $Z_c = B_{31}X_b + B_{32}Y_b + B_{33}$. The previous equation can thus be rewritten as:

$$(B_{31}X_b + B_{32}Y_b + B_{33}) \begin{bmatrix} X_i \\ Y_i \end{bmatrix} = \begin{bmatrix} B_{11}X_b + B_{12}Y_b + B_{13} \\ B_{21}X_b + B_{22}Y_b + B_{23} \end{bmatrix}. \tag{3.20}$$

This equation is valid for all the intersections of the checkerboard. The coordinates of the i^{th} intersection (X_b^i, Y_b^i) are known as the length of the squares of the checkerboard is known and equal to 0.09 m. The image coordinates of the checkerboard corners are obtained using the Matlab function **detectCheckerboardPoints**. A picture of the checkerboard is depicted in figure 3.7. The red crosses correspond to the detected intersections. The application of the previous relation to all the checkerboard intersections leads to the following system of equations:

$$\underbrace{\begin{bmatrix} X_b^1 & Y_b^1 & 1 & 0 & 0 & 0 & -X_b^1X_i^1 & -Y_b^1X_i^1 & -X_i^1 \\ 0 & 0 & 0 & X_b^1 & Y_b^1 & 1 & -X_b^1Y_i^1 & -Y_b^1Y_i^1 & -Y_i^1 \\ \vdots & \vdots & \vdots & \vdots & \vdots & \vdots & \vdots & \vdots & \vdots \\ X_b^n & Y_b^n & 1 & 0 & 0 & 0 & -X_b^nX_i^n & -Y_b^nX_i^n & -X_i^n \\ 0 & 0 & 0 & X_b^n & Y_b^n & 1 & -X_b^nY_i^n & -Y_b^nY_i^n & -Y_i^n \end{bmatrix}}_{\mathbf{W}} \underbrace{\begin{bmatrix} B_{11} \\ B_{12} \\ B_{13} \\ B_{21} \\ B_{22} \\ B_{23} \\ B_{31} \\ B_{32} \\ B_{33} \end{bmatrix}}_{\vec{\mathbf{B}}} = 0, \tag{3.21}$$

where n is the number of corners in the checkerboard and the superscript indices denote the corners number. A non-trivial solution $\vec{\mathbf{B}}'$ of equation 3.21 in the least square sense can be obtained by computing the right-singular vector of $\mathbf{W}$ associated to the smallest singular value of $\mathbf{W}$. Note that any vector proportional to $\vec{\mathbf{B}}'$ is solution of 3.21. Using equation 3.19 and matrix $\mathbf{B}'$, we are able to transform the image coordinates (X_i, Y_i) of a point into a vector $\vec{b} = (b_1, b_2, b_3)^T$ proportional to $(X_b, Y_b, 1)$:

$$\vec{b} = \mathbf{B'}^{-1} \begin{bmatrix} X_i \\ Y_i \\ 1 \end{bmatrix} = b_3 \begin{bmatrix} X_b \\ Y_b \\ 1 \end{bmatrix}. \tag{3.22}$$

The checkerboard coordinates (X_b, Y_b) of the image point are thus obtained as

$$\begin{bmatrix} X_b \\ Y_b \end{bmatrix} = \frac{1}{b_3} \begin{bmatrix} b_1 \\ b_2 \end{bmatrix}. \tag{3.23}$$

In order to assess the accuracy of the measurement, we compare in figure 3.8 the theoretical position of the checkerboard points with the position of the detected intersections in the checkerboard frame of reference. It appears that the maximum distance between the theoretical and measured points is of the order of 3 millimeters.

3.2.3 Detection of the free-surface profile and computation of the flume coordinates

The implicit camera calibration presented in the previous section makes it possible to define a transformation between the image coordinate system and the checkerboard coordinate system. Finally, the checkerboard coordinates must be linked to the coordinates of the flume frame of reference $(O_f, \vec{x_f}, \vec{y_f}, \vec{z_f})$. This frame of reference is defined in figure 3.9, which presents a side view of the flume. The origin of this frame is located at the intersection between the SWL and the paddle at its neutral position. The x-axis is in the direction of the wave propagation and the y-axis is directed upward. The flume coordinates are obtained through a two-dimensional rotation of $\pi - \theta$ and a translation t_{2D} of the checkerboard frame of reference. The horizontal direction is computed using a linear interpolation of the points of the free surface detected at an instant at which the water is still. This allows to determine the angle θ defined in figure 3.9. The red cross drawn in figure 3.9 corresponds to the position of a mark on the wall located at a distance of 21

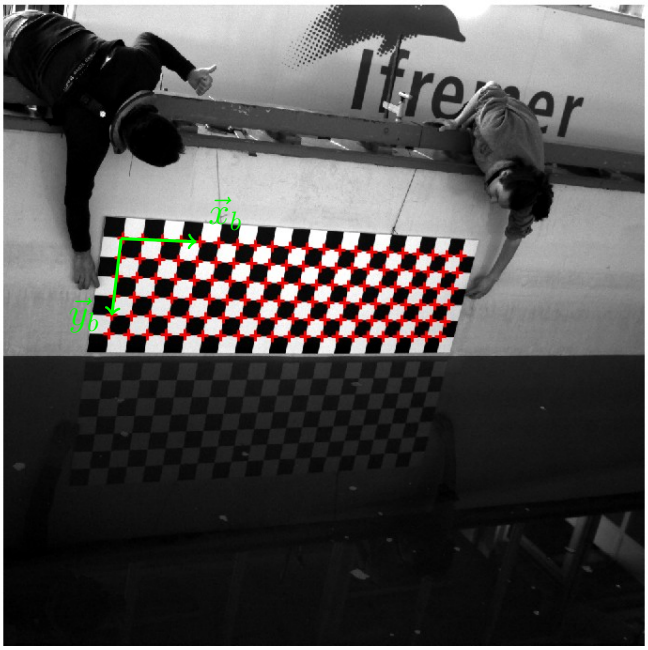

Figure 3.7 – Image of the checkerboard used for the implicit calibration of the video camera. The red crosses correspond to the detected corners of the checkerboard.

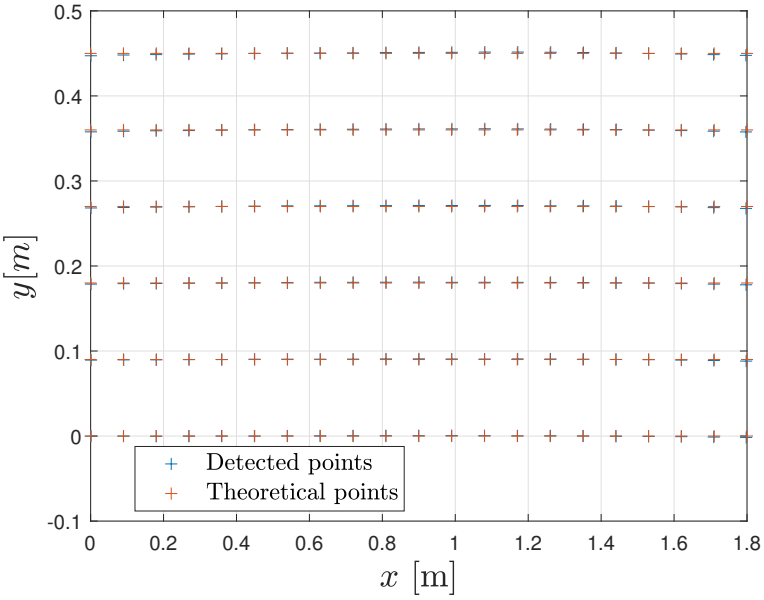

Figure 3.8 – Comparison of the theoretical and measured positions of the checkerboard corners in the checkerboard frame of reference.

m from the wave paddle. The translation vector allowing to translate the $\pi - \theta$ rotated checkerboard frame of reference is $t_{2D} = \begin{bmatrix} 21 - x_{cross} \\ -y_{SWL} \end{bmatrix}$, where x_{cross} is the longitudinal coordinate of the cross in the rotated checkerboard frame of reference and y_{SWL} is the vertical coordinate of the SWL in the rotated checkerboard frame of reference.

The pixels belonging to the free-surface profile are detected using a Canny contour detection algorithm, with a lower threshold set to 0.55 and a higher threshold set to zero. This means that all edges with a "strength" above 0.55 are kept, while the weak edges are kept only if they are connected to a strong edge. The strength corresponds to the gradient of the pixel values. To avoid detecting edges that do not correspond to the intersection between the wall and the water, the picture was cropped. The cropped picture is delimited by the two red horizontal lines in figure 3.10. The blue dots, which appear as a line due to their large number, correspond to the detected free-surface profile points.

3.2.4 Free-surface profile measurement of the breaking waves

We measured the free-surface profiles of all the waves listed in table 3.2 in the absence of the cylinder with the technique presented in the previous sections. As in the

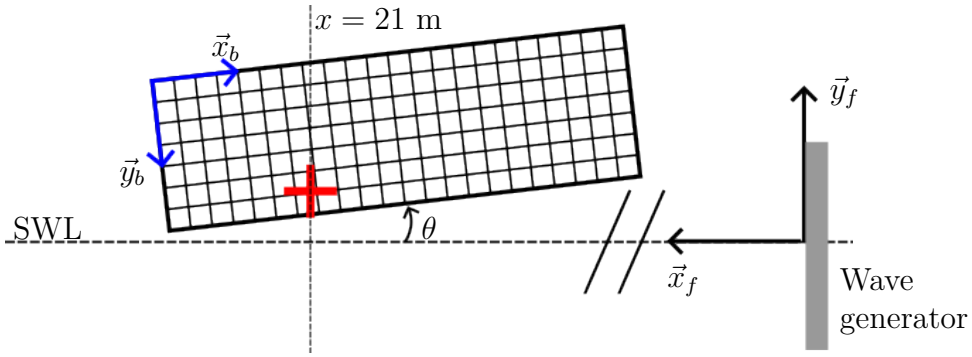

Figure 3.9 – Rotation and translation allowing to pass from the checkerboard frame of reference to the flume frame of reference.

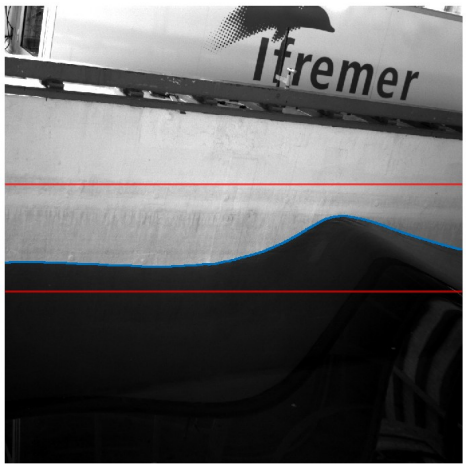

Figure 3.10 – Detection of the points corresponding to the intersection between the wall and the free surface profile. The red lines delimit the part of the image on which the contour detection algorithm is applied and the blue dots correspond to the detected pixels.

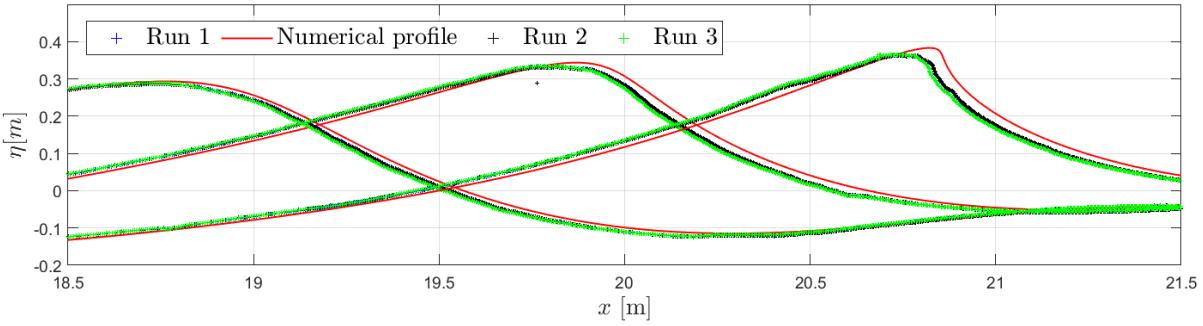

Figure 3.11 – Comparison of the free-surface profiles derived from 3 measurements for wave 24 at 3 different times. The numerical free-surface profiles obtained with the FNPF solver are also shown.

experimental campaigns, a resting time of at least 45 min was observed between two measurements. Some of the measurements were repeated three times to investigate the variability of the free-surface profile for the same experimental conditions. As we did not record the trigger sent by the wave paddle at the start of the wave generation during the wave measurements, we identified the time at which the wave generations started with the paddle position measurement (see section 2.2.3.4). A comparison between three experimental profiles for wave 24 and the corresponding numerical profile is depicted in figure 3.11. Note that no time-shift between the numerical and experimental profiles was applied. A zoomed-in view on the profiles at an instant close to breaking is shown in figure 3.12. It appears that the different experimental profiles are very close to each other. The distance between the front for the first 2 runs and for run 3 is of the order of one centimeter. The distance between the numerical front and the measured fronts is of approximately 5 cm. Considering a crest speed of 2.83 m/s, which corresponds to the crest speed at breaking in the NWT, the time delay between the front of the wave in the numerical wave tank and the front of the measured wave is of 18 ms. The distance between the different wave fronts measured in the flume corresponds to a time delay of approximately 3.5 ms. For wave 23, the experimental and numerical free-surface profiles are shown in figures 3.13 and 3.14. It appears that the three experimental profiles are closer to each other than the experimental profiles of wave 24. The distance between the experimental profiles and the numerical profile is also of approximately 5 cm close to the instant of breaking.

Note that due to the viscous effects, the free-surface profile at the wall differs from the free-surface profile in the rest of the flume. The viscous effects tend to trigger breaking earlier at the wall than in the rest of the flume (Rapp et al. 1990). In the present exper-

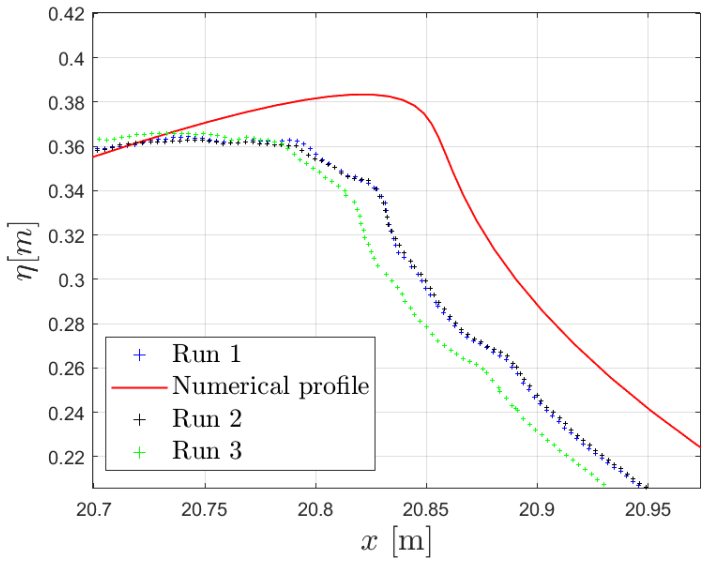

Figure 3.12 – Zoomed-in view on the free-surface profile close to the breaking time depicted in figure 3.11.

iments, we observed a shift of approximately 5 cm between the modelled and measured free-surface profiles close to the instant of breaking for the different wave cases.

3.2.5 Synchronisation of the modelled free-surface profiles with the measured profiles

It appeared in the previous section that the measured and experimental free-surface profiles are shifted in space close to the instant of breaking. We believe that this space shift is due to differences in the propagation of the waves between the flume and the model. In this section, we propose a method to synchronise the numerical and experimental profiles. This will allow to have a more accurate description of the shape of the wave at the instant of impact.

The synchronisation method is illustrated in figure 3.15. The numerical and experimental profiles at the instant of breaking $t_b = 26.584$ s are plotted. The experimental profile which is the closest to the numerical one is found at $t = 26.604$ s, *i.e.* 20 ms later. The selection of the time shift is done visually. To assess the accordance between the two profiles, we did not account for the crest region. Indeed, in the crest region, the experimental profile is known to be significantly disturbed by the wall of the flume. For most of the waves, a time shift of 20 ms improves the agreement between the measured

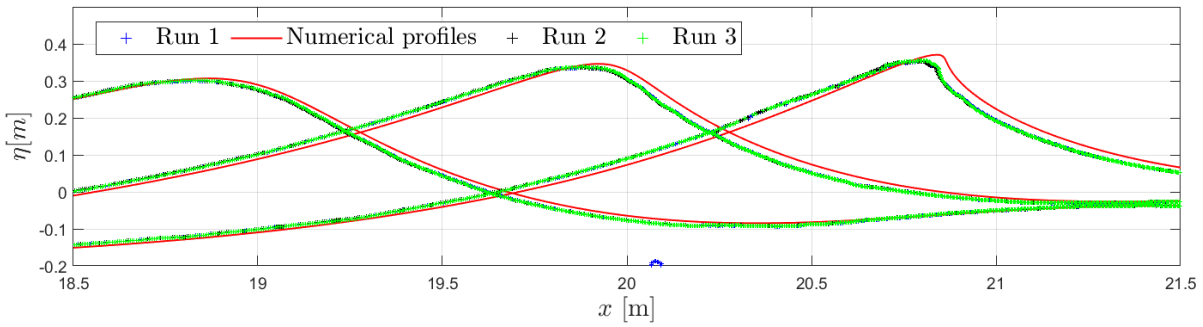

Figure 3.13 – Comparison of the free-surface profiles derived from 3 measurements for wave 23 at 3 different times. The numerical free-surface profiles obtained with the FNPF solver are also shown.

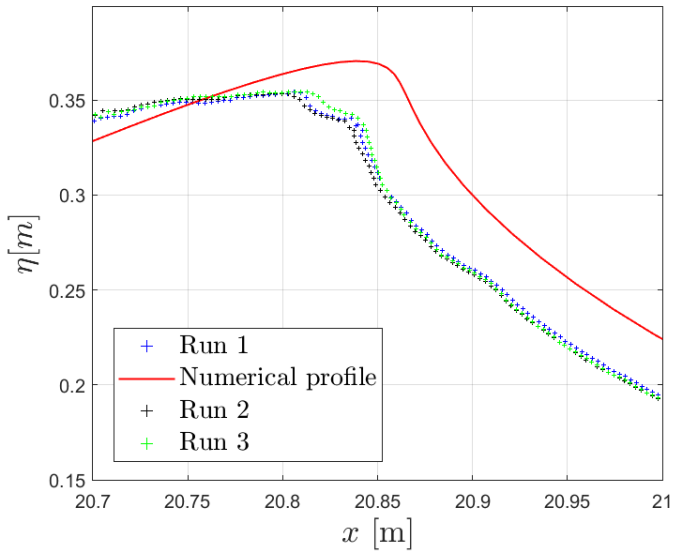

Figure 3.14 – Zoomed-in view on the free-surface profile close to the breaking time depicted in figure 3.13.

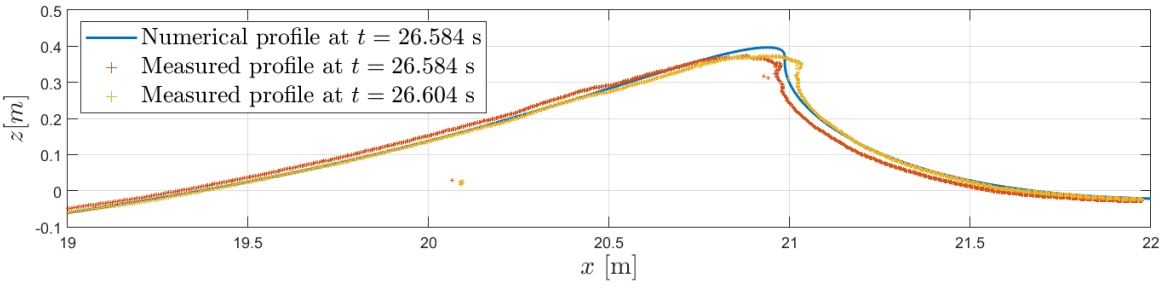

Figure 3.15 – Illustration of the computation of the time-shift between the measured and numerical free-surface profiles at the instant of breaking.

and modelled free-surface profiles. In the following, we will use the time-shifted numerical free-surface profiles to relate the measured impact force to the shape of the wave at impact (see section 4.2.1.3 for instance).

3.3 Numerical characterisation of the breaking waves

The numerical simulations have been used to determine the characteristics of the breaking waves which are known to affect the impact force and which cannot be measured during the experiments. These parameters are the breaking location x_b, the time of breaking t_b, the crest height η_b, the crest speed c_b, the time derivative of B at $B = 0.85$ and the breaking strength Γ. The crest height η_b and the crest speed c_b are computed at the instant of breaking t_b. As a reminder, the instant of breaking corresponds to the instant at which the free-surface profile first displays a vertical slope. The values of the different parameters derived from the numerical simulations are summarized in table 3.3. In the following sections, we detail the methods employed to compute the crest speed c_b (section 3.3.1) and the breaking strength Γ (section 3.3.2).

3.3.1 Computation of the crest speed of the waves

The computation of the crest speed must be done carefully to avoid oscillations induced by the discretisation of the free surface. This requires to precisely determine the position of the wave crest, *i.e.* the position at which the free-surface elevation is maximum. This position is often situated between two nodes. To do this, we first identify the highest node $\mathbf{x}_M$, where M corresponds to the index of this node. We select the 21 adjacent

Wave Number	x_b [m]	t_b [s]	$t_{B=0.85}$ [s]	η_b [m]	c [m/s]	Γ [1]	$\frac{dB}{dt}$ [s^{-1}]
1	21.00	30.56	30.45	0.39	2.7	0.97	0.57
2	21.04	27.25	27.13	0.33	2.49	0.8	0.51
23	20.99	26.93	26.87	0.37	2.74	1.29	0.73
24	20.99	26.77	26.73	0.39	2.83	1.82	0.99
3	20.99	26.58	26.59	0.4	2.89	3.01	1.6
4	20.98	23.48	23.45	0.33	2.62	1.84	1.08
5	20.99	23.51	23.59	0.34	3.33	3.82	2.3
6	21.01	30.56	30.47	0.41	2.77	0.96	0.55
7	20.97	30.12	30.09	0.41	2.85	1.93	1.03
8	21.07	27.02	26.94	0.35	2.65	1.09	0.65
9	21.06	26.73	26.71	0.39	2.85	2.09	1.12
10	21.08	26.61	26.62	0.4	2.94	3.15	1.65
11	20.99	26.57	26.61	0.41	3.03	3.88	2.04
12	20.96	26.6	26.71	0.42	3.16	3.69	1.99
15	21.01	27.06	27.03	0.3	2.41	1.83	1.17

Table 3.3 – Parameters of the breaking waves used during the experimental campaigns

nodes, which indices are comprised in the interval $[M-10; M+10]$. Let us note (x_j, z_j) the coordinates of the j^{th} node $\mathbf{x}_j$. We use the Matlab function **csaps** to determine two functions, X and Z, that approximate continuously the relation between the nodes indices and the nodes coordinates x_j and z_j. The functions X and Z are the cubic smoothing splines which minimize the following quantity:

$$\sum_{j=M-10}^{M+10} |f_j - F(j)|^2 + (1-p) \int_{M-10}^{M+10} \left| \frac{\mathrm{d}^2 F}{\mathrm{d}l^2}(l) \right|^2 \mathrm{d}l, \tag{3.24}$$

where $p = 0.8$ is the smoothing parameter, F corresponds to X or Z and f_j corresponds to x_j or z_j. Once the functions X and Z are determined, we determine the real number $J_{max} \in [M-10; M+10]$ for which the function Z is maximum. The longitudinal position of the crest is computed as $X(J_{max})$.

As an example, the time evolution of the longitudinal position of the wave crest obtained with this method for wave 3 is shown in figure 3.16a. As the evolution is rather smooth, it can be numerically differentiated to obtain the velocity of the crest, which is depicted in figure 3.16b. The cubic spline smoothing of the position of the maximum prevented the appearance of important oscillations of the crest velocity. The higher node density near the crest (see figure 3.1) also contributes to avoid oscillations in the time evolution of the crest speed. The characterisation of the breaking strength of the waves, which is presented in section 3.3.2, requires to compute the horizontal fluid velocity at the crest. Therefore, a continuous function U corresponding to the horizontal fluid velocity at the free surface is computed as the smoothing spline minimizing equation 3.24 when $f_j = u_j$, where u_j is the horizontal velocity of the nodes. The horizontal velocity at the crest, u_c, is given by $U(J_{max})$.

In analytical wave impact models and in wave breaking criteria, the speed of the crest is often used as an estimate of the horizontal fluid velocity in the crest of a breaking wave. However, we observed that for some of the waves listed in table 3.2, the speed of the crest may increase and decrease rapidly during breaking, so that the crest speed is no longer representative of the fluid velocity. This phenomenon is illustrated thereafter for wave 5, which is one of the strongest plunging breakers. The time evolution of the crest celerity of wave 5 is depicted in figure 3.17 along with the horizontal fluid velocity at the crest u_c and the maximum horizontal fluid velocity at the free surface. An important increase of the crest velocity appears slightly before the red vertical line, which represents the instant of breaking. This increase of the crest speed is due to the fact that the crest of

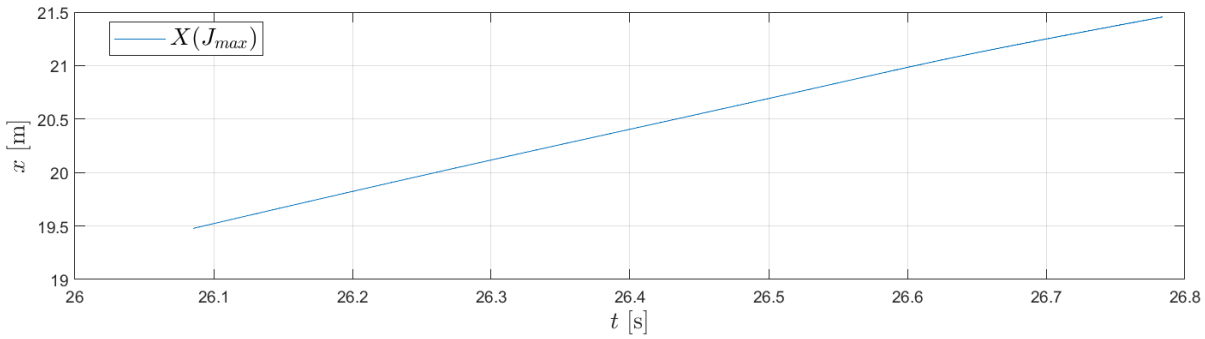

(a)

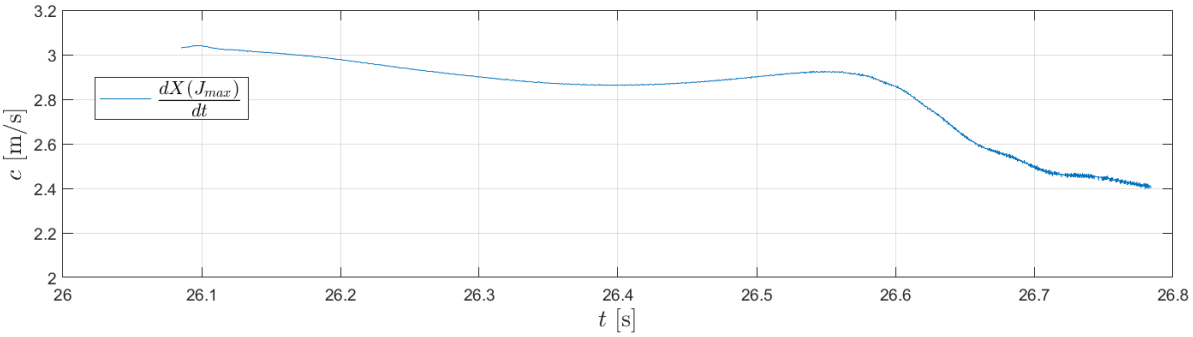

(b)

Figure 3.16 – (a) Position of the crest and (b) velocity of the crest as a function of time for wave 3

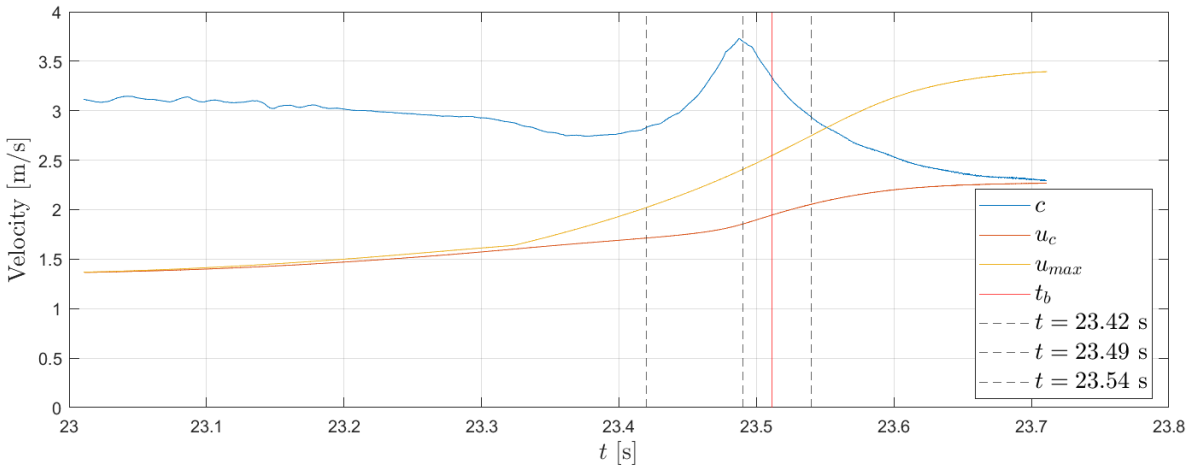

Figure 3.17 – Evolution of the crest celerity c, of the horizontal fluid velocity at the crest u_c and of the maximum horizontal velocity at the free surface for wave 5. The red vertical line corresponds to the instant of breaking. The dashed vertical lines correspond to the instants at which the free-surface profiles of the wave are depicted in figure 3.18.

the wave is rather flat, and the maximum free-surface elevation may move rapidly over this flat area. This can be seen in figure 3.18 where the free-surface profiles of the wave at the instants corresponding to the dashed vertical lines in figure 3.17 are shown. For each profile, the circle indicates the position of the maximum free-surface elevation. It appears that for the later profiles, the circle gets closer to the front of the wave. For this wave case, even if the crest velocity increases, the horizontal fluid velocity at the crest does not evolve significantly during this stage. Neither does the maximum horizontal fluid velocity at the free surface. In chapter 4, the velocity of the crest at breaking will be used as a non-dimensionalization parameter. However, one should keep in mind that for the strongest plunging breakers, this velocity may be rather different from the fluid velocity in the crest region. In the wave list given in table 3.2, such a rapid increase and decrease of the crest velocity was observed only for wave 5.

3.3.2 Computation of the breaking strength of the waves

As discussed in section 1.4.1, the influence of the breaking strength in analytical impact formulas is taken into account through the curling factor λ. However, there is no established theory to estimate the curling factor of a particular wave. In order to address this problem, we suggest to investigate the evolution of the impact force as a function of

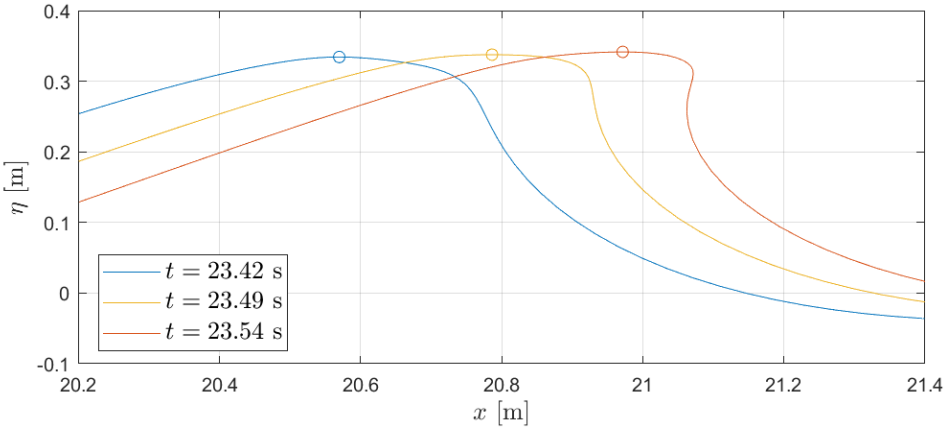

Figure 3.18 – Free-surface profiles of wave 5 at different instants which correspond to the dashed vertical lines in figure 3.17. The circles indicate the position of the wave crest.

the parameter Γ proposed by Derakhti et al. 2018. This parameter is based on the breaking onset threshold introduced by Barthelemy et al. 2018. This breaking onset threshold states that if the ratio $B = u_c/c$ between the horizontal fluid velocity at the crest u_c and the crest velocity c reaches 0.85, the wave will inevitably evolve towards breaking. Later, Derakhti et al. 2018 showed that the energy dissipated during a breaking event was proportional to the parameter Γ defined as:

$$\Gamma = T_b \left. \frac{\mathrm{d}B}{\mathrm{d}t} \right|_{B=0.85}, \tag{3.25}$$

where T_b is the characteristic period of the breaking wave. Derakhti et al. 2018 showed that the parameter Γ is linked to the energy dissipated by a breaking wave. In Derakhti et al. 2018, the wavelength, L, of the breaking wave is used to compute the characteristic period T_b of the breaking wave via the linear dispersion relation ($L = \frac{gT_b^2}{2\pi} \tanh \frac{2\pi h}{L}$). The computation of the wavelength L is done with the zero-crossings, as illustrated in figure 3.19. In the following, we approximate the time derivative of B as the slope of a linear interpolation of B over a time interval during which $|B - 0.85| < 0.03$, as suggested in the work of Derakhti et al. 2018.

Let us illustrate the computation of Γ for waves 1 and 3. The time evolution of the crest velocity and of the horizontal fluid velocity at the crest are depicted in figures 3.20a and 3.20b for these two waves. Both quantities display a rather smooth evolution. The time evolution of the ratio B is depicted in figures 3.21a and 3.21b for waves 1 and 3,

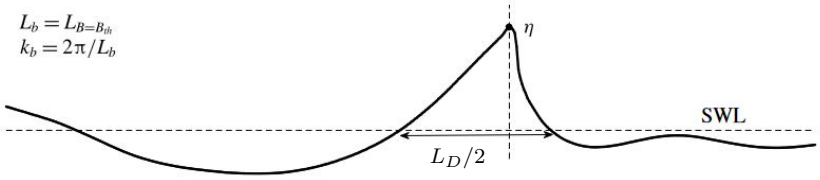

Figure 3.19 – Illustration of the computation of the zero-crossing wavelength L_D used in the study of Derakhti et al. 2018.

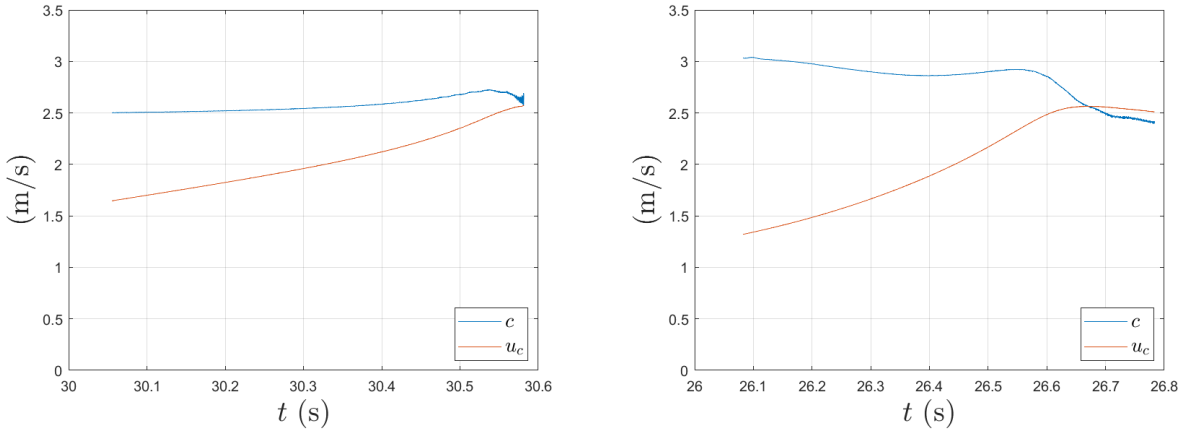

Figure 3.20 – Time evolution of the crest velocity and of the horizontal fluid velocity at the crest for waves 1 (a) and 3 (b).

respectively. The dashed horizontal line corresponds to $B = 0.85$ and the solid horizontal lines correspond to $B = 0.85 \pm 0.03$. The linear interpolation, which corresponds to the bold orange line, is carried out between the two horizontal solid lines. The vertical red line is the instant at which the wave is breaking, *i.e.* the instant at which the front of the wave becomes locally vertical. The values of the slope of the orange curves $\frac{\mathrm{d}B}{\mathrm{d}t}\Big|_{B=0.85}$ for the breaking waves used in the present work are given in table 3.3.

In the current work, we modified the method for the computation of the characteristic wave period T_b because the approach used by Derakhti et al. 2018 led to unphysical results for some wave cases. For instance, for wave 11, which free-surface profile is depicted in figure 3.22, one can see that the wavelength L_D obtained with Derakhti's approach is "artificially" longer than one would intuitively expect because of the small bump ahead of the breaking wave front. Indeed, the half wavelength defined by the local minimum ahead of the main wave front seems more representative of the actual wavelength than L_D. This

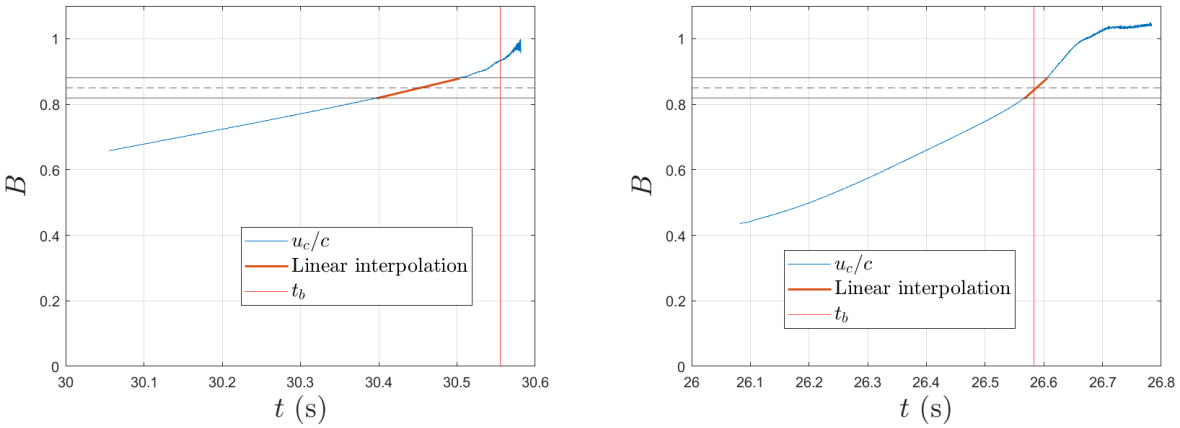

Figure 3.21 – Time evolution of parameter B for the waves 1 (a) and 3 (b). The vertical red line corresponds to the instant of breaking. The dashed horizontal line corresponds to $B = 0.85$ and the solid horizontal lines correspond to $B = 0.85 \pm 0.03$.

overestimation is due to the fact that the breaking wave is "riding" another wave, so that the forward trough of the breaking wave is above the SWL. To avoid overestimating the characteristic wave period T_b, we propose compute T_b using the crest speed and the dispersion relation. The following equation

$$c = \sqrt{\frac{g}{k}\tanh(kh)}, \tag{3.26}$$

is used to determine the value of the wave number k associated to the crest speed c of the wave at $B = 0.85$. The characteristic wave period is defined by:

$$T_b = \sqrt{\frac{2\pi L}{g\tanh\frac{2\pi h}{L}}}. \tag{3.27}$$

The values of Γ obtained with this definition are given in table 3.3 for the waves listed in table 3.2. With this definition of T_b, the computation of Γ appeared to be more robust. However, this definition depends on the crest speed which, as we saw in section 3.3.1, may differ from the phase speed of the wave in some cases. This definition of T_b could be improved for future works.

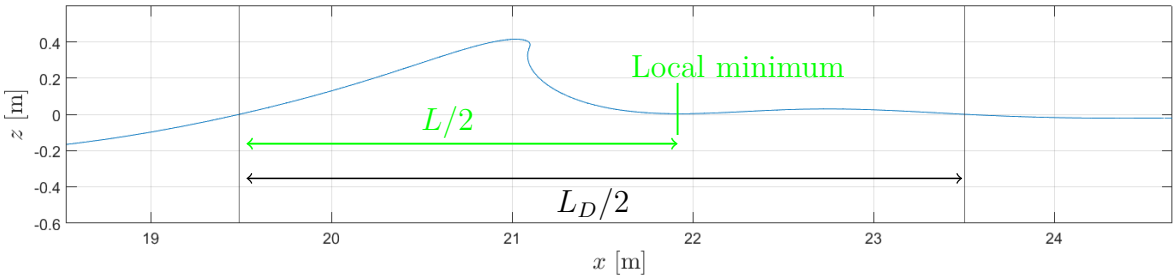

Figure 3.22 – Estimation of the half wavelength $L_D/2$ of breaking wave 11 using the zero-crossing method method proposed by Derakhti et al. 2018. The zero-crossings are given by the vertical lines. Intuitively, the half wave length should be closer to $L/2$.

Comments on the breaking inception threshold and on the Γ parameter

During the computation of the breaking strength Γ of the waves listed in table 3.2, it appeared that the breaking onset threshold of Barthelemy et al. 2018 was not always verified. We always observed that the parameter B overcomes 0.85 for the waves that break. However, for the stronger plunging breakers, the threshold $B = 0.85$ is generally reached after the appearance of the vertical front. In this case, the threshold cannot be considered as an indication of imminent breaking, as argued by Barthelemy et al. 2018. Let us for example investigate the case of wave 11, which has a breaking strength $\Gamma = 3.88$. The time evolution of B is depicted in figure 3.23. The dashed horizontal line corresponds to $B = 0.85$ and the red vertical line is the breaking time. It appears that B crosses 0.85 significantly after the appearance of a vertical front. We think that this is due to the fact that the position at which the horizontal fluid velocity is maximum in a breaking wave is not located at the crest but on the wave front. For strong plunging breakers, the location at which the fluid velocity is maximum may significantly depart from the crest location (the position of the maximum free-surface elevation). This is exemplified in figure 3.24, where the free-surface profiles of waves 8 ($\Gamma = 1.09$) and 11 ($\Gamma = 3.88$) at the instant of breaking are depicted. The orange dot corresponds to the crest position and the yellow dot to the location at which the horizontal fluid velocity is maximum on the free surface. It appears that the distance between these two points is significant for wave 11. For this reason, in this case, the fluid velocity at the position of the crest is not representative of the maximum fluid velocity in the wave. The values of the instant of breaking t_b and

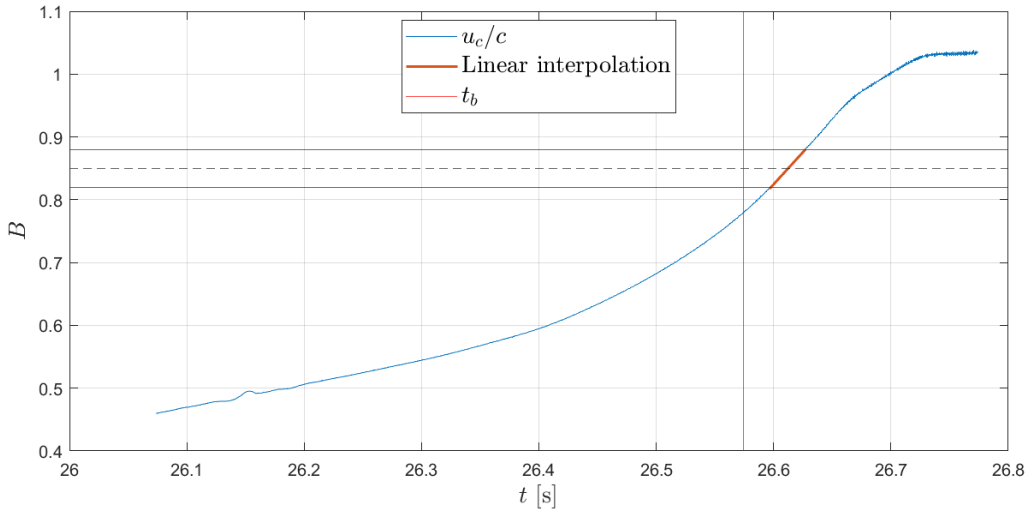

Figure 3.23 – Evolution of parameter $B = \frac{u_c}{c}$ for wave 11.

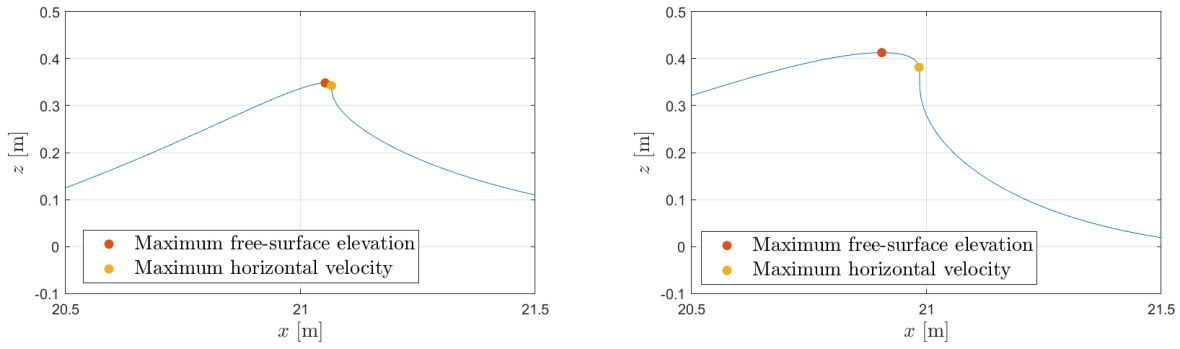

(a) Wave 8, $\Gamma = 1.09$ (b) Wave 11, $\Gamma = 3.88$

Figure 3.24 – Position of the maximum free-surface elevation and of the maximum horizontal fluid velocity for waves 8 (a) and wave 11 (b)

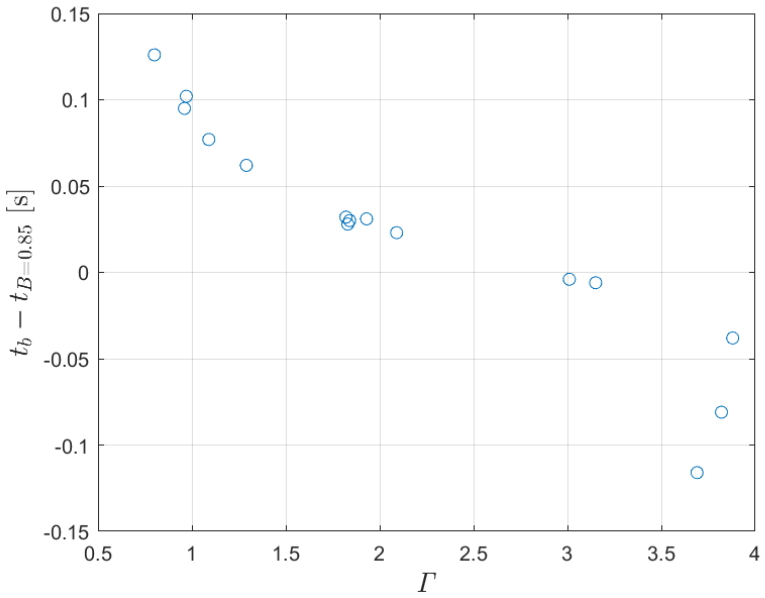

Figure 3.25 – Evolution of the time interval between the instant of breaking and the instant at which B reaches 0.85 as a function of Γ

the instant $t_{B=0.85}$ at which B crosses 0.85 are given in table 3.3 for the wave listed in table 3.2. Figure 3.25 shows the evolution of $t_b - t_{B=0.85}$ between these two instants as a function of the breaking strength Γ. It appears that the time difference between these two instants decreases when Γ increases. Moreover, for Γ higher than 2.5, $t_b - t_{B=0.85}$ becomes negative, meaning that $B = 0.85$ is reached after breaking. We believe that this issue was not identified by Barthelemy et al. 2018 because they focused on weak breaking cases. Indeed, they reported that "the high chirp rate [used to obtain the breaking waves] restrict[ed] [their] attention to weak breaking cases, as further small increments in paddle amplitude only produce[d] wave breaking at the paddle".

One possibility to circumvent this issue could be to consider the ratio u_{max}/c between the maximum fluid velocity close to the crest and the crest velocity, as it has been proposed by Varing et al. 2021. However, as no investigations have been carried out concerning the possibility of using this ratio to compute the breaking strength, we decided to continue to use the ratio proposed by Barthelemy et al. 2018.

Given the issues encountered during the computation of the crest speed c and the ratio u/c, we think that for the strong plunging breakers, which typically display a Γ value above 3, the parameter Γ should rather be considered as a rough estimate of the breaking strength than as an accurate measure of the breaking strength. For these cases,

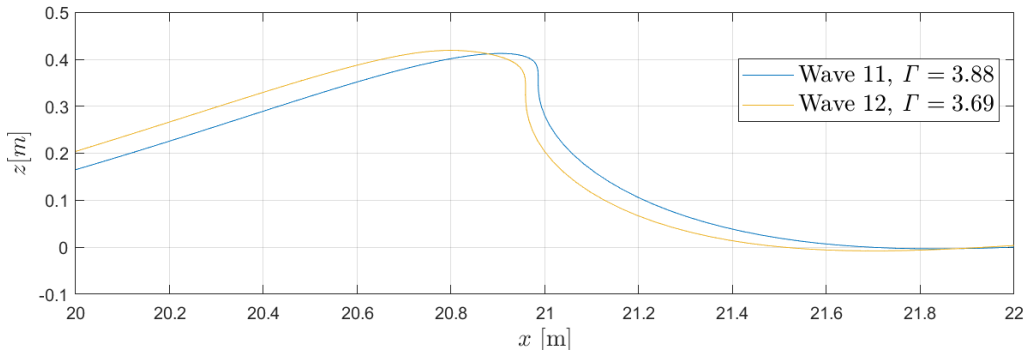

Figure 3.26 – Comparison of the free-surface profiles of waves 11 and 12 at the instant of breaking.

the ratio B is computed at a location rather distant from the initiation of the instability. Moreover, as we saw in section 3.3.1, the flat crest of these breaking waves may induce important variations of the crest speed which are not representative of the wave celerity. To highlight the inaccuracy of the Γ parameter for the strong plunging breakers, we compare the free-surface profiles of waves 11 and 12 at the instant of breaking in figure 3.26. Visually, wave 12 seems to be breaking more violently than wave 11. Indeed, its front is higher and the wave is even more asymmetric. However, the Γ value of wave 12 is lower than the Γ value of wave 11. Note also that the values of Γ obtained in the present study are much larger than the values obtained by Derakhti et al. 2018. Indeed, they reported values of Γ in the interval $[0.44; 1.44]$. In the present study, the values of Γ are in the interval $[0.8; 3.88]$. We have no explanation concerning this point. It is unlikely that it is related to the different definition of Tb. Indeed, we have also computed Γ using the definition Derakhti et al. 2018 for our waves, and the obtained values are still much larger than those reported in their paper.

In spite of the limitations of the parameter Γ, the fact that its computation should be done with great care and the fact that it is questionable whether a single parameter can fully characterise the intensity of breaking, we believe that Γ is nevertheless a useful indicator. In chapter 4, we will investigate if there is a correlation between Γ and the load generated during the impact of a breaking wave on a cylinder.

3.4 On the prediction of wave breaking with a linear approach

Fully non-linear computations of wave propagation and breaking are computationally demanding. Moreover, with the numerical model used in the present study, the occurrence of breaking leads the simulation to stop. Therefore, fully non linear simulations are not well suited to analyse the occurrence of wave breaking in a sea state over a long period of time. To circumvent this problem, a probabilistic model of wave breaking based on a linear wave theory has been developed previously by France Energies Marines (Stringari et al. 2021). It relies on the use of a linear equivalent to the breaking inception threshold of Barthelemy et al. 2018. This probabilistic model was further used during the DIMPACT project. In the present section, we investigate the validity of the prediction of breaking using a linear model. For this purpose, the results of the fully non-linear numerical simulations will be employed. The objectives of the study and the theoretical framework developed by Stringari et al. 2021 are presented in section 3.4.1, the definition of the linear equivalent breaking wave in section 3.4.2, the waves used in this study in section 3.4.3 and the results in section 3.4.4.

3.4.1 Context and objectives of the study

The problem of predicting the breaking frequency in a sea state remains an unresolved problem that has important implications in several research fields. For instance, to assess the importance of wave impact loads during the design of a wind farm, it is of primary importance to predict the frequency at which the waves will break at the considered site. Furthermore, it would also be of interest to access to the breaking strength, which will affect the magnitude of the impact loads that should be considered during the design phase.

Several of the existing probabilistic models are based on empirical formulations and lack an extensive validation due to the few available field datasets. Recently, Stringari et al. 2021 proposed a new probabilistic wave breaking model based on Gaussian wave field theory. They derived the joint probability density function $p(c, u_c)$ of the crest speed c of a wave and the horizontal fluid velocity at the wave crest u_c. Stringari et al. 2021 made use of the work by Barthelemy et al. 2018 who showed that for a given wave, if the ratio $B = u_c/c$ reaches the threshold $\beta = 0.85$, the wave will inevitably break. Waves that

do not exceed this value do not break. The probabilistic model of Stringari et al. 2021 relies on the assumption that in a phase-resolved linear wave field, an equivalent threshold β_l exists. This means that breaking occurs when the ratio $B_l = u_l/c_l$ between the linear fluid velocity at the crest of a wave u_l and the linear crest velocity c_l reaches β_l. They computed the parameter β_l as the ratio u_l/c_l of a linear wave which energy is equivalent to the energy of a fully non-linear regular deep-water wave at the breaking onset. They obtained a threshold $\beta_l = 0.3817$. Using this linear breaking threshold, the probability of breaking P_b can be computed as:

$$P_b = \int_{u>\beta_l c} \int_0^\infty p(c,u)\mathrm{d}c\mathrm{d}u. \tag{3.28}$$

The results of the model were compared to field datasets, and it was found that its performance were comparable to that of other state-of-the-art models. Nevertheless, important discrepancies were observed with field data, and the validation is based on the breaking probability for an ensemble of waves.

The present study aimed to determine whether a linear equivalent threshold β_l exists. We also aimed to refine the value of β_l. We first defined a linear equivalent for the breaking waves simulated with the FNPF solver presented in section 3.1.1. Based on this linear equivalent, we computed the ratio u_l/c_l for the different waves. As we know if the corresponding fully non-linear waves break or not, we should be able to identify the value of β_l.

3.4.2 Definition of the linear equivalent wave

The linear equivalent of a breaking wave is computed in a wave tank which dimensions are equivalent to the dimensions of the numerical wave tank. The linear equivalent is defined as the wave field generated by the same paddle motion if one uses the first order transfer functions and first order wave theory. The free-surface elevation in the wave tank is thus given by equation 3.7 and the linear horizontal fluid velocity at the free surface are given by:

$$\eta(x,t) = \sum_{n=1}^{N} a_n \cos(k_n x - \omega_n t - \phi_n), \tag{3.29a}$$

$$u\,(x,t) = \sum_{n=1}^{N} a_n \frac{g k_n}{\omega_n} \cos\left(k_n x - \omega_n t - \phi_n\right). \tag{3.29b}$$

We compute analytically the crest speed of a linear wave using the following formula:

$$c(t) = -\frac{\eta_{xt}\left(x_{max}, t\right)}{\eta_{xx}\left(x_{max}, t\right)}, \tag{3.30}$$

where x_{max} corresponds to the longitudinal position of the wave crest.

3.4.3 Investigated wave cases

For the sake of the current investigations, we had to define new wave cases. Indeed, the cases listed in table 3.2 were generated with a focusing time $t_f = 30$ s. The slowest component has a frequency $f = 0.8$ Hz, its phase speed is $C_p = 1.95$ m/s and its group speed is $C_g = 0.98$ m/s. For the wave cases 4 and 5, breaking occurs two waves before the focused wave, at $t_b = 23.45$ s (see table 3.2). During this time, the slowest component travels a distance $t_b C_g = 22.88$ m, which is just enough to reach the breaking point. Our first attempt to identify a consistent linear threshold β_l was successful, except for waves 4 and 5. These two waves being the only waves of the list which display such an early breaking time, we attributed this inconsistency to the fact that the high frequency content had not reached the breaking location at the breaking time. For this reason, we reproduced the breaking waves listed in table 3.2 with a focusing time of 50 s. Some non-breaking cases were also added. All the wave cases used for this study are listed in table 3.4 along with the spectrum parameters. The waves are separated in group A, for which $T_p = 2.25$ s, and group B, for which $T_p = 2.49$ s. Similarly to the waves used during the experimental campaigns, we used the iterative procedure to shift the breaking location so that breaking occurs around $x = 21$ m. This allows the waves to break in the zone displaying a higher node density (see figure 3.1) and to obtain more accurate results for the Γ values. The characteristics of the waves such as their breaking strength, location and time are given in table 3.5. The number labelled breaking crest corresponds to the number of the first breaking crest: 1 means that the focused crest breaks, 2 means that the crest before the focused crest breaks, and 3 means that breaking occurs two crests before the focused crest.

3.4.4 Results

For the waves listed in table 3.4, the time evolution of the ratio u_l/c_l of the linear equivalent is depicted in figures 3.27a and 3.27b. We computed the ratio for all the wave

Number	H_S [m]	T_p [s]	γ [1]	f_c [Hz]	x_f [m]	t_f [s]
A1	0.11	2.25	3.3	0.8	19.37	50
A2	0.115	2.25	3.3	0.8	18.97	50
A3	0.12	2.25	3.3	0.8	18.80	50
A4	0.13	2.25	3.3	0.8	22.99	50
A5	0.135	2.25	3.3	0.8	23.57	50
A6	0.14	2.25	3.3	0.8	23.87	50
A7	0.15	2.25	3.3	0.8	24.15	50
A8	0.17	2.25	3.3	0.8	27.04	50
A9	0.20	2.25	3.3	0.8	27.16	50
B1	0.11	2.49	1.4	0.8	19.47	50
B2	0.12	2.49	1.4	0.8	18.84	50
B3	0.13	2.49	1.4	0.8	19.69	50
B4	0.14	2.49	1.4	0.8	23.42	50
B5	0.15	2.49	1.4	0.8	23.92	50
B6	0.16	2.49	1.4	0.8	24.08	50
B7	0.17	2.49	1.4	0.8	23.94	50
B8	0.18	2.49	1.4	0.8	23.72	50

Table 3.4 – List of the breaking waves used to determine the linear equivalent breaking threshold. The parameters of the JONSWAP spectrum are the significant wave height H_S, the peak period T_p, the peak enhancement factor γ and the cut-off frequency f_c. Parameters x_f and t_f correspond to the focusing position and to the focusing time, respectively.

Number	x_b [m]	t_b [s]	η_b [m]	c_b [m/s]	Γ [1]	Breaking crest
A1	20.99	50.42	0.32	2.39		
A2	20.99	50.55	0.35	2.39		
A3	21.01	50.56	0.39	2.72	0.93	1
A4	20.86	47.17	0.34	2.55	0.82	2
A5	20.90	46.89	0.37	2.74	1.21	2
A6	20.92	46.74	0.39	2.82	1.67	2
A7	20.93	46.56	0.40	2.89	2.78	2
A8	21.02	43.89	0.30	2.54	1.15	3
A9	20.97	43.63	0.36	2.92	2.97	3
B1	20.99	50.39	0.33	2.44		
B2	21.05	50.57	0.41	2.76	0.92	1
B3	21.00	50.1	0.41	2.86	1.90	1
B4	20.95	46.97	0.35	2.64	1.06	2
B5	20.99	46.70	0.39	2.84	1.90	2
B6	21.02	46.59	0.41	2.93	2.89	2
B7	20.92	46.55	0.41	3.00	3.70	2
B8	20.90	46.57	0.41	3.39	3.92	2

Table 3.5 – Parameters of the waves listed in table 3.4. The column breaking crest gives the crest which breaks in the simulation: 1 corresponds to the focused crest, 2 corresponds to the crest before the focused crest, and 3 to two crests before.

crests, and we showed its time evolution for the wave crest at which the ratio is maximum. The sharp variations are due the fact that the wave crest at which the ratio is maximum may move from one crest to the other. The wave crest with the maximum ratio is not always the highest wave crest. The change from a bold solid line to a thin dashed line corresponds to the instant of breaking in the fully non-linear simulations. We observed that the maximum value of u_l/c_l attained by the non-breaking waves is approximately equal to 0.34. The grey horizontal line corresponds to this value.

Let us detail the wave cases A1 to A9 depicted in figure 3.27a. It appears that the linear equivalents of waves A1 and A2, which are the only non-breaking waves, do not cross 0.34. For wave A3, which breaking crest is the focused crest, 0.34 is crossed for the first time slightly before the focus time $t_f = 50$ s. For waves A4, A5, A6 and A7, the ratio u_l/c_l crosses 0.34 for the first time between 45 and 46 s, well before the focusing time. This corresponds to the fact that the breaking crest is the crest preceding the focused crest. For waves A8 and A9, the threshold is crossed two periods before the focused crest. This is in agreement with the fact that breaking occurs around two periods before the focus time in the non-linear simulations.

A similar agreement is found for the wave cases B1 to B8 (see figure 3.27b). Indeed, wave B1 does not break and its linear equivalent does not cross 0.34. For waves B2 and B3, the focused crest breaks and the linear equivalent crosses 0.34 for the first time slightly before the focus time. For waves B4, B5, B6, B7 and B8, the crest preceding the focused crest breaks and the linear equivalent wave crosses 0.34 for the first time one period before the focus time.

These results suggest that a linear equivalent breaking threshold may exist. Its value appears to be $\beta_l \approx 0.34$, which is not far from the value of 0.38 proposed by Stringari et al. 2021. During the DIMPACT project, Marc Prevosto extended this study and showed that it was also possible to compute an equivalent linear breaking strength Γ_l, which value appears to be proportional to the breaking strength Γ. He also proposed a theoretical method to compute the threshold β_l.

3.5 Conclusion

In this chapter, we presented the breaking waves that were used during the experimental campaign. We generated a set of 15 waves displaying different wavelengths, heights and breaking strengths. The breaking waves were obtained through focalisation. They

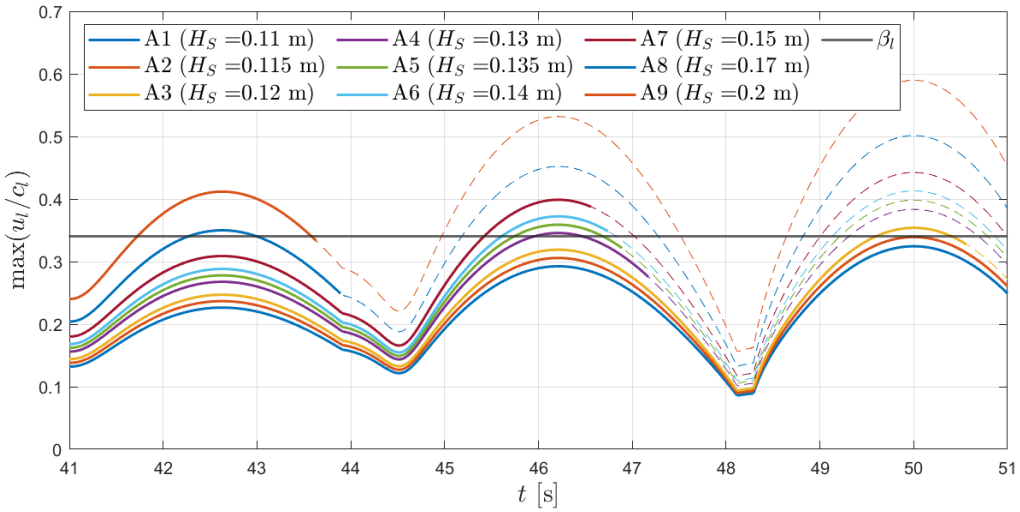

(a) Waves A1 to A9 ($T_p = 2.25$ s)

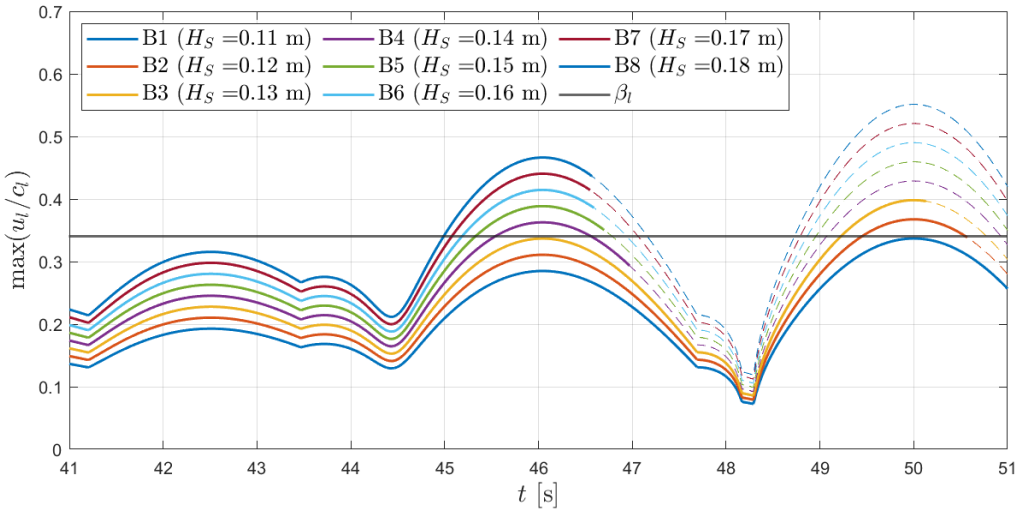

(b) Waves B1 to B8 ($T_p = 2.49$ s)

Figure 3.27 – Time evolution of the ratio u_l/c_l for wave cases A1 to A9 (a) and B1 to B8 (b) (see table 3.4). The horizontal line corresponds to the proposed threshold $\beta_l = 0.34$. The change from a bold solid line to a thin dashed line corresponds to the time of breaking in the non-linear simulations.

were first modelled using the FNPF solver developed by Grilli et al. 1989. An iterative procedure was applied to obtain breaking at the location of the model. All the waves were measured in the flume with a video camera prior to the installation of the mockup. We obtained a good agreement between the numerical simulations and the measurements. The characterisation of the waves, which consisted into determining the wave parameters that influence the impact loads, was done using the numerical simulations. The parameters of importance are the height of the wave crest, the crest speed and the breaking strength. We quantified the breaking strength with the Γ parameter proposed by Derakhti et al. 2018, which allows to link the fluid kinematics in the wave to the energy dissipated during a breaking event. However, we noted that the parameter Γ seems to be inappropriate for the stronger plunging breakers. The waves generated for the experimental campaigns were also used to investigate the validity of a linear equivalent to the breaking inception threshold proposed by Barthelemy et al. 2018. This linear equivalent was used by Stringari et al. 2021 to predict the probability of breaking in a sea state using Gaussian wave theory. Our results suggest that such a linear equivalent threshold exist, and that its value is close to the value proposed by Stringari et al. 2021.

Chapter 4

Analysis of the experimental results

The present chapter is devoted to the analysis of the experimental results. All the results have been obtained during the second experimental campaign. For this campaign, the vibration induced oscillations of the force measurements have been compensated using the methodology presented in section 2.4. All the impact cases investigated during the first campaign were reproduced during the second campaign. **Unless otherwise specified, the compensation methodology was applied.** We first investigate the repeatability of the measurements in section 4.1. We also detail the computation of the δ parameter and we define the impact force. Section 4.2 focuses on the influence of the distance δ and of the breaking strength Γ on the impact load. An empirical formula is proposed to relate these two parameters to the maximum impact force. The influence of the diffraction of the wave by the cylinder is investigated in section 4.3 using the video camera recordings. In section 4.4, the influence of the tilt angle and of the horizontal velocity of the mockup on the impact load is investigated for two wave cases. The list of the impact cases that were investigated during the second campaign is given in appendix A.2.

4.1 Repeatability and data processing

4.1.1 Definition of the impact force

As discussed in section 1.3.3, there is no consensus concerning the methodology that should be used to isolate the slamming term from the other terms of the measured hydrodynamic force. In the present investigation, we follow the approach of Sawaragi et al. 1984 who analyzed the force acting above the still water level (SWL). In their approach, a part of the non-impulsive force remains, but this is inevitable because of the difficulty of determining in advance the area over which the impact takes place. This area also de-

pends on the wave case. One should also keep in mind that the decomposition defined in equation 1.1 remains a simplified view of the impact and that in reality the phenomenon is more complex. Hence, it is not possible to divide the mockup into a part subjected to the impact force and a part subjected to the non-impact hydrodynamic force. From our point of view, the approach adopted by Sawaragi et al. 1984 has several advantages. First, it is simple and unambiguous. In the DIMPACT experiments, the intersection between sections S_3 and S_4 was at the SWL. The impact force is thus easily computed as the sum of the forces measured on the three upper sections and the effect of the force acting below the SWL is not taken into account. To minimize the importance of the non-impulsive force in the measurements, we could consider the impact force as the force acting on the two upper sections. Even then, a small part of the non-impulsive force would still be included in the impact force. Moreover, we might miss a part of the impact force for the breaking waves with a smaller crest height, which may also impact on section S_3. Finally, using only the two upper sections, the percentage of the crest that would be considered in the impact force would depend on the crest height η_b, and thus on the wave case. Using the proposed approach, we always consider the totality of the wave crest. In the rest of this chapter, unless otherwise mentioned, the impact force corresponds to the sum of the forces measured on the three upper sections which are above the SWL. This force is labelled F_{SWL}.

4.1.2 Computation of the δ parameter

The phase of the different components of the breaking waves were tuned so that breaking occurs at $x = 21 \pm 0.1$ m in the numerical computations. However, due to the discrepancies observed between the measured and numerically modeled free-surface profiles (see section 3.2.4), breaking may occur at a slightly different location in the flume. The free-surface profile measurements of the breaking waves do not allow to precisely determine the breaking location. Consequently, when we realized the experiments, we had to estimate the value of δ. We call this estimation δ_r, where the index stands for raw. It corresponds to the distance between the position of the front face of the cylinder and $x = 21$ m. This distance was controlled using the hexapod. It is the distance which is given to describe the impact cases listed in tables A.1 and A.2. In the present work, the distance δ is estimated as the distance between the numerically obtained breaking location and the front face of the cylinder. Note that this estimation likely includes an error due to the limitations of the numerical model. This error may depend on the wave

case.

In some of the following sections, the distance δ is non-dimensionalized with respect to the characteristic wavelength of the spectrum such that:

$$\bar{\delta} = \frac{\delta}{L}, \qquad \text{where} \qquad L = \frac{gT_p^2}{2\pi} \tanh \frac{2\pi h}{L}, \tag{4.1}$$

where L is the wavelength estimated with the dispersion relation, h is the water depth and T_p is the peak period of the focused JONSWAP spectrum. The bar stands for a non-dimensionalized quantity.

4.1.3 Attenuation of the force oscillations

In this section, we compare the compensated impact force signals to the non-compensated force signals for different values of the δ parameter. We aim to illustrate that, even if residual oscillations are present in the compensated force measurements, the level of oscillations is greatly reduced with respect to the original force signals. In figure 4.1, we compare the time evolutions of the non-compensated impact force and of the compensated impact force acting above the SWL for different values of δ during the impact of wave 3. The non-compensated impact force corresponds to the sum of the force F_1 acting on S_1 low-pass filtered at $f_c^1 = 1000$ Hz, the force F_2 acting on S_2 low-pass filtered at $f_c^2 = 700$ Hz and the force F_3 acting on S_3 low-pass filtered at $f_c^3 = 300$ Hz. These low-pass filtered forces correspond to the signals which are used to apply the compensation methodology. As a reminder, the cut-off frequencies were varied based on the number of accelerometers on the skin elements (see section 2.4.3). It appears that the compensation methodology greatly reduces the amplitude of the force oscillations. It also appears that the level of oscillations depends on the experimental conditions, *i.e.* on the value of δ. Note that the evolution of the maximum of the impact force as a function of δ seems more consistent when the compensation methodology is applied. In this case, the maximum impact force increases monotonically up to $\delta = 0.42$ m and then decreases monotonically. For the non-compensated measurements, the peak occurs for $\delta = 0.32$ m and the decrease is not monotonic. In the following, all the presented force measurements are compensated.

The evolution of the level of residual oscillations as a function of δ for wave 3 estimated using the methodology proposed in section 2.4.6 is depicted in figure 4.2. The values presented in figure 4.2 correspond to the mean value of the level of residual oscillations computed over the different repeats with the same value of δ . The methodology used

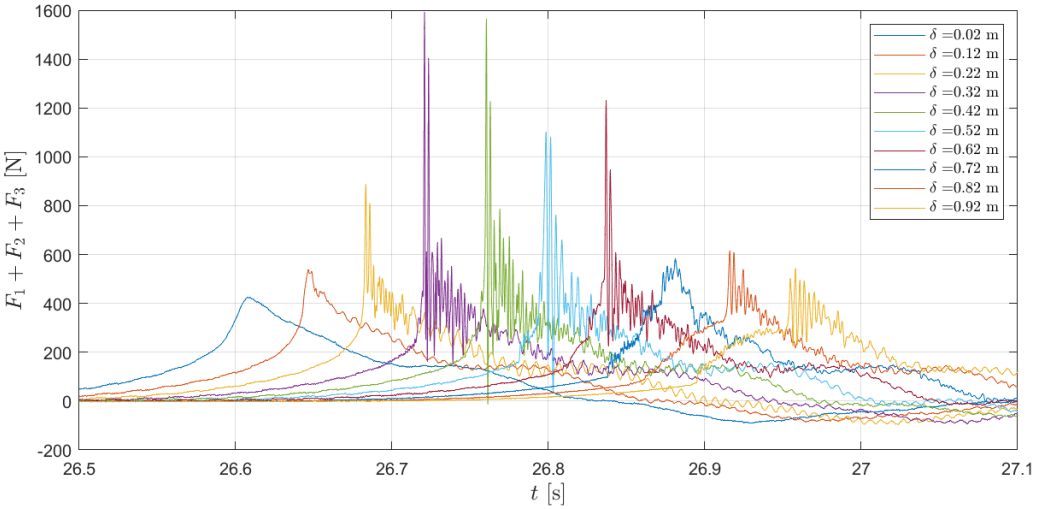

(a) Non-compensated force measurements

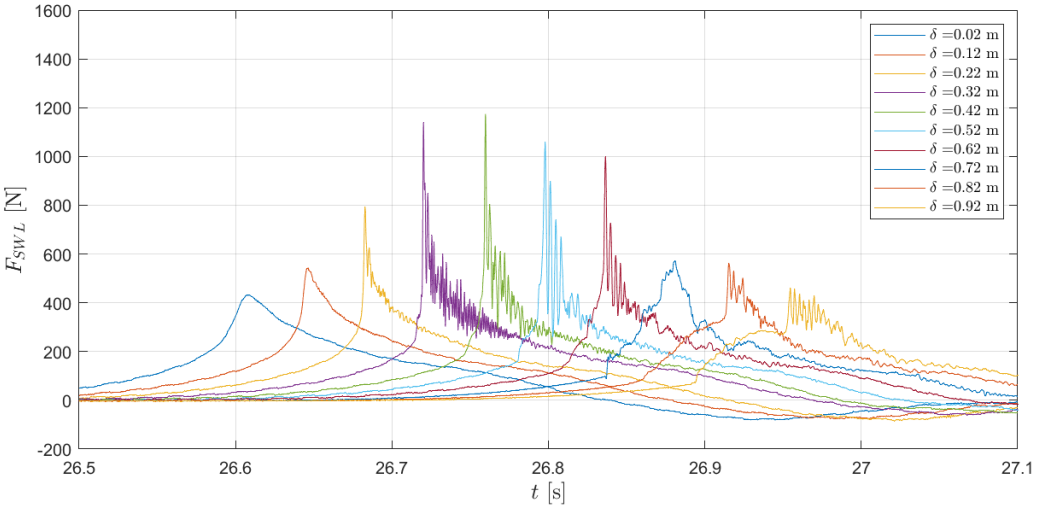

(b) Compensated force measurements

Figure 4.1 – Comparison of the filtered force measurements (a) to the compensated force measurements (b) for different values of δ during the impacts of wave 3. The force measured on S_1 is low-pass filtered at $f_c^1 = 1000$ Hz, the force on S_2 at $f_c^2 = 700$ Hz and the force on S_3 at $f_c^3 = 300$ Hz.

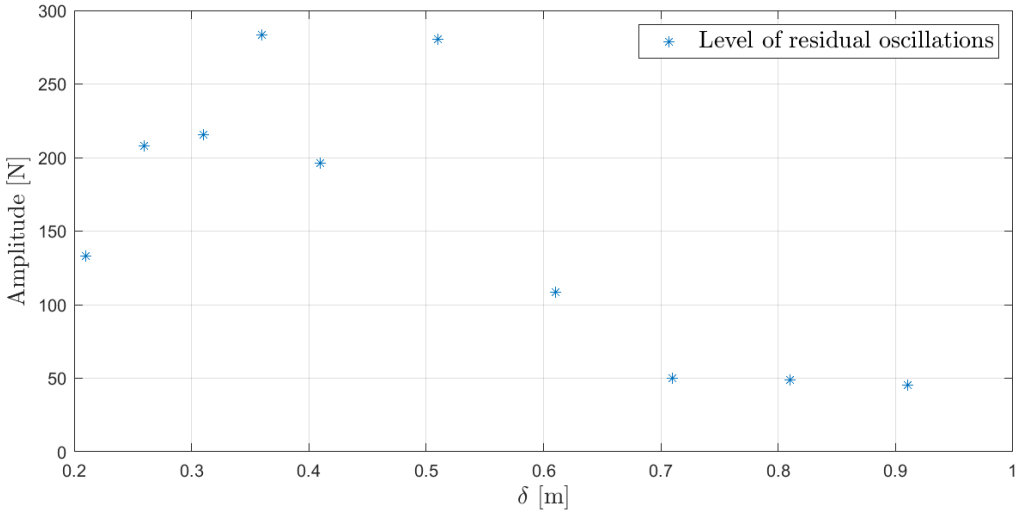

Figure 4.2 – Level of residual oscillations for wave 3. The points correspond to the mean of the levels of residual oscillations obtained for the different repeats with the same value of δ.

to quantify the level of residual oscillations is not applicable to the smallest values of δ because the level of oscillations is too low. As it is visible in figure 4.1b, the level of oscillation is the highest for values of δ in the range $[0.2; 0.5]$ m. It decreases for higher values of δ.

4.1.4 Repeatability of the force measurements

As mentioned in section 1.3.2.4, wave impact load measurements are often reported to display a low repeatability. It is thought that small variations in the initial conditions may induce a modification of the free-surface profile of the wave at impact. Even slight variations of the free-surface profile may induce important discrepancies in the measured force.

During the DIMPACT experiments, a resting time of 45 min was observed between each run to ensure that the low frequency oscillations of the flume were damped. The height of the SWL was checked visually every day using a depth gauge fixed on the side of the flume. If needed, the tank was refilled. As explained in chapter 3, the frequencies of the focused spectrum above 0.8 or 0.9 Hz were removed. This value is well below the 2 Hz high frequency limit of the wave generator. It has been shown in chapter 3 that we obtained a good repeatability in terms of measured free-surface profile before breaking

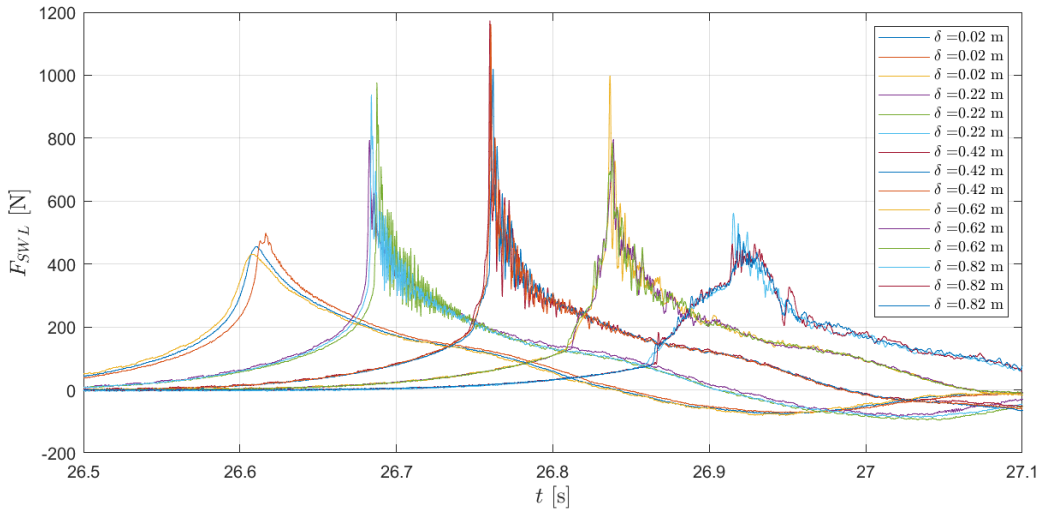

Figure 4.3 – Time evolutions of the impact forces obtained during three repetitions of the impacts of wave 3 for different values of δ.

(see figures 3.11 and 3.13). For each investigated experimental condition, the wave impact test was repeated at least three times. The impact forces obtained during the three repeats of some impacts of wave 3 are depicted in figure 4.3. Time shifts of the order of 10 ms are observed between the different repeats of the same impact case. The more impulsive the impact is, the more important the discrepancies on the force maxima are. Besides, for $\delta = 0.22$ m, the level of residual oscillations varies from one repeat to the other.

A more detailed repeatability analysis has been performed by repeating 10 times the same breaking wave impact case. The chosen impact case corresponds to wave 3 and $\delta = 0.32$ m. This case was chosen because it induces a high level of vibrations. The time evolution of the impact force for the different repeats of this case are depicted in figure 4.4a. For this particular case, the average maximum value of the compensated force is 1151 N and its standard deviation is 58 N. This corresponds to 5 % of the mean impact force. In figure 4.4b, the force signals were time-shifted so that all maxima coincide. It appears that the force increases are rather similar and that the first residual oscillations are repeatable.

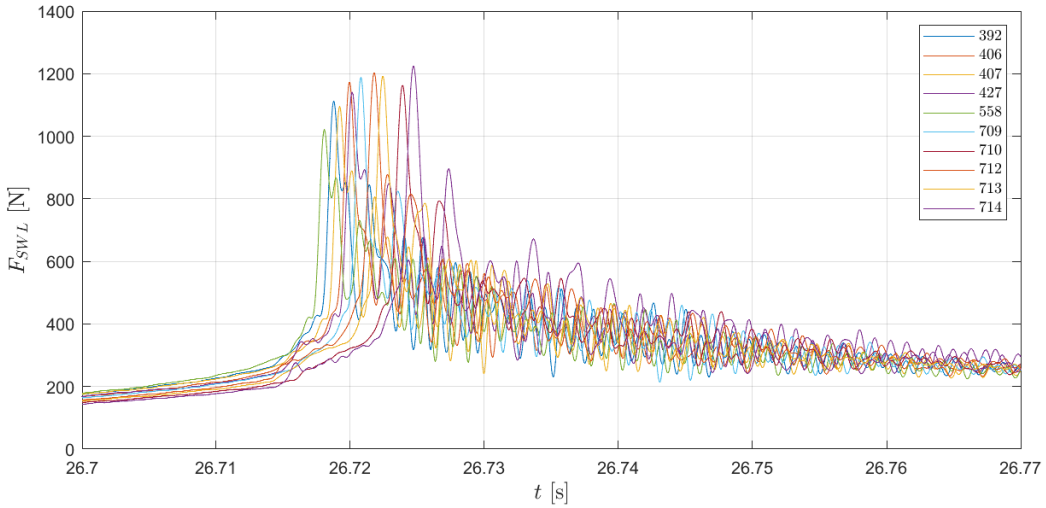

(a)

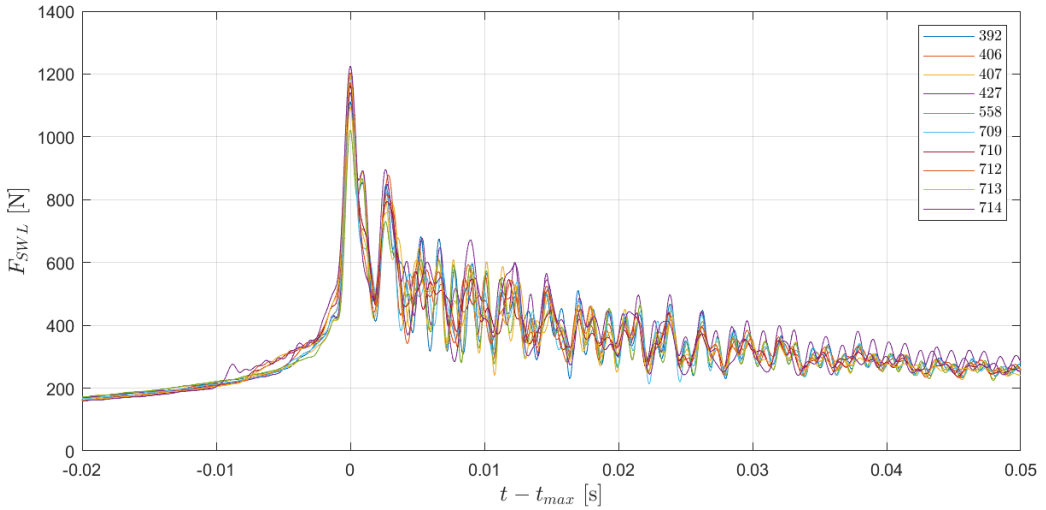

(b)

Figure 4.4 – Time evolutions of the impact forces obtained during 10 repetitions of the impact of wave 3 for $\delta = 0.32$ m. In figure (b), the force signals are time-shifted so that their maxima coincide. The numbers given in the legend correspond to the experiment numbers listed in appendix A.2.

4.2 Influence of the breaking strength and of the distance between the breaking location and the cylinder

In this section, we investigate the influence of the breaking strength Γ and of the distance δ. For seven waves, which are the waves number 1, 2, 23, 24, 3, 7 and 15 (see table 3.3), the distance δ was varied. The seven waves display different breaking strength values. The waves number 24, 7 and 15 display similar breaking strengths, but different characteristic wavelengths. The characteristics of the obtained impact force time histories are detailed in section 4.2.1. In particular, the influence of δ and Γ on the force history is investigated. In section 4.2.2, the evolution of the maximum impact force as a function of the δ parameter is presented for the 7 waves. The results are non-dimensionalized in order to ease the comparison between the different waves. Based on this non-dimensionalization, we propose in section 4.2.3 an empiric parametric formula to predict the maximum impact force generated by a breaking wave as a function of δ and Γ.

4.2.1 Characteristics of the impact force time history

In this section, we present the different characteristics of the time history of the impact force and the influence of different parameters on the time history. The influence of the distance δ and of the breaking strength Γ on the time history of the impact force are investigated in section 4.2.1.1. In section 4.2.1.2, we investigate the effect of these parameters on the frequency content of the force. The influence of the shape of the breaking wave at impact on the force time history is discussed in section 4.2.1.3 for wave 3. The case of a wave displaying a two-phase impulsive force increase is analyzed in section 4.2.1.4.

4.2.1.1 Evolution of the time history of the force with the distance δ

In this section, we present the evolution of the history of the impact force with the distance δ. The evolutions are depicted in figure 4.5 for the different investigated wave cases. For each investigated value of δ, the force obtained during one repeat of the experiment is shown. It appears that some of the impact cases are more impulsive than others. In the following, we will consider that an impact case is impulsive if the force displays a nearly instantaneous increase compared to the wave period. We use this subjective description to describe the time evolution of the force measured in the different impact cases. For

instance in figure 4.5d, we consider that the force labelled $\delta = 0.22$ m is impulsive and that the force labelled $\delta = 0.02$ m is not impulsive.

Let us focus on the waves 2, 23, 24 and 3. The breaking strength Γ of these four waves increases. As explained in chapter 3, they all break one wave before the focused wave. It appears on figure 4.5a that for wave number 2, which breaking strength is $\Gamma = 0.8$, no value of δ leads to an impulsive increase of the load. The maximum of the force decreases when δ increases. This may be due to the fact that breaking dissipates the wave energy. Indeed, the wave front is less steep and the crest height smaller when the wave reaches the structure for the higher values of δ, thus the wave is likely to generate a gentler load. The corresponding figure for wave 23 is depicted in figure 4.5b. This wave, which breaking strength is $\Gamma = 1.29$, displays an impulsive force increase for δ values in the range $[0.32; 0.52]$ m. Even for the non-impulsive cases, the force generated by wave 23 above the SWL is more important than the force generated by wave 2. The time histories of the forces induced by the plunging wave 24, for which $\Gamma = 1.82$, are depicted in figure 4.5c. A clear impulsive increase of the force is obtained for values of δ in the range $[0.32; 0.62]$ m. A small impulsive increase is also observed for the higher values of δ. For these higher values, the wave is significantly overturned at impact. The time evolution of the force is more complex. For $\delta = 0.22$ m, the force increase is more impulsive than for smaller values of δ, while it is much less impulsive than for the higher values of δ. This figure also highlights that it is not always clear if the force should be considered as impulsive or not. The force time histories generated by the strong plunging wave 3, which breaking strength is $\Gamma = 3.01$, is depicted in figure 4.5d. The range of δ values for which the force is clearly impulsive is slightly more important than for wave 24.

Similar evolutions are observed for waves 1, 7 and 15. The time evolutions for wave 1, which breaking strength $\Gamma = 0.97$ is similar to the breaking strength of wave 2, are depicted in figure 4.5e. Similarly to wave 2, no impulsive increase of the load is observed. However, for wave 1, the maximum force does not decrease when the distance δ increases. The time histories obtained for waves 7 and 15 are respectively shown in figures 4.5f and 4.5g. These two waves have breaking strengths Γ of 1.93 and 1.83. These two values are close to the breaking strength $\Gamma = 1.82$ of wave 24. However, the wavelength of wave 7 is longer while the wavelength of wave 15 is shorter. It appears from figures 4.5d, 4.5f and 4.5g that the range of δ values leading to an impulsive increase of the force increases when the wave length increases. In section 4.2.2, we will further investigate the effect of the distance δ and of the breaking strength Γ on the maximum impact force.

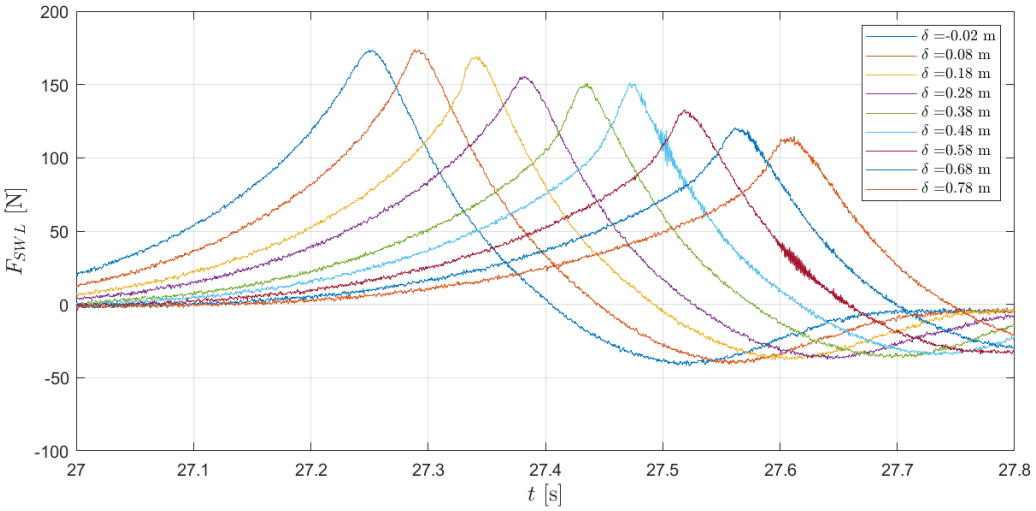

(a) Wave 2: $\Gamma = 0.8$, $T_p = 2.25$ s, $H_s = 0.13$ m

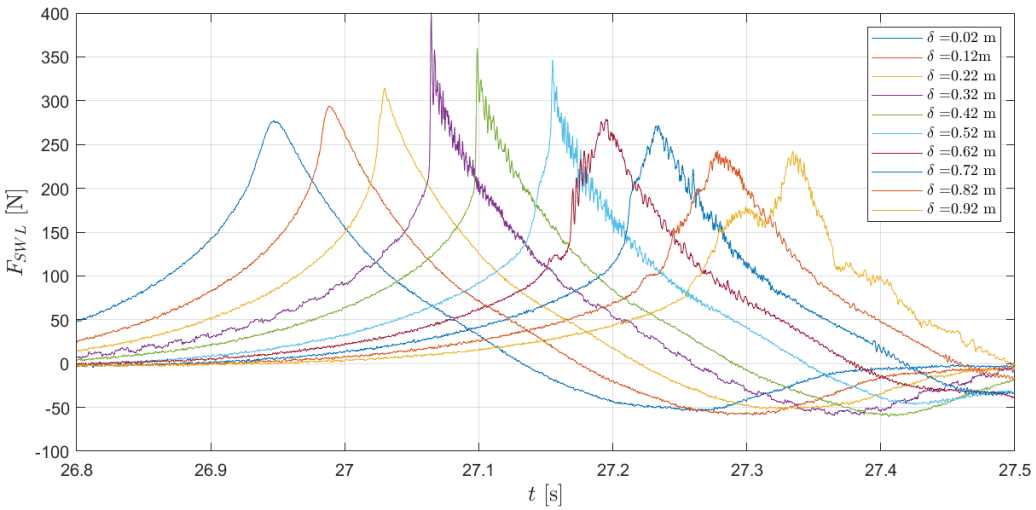

(b) Wave 23: $\Gamma = 1.29$, $T_p = 2.25$ s, $H_s = 0.135$ m

Figure 4.5 – Evolution of the time histories of the force with the distance δ for the different waves

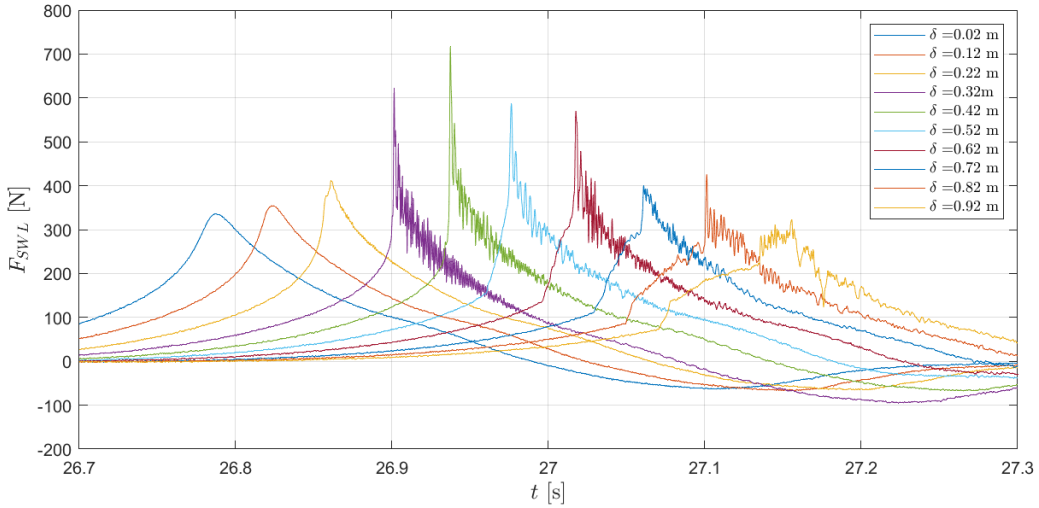

(c) Wave 24: $\Gamma = 1.82$, $T_p = 2.25$ s, $H_s = 0.14$ m

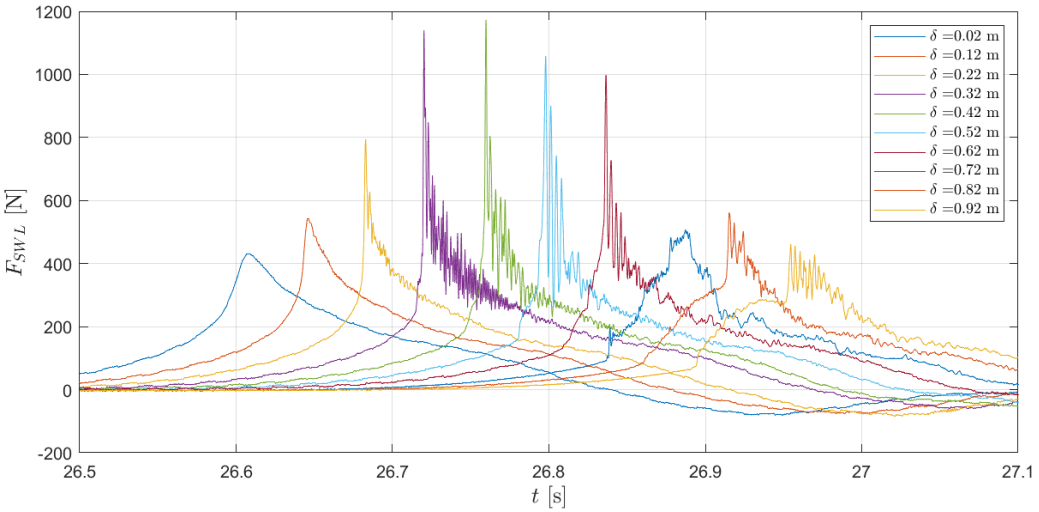

(d) Wave 3: $\Gamma = 3.01$, $T_p = 2.25$ s, $H_s = 0.15$ m

Figure 4.5 – Evolution of the time histories of the force with the distance δ for the different waves

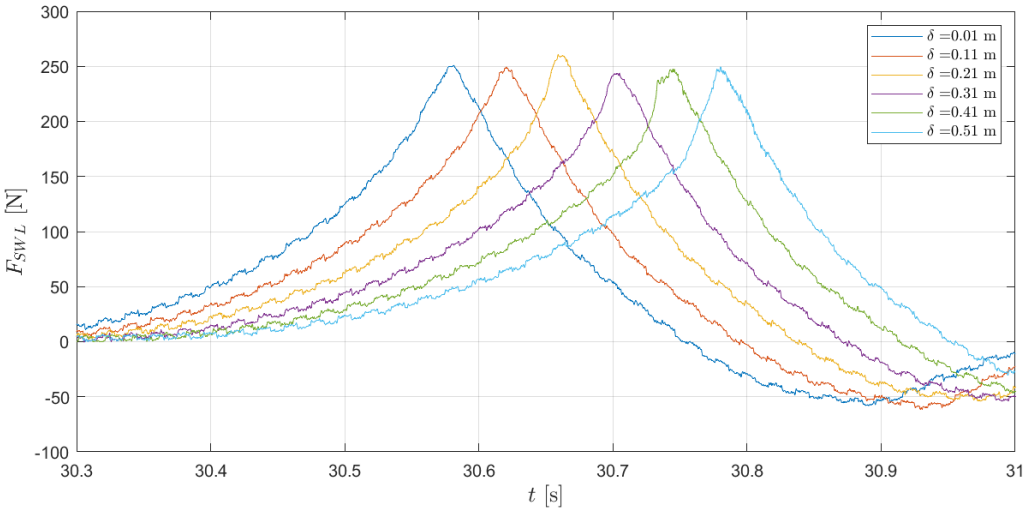

(e) Wave 1: $\Gamma = 0.97$, $T_p = 2.25$ s, $H_s = 0.12$ m

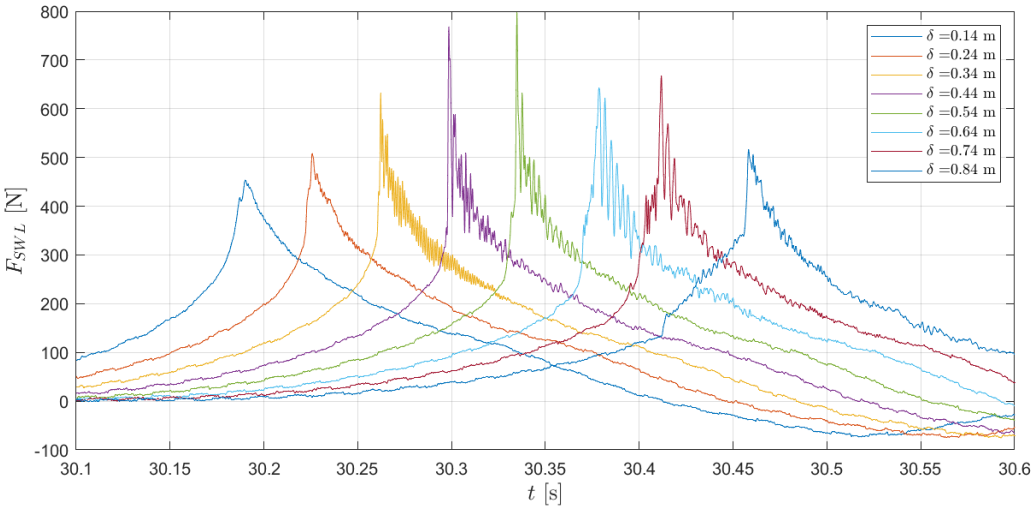

(f) Wave 7: $\Gamma = 1.93$, $T_p = 2.49$ s, $H_s = 0.13$ m

Figure 4.5 – Evolution of the time histories of the force with the distance δ for the different waves

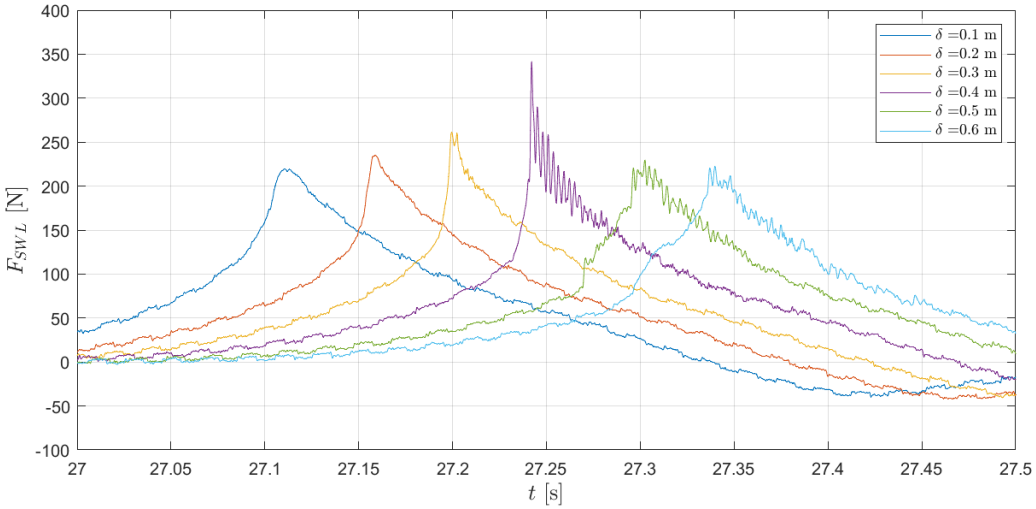

(g) Wave 15: $\Gamma = 1.83$, $T_p = 2$ s, $H_s = 0.1$ m

Figure 4.5 – Evolution of the time histories of the force with the distance δ for the different waves

4.2.1.2 Evolution of the frequency content of the impact force

In this section, we investigate the evolution of the frequency content of the impact force with the distance δ for wave 3. The amplitude of the Fourier transforms of the force signals shown in figure 4.5d are depicted in figure 4.6. For clarity, the curves corresponding to values of δ above 0.62 m were plotted in a separate figure. It appears on figure 4.6 that the high frequency content of the force history increases with δ up to a value of $\delta = 0.32$ m. Indeed, the higher δ is, the more important the tail towards the high frequencies is. For larger values of δ, the high frequency content decreases with δ. Peaks corresponding to the residual oscillations are visible in the spectra for the values of δ inducing the more impulsive forces. The narrow peaks appearing at multiples of 50 Hz correspond to electric noise. This issue was identified and fixed during the experimental campaign and the later measurements do not present these peaks.

4.2.1.3 Wave shapes at impact

In this section, we qualitatively describe the shape of the impacting wave for different distances δ by presenting the images captured by the two high-speed video cameras. We focus on the case of wave 3. The pictures of the impacting wave captured at the instant at which the impact force is maximum are depicted in figure 4.7 for different values of

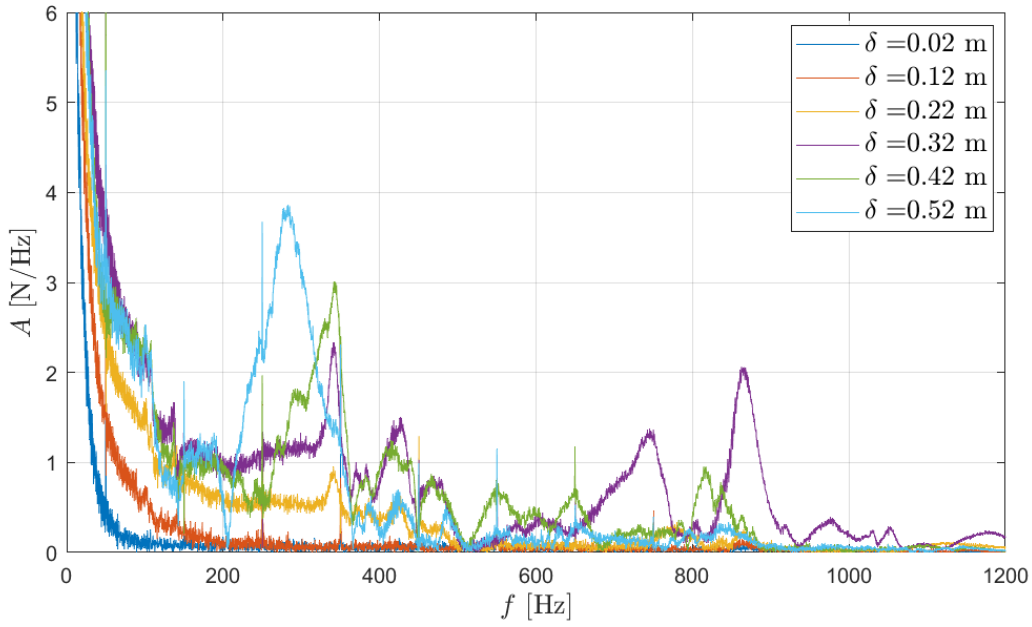

(a)

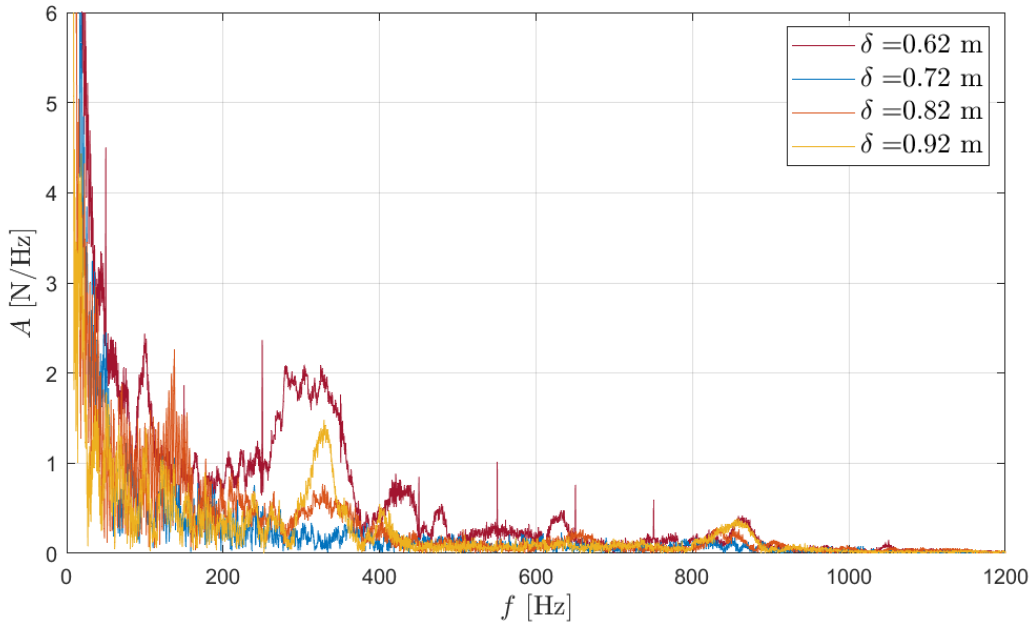

(b)

Figure 4.6 – Amplitude of the Fourier transforms of the force measurements depicted in figure 4.5d.

δ. The corresponding impact force time histories were presented in figure 4.5d. For each value of δ, the left picture corresponds to the video camera filming the rear of the mockup and the right picture to the video camera filming the front of the mockup. It can be observed that for the higher values of δ, the wave is fully overturned at the instant of maximum load. The pictures also highlight that the maximum force, which is reached for $\delta = 0.42$ m (figure 4.7e), is obtained when the wave is significantly overturned. The graphics in the upper left corners correspond to the time-shifted numerical free-surface profiles at the instant at which the impact force is maximum. The time-shifting procedure was detailed in section 3.2.5. The vertical line corresponds to the position of the front face of the cylinder. For $\delta = 0.72$ m and higher values, these plots are not available because the simulation stopped before the force reached its maximum value.

Let us detail the pictures for the different values of δ. For $\delta = 0.02$ m (see figure 4.7a), runup is visible at the instant at which the force reaches its maximum. We will see in section 4.3 that this runup is due to the deformation of the wave front by the cylinder and not to the impact of the crest. For $\delta = 0.12$ m, 0.22 m and 0.32 m, the maximum force occurs very close to the instant at which the front of the wave touches the cylinder. Indeed, no expansion of the wetted surface around the cylinder is visible. This is no longer the case for $\delta = 0.42$ m (see figure 4.7e). For this case, runup, which is likely due to the impact of the jet, is visible along the cylinder. Consequently, the rapid force increase visible in figure 4.5d is likely due to the impact of the vertical front behind the jet of the wave and not to the impact of the jet. Note that for wave 3, $\delta = 0.42$ m corresponds to the distance leading to the highest impact force. For higher values of δ, the maximum force is also obtained after the jet impacted the cylinder. The maximum force is thus likely related to the impact of the vertical front behind the jet. This will be illustrated in the following section, in which we discuss the two-phase force increases that occur for high values of δ.

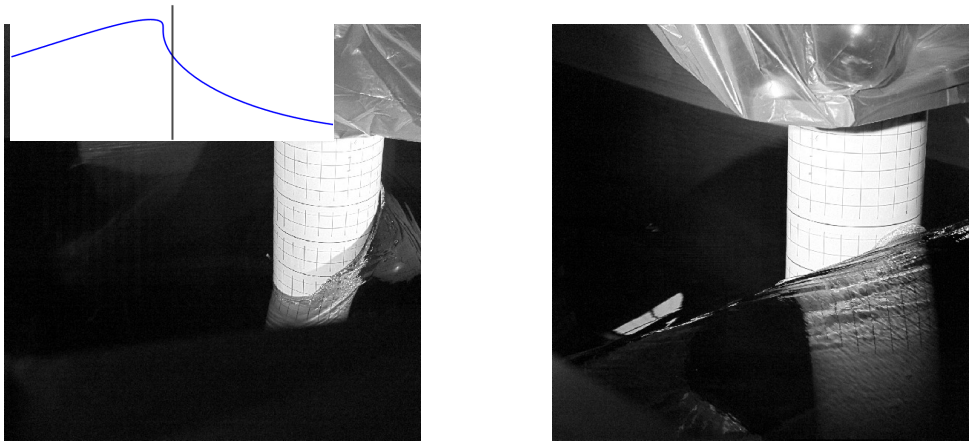

(a) $\delta = 0.02$ m

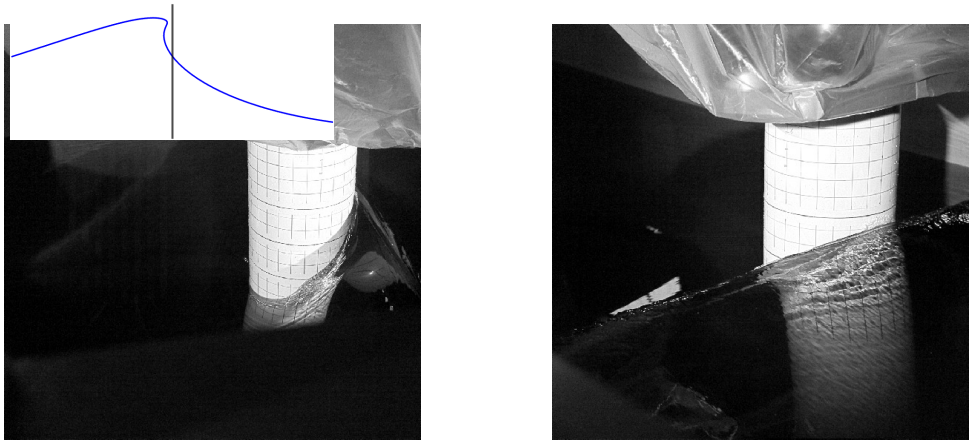

(b) $\delta = 0.12$ m

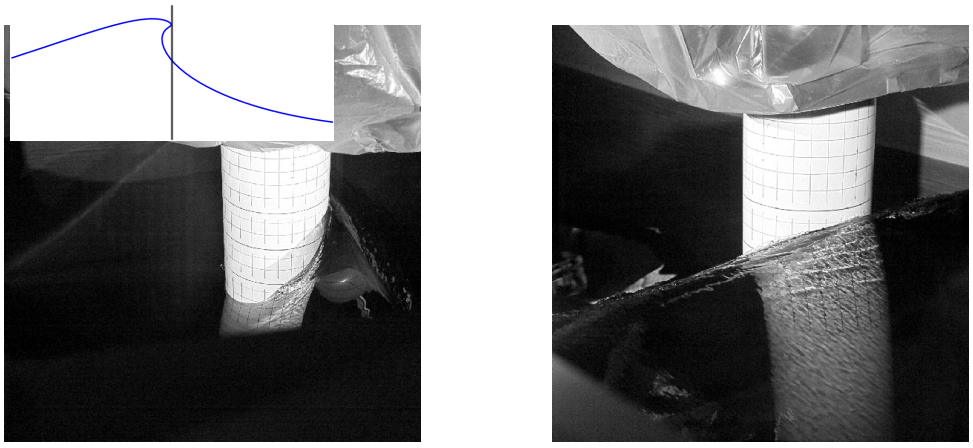

(c) $\delta = 0.22$ m

Figure 4.7 – Images of wave 3 impacting the mockup for various values of δ. All the images are taken at the instant at which the impact load is maximum. The plot in the upper left corner corresponds to the time-shifted numerical free-surface profile at the same instant. The vertical line gives the position of the front face of the cylinder.

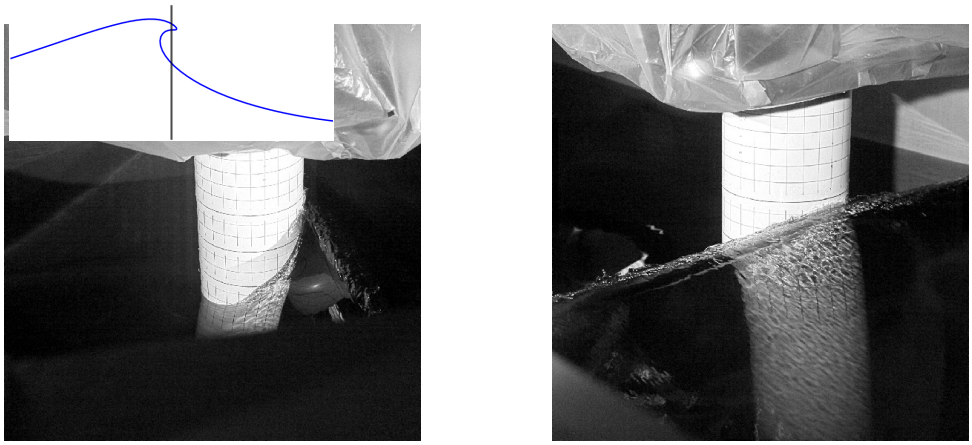

(d) $\delta = 0.32$ m

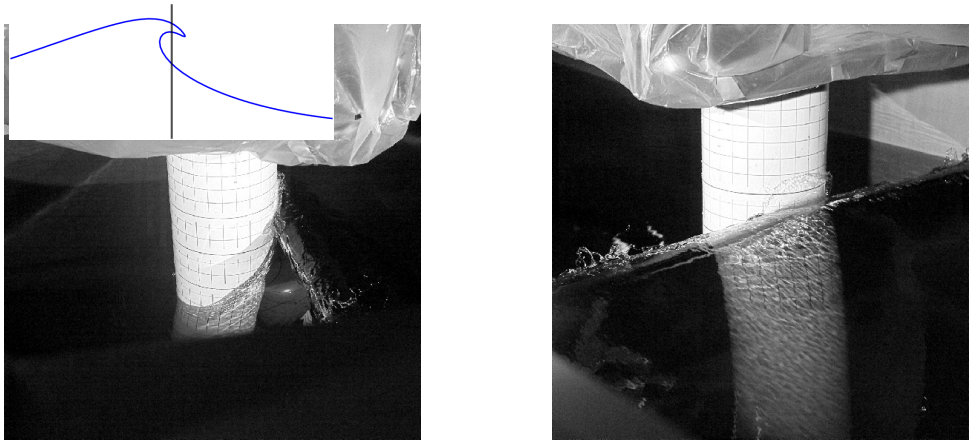

(e) $\delta = 0.42$ m

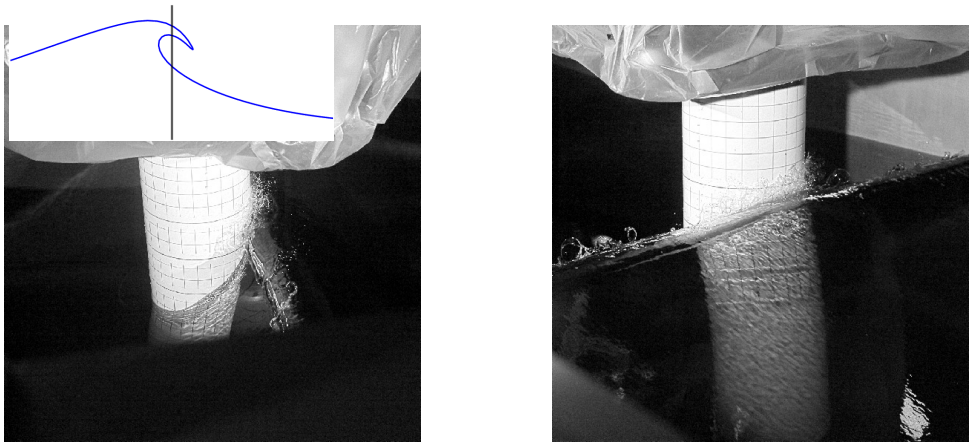

(f) $\delta = 0.52$ m

Figure 4.7 – Images of wave 3 impacting the mockup for various values of δ. All the images are taken at the instant at which the impact load is maximum. The plot in the upper left corner corresponds to the time-shifted numerical free-surface profile at the same instant. The vertical line gives the position of the front face of the cylinder.

(g) $\delta = 0.62$ m

(h) $\delta = 0.72$ m

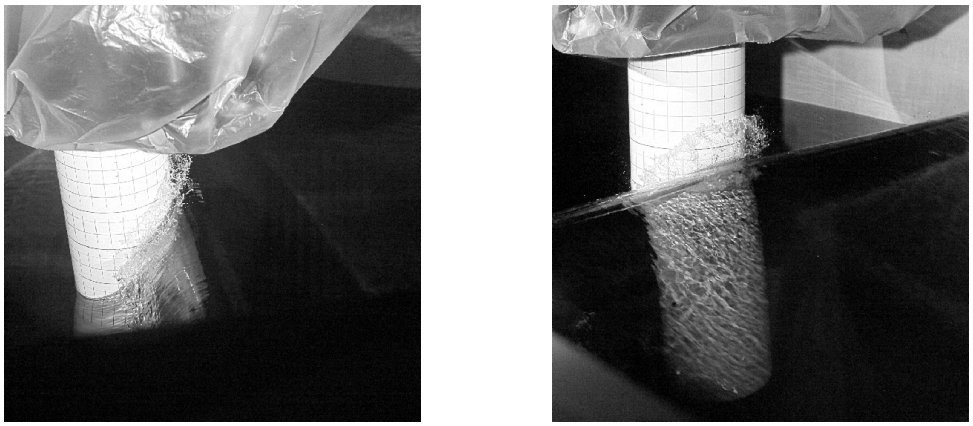

(i) $\delta = 0.82$ m

Figure 4.7 – Images of wave 3 impacting the mockup for various values of δ. All the images are taken at the instant at which the impact load is maximum. The plot in the upper left corner corresponds to the time-shifted numerical free-surface profile at the same instant. The vertical line gives the position of the front face of the cylinder.

(j) $\delta = 0.92$ m

Figure 4.7 – Images of wave 3 impacting the mockup for various values of δ. All the images are taken at the instant at which the impact load is maximum. The plot in the upper left corner corresponds to the time-shifted numerical free-surface profile at the same instant. The vertical line gives the position of the front face of the cylinder.

4.2.1.4 Appearance of a two-phase force increase

In some of the time histories depicted in figure 4.5, we observe a double impulsive increase of the force. This is especially visible for wave 3 and $\delta = 0.72$ m (see the blue curve in figure 4.5d). This double increase occurs for high values of δ for which the wave is significantly overturned at impact. Even if it is less visible, this two-phase increase also occurs for $\delta = 0.52$ m. As the numerical simulation stopped before the recorded impact time for $\delta = 0.72$ m, we will detail the two-phase increase observed for wave 3 and $\delta = 0.52$ m. A zoomed-in view of the force history for this case is shown in figure 4.8. The step occurring before the main force peak appears clearly in this figure. Two vertical lines corresponding to the start of the first force step and to the maximum impact force are drawn. The pictures taken by the video camera at these two instants are shown in figures 4.9a and 4.9b, respectively. In figure 4.9a, the breaker jet starts impacting the front face of the cylinder. Note that, even though the jet did not impinge on the free surface at this instant, important instabilities are observed along the jet. At the instant at which the force is maximum, the cylinder is already significantly wetted by the wave. The numerical free-surface profiles obtained at these two time instants are depicted in figure 4.10. The profiles were time-shifted following the approach detailed in section 3.2.5 so that they correspond to the measured profiles. Considering the instabilities developing along the jet (see figure 4.9a), the green profile may indeed correspond to the impact of the jet

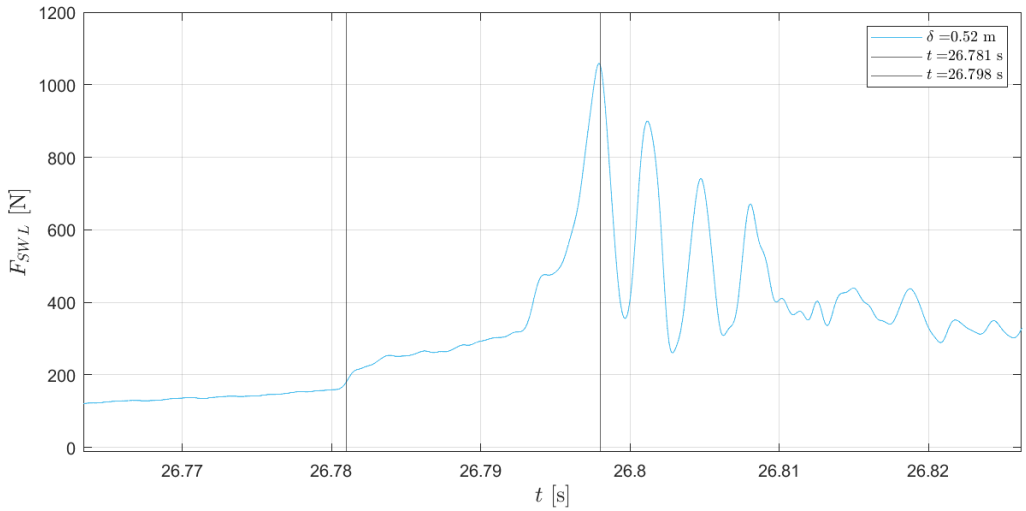

Figure 4.8 – Time history of the impact load of wave 3 for $\delta = 0.52$ m (impact case 430)

on the cylinder. However, for the orange profile, the vertical front of the wave, which is thought to produce the force peak, is rather far from the front face of the cylinder. This discrepancy may be explained by the modification of the wave shape induced by the presence of the cylinder. This phenomenon was highlighted by Batlle Martin et al. 2023, who modelled the DIMPACT impact cases with high-fidelity numerical approaches (see also section 4.3). Because of this modification, the impact may occur earlier than if the wave was not disturbed. The modification of the wave field by the presence of the cylinder is discussed in more details in section 4.3.

The appearance of a double peak in the pressure history during the impact of a breaking wave on a cylinder has been reported by several authors (Zhou et al. 1991; Chan et al. 1995; Manjula et al. 2013; Govindasamy et al. 2023). As an example, the double peak pressure measured by Manjula et al. 2013 is depicted in figure 4.11. These peaks are reported to appear during the impact of significantly overturned waves. They probably correspond to the two-phase impulsive force increase observed in the current study. The double impulsive force increase has rarely been observed in previous studies focusing on force measurements. Similar increases were nevertheless observed in the raw force measurements presented by Choi et al. 2015. However, this double increase does not appear clearly in the post-processed results. This may be due to the EMD filtering applied to the measurements. In the present measurements, we think that the application of the compensation methodology allowed to preserve the two-phase impulsive force increase.

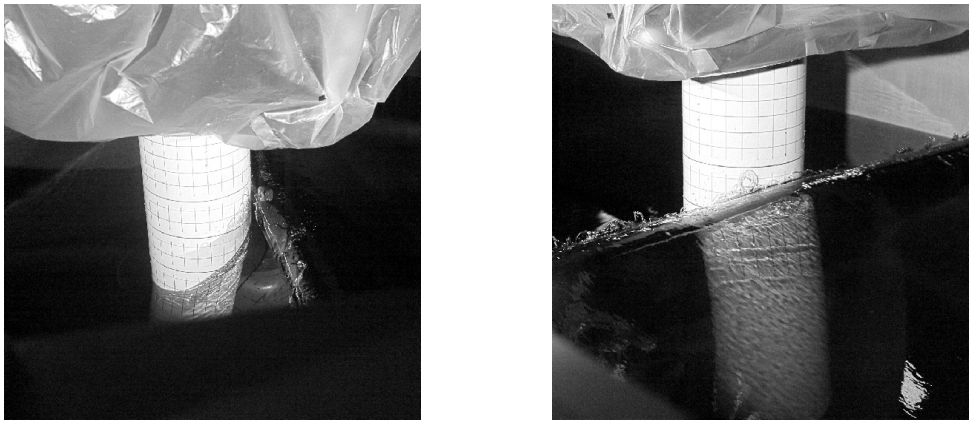

(a) $t = 26.781$ s

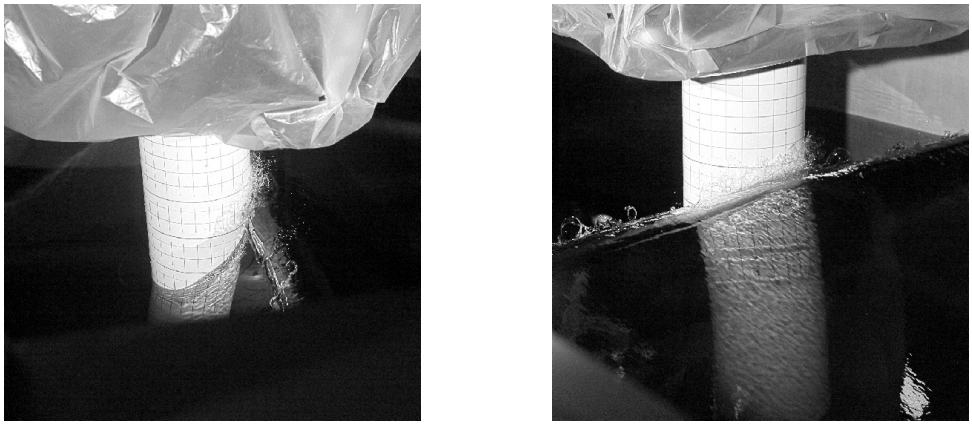

(b) $t = 26.798$ s

Figure 4.9 – Images of wave 3 impacting the mockup for $\delta = 0.52$ m (impact case 430). The images are taken at the instants corresponding (a) to the first increase of the force and (b) to the time at which the force is maximum. These two time instants correspond to the vertical lines depicted in figure 4.8.

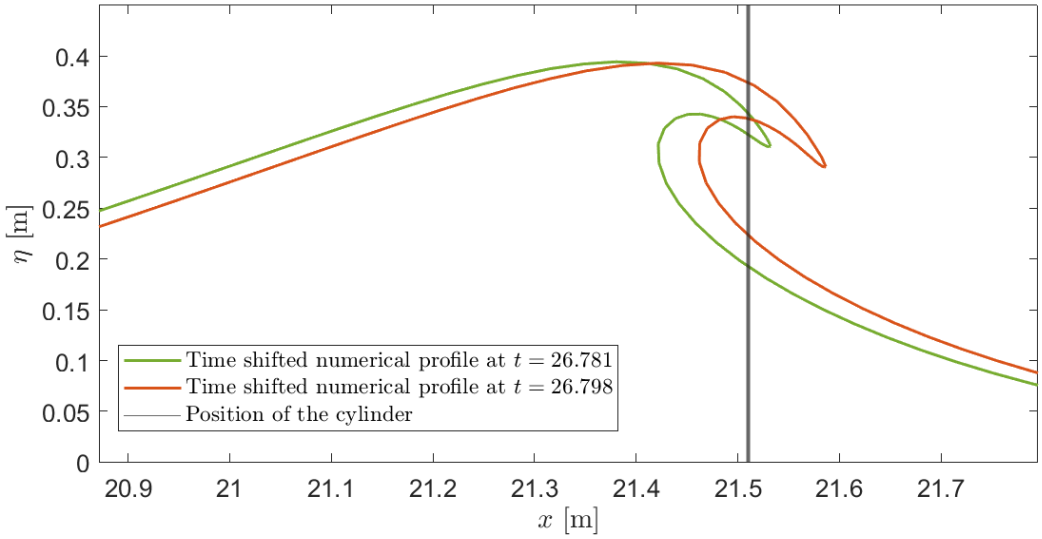

Figure 4.10 – Numerical free-surface profiles at the time instants corresponding to the first increase of the force in green and to the time instant at which the force is maximum in orange. These two time instants correspond to the vertical lines depicted in figure 4.8. The profiles were time-shifted following the approach proposed in section 3.2.5.

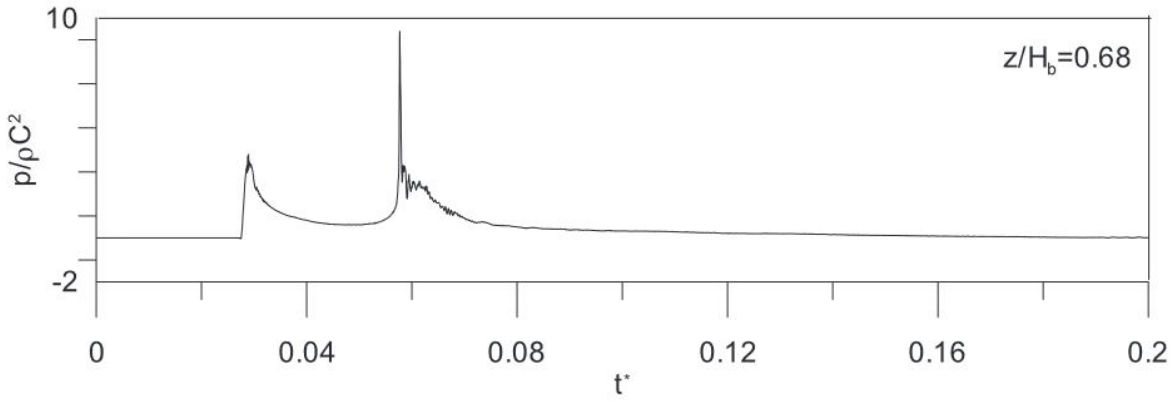

Figure 4.11 – Pressure history depicting a double peak measured during the experiments of Manjula et al. 2013.

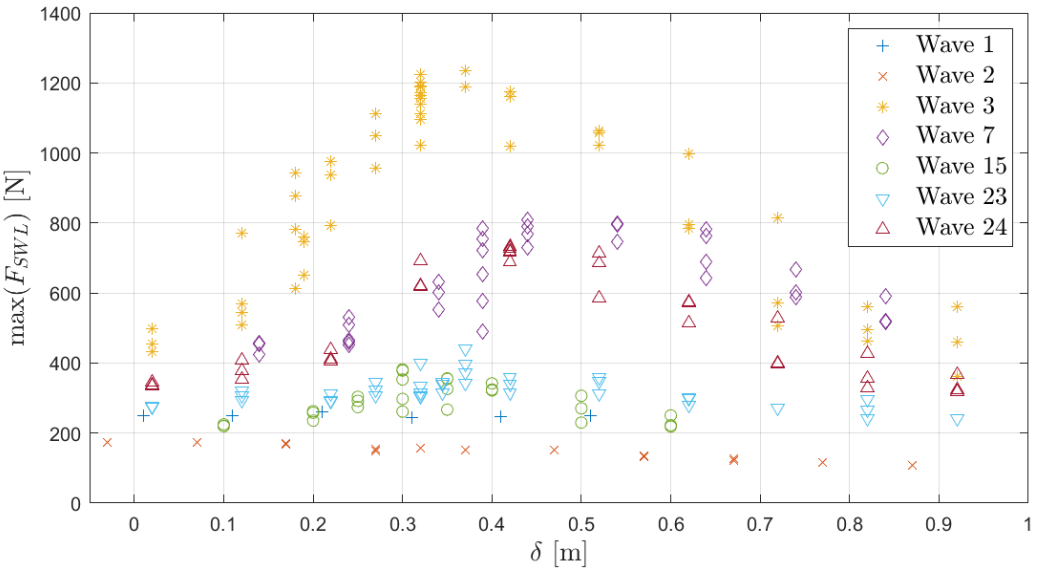

Figure 4.12 – Evolution of the maximum impact force as a function of the δ parameter

Indeed, a filtering approach would probably blur these characteristics.

4.2.2 Evolution of the maximum impact force as a function of the distance δ

The evolution of the maximum force as a function of the distance δ is plotted in figure 4.12 for the seven investigated wave cases. Each point corresponds to one repeat of the experiments. For the gentle breaking waves, which correspond to a value of Γ lower than one, no important variation of the maximum force is observed. This is in good accordance with the results of Manjula et al. 2013. They observed that, for the smallest spilling breakers, varying the δ parameter does not influence the maximum measured pressure. For the other wave cases, we observe that the maximum impact force rapidly increases with δ until it peaks. The peak is followed by a slower decrease. In agreement with previous studies, the peak value is obtained when the wave impacts the cylinder as it is significantly overturned. The non-dimensionalized results are presented in figure 4.13. Following Sawaragi et al. 1984, the impact force can be non-dimensionalized as

$$\bar{F}_{SWL} = \frac{F_{SWL}}{\pi \rho c_b^2 R \eta_b}. \tag{4.2}$$

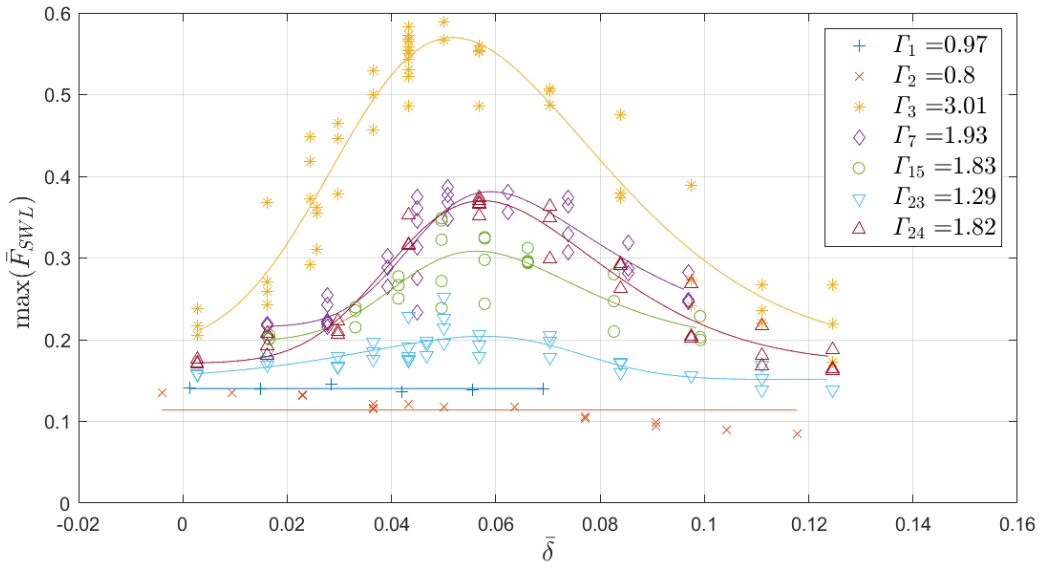

Figure 4.13 – Evolution of the non-dimensionalized maximum impact force as a function of the non-dimensionalized δ parameter. The wave numbers correspond to the index of Γ.

The quantity $\pi\rho c_b^2 R\eta_b$ corresponds to the theoretical value of the maximum force acting on a cylinder of length η_b and radius R slamming into calm water with a velocity c_b following the theory of Karman 1929. As explained in section 4.1.2, the distance δ is non-dimensionalized by the characteristic wavelength L. The evolution of the non-dimensional maximum impact force with the δ parameter was fitted with a skewed Gaussian law defined as:

$$G(\bar{\delta}) = a_1 \exp\left(-\left(\frac{\bar{\delta}-b_1}{c_1}\right)^2\right)\left(1+\operatorname{erf}\left(\xi\frac{\bar{\delta}-b_1}{c_1}\right)\right)+d_1 \tag{4.3}$$

where erf is the error function defined as:

$$\operatorname{erf}(x) = \frac{1}{\sqrt{\pi}}\int_0^x e^{-t^2}\mathrm{d}t. \tag{4.4}$$

The skewed Gaussian law was chosen because it allows to model the non-symmetric increase and decrease of the force as a function of δ. Parameters a_1, b_1, c_1, d_1 and ξ are optimized to fit the skewed Gaussian law. Parameter ξ characterises the skewness of the function. Parameter d_1 accounts for the non-impulsive term of the force. With this approach, we assume that the non-impulsive term does not evolve significantly with the distance $\bar{\delta}$. This fit was applied to the wave cases displaying a Γ value higher than one.

Number	Γ	a_1	b_1	c_1	d_1	ξ	$\max_{\delta}\left(\max_{t}(\bar{F}_{SWL})\right)$	$\bar{\delta}_{\max}$
1	0.97	0	0	0	0.14	0	0.14	0
2	0.8	0	0	0	0.114	0	0.114	0
3	3.01	0.251	0.031	0.056	0.188	2.164	0.57	0.052
7	1.93	0.103	0.044	0.042	0.216	2.708	0.381	0.059
15	1.83	0.073	0.042	0.038	0.198	2.102	0.308	0.057
23	1.29	0.034	0.075	0.048	0.151	-2.41	0.204	0.058
24	1.82	0.13	0.041	0.045	0.171	2.196	0.37	0.058

Table 4.1 – Parameters of the skewed Gaussian fits for the different waves

For the other wave cases, only parameter d_1, which corresponds to the mean of the different measurements for these two cases, was computed. The obtained fits are depicted with solid lines in figure 4.13 along with the experimental data. For the different waves, the parameters obtained from the fit are given in table 4.1. The maximum over δ of the maximum of the non-dimensional impact force and the position $\bar{\delta}_{max}$ at which this maximum is reached are also given. It appears that, for all the waves, the highest load is obtained for a value of $\bar{\delta}_{max}$ between five and six percent of the wavelength. In average, this maximum is obtained for $\bar{\delta} = 0.057$. The evolution of parameter a_1 is depicted as a function of Γ in figure 4.14. The orange line corresponds to a linear fit of the values of a_1 for the waves displaying a Γ value above 1. For the five available points, a rather good accordance is obtained. For the other fitting parameters, we did not observe a correlation with the breaking strength. Except for wave 23, the skewness parameter ξ lies between 2.1 and 2.7. The parameter b_1, which defines where the maximum of the Gaussian part of the function G is reached, is also similar for all the waves, except for wave 23. For wave 23, the impulsive part of the force $\bar{F}_{SWL}$ is smaller than the non-impulsive part. As it is the case for wave 2, which does not display an impulsive force increase, the magnitude of the non-impulsive part may vary with $\bar{\delta}$ (see figure 4.5a). Consequently, the skewed Gaussian fit would also account for these variations. We think that this may explain why the values of ξ and b_1 are similar for waves 7, 15, 24 and 3 but not for wave 23.

In figure 4.15, we applied the methodology proposed in section 2.4.6 to estimate the level of residual oscillations for different values of δ for waves 23, 24, 3, 7 and 15. The solid lines correspond to the skewed Gaussian fits proposed in section 4.2.2. The amplitudes of the error bars correspond to the level of residual oscillations obtained for the different

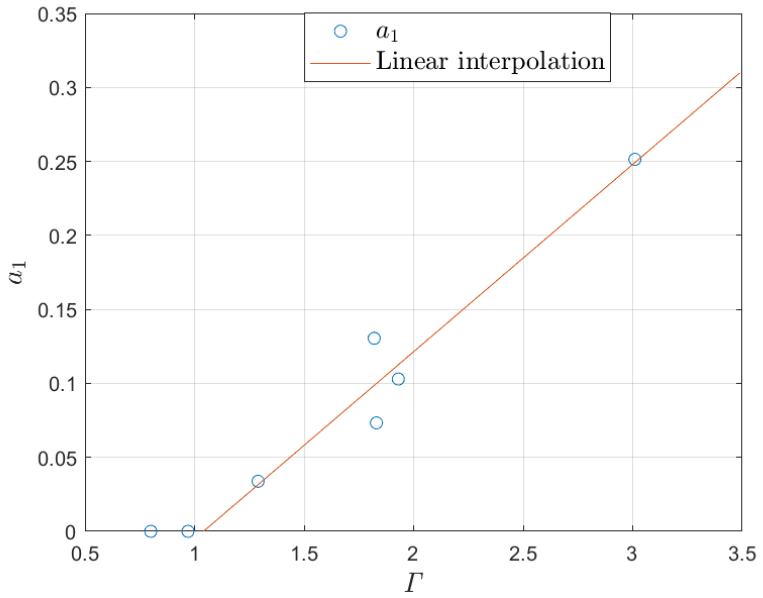

Figure 4.14 – Evolution of parameter a_1 as a function of Γ

values of δ. For the different waves and for the different values of δ, the upper and lower bounds correspond to the mean of the values obtained during the different repeats of the same impact case (same wave and same value of δ). As explained in section 2.4.6, the upper bound corresponds to the maximum of the compensated impact force. The low level of oscillations for the small values of δ does not allow to apply the estimation. One can see that the cases for which the magnitude of the impact force is high display a more important level of residual oscillations. We shall recall that the error bars are not strictly speaking the confidence interval, but it gives an indication on the uncertainty of the maximum force estimation.

4.2.3 An empirical formula for the maximum impact force

In this section, we propose a formula linking the maximum value of the non-dimensional impact force to the breaking strength Γ and the $\bar{\delta}$ parameter. The formula is based on the parameters of the skewed Gaussian curve fits obtained in the previous section. The rather small number of wave cases only allows to identify a clear dependence of the parameter a_1 with Γ (see figure 4.14), which writes:

$$a_1(\Gamma) = a_\Gamma \Gamma + b_\Gamma, \tag{4.5}$$

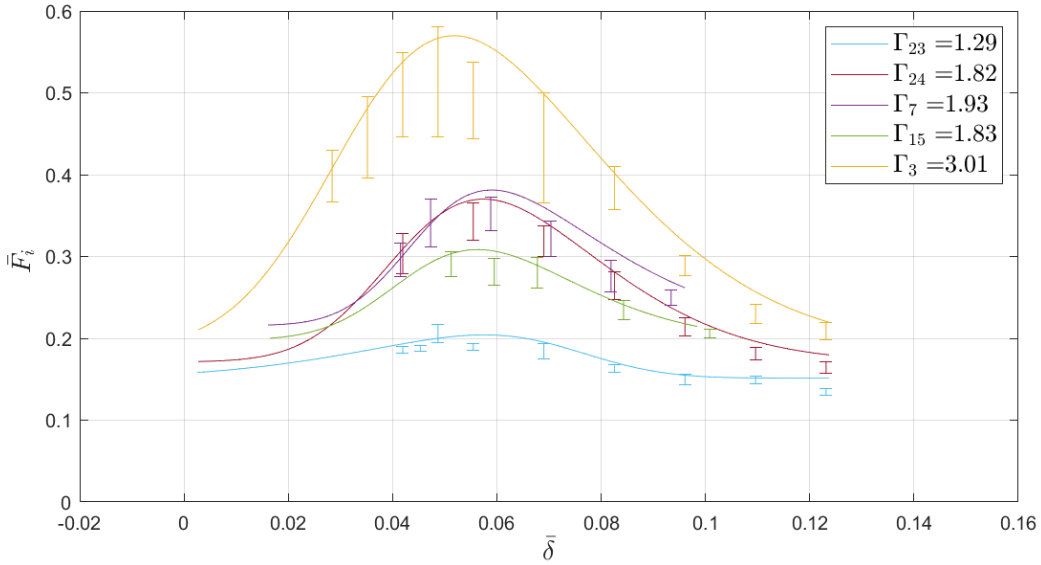

Figure 4.15 – Level of the residual oscillations for waves 23, 24, 3, 7 and 15. The upper bound of the error bar corresponds to the maximum impact force. The amplitude of the error bars correspond to the level of residual oscillations. The skewed Gaussian fits are displayed with solid lines.

where $a_\Gamma = 0.13$ and $b_\Gamma = -0.13$. For parameters b_1 and ξ, no clear correlation with Γ was observed and we decided to take the mean of the values obtained for waves 3, 24, 7 and 15. This leads to $b_1 = 0.040$ and $\xi = 2.29$. The evolutions of parameters c_1 and d_1 as functions of Γ are depicted in figures 4.16a and 4.16b, respectively. Parameter c_1 characterises the spreading of the skewed Gaussian function. It is thus linked to the width of the interval over which an impulsive increase of the load is observed. The time histories of the impact force presented in section 4.2.1 suggest that the $\bar{\delta}$ interval over which an impulsive increase of the force occurs is related to the breaking strength Γ. However, the link between parameter c_1 and Γ does not appear clearly in figure 4.16a. Consequently, we decided not to account for the dependence of c_1 to the breaking strength. For the global formula, we propose to take the mean of the values obtained for waves 3, 23, 24, 7 and 15, which corresponds to $c_1 = 0.046$. Parameter d_1 represents the non-impulsive part of the force acting above the SWL. No clear correlation between d_1 and Γ is observed in figure 4.16b. As we aim to predict the magnitude of the impulsive part of the force, we decided to not account for this term in the following. We thus compare the predictions of the proposed model to the magnitude of the experimental force minus the non-impulsive part of the force d_1.

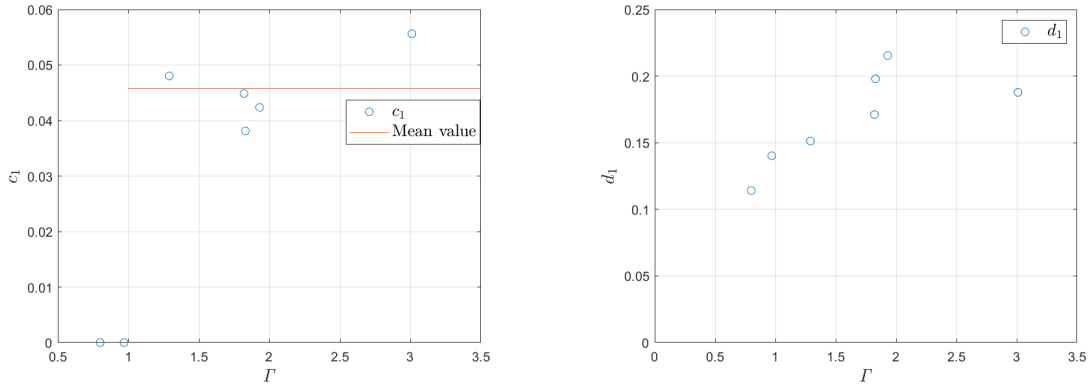

(a) (b)

Figure 4.16 – Evolution of the parameters (a) c_1 and (b) d_1 as a function of Γ. For parameter c_1, the mean value only accounts for the wave displaying a value of Γ above 1.

To summarize our approach, we propose the following relationship to compute the maximum of the impulsive part of the non-dimensional impact force:

$$\bar{F}_{SWL} - d_1 = G(\bar{\delta}, \Gamma) - d_1, \tag{4.6}$$

where function G is defined in equation 4.3 with the following values of the parameters:

$$\begin{aligned} a_1(\Gamma) &= a_\Gamma \Gamma + b_\Gamma \qquad \text{with } a_\Gamma = 0.13 \text{ and } b_\Gamma = -0.13 \\ b_1 &= 0.040 \\ c_1 &= 0.046 \\ \xi &= 2.29. \end{aligned} \tag{4.7}$$

Parameter d_1 depends on the wave case and is given in table 4.1. In figure 4.17, we compare the experimental maxima of the impulsive part of the impact force, *i.e.* $\max(\bar{F}_{SWL}) - d_1$, to those predicted by the proposed formula, *i.e.* $G(\bar{\delta}, \Gamma) - d_1$. The points correspond to the experimental measurements and the solid lines to the proposed formula. Note that the values of $\bar{\delta}$ are shifted so that the maxima coincide and correspond to zero. As a reminder, the maximum impact force attains a maximum for $\bar{\delta} = 0.057$ in average. Overall, a good agreement is obtained between the proposed formula and the measured values. However, for waves 15, 7 and 24, which display similar Γ values, the differences observed between the measured force maxima are not well reproduced by the proposed empirical formula. The magnitude of the force induced by wave 15 is overestimated while the magnitude is

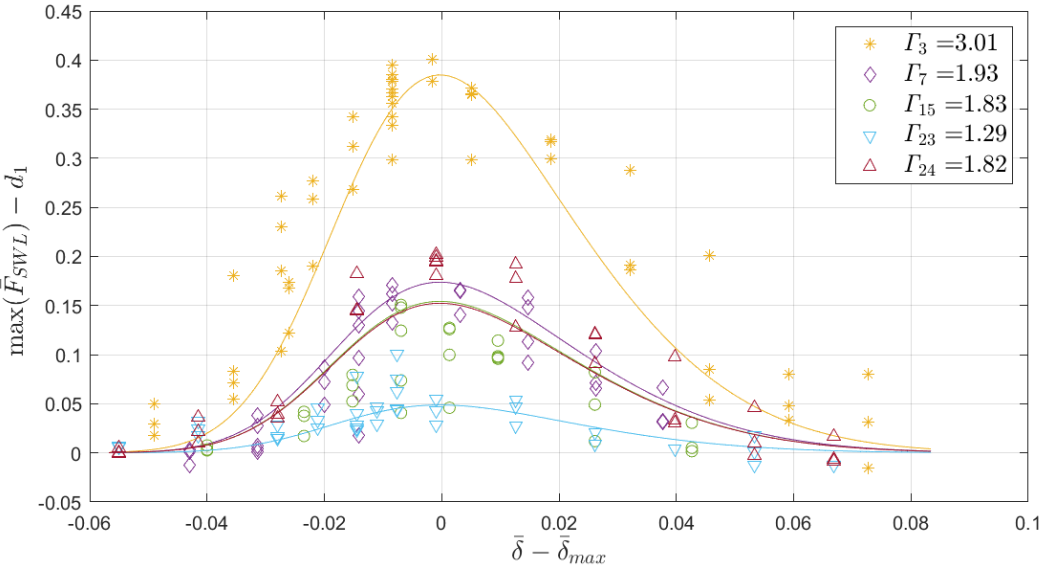

Figure 4.17 – Comparison between the experimental maxima of the impact force and the proposed formula.

underestimated for wave 24. This may be due to the fact that in the current approach, we only partially account for the effect of the diffraction of the wave by the cylinder. Indeed, for different ratios R/L between the radius of the cylinder and the characteristic wavelength, the relative effect of the diffraction is likely to vary. We will discuss the effect of the diffraction in section 4.3 in more details. Furthermore, as we saw in section 3.3.2, the Γ value should rather be considered as an estimate of the breaking strength than as an accurate indicator for the strong plunging breakers. As such, small variations of Γ will not necessarily induce a corresponding variation of the magnitude of the impact force.

4.3 Effect of the diffraction on the impact force

A wave approaching a structure is affected by the presence of the structure. This phenomenon is called diffraction in linear wave-structure interaction approaches. Following Goda's approach, the impact force is mainly due to the part of the wave which displays a vertical front. As it will be shown in the following, the diffraction tends to modify the front of the impacting wave, and consequently the magnitude of the impact force.

We will first highlight the effect of the diffraction in the impact phenomenon by considering two experimental impact cases, which are the impact of wave 24 for $\delta = 0.12$ m

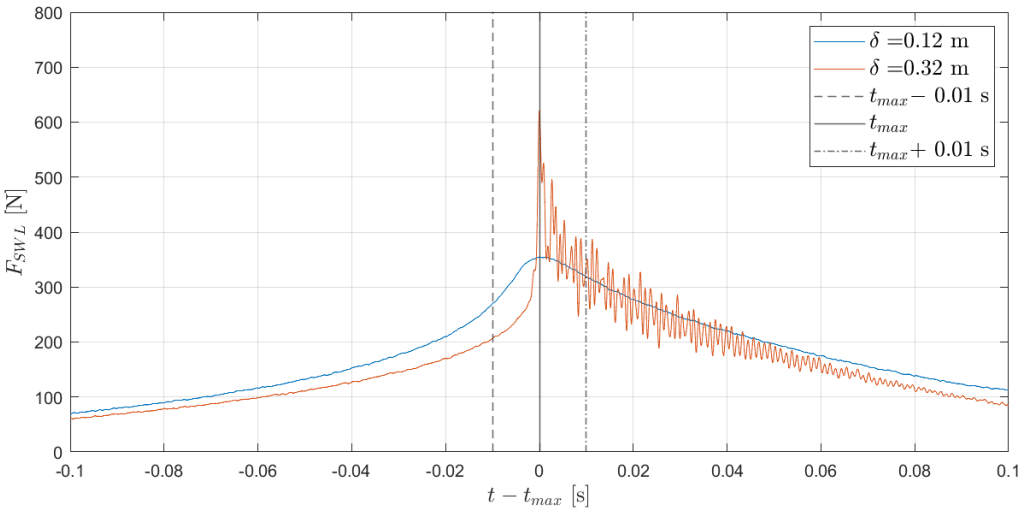

Figure 4.18 – Time histories measured during the impact of wave 24 for two values of δ. The time reference was shifted so that the maximum of the force corresponds to $t = 0$.

and $\delta = 0.32$ m. In figure 4.18, the time history of the impact force F_{SWL} for these two cases is shown. The curves are shifted in time so that the instant t_{max} at which they reach their maximum corresponds to zero. It appears that for $\delta = 0.12$ m, no impulsive force increase is observed while an impulsive increase is observed for $\delta = 0.32$ m. Let us now examine the images obtained from the high-speed video cameras during these impacts. Figure 4.19 shows a synopsis of both impact cases. The images on the left correspond to the case $\delta = 0.12$ m and the images on the right to the case $\delta = 0.32$ m. The images were taken close to the instant t_{max} at which the impact force reaches its maximum. The first raw of images were taken 0.01 s before t_{max}. This instant corresponds to the dashed vertical line in figure 4.18 showing the time histories of the impact forces. One can see in figure 4.19a that some runup is already visible for $\delta = 0.12$ m (left) while the wave front remains rather undisturbed for $\delta = 0.32$ m (right). At the instant t_{max} at which the force is maximum, the runup is very pronounced for $\delta = 0.12$ m (see figure 4.19b left). Note however that for $\delta = 0.32$ m, the wetting of the cylinder has hardly started at t_{max} (see figure 4.19b right). At $t = t_{max} + 0.01$ s, one can see in figure 4.19c that the wetted portion of the cylinder is similar for both values of δ. This indicates that the duration of the wetting process is much shorter for $\delta = 0.32$ m than for $\delta = 0.12$ m. Also note that the fragmentation of the jet for $\delta = 0.32$ m confirms the more violent nature of the flow in this case. In contrast, the expansion of the surface affected by the runup for $\delta = 0.12$ m is more progressive, although it happens in a short period of time compared to the

characteristic period of the wave. The comparison between these two impact cases shows that the effect of the diffraction, which may hinder the impact of the wave front on the cylinder, depends on the distance δ. A similar wave-structure interaction is observed for the spilling breakers 1 and 2. For these waves, there is no value of δ leading to an impulsive increase of the force. Similarly, the development of the runup before the arriving of the vertical front is visible on the videos.

During the DIMPACT project, numerical and analytical simulations were carried out to reproduce the experimental results. These simulations also give some insights regarding the importance of the diffraction in the wave-impact phenomenon. Batlle Martin et al. 2023 reproduced numerically some of the impact cases that were investigated during the DIMPACT experimental campaign using a high fidelity CFD approach. In particular, they reproduced the impact of wave 3 on the vertical cylinder for a value of δ_r equal to 0.16 m. The free-surface profiles obtained at different instants are depicted in figure 4.20. The dashed lines (labelled 2D) correspond to a two-dimensional simulation which does not account for the presence of the cylinder. The solid lines (labelled 3D) correspond to a three-dimensional simulation in which the cylinder is modeled and modifies the incident wave. The profiles were taken in the y-plane which passes through the axis of the cylinder and which is a symmetry plane of the flow. Let us examine the blue solid line which represents the free-surface profile obtained from the three-dimensional simulation just before the impact occurs. One can see that the water level at the front of the cylinder is much higher than the water level in the two-dimensional simulation. As a consequence, the portion of the wave front which can impact the cylinder is much reduced in the three-dimensional simulation compared to the two-dimensional simulation. If one uses the analytical formulas presented in section 1.2.1, this corresponds to a reduction of the curling factor λ. One may thus expect that a Froude-Krylov approach, in which the flow is assumed undisturbed by the cylinder, would overestimate the impact load acting on the cylinder. This was indeed observed by Renaud et al. 2023b who compared the load obtained with different semi-analytical formulas based on strip-theory to the VOF approach used by Batlle Martin et al. 2023. The fluid kinematics were obtained with a 2D VOF simulation where the presence of the cylinder is not accounted for. They observed that for spilling breakers, the strip-theory approaches predict an impulsive force increase while the three-dimensional simulations do not. This non-impulsive force increase was attributed by Renaud et al. 2023b to the distortion of the wave front by the cylinder.

In their study, Batlle Martin et al. 2023 also investigated the influence of the ratio

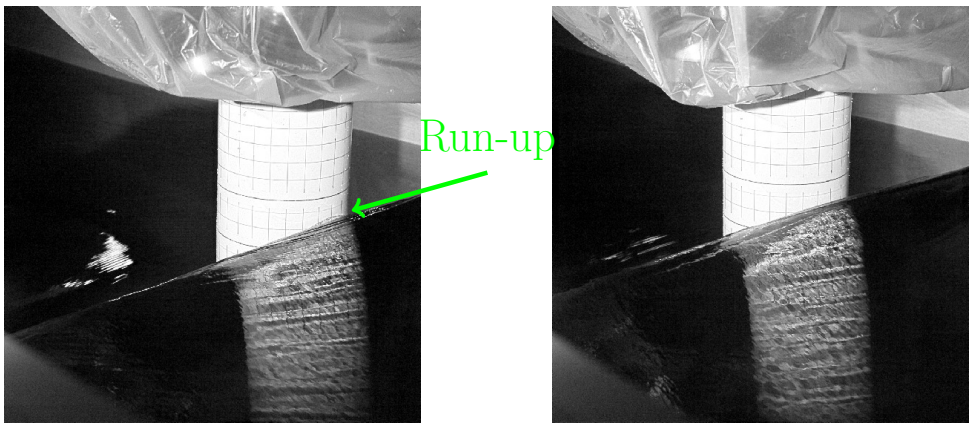

(a) $t_{max} - 0.01$ s

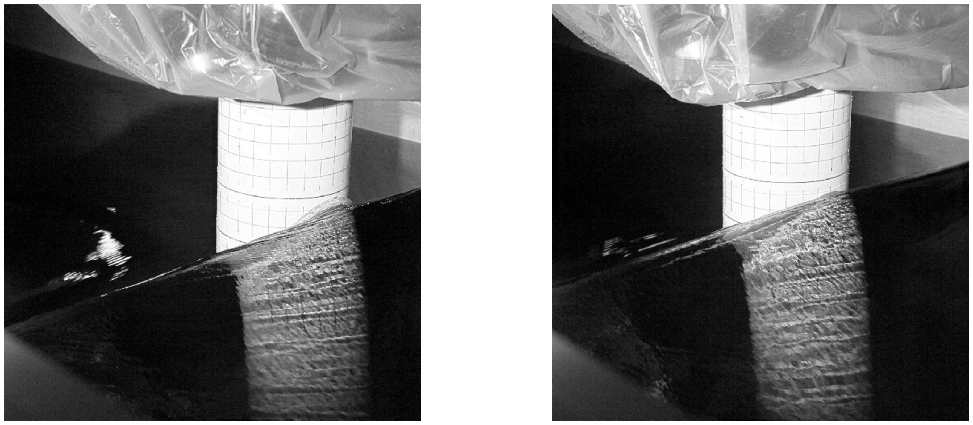

(b) t_{max}

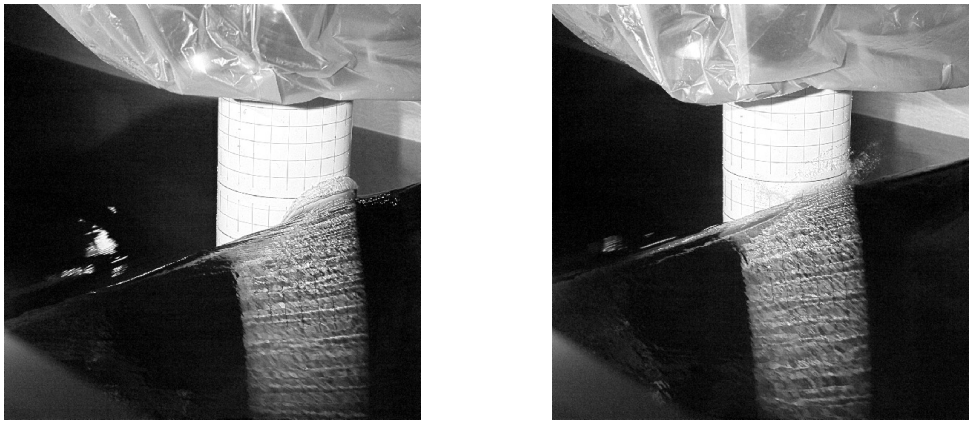

(c) $t_{max} + 0.01$ s

Figure 4.19 – Images of the impact of wave 24 on the vertical cylinder at different instants around the instant of the maximum force t_{max}. The pictures on the left correspond to $\delta = 0.12$ m while the pictures on the right correspond to $\delta = 0.32$ m.

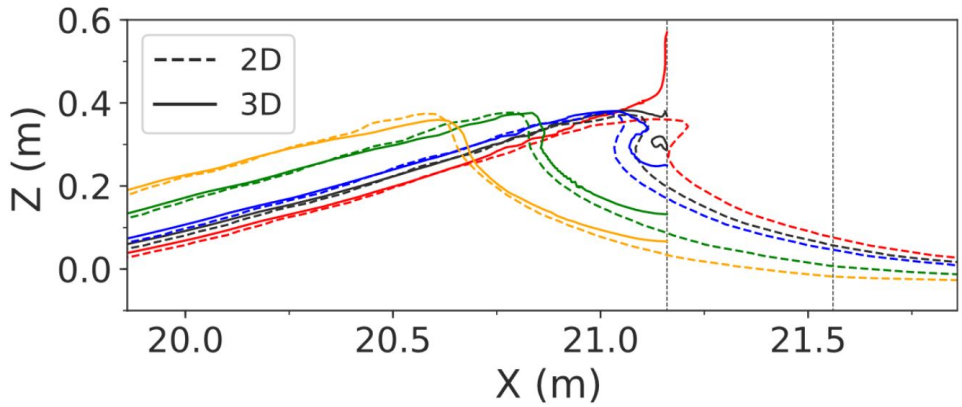

Figure 4.20 – Comparison of the undisturbed free-surface profiles (2D) and of the free-surface profiles affected by the presence of the cylinder (3D). Each color corresponds to a different time. Extracted from Batlle Martin et al. 2023.

between the characteristic wavelength and the diameter of the cylinder on the diffraction. In figure 4.21, the free-surface profiles obtained with their VOF approach are depicted for the impact of wave 3 and $\delta_r = 0.36$ m on cylinders of different diameters. It appears that the higher the diameter of the cylinder, the higher the water level at the front of the cylinder is. As a consequence, the height over which impact may occur is reduced.

It appears from the high speed video camera images that the occurrence of the runup, which is induced by the diffraction of the wave, affects the impulsive nature of the load. The run-up seems to depend on several parameters, such as the value of δ and the breaking strength Γ. Moreover, it was highlighted in Batlle Martin et al. 2023 that the ratio between the characteristic wavelength and the radius of the cylinder is also of importance. This parameter was not investigated in the current study. The influence of diffraction may limit the validity of the formula proposed in section 4.2.3. For instance, waves 24, 7 and 15 have different wavelengths. The ratio between the characteristic wavelength and the radius of the cylinder is thus different for each wave. The mitigation of the impact force induced by the diffraction will thus have different importances. This is not accounted for in the proposed formula. For the gentle breaking cases, the effect of the diffraction was taken into account through the fact that the amplitude a_1 of the skewed Gaussian is equal to zero for waves which display a Γ value smaller than one. Note that for smaller ratios R/L, the value of Γ not leading to an impulsive load increase may be smaller.

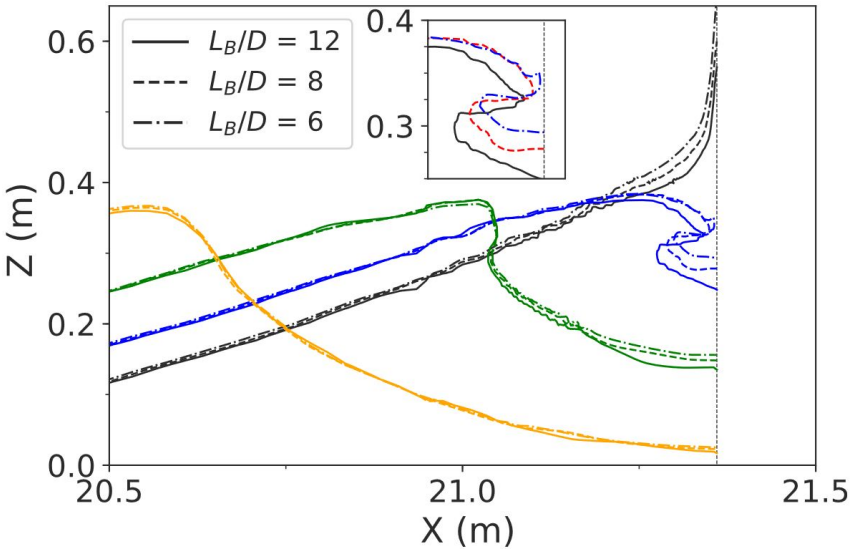

Figure 4.21 – Free-surface profiles obtained with the VOF approach of Batlle Martin et al. 2023 during the impact of wave 3 on cylinders of different radii D, but the same value of characteristic wavelength L_B

4.4 Influence of the parameters of the mockup on the impact force

During a breaking wave impact, a FOWT may be moving or tilted. It is likely that the motion and the inclination of the turbine will influence the impact load. However, very few studies have investigated the influence of these parameters so far. In order to address this question, we have performed two series of experiments: for waves 3 and 7, we varied the pitch angle of the mockup and its horizontal velocity.

The conditions of the experiments in terms of tilt angle and velocity were defined based on the conclusions of a preliminary study (Peyrard et al. 2021) conducted within the DIMPACT project by different partners of the project (EDF R&D and France Énergies Marines). This earlier study, which has not been published yet, analyzed the motions of different FOWTs floaters using linear sea-keeping approaches implemented in DIEGO, a code developed by EDF R&D, and Deeplines, a commercial software developed by Principia. In both approaches, the hydrodynamic loads are computed to the first order using the open-source potential-flow solver NEMOH (Babarit et al. 2015). The impact loads were not taken into account in the computations of the FOWT motions. The occurrence of breaking close to the floater was detected using the linear breaking criterion presented

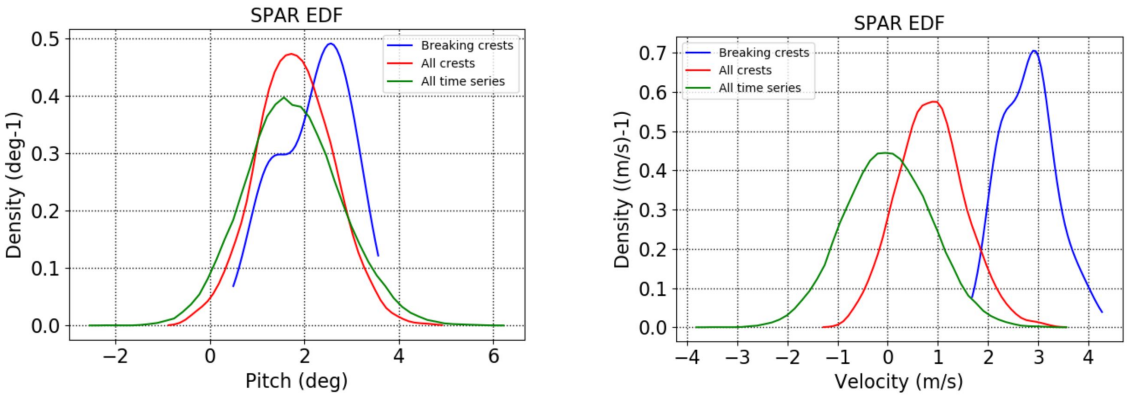

(a) (b)

Figure 4.22 – Probability density functions (PDF) (a) of the pitch angle and (b) of the horizontal velocity of a SPAR-type floater. The blue curves correspond to the PDF when a breaking event is detected at the floater location, the red curve to the PDF when a wave crest is at the floater location and the green curve to the PDF during all time series. These results have been obtained from sea-keeping computations for a sea state characterised by $H_s = 11.13$ m and $T_p = 12.43$ s. Extracted from Peyrard et al. 2021.

in section 3.4. When this criterion was reached at the floater location, the pitch angle and the horizontal velocity of the floater were recorded. This allowed to obtain probability density functions (PDF) for the pitch angle and for the horizontal velocity of the turbine at breaking events. The PDFs are depicted in figure 4.22a and 4.22b for the case of a SPAR in a sea state with a significant wave height $H_S = 11.13$ m and a peak period $T_p = 12.43$ s. It appears in figure 4.22a that the pitch angle at breaking is almost always positive. This is due to the fact that the wind acts on the rotor and tends to tilt the upper part of the turbine in the direction of wave propagation. Based on these results, it was recommended to investigate the effect of the pitch angle in the range [-5; 10]° for the experimental campaign. Similarly, it was recommended to investigate horizontal velocities in the range [0; 4] m/s. At the scale of the experiments, this velocity range corresponds to [0; 0.8]m/s. To the best of the author's knowledge, this is the first time that the effect of a positive horizontal velocity during the impact of a breaking wave on a cylinder is investigated.

Note that the results obtained during the preliminary DIMPACT investigations are supported by the results presented by Guo et al. 2020. In this study, the behavior of a moored reduced-scale semi-submersible platform is tested in a wave tank for different breaking sea states. For each impact event, the position, the velocity and the pitch angle of

the platform were recorded. They also observed that during breaking wave impact events, the platform was moving in the wave propagation direction and its upper part was inclined in the same direction. We first present the experimental results with an inclined mockup in section 4.4.1. The results with a moving cylinder are presented in section 4.4.2.

4.4.1 Breaking-wave impacts on an inclined mockup

In this section, we present the experimental results obtained when the cylinder is inclined. A description of a wave impact on the inclined cylinder is depicted in figure 4.23. The pitch angle θ is defined as positive when the upper part of the cylinder is inclined towards the incoming waves (see figure 4.23). Note that this definition differs from the definition used during the preliminary study of the DIMPACT project, and consequently from the definition used in figure 4.22a. We extended the recommended range of pitch angles to [-10 10]° for wave 7 and to [-15 20]° for wave 3. The distance δ_θ between the front face of the cylinder and the breaking location is close to the value δ_{max} for which the impact force reaches its maximum when the cylinder is vertical. As mentioned in the introduction (see section 1.4.4), inclining the mockup may modify the distance between the breaking location and the point of the cylinder first impacted by the wave. In order to mitigate a possible coupling effect between a variation of the tilt angle θ and the distance δ, we decided to set the center of rotation of the mockup on the front line of the cylinder, at the intersection between the sections S_3 and S_4. The rotation point corresponds to the red point in figure 4.23. Although the location of impact is not known accurately and varies from one wave to the other, the two top sections are the most affected by the wave impacts considered for this study. Rotating the mockup around this point should limit the coupling between θ and δ. The obtained evolution of the maximum impact force as a function of θ is depicted in figure 4.24 for waves 3 and 7. In accordance with the results of previous studies, it appears that a negative pitch angle decreases the maximum impact force while a positive pitch angle increases the maximum impact force. In figure 4.25, the results were non-dimensionalized by the maximum impact force measured when the cylinder is vertical. In the range of interest [-10; 5] °, the maximum impact force is within ± 20% of the maximum impact force measured on the vertical cylinder. For comparison, the results obtained by Tanimoto et al. 1987 for three different wave cases were also added. The impact force was only measured for angle values of -15°, 0° and 15°. It appears that they measured a more important increase of the load for $\theta = 15°$ and a smaller decrease for $\theta = -15°$. This may be due to the differences between the considered wave breaking

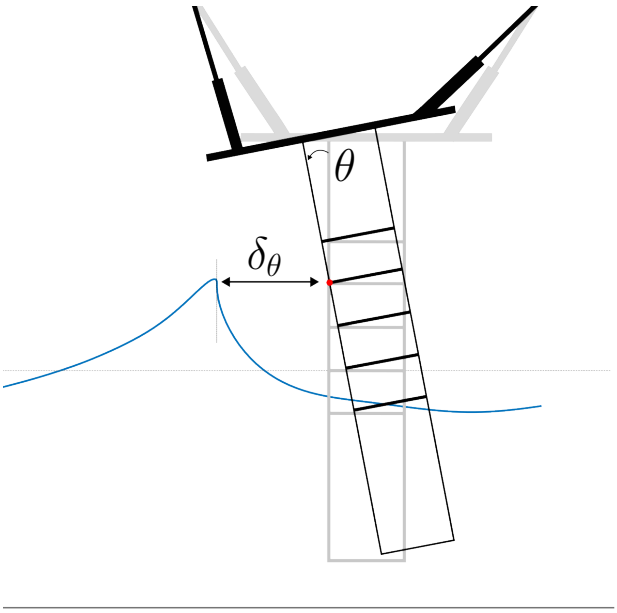

Figure 4.23 – Description of the inclined mockup during a breaking wave impact. The red point is the rotation point.

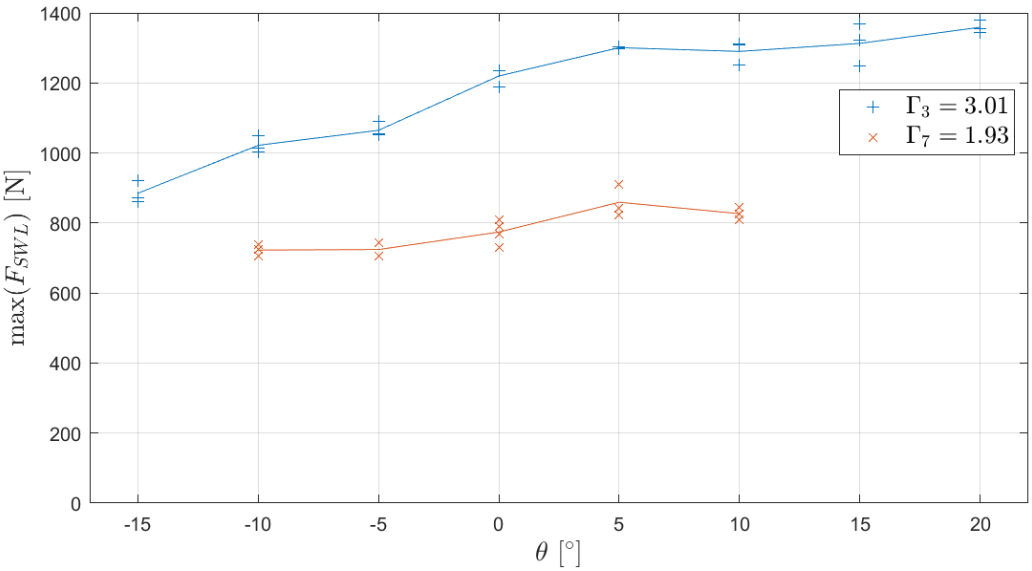

Figure 4.24 – Evolution of the maximum impact force as a function of the pitch angle θ for waves 3 and 7.

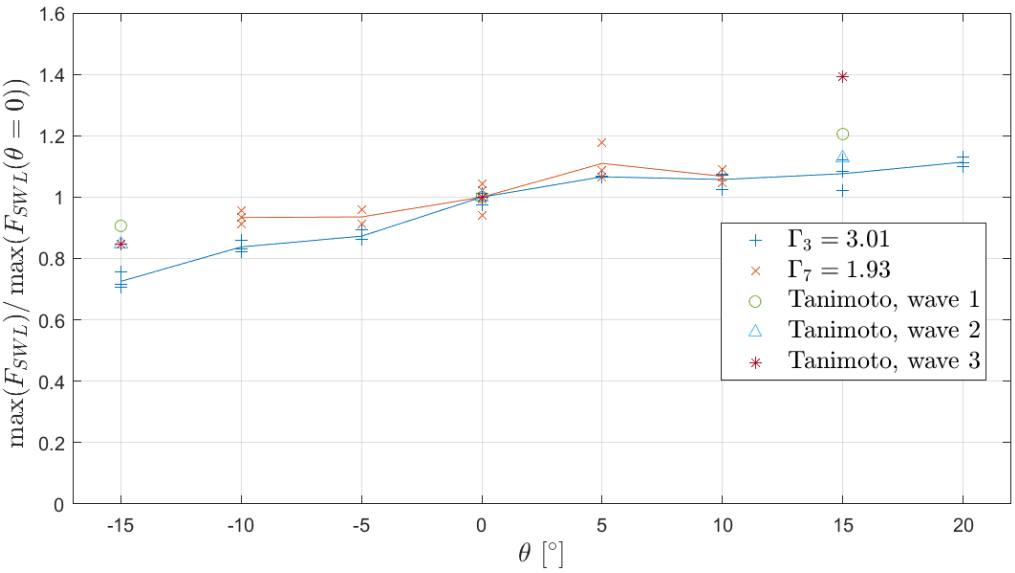

Figure 4.25 – Evolution of the non-dimensionalized maximum impact force as a function of the pitch angle θ for waves 3 and 7.

cases or to the different point of rotation. In the present study, the position of the mockup corresponds to the position $\delta_{\max}$ where the force is maximum for the vertical cylinder. It is possible that higher forces are attained for other values of δ when the cylinder is tilted. In future studies, it could be of interest to identify the value of δ leading to the strongest force for the different inclinations.

4.4.2 Breaking-wave impacts on a moving mockup

We now discuss the effect of a horizontal motion of the mockup on the impact loads. Based on the preliminary study presented above, we focused on the case of a mockup moving in the wave propagation direction during impact. Different velocities in the range $[0; 0.8]$ m/s were investigated. The mockup was set in motion by the hexapod. The set-points were chosen so that the mockup was at the location δ_{max} and moving with a constant velocity V at the time t_{max}. Recall that the position δ_{max} is the position where the maximum impact force was measured for the fixed vertical cylinder and t_{max} is the instant at which the maximum force was measured. In order to minimize the perturbation of the free-surface by the motion of the mockup (radiation), it was decided to start the motion of the mockup a few seconds before the arrival of the breaking wave (instead of a periodic motion). The time evolution of the position of the mockup is given by the

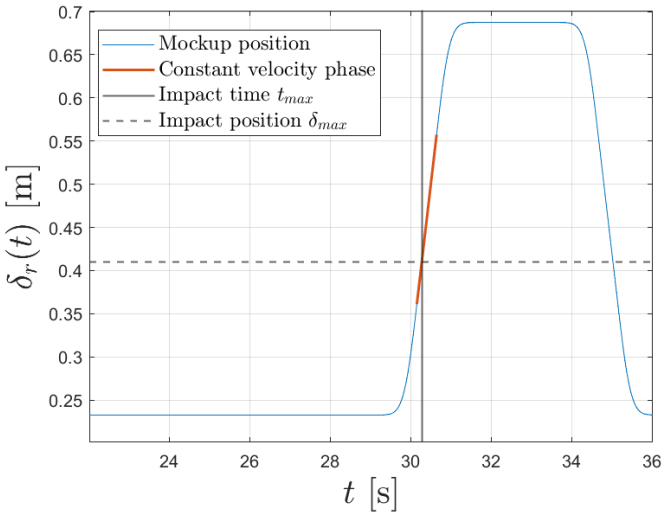

Figure 4.26 – Position $\delta_r(t)$ of the front face of the mockup during the impact of wave 7 with a velocity V = 0.4 m/s.

following equation:

$$\delta_r(t) = \begin{cases} \delta_0 - A & \text{if } t \leq t_c - T \\ \delta_0 + A\ \mathrm{erf}(B(t - t_c)) & \text{if } t \in [t_c - T, t_c] \\ \delta_0 + V(t - t_c) & \text{if } t \in [t_c, t_c + T/4] \text{ (constant velocity)} \\ \delta_0 + TV/4 + A\ \mathrm{erf}(B(t - t_c - T/4)) & \text{if } t \in [t_c + T/4, t_c + 5T/4] \end{cases} \tag{4.8}$$

where δ_0 is the position of the mockup at the start of the constant velocity phase, erf is the error function defined in equation 4.4, T is the duration of the acceleration phase and t_c is the instant at which the constant velocity phase starts. The amplitude of the acceleration phase is $A = \frac{VT}{2\pi}$ and the constant B is $B = \frac{V\sqrt{\pi}}{2A}$. The position δ_0 and the time t_c are chosen so that impact occurs during the constant velocity phase at the time t_{max} and at the location δ_{max}. The error function, erf, ensures a smooth acceleration phase in order to avoid undesired vibrations of the mockup before the impact. The constant velocity stage which follows limits the inertial effects and ensures that the velocity is correct at the instant of impact. After the deceleration phase, a symmetric motion was applied after the impact so that the mockup returns to its initial position. An example of the time evolution of the position of the front face of the mockup is depicted in figure 4.26 for $V = 0.4$ m/s. The bold orange line corresponds to the constant velocity phase. The vertical line corresponds to the impact time t_{max} and the dashed horizontal to the

impact location δ_{max}.

The effect of the horizontal velocity on the impact force was investigated through waves 3 and 7. Four velocities were investigated for each wave case. The time histories of the forces measured for the different horizontal velocities are depicted in figure 4.27a for wave 3 and in figure 4.27b for wave 7. The signals were time-shifted so that the force maxima are separated with time intervals of 0.1 s. For both waves, the magnitude of the impact force decreases as the horizontal velocity increases. For $V = 0.8$ m/s, the impulsive part of the force is significantly reduced. It also appears that the higher the velocity, the higher the level of residual oscillations. This is due to the vibrations induced by the motion of the mockup.

Let us now focus on the effect of the horizontal velocity on the magnitude of the impact force. The maximum impact force $\max(F_{SWL})$ is depicted in figure 4.28 as a function of the mockup velocity. Each point corresponds to one repeat of the measurements while the solid lines correspond to the mean value of the measurements for a given horizontal velocity. The maximum impact force decreases when the velocity of the mockup increases. In figure 4.29, the force is non-dimensionalized by $\pi\rho R\eta_b(c_b-V)^2$, where c_b-V corresponds to the relative velocity between the breaking wave and the cylinder. The values of the crest speed at breaking c_b are given in table 3.3. The solid line corresponds to a linear fit of the evolution of the non-dimensional impact force with the horizontal velocity. If the impact force were indeed proportional to the square of the relative velocity between the wave and the mockup, we should obtain a horizontal line for each wave case. It appears in figure 4.29 that the non-dimensional impact force tends to decrease when the relative velocity decreases. Different explanations may be proposed. First, the part of the crest in which the fluid velocity is close to the crest celerity is smaller than the height over which the impact occurs. Indeed, there is only a small part of the wave front in which the fluid velocity is close to the crest velocity c_b. The total force would thus not be proportional to the square of the relative velocity. We carried out the same analysis by considering only the force acting on the upper section or on the two upper sections. These sections being close to the crest of the wave, the velocity of the fluid impacting these sections should be close to the crest velocity. However, a similar decrease of the maximum impact force is observed. Another possible explanation is that the wave may be disturbed by the motion of the cylinder. Indeed, as the cylinder is moving in the wave propagation direction, the wave breaks in the wake of the cylinder. Pictures of wave 3 impacting the fixed cylinder (left) and the cylinder moving at a velocity of 0.6 m/s (right) are depicted in figure 4.30.

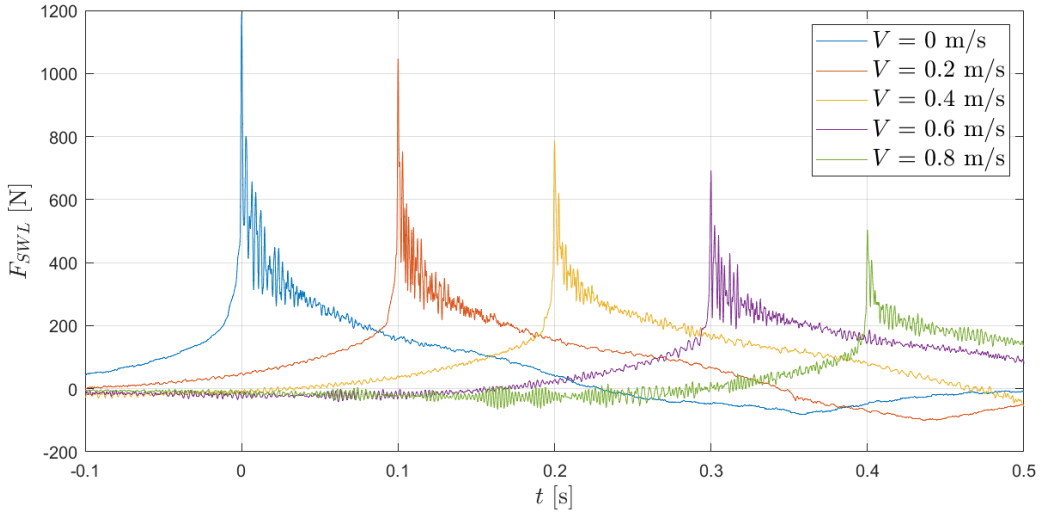

(a) Wave 3

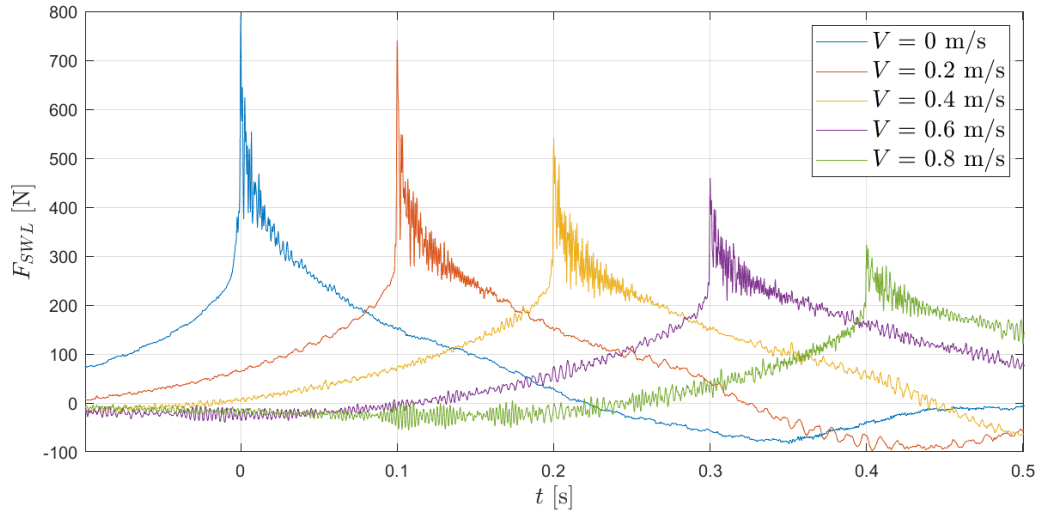

(b) Wave 7

Figure 4.27 – Time histories of the force for the different horizontal velocities V for waves 3 (a) and 7 (b). The force signals were time-shifted so that the maxima are separated with time intervals of 0.1 s.

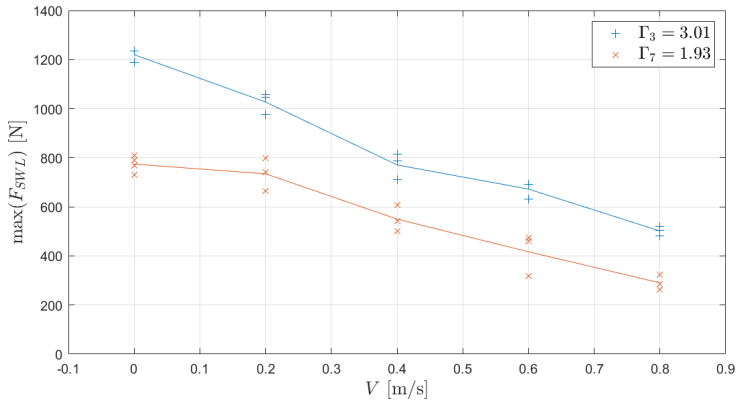

Figure 4.28 – Evolution of the maximum impact force as a function of the horizontal velocity of the mockup V

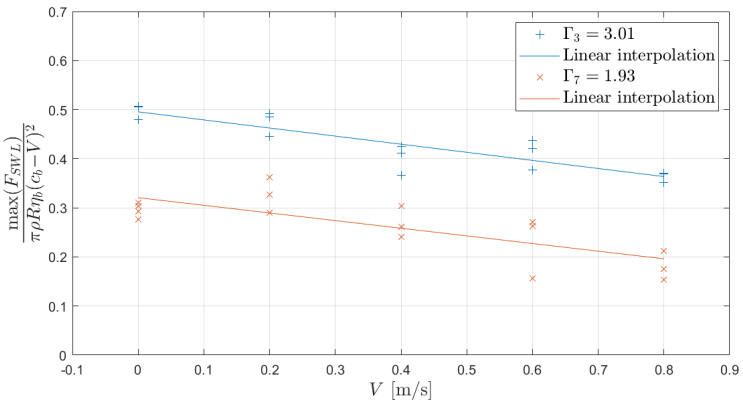

Figure 4.29 – Evolution of the non-dimensionalized maximum impact force as a function of the horizontal velocity of the mockup V. The force is non-dimensionalized by $\pi\rho R\eta_b(c_b - V)^2$.

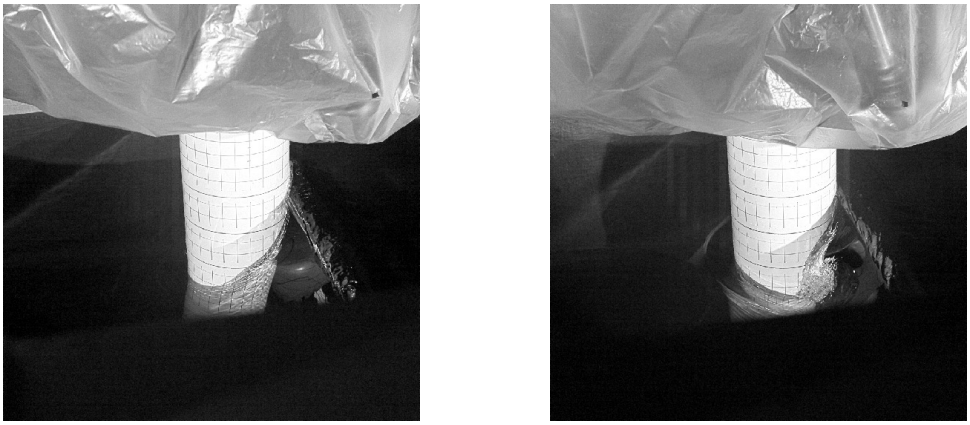

Figure 4.30 – Images of wave 3 impacting the mockup when it is fixed (left) and moving at $V = 0.6$ m/s (right). The images are taken at the instant at which the impact force is maximum.

Both pictures were captured at the instant at which the impact force is maximum. It appears on the picture on the right that a complex phenomenon is occurring below the front of the wave. This phenomenon may disturb the crest of the wave and limit the magnitude of the impact force.

4.5 Conclusion

In this chapter, we presented the results and conclusions of the second experimental campaign. We studied the influence of several parameters on the impact force, which we defined as the force acting above the SWL. We showed that the compensation methodology allows to greatly reduce the level of oscillations in the force measurements and that the measurements present a rather good repeatability. In section 4.2, we studied the influence of the distance δ and of the breaking strength Γ on the impact force. For seven wave cases displaying various breaking strengths, we varied the distance δ. It appeared that the distance δ, which determines the breaking stage at which the wave impacts the cylinder, strongly influences the time history, the magnitude and the frequency content of the impact force. The waves with a value of Γ smaller than one are the only waves for which we did not observe an impulsive increase of the impact force. For the other waves, the higher the value of Γ, the higher the impact force. For the impacts of significantly overturned waves, we observed a two-phase increase of the impact force. We analysed the maximum of the impact force as a function of the distance δ. It appeared that the waves which

display similar Γ values also display similar evolutions of the maximum impact force as a function of δ. We proposed an empirical formula to relate this maximum impact force to the distance δ, the breaking strength Γ, the crest height η_b and the crest speed c_b. This formula could be used to extend the probabilistic breaking model of Stringari et al. 2021 to the prediction of breaking wave impact loads on FOWTs. In section 4.3, we investigated the effect of the diffraction on the impact force. We attributed the fact that some waves do not induce an impulsive force increase to the presence of the diffraction. For stronger waves, the diffraction tends to reduce the vertical extent of the wave front and to mitigate the impact force. We think that diffraction has a rather strong effect on the impact force, and we recommend to further investigate its effect through numerical and experimental investigations. In section 4.4, we investigated the effect of the pitch angle and of the motion of the mockup on the impact force. It appeared that an inclination in the wave propagation direction decreases the impact force while an inclination in the opposite direction increases the impact force. We also studied the effect of a motion of the cylinder in the wave propagation direction. It appeared that the maximum impact force decreases when the relative velocity between the wave front and the mockup decreases. However, this decrease does not seem to be proportional to the square of the relative velocity, as it was expected prior to the experiments. Indeed, the impact force decreases a bit faster than the squared relative velocity. Note that this may be due to the perturbation of the wave by the motion of the cylinder.

Chapter 5

Conclusion and perspectives

5.1 Conclusions

We reviewed in chapter 1 the existing approaches to measure and model breaking wave impacts on FOWTs. The review focused on wave impacts on a circular cylinder, which is an idealized structure representative of a SPAR-type FOWT design. This review highlighted that some important parameters influencing the force generated by breaking wave impacts are either not taken into account or inconsistently taken into account in analytical wave impact models. The parameter δ, which we defined as the distance between the breaking location of a wave and the front face of the cylinder, was reported to strongly influence the impact force. However, there was no attempt to include it into analytical or empirical impact models so far. The breaking strength of a wave is also reported to have a strong effect on the impact load. It is usually accounted for through the curling factor λ. We highlighted that several definitions of the curling factor exist and that they are not always consistent with each other. In some of the analytical approaches, which do not account for the parameter δ, the same wave may display different curling factors. This is, for instance, the case during impacts at different distances δ. It also appeared that the case of a wave impacting a tilted or moving cylinder, which is of importance for FOWTs, was barely studied. In particular, no experiment investigating the effect of a horizontal motion of the cylinder in the wave propagation direction has been reported. The studies investigating the influence of the tilt angle of the cylinder focused on high angles, which should not be attained by FOWTs. This review led us to study experimentally the effects of these different parameters on breaking wave impact loads. In our investigations, an important effort has been devoted to the characterisation of the breaking waves in order to precisely link the wave characteristics to the impact loads.

We presented our experimental approach in chapter 2. The mockup used for the present experiments consisted in a segmented cylinder with a 40 cm diameter. It was divided into six sections, out of which four were instrumented with a load cell. Each instrumented sec-

tion allowed to independently measure the hydrodynamic force acting on it. The mockup was mounted on a six degree-of-freedom motion generator used to precisely control the position, inclination and motion of the mockup. Two high-speed video cameras were placed downstream and upstream of the mockup to film the wave impacts on the cylinder. We applied a novel methodology to address the frequently encountered issue of force signal oscillations induced by vibrations of the mockup. The methodology relies on the use of accelerometers to compensate for the oscillations in the measured force signals. For this purpose, we placed a set of six accelerometers on the two upper sections, which display the highest level of oscillations. A linear combination of the measured accelerations was added to the force measurements to compensate for the force oscillations. We first used this methodology to compensate for the force oscillations observed during hammer tests. We observed a very good accordance between the compensated force and the force measured by the hammer. For breaking wave impacts, the compensation methodology allowed to drastically reduce the amplitude of the oscillations over a wide frequency band, while retaining most of the frequency content of the hydrodynamic force.

The breaking waves considered in the study and the generation methodology were presented in chapter 3. We generated waves with different breaking strengths through focalisation. Important efforts were devoted to the modelling and measurement of the breaking waves. All the waves were modelled with a fully non-linear potential flow solver. This solver allowed to compute the following wave characteristics which influence the wave impact phenomenon: the crest speed, the height of the wave crest, the breaking strength and the breaking location. The quantification of the breaking strength is based on the Γ parameter proposed by Derakhti et al. 2018. Spatial measurements of the free-surface profiles of the waves were carried out with a high-speed video camera. Good agreements were obtained between the measured and modelled free-surface profiles. This supports the validity of the wave parameters obtained with the non-linear simulations. It appeared during the characterisation of the waves that the breaking inception parameter of Barthelemy et al. 2018 and the Γ parameter present some limitations. Indeed, for strong plunging breakers, we showed that breaking may appear before the threshold $B = 0.85$ is crossed, and that the Γ parameter may not accurately represent the breaking strength. We think that the observed inconsistencies are mainly due to the fact that the B parameter is computed at the crest of the wave, which may be rather distant from the point at which the fluid velocity is maximum for strong plunging breakers. In this chapter, we also used the breaking waves to validate a linear equivalent to the breaking inception parameter of

Barthelemy et al. 2018. This linear equivalent will be used in further works to predict the probability of slamming in a sea state.

In the experimental results presented in chapter 4, we analyzed the effect of different wave parameters on the breaking wave impact force. First, the effect of the breaking strength Γ and of the distance δ on the time history of the force were investigated. It appeared that for the waves displaying small breaking strengths, typically with a Γ value lower than one, no impulsive force increase was observed. For stronger waves, an impulsive force increase occurred for a range of δ values. The magnitude of the impact force was shown to greatly depend on the values of δ and Γ. The numerical simulations and the high-speed video camera images were used to link the shape of the wave to the time history of the impact force. During the impact of a significantly overturned wave, we observed a two-phase impulsive force increase. This two-phase increase is likely due to the successive impacts of the tongue and of the front of the wave. It also appeared that the diffraction of the wave field by the cylinder likely dampens the wave impact force. It ensues that a Froude-Krylov approach, in which the distortion of the wave by the cylinder is not accounted for, is likely to over-predict the breaking wave impact force. Another difficulty with this kind of approach is to predict whether or not their will be an impact, and if an impact model should be "activated". In a following section, we focused on the effect of the breaking strength and of the distance δ on the maximum of the impact force. For each wave, the evolution of the maximum impact force with the distance δ was fitted to a skewed Gaussian. This function was chosen to model the asymmetric increase and decrease of the maximum impact force as a function of δ. For all the breaking waves, the distance δ generating the highest impact force is found to lie between 5 and 6 percent of the characteristic wave length. Based on the skewed Gaussian fits, we proposed an empirical formula to describe the evolution of the impulsive part of the impact force as a function of the breaking strength Γ, the distance δ, the crest height η_b and the crest speed c_b. Finally, we investigated the effect of the inclination and motion of the mockup during impact. The rotation point of the mockup was chosen so as to minimize the variation of the distance δ. It appeared that an inclination of the mockup towards the waves increases the impact force while an inclination in the opposite direction decreases the impact force. In the range [-10; 5]°, which is of interest for FOWTs, the variation of the impact force was found to be within ± 20 % of the force measured for a vertical cylinder. The wave impacts on a moving mockup showed that a motion in the wave propagation direction decreases the impact force. However, this decrease is not proportional to the square of the

relative velocity between the crest of the wave and the mockup, as it was expected prior to the experiments. Indeed, we found that the impact force decreases a bit faster than the squared relative velocity. Also, some additional perturbations of the wave front were observed when the cylinder was moving.

5.2 Recommendations

5.2.1 Improvements of the experimental approach

During the experimental campaign, we successfully compensated most of the force oscillations. Note that the compensation methodology was applied *a posteriori*, *i.e.* the mockup was not designed to optimise the performance of the compensation methodology. In future works, better results could be obtained by accounting for the compensation methodology in the design phase. As it is suggested by Tassin et al. 2023, the mass and the stiffness of the mock-up could be increased to reduce the amplitude of the oscillations, and thus also the amplitude of the added-mass force, which is thought to be responsible for the residual oscillations.

During the DIMPACT experiments, only focused breaking waves were used. It would be interesting to extend our investigations to non-focused breaking waves in order to investigate the validity of our conclusions on other types of waves. Moreover, the results presented here are based on a reduced number of wave cases. They need to be further validated with more breaking wave cases.

To further investigate the effect of the diffraction of the waves by the cylinder, we could measure the evolution of the wetted surface of the cylinder during a wave impact. This could be done using a transparent mockup and a LED edge-lighting system, as proposed by Breton et al. 2020. The implementation of the technique would however require a dedicated experimental set-up.

5.2.2 Improvements of the wave characterisation

As it has been highlighted in section 3.3, the parameter Γ does not seem appropriate to characterise the breaking strength of strong plunging breakers. Varing et al. 2021 showed that in shallow water, if the ratio between the norm of the maximum fluid velocity close to the crest and the crest speed reaches 0.85, the wave will evolve towards breaking. For gentle and mild plunging breakers, this criterion is very close to the criterion proposed by

Barthelemy et al. 2018 as the maximum fluid velocity is very close to the crest location. However, it is attained earlier than the criterion of Barthelemy et al. 2018 for strong plunging breakers. The accuracy of the Γ parameter may be improved for strong plunging breakers by considering the maximum fluid velocity instead of the fluid velocity at the crest for the ratio u/c.

Given the recent progresses achieved at Ifremer, we may soon be able to use a stereo-video system to measure the free-surface profile of the waves. This would allow to measure the wave profiles in the middle of the flume, where the waves are not disturbed by the wall of the flume. Stereo video would also be useful to measure the effect of the diffraction of the waves, as well as to measure the free-surface profile of short-crested waves.

5.2.3 Further investigations

It appeared in section 4.3 that the diffraction of the waves by the cylinder decreases the magnitude of the impact force. The diffraction depends on the ratio between the characteristic wavelength and the radius of the cylinder. For different wavelength to radius ratios, the empirical formula proposed in section 4.3 may not be valid anymore. We thus recommend to investigate the effect of the wavelength to radius ratio. The influence on the force could be measured either by modifying the radius of the cylinder, which implies to work with different mockups, or by changing the scale of the impacting waves. The edge-lighting technique proposed by Breton et al. 2020 and high fidelity numerical simulations would give more insights in the diffraction process.

We showed in section 4.2.1.2 that the time history and the frequency content of the impact force evolve with the distance δ. Even if we did not study the influence of the breaking strength Γ on the frequency content, it is likely to be of importance to predict the structural response of an offshore wind turbine. As we did for the maximum impact force in section 4.2.3, it would be interesting to propose an empirical formula giving the time evolution (rise and decay) of the impact force as a function of the parameters of the breaking wave. This may also give some insights on whether or not the force generated by a wave should be considered as an impact. Indeed, we observed that it is not an easy task to segregate the waves that induce an impact force from the waves that do not.

The validation of the existence of a linear breaking threshold proposed in section 3.4.2 paved the way to extend the probabilistic wave breaking model of Stringari et al. 2021 to the prediction of breaking wave impact loads. Indeed, during the DIMPACT project, partners of the project proposed a way to compute the breaking strength based on the

linear equivalent. The formula proposed in section 4.2.3, which gives the magnitude of the impact force as a function of the breaking strength, the distance δ, the crest speed and the crest height, could be applied using the wave parameters computed with the equivalent linear model.

BIBLIOGRAPHY

Andersen, Thomas Lykke and Peter Frigaard (2014), *Wave Generation in Physical Models: Technical documentation for AwaSys 6*, DCE Lecture notes 34, Denmark: Department of Civil Engineering, Aalborg University.

Antonini, Alessandro, James Mark William Brownjohn, Darshana Dassanayake, Alison Raby, James Bassit, Athanasios Pappas, and Dina D'Ayala (Sept. 1, 2021), « A Bayesian inverse dynamic approach for impulsive wave loading reconstruction: Theory, laboratory and field application », *in*: *Coastal Engineering* 168, p. 103920, ISSN: 0378-3839, DOI: 10.1016/j.coastaleng.2021.103920.

Babarit, A. and Gérard Delhommeau (Sept. 6, 2015), « Theoretical and numerical aspects of the open source BEM solver NEMOH », *in*: *11th European Wave and Tidal Energy Conference (EWTEC2015)*.

Baldock, T. E. and C. Swan (Jan. 1, 1994), « Numerical calculations of large transient water waves », *in*: *Applied Ocean Research* 16.*2*, pp. 101–112, ISSN: 0141-1187, DOI: 10.1016/0141-1187(94)90006-X.

Barthelemy, X., M. L. Banner, W. L. Peirson, F. Fedele, M. Allis, and F. Dias (2018), « On a unified breaking onset threshold for gravity waves in deep and intermediate depth water », *in*: *Journal of Fluid Mechanics* 841, Edition: 2018/02/23 Publisher: Cambridge University Press, pp. 463–488, ISSN: 0022-1120, DOI: 10.1017/jfm.2018.93.

Basco, D.R. and J.M. Niedzwecki (May 1, 1989), « Breaking Wave Force Distributions and Design Criteria for Slender Piles », *in*: Offshore Technology Conference, OTC–6009–MS, DOI: 10.4043/6009-MS.

Batlle Martin, Marc, Jeffrey C. Harris, Jean-François Filipot, F. Hulin, Alan Tassin, and Paul Renaud (Dec. 1, 2023), « Deep water focused breaking wave loads on a fixed cylinder », *in*: *Coastal Engineering* 186, p. 104397, ISSN: 0378-3839, DOI: 10.1016/j.coastaleng.2023.104397.

Biogradlija, Arnes (Dec. 29, 2022), *World's first floating offshore wind farm marks five years* -, URL: https://www.industryandenergy.eu/renewables/worlds-first-floating-offshore-wind-farm-marks-five-years/ (visited on 08/29/2023).

Breton, T., A. Tassin, and N. Jacques (2020), « Experimental investigation of the water entry and/or exit of axisymmetric bodies », *in*: *Journal of Fluid Mechanics* 901, Publisher: Cambridge University Press, A37.

British Standards Document BS EN IEC 61400-1 for wind energy generation systems (2019).

Campbell, I. M. C. and P. A. Weynberg (1980), *Measurement of parameters affecting slamming*, University of Southampton, Department of Aeronautics and Astronautics.

Canard, Maxime, Guillaume Ducrozet, and Benjamin Bouscasse (Oct. 13, 2022), « Generation of Controlled Irregular Wave Crest Statistics in a Numerical Wavetank Using HOS-NWT Solver », *in*: ASME 2022 41st International Conference on Ocean, Offshore and Arctic Engineering, American Society of Mechanical Engineers Digital Collection, DOI: 10.1115/OMAE2022-79880.

Chan, Eng-Soon, Hin-Fatt Cheong, and Boon-Cheng Tan (May 1995), « Laboratory study of plunging wave impacts on vertical cylinders », *in*: *Coastal Engineering* 25.*1*, pp. 87–107, ISSN: 03783839, DOI: 10.1016/0378-3839(94)00042-V.

Choi, Sung-Jin, Kwang-Ho Lee, and Ove Tobias Gudmestad (Mar. 1, 2015), « The effect of dynamic amplification due to a structures vibration on breaking wave impact », *in*: *Ocean Engineering* 96, pp. 8–20, ISSN: 0029-8018, DOI: 10.1016/j.oceaneng.2014.11.012.

Cooker, Mark J. and D. H. Peregrine (Aug. 1995), « Pressure-impulse theory for liquid impact problems », *in*: *Journal of Fluid Mechanics* 297, Publisher: Cambridge University Press, pp. 193–214, ISSN: 1469-7645, 0022-1120, DOI: 10.1017/S0022112095003053.

Derakhti, Morteza, Michael L. Banner, and James T. Kirby (Aug. 2018), « Predicting the breaking strength of gravity water waves in deep and intermediate depth », *in*: *Journal of Fluid Mechanics* 848, Publisher: Cambridge University Press, R2, ISSN: 0022-1120, 1469-7645, DOI: 10.1017/jfm.2018.352.

Dorfman, Boris and Lev Shemer (Sept. 2007), « Video image-based technique for measuring wave field evolution in a laboratory wave tank », *in*: *Proceedings of the 12th International Congress of the International Maritime Association of the Mediterranean*, IMAM 2007, Varna, Bulgaria.

Ducrozet, Guillaume, Félicien Bonnefoy, David Le Touzé, and Pierre Ferrant (July 1, 2012), « A modified High-Order Spectral method for wavemaker modeling in a numerical wave tank », *in*: *European Journal of Mechanics - B/Fluids* 34, pp. 19–34, ISSN: 0997-7546, DOI: 10.1016/j.euromechflu.2012.01.017.

Engsig-Karup, A. P., H. B. Bingham, and O. Lindberg (Apr. 1, 2009), « An efficient flexible-order model for 3D nonlinear water waves », *in*: *Journal of Computational Physics* 228.*6*, pp. 2100–2118, ISSN: 0021-9991, DOI: 10.1016/j.jcp.2008.11.028.

Esandi, Javier Murgoitio, Eugeny Buldakov, Richard Simons, and Dimitris Stagonas (2020), « An experimental study on wave forces on a vertical cylinder due to spilling breaking and near-breaking wave groups », *in*: *Coastal Engineering* 162, Publisher: Elsevier, p. 103778.

Filipot, J.-F., P. Guimaraes, F. Leckler, J. Hortsmann, R. Carrasco, E. Leroy, N. Fady, M. Accensi, M. Prevosto, R. Duarte, V. Roeber, A. Benetazzo, C. Raoult, M. Franzetti, A. Varing, and N. Le Dantec (Aug. 19, 2019), « La Jument lighthouse: a real-scale laboratory for the study of giant waves and their loading on marine structures », *in*: *Philosophical Transactions of the Royal Society A: Mathematical, Physical and Engineering Sciences* 377.*2155*, Publisher: Royal Society, p. 20190008, DOI: 10.1098/rsta.2019.0008.

Ghadirian, Amin and Henrik Bredmose (2019), « Pressure impulse theory for a slamming wave on a vertical circular cylinder », *in*: *Journal of Fluid Mechanics* 867, Edition: 2019/03/20 Publisher: Cambridge University Press, R1, ISSN: 0022-1120, DOI: 10.1017/jfm.2019.151.

Ghadirian, Amin, Fabio Pierella, and Henrik Bredmose (Jan. 1, 2023), « Calculation of slamming wave loads on monopiles using fully nonlinear kinematics and a pressure impulse model », *in*: *Coastal Engineering* 179, p. 104219, ISSN: 0378-3839, DOI: 10.1016/j.coastaleng.2022.104219.

Goda, Yoshimi, Suketo Haranake, and Masaki Kitahata (1966), *Study of impulsive breaking wave forces on piles*.

Govindasamy, Vijaya Kumar, Mayilvahanan Alagan Chella, Sannasiraj Sannasi Annamalaisamy, and Panneer Selvam Rajamanickam (Mar. 1, 2023), « Impact pressure distribution and characteristics of breaking wave impact on a monopile », *in*: *Ocean Engineering* 271, p. 113771, ISSN: 0029-8018, DOI: 10.1016/j.oceaneng.2023.113771.

Grilli, S. T., J. Skourup, and I.A. Svendsen (June 1, 1989), « An efficient boundary element method for nonlinear water waves », *in*: *Engineering Analysis with Boundary Elements* 6.*2*, pp. 97–107, ISSN: 0955-7997, DOI: 10.1016/0955-7997(89)90005-2.

Grilli, S. T. and R. Subramanya (Apr. 1, 1996), « Numerical modeling of wave breaking induced by fixed or moving boundaries », *in*: *Computational Mechanics* 17.*6*, pp. 374–391, ISSN: 1432-0924, DOI: 10.1007/BF00363981.

Guo, Yinghao, Longfei Xiao, Xiaoqing Teng, Yufeng Kou, and Jiancheng Liu (Jan. 1, 2020), « Processing method and governing parameters for horizontal wave impact loads on a semi-submersible », *in*: *Marine Structures* 69, p. 102673, ISSN: 0951-8339, DOI: 10.1016/j.marstruc.2019.102673.

Ha, Yoon-Jin, Kyong-Hwan Kim, Bo Woo Nam, and Sa Young Hong (2020), « Experimental investigation for characteristics of wave impact loads on a vertical cylinder in breaking waves », *in*: *Ocean Engineering* 209, Publisher: Elsevier, p. 107470.

Hallowell, S., A. T. Myers, and S. R. Arwade (2016), « Variability of breaking wave characteristics and impact loads on offshore wind turbines supported by monopiles », *in*: *Wind Energy* 19.*2*, _eprint: https://onlinelibrary.wiley.com/doi/pdf/10.1002/we.1833, pp. 301–312, ISSN: 1099-1824, DOI: 10.1002/we.1833.

Hansen, Hans Fabricius and Henrik Kofoed-Hansen (2017), « An engineering-model for extreme wave-induced loads on monopile foundations », *in*: *ASME 2017 36th International Conference on Ocean, Offshore and Arctic Engineering*, American Society of Mechanical Engineers Digital Collection.

Hernández, Irving D., Jassiel V. Hernández-Fontes, Marcelo A. Vitola, Monica C. Silva, and Paulo T.T. Esperança (June 1, 2018), « Water elevation measurements using binary image analysis for 2D hydrodynamic experiments », *in*: *Ocean Engineering* 157, pp. 325–338, ISSN: 0029-8018, DOI: 10.1016/j.oceaneng.2018.03.063.

Hulin, F., A Tassin, J F Filipot, and N Jacques (Nov. 2022), « Étude expérimentale des chargements hydrodynamiques générés par les impacts de vagues déferlantes sur des éoliennes flottantes SPAR », *in*: *18èmes journées de l'hydrodynamique*.

Irschik, Kai, Uwe Sparboom, and Hocine Oumeraci (Jan. 1, 2004), « Breaking wave loads on a slender pile in shallow water », *in*: *Proc. 29th Int. Conf. Coastal Eng. (ICCE 2004), ASCE, Lisbon*, DOI: 10.1142/9789812701916_0045.

Karman, T. H. von (Oct. 1, 1929), *The impact on seaplane floats during landing*, Technical note number 321.

Kimmoun, O., A. Ratouis, and L. Brosset (June 20, 2010), « Sloshing And Scaling: Experimental Study In a Wave Canal At Two Different Scales », *in*: The Twentieth International Offshore and Polar Engineering Conference, ISOPE–I–10–185.

Kjeldsen, Søren Peter, Alf Tørum, and Robert G. Dean (1986), « Wave Forces on Vertical Piles Caused by 2- and 3-Dimensional Breaking Waves », *in*: Publisher: American Society of Civil Engineers, pp. 1929–1942, DOI: 10.1061/9780872626003.142.

Korobkin, A., R. Guéret, and Š. Malenica (May 1, 2006), « Hydroelastic coupling of beam finite element model with Wagner theory of water impact », *in*: *Journal of Fluids and Structures* 22.*4*, pp. 493–504, ISSN: 0889-9746, DOI: 10.1016/j.jfluidstructs.2006.01.001.

Le Page, Sacha, Alan Tassin, Julien Caverne, Yves Le Gall, Benoit Gomez, and Guillaume Ducrozet (Aug. 1, 2023), « Towards accurate stereo-video based free-surface reconstruction for wave tank experiments », *in*: *IOP Conference Series: Materials Science and Engineering* 1288.*1*, Publisher: IOP Publishing, p. 012009, ISSN: 1757-899X, DOI: 10.1088/1757-899X/1288/1/012009.

Lian, G. (2018), « Slamming loads on large volume structures from breaking waves », PhD thesis, University of Stavanger.

Longuet-Higgins, M. S. and E. D. Cokelet (1976), « The Deformation of Steep Surface Waves on Water. I. A Numerical Method of Computation », *in*: *Proceedings of the Royal Society of London. Series A, Mathematical and Physical Sciences* 350.*1660*, Publisher: The Royal Society, pp. 1–26, ISSN: 0080-4630.

Ma, Yuxiang, Bing Tai, Guohai Dong, and Marc Perlin (Apr. 15, 2020), « Experimental study of plunging solitary waves impacting a vertical slender cylinder », *in*: *Ocean Engineering* 202, p. 107191, ISSN: 0029-8018, DOI: 10.1016/j.oceaneng.2020.107191.

Maes, K., W. Weijtjens, E.-J. De Ridder, and G. Lombaert (Sept. 2018), « Inverse estimation of breaking wave loads on monopile wind turbines », *in*: *Ocean Engineering* 163, pp. 544–554, ISSN: 00298018, DOI: 10.1016/j.oceaneng.2018.05.049.

Manjula, R., S. A. Sannasiraj, and K. Palanichamy (2013), « Laboratory Measurements of Breaking Wave Impact Pressures on a Slender Cylindrical Member », *in*: *The International Journal of Ocean and Climate Systems* 4.*3*, _eprint: https://doi.org/10.1260/1759-3131.4.3.151, pp. 151–169, DOI: 10.1260/1759-3131.4.3.151.

Mei, Xuan and Min Xiong (Nov. 2021), « Effects of Second-Order Hydrodynamics on the Dynamic Responses and Fatigue Damage of a 15 MW Floating Offshore Wind Turbine », *in*: *Journal of Marine Science and Engineering* 9.*11*, Number: 11 Publisher: Multidisciplinary Digital Publishing Institute, p. 1232, ISSN: 2077-1312, DOI: 10.3390/jmse9111232.

Mohanlal, Sunil, Jeffrey C. Harris, Marissa L. Yates, and Stephan T. Grilli (Aug. 1, 2023), « Unified depth-limited wave breaking detection and dissipation in fully nonlinear

potential flow models », *in*: *Coastal Engineering* 183, p. 104316, ISSN: 0378-3839, DOI: 10.1016/j.coastaleng.2023.104316.

Molin, Bernard (2002), *Hydrodynamique des structures offshore*, Editions TECHNIP, 446 pp., ISBN: 978-2-7108-0815-2.

Nestegard, Arne, Arve Johan Kalleklev, Kjell Hagatun, Yu Lin Wu, Sverre Haver, and Erik Lehn (2004), « Resonant Vibrations of Riser Guide Tubes Due to Wave Impact », *in*: ASME 2004 23rd International Conference on Offshore Mechanics and Arctic Engineering, American Society of Mechanical Engineers Digital Collection, pp. 987–994, DOI: 10.1115/OMAE2004-51545.

Paulsen, Bo Terp, Henrik Bredmose, and Harry B. Bingham (Apr. 2014), « An efficient domain decomposition strategy for wave loads on surface piercing circular cylinders », *in*: *Coastal Engineering* 86, pp. 57–76, ISSN: 03783839, DOI: 10.1016/j.coastaleng.2014.01.006.

Paulsen, Bo Terp, Ben de Sonneville, Michiel van der Meulen, and Niels Gjøl Jacobsen (2019), « Probability of wave slamming and the magnitude of slamming loads on offshore wind turbine foundations », *in*: *Coastal Engineering* 143, pp. 76–95, ISSN: 0378-3839, DOI: https://doi.org/10.1016/j.coastaleng.2018.10.002.

Peyrard, Christophe, Maria Teles, T. Bouard, Fabien Leckler, and Jean-François Filipot (July 2021), *Report on the definition of the slamming scenarios*, Deliverable of the DIMPACT project.

Poncet, P. A., B. Liquet, B. Larroque, D. D'Amico, D. Sous, and S. Abadie (Aug. 1, 2022), « In-situ measurements of energetic depth-limited wave loading », *in*: *Applied Ocean Research* 125, p. 103216, ISSN: 0141-1187, DOI: 10.1016/j.apor.2022.103216.

Rapp, Ronald James and W Kendall Melville (1990), « Laboratory measurements of deep-water breaking waves », *in*: *Philosophical Transactions of the Royal Society of London. Series A, Mathematical and Physical Sciences* 331.*1622*, Publisher: The Royal Society London, pp. 735–800.

Renaud, P., F. Hulin, M.B. Martin, Y. M. Scolan, Alan Tassin, N. Jacques, J. Harris, and J .F. Filipot (June 2023a), « Semi-Analytical Load Models Accounting for the Tilt and Motion of a Cylinder Impacted by a Plunging Breaking Wave », *in*: *Proceedings of the ASME 2023*, 42nd International Conference on Ocean, Offshore & Arctic Engineering, Melbourne, Australia.

Renaud, P., M.B. Martin, F. Hulin, J. Harris, J. F. Filipot, and Y. M. Scolan (May 15, 2023b), « Semi-analytical load models describing the progressive immersion of a fixed

vertical cylinder in a breaking wave », *in*: *Ocean Engineering* 276, p. 114116, ISSN: 0029-8018, DOI: 10.1016/j.oceaneng.2023.114116.

RTE (Oct. 2021), *Futurs énergétiques 2050. Principaux résultats*, Résumé exécutif.

Saincher, Shaswat, V. Sriram, Shagun Agarwal, and T. Schlurmann (May 1, 2022), « Experimental investigation of hydrodynamic loading induced by regular, steep non-breaking and breaking focused waves on a fixed and moving cylinder », *in*: *European Journal of Mechanics - B/Fluids* 93, pp. 42–64, ISSN: 0997-7546, DOI: 10.1016/j.euromechflu.2021.12.009.

Sánchez, Sergio, José-Santos López-Gutiérrez, Vicente Negro, and M. Dolores Esteban (Dec. 2019), « Foundations in Offshore Wind Farms: Evolution, Characteristics and Range of Use. Analysis of Main Dimensional Parameters in Monopile Foundations », *in*: *Journal of Marine Science and Engineering* 7.*12*, Number: 12 Publisher: Multidisciplinary Digital Publishing Institute, p. 441, ISSN: 2077-1312, DOI: 10.3390/jmse7120441.

Savelyev, Ivan and Julian Fuchs (2018), « Stereo Thermal Marking Velocimetry », *in*: *Frontiers in Mechanical Engineering* 4, ISSN: 2297-3079.

Sawaragi, Toru and Masao Nochino (Dec. 1, 1984), « Impact Forces of Nearly Breaking Waves on a Vertical Circular Cylinder », *in*: *Coastal Engineering in Japan* 27.*1*, Publisher: Taylor & Francis, pp. 249–263, ISSN: 0578-5634, DOI: 10.1080/05785634.1984.11924391.

Scharnke, Jule and Joop Helder (June 9, 2019), « Elementary Loading Processes and Scale Effects Involved in Wave-in-Deck Type of Loading: A Summary of the BreaKin JIP », *in*: *OMAE2019*, Volume 3: Structures, Safety, and Reliability, DOI: 10.1115/OMAE2019-95004.

Seiffert, Betsy R. and Guillaume Ducrozet (Jan. 1, 2018), « Simulation of breaking waves using the high-order spectral method with laboratory experiments: wave-breaking energy dissipation », *in*: *Ocean Dynamics* 68.*1*, pp. 65–89, ISSN: 1616-7228, DOI: 10.1007/s10236-017-1119-3.

Shi, Wei, Songhao Zhang, Constantine Michailides, Lixian Zhang, Puyang Zhang, and Xin Li (Mar. 1, 2023), « Experimental investigation of the hydrodynamic effects of breaking waves on monopiles in model scale », *in*: *Journal of Marine Science and Technology* 28.*1*, pp. 314–325, ISSN: 1437-8213, DOI: 10.1007/s00773-023-00926-9.

Spinosa, Emanuele and Alessandro Iafrati (Apr. 1, 2022), « A noise reduction method for force measurements in water entry experiments based on the Ensemble Empirical

Mode Decomposition », *in*: *Mechanical Systems and Signal Processing* 168, p. 108659, ISSN: 0888-3270, DOI: 10.1016/j.ymssp.2021.108659.

Stringari, C. E., M. Prevosto, J.-F. Filipot, F. Leckler, and P. V. Guimarães (Apr. 1, 2021), « A New Probabilistic Wave Breaking Model for Dominant Wind-Sea Waves Based on the Gaussian Field Theory », *in*: *Journal of Geophysical Research: Oceans* 126.*4*, ISSN: 2169-9291.

Suja-Thauvin, Loup, Jørgen R Krokstad, Erin E Bachynski, and Erik-Jan de Ridder (2017), « Experimental results of a multimode monopile offshore wind turbine support structure subjected to steep and breaking irregular waves », *in*: *Ocean Engineering* 146, Publisher: Elsevier, pp. 339–351.

Swan, Chris and Rubab Sheikh (2015), « The interaction between steep waves and a surface-piercing column », *in*: *Philosophical Transactions of the Royal Society A 373: 20140114*.

Tanimoto, K., S. Takahashi, T. Kaneko, and K. Shiota (Nov. 30, 1987), « Impulsive Breaking Wave Forces on an Inclined Pile Exerted by Random Waves », *in*: *Coastal Engineering 1986*, 20th International Conference on Coastal Engineering, Taipei, Taiwan: American Society of Civil Engineers, pp. 2288–2302, DOI: 10.1061/9780872626003.168.

Tassin, Alan, F. Hulin, and Nicolas Jacques (2023), « A direct multimode method for the reduction of vibration induced oscillations on force signals during “pseudo-rigid” water impact experiments », *in*: *Preprint submitted to Sound and Vibrations*.

Tassin, Alan, F. Hulin, Mathieu Laurent, and Jean-François Filipot (May 19, 2022), *Report on the definition of the wave tank experiments*, Deliverable of the DIMPACT project, France Énergies Marines.

Van Nuffel, Diederik, Sridhar Vepa, Ives De Baere, Joris Degrieck, Julien De Rouck, and Wim Van Paepegem (Oct. 31, 2011), « Pressure Measurement on the Surface of a Rigid Cylindrical Body During Slamming Wave Impact », *in*: ASME 2011 30th International Conference on Ocean, Offshore and Arctic Engineering, American Society of Mechanical Engineers Digital Collection, pp. 303–312, DOI: 10.1115/OMAE2011-49390.

Varing, Audrey, Jean-Francois Filipot, Stephan Grilli, Rui Duarte, Volker Roeber, and Marissa Yates (Mar. 1, 2021), « A new definition of the kinematic breaking onset criterion validated with solitary and quasi-regular waves in shallow water », *in*: *Coastal Engineering* 164, p. 103755, ISSN: 0378-3839, DOI: 10.1016/j.coastaleng.2020.103755.

Veic, Duje, Marek Kraskowski, and Tomasz Bugalski (2016), « Bottom Fixed Substructure Analysis, Model Testing and Design for Harsh Environment », *in*: *MARE-WINT: New Materials and Reliability in Offshore Wind Turbine Technology*, ed. by Wiesław Ostachowicz, Malcolm McGugan, Jens-Uwe Schröder-Hinrichs, and Marcin Luczak, Cham: Springer International Publishing, pp. 193–211, ISBN: 978-3-319-39095-6, DOI: 10.1007/978-3-319-39095-6_13.

Vested, Malene Hovgaard, Stefan Carstensen, and Erik Damgaard Christensen (Apr. 1, 2020), « Experimental study of wave kinematics and wave load distribution on a vertical circular cylinder », *in*: *Coastal Engineering* 157, p. 103660, ISSN: 0378-3839, DOI: 10.1016/j.coastaleng.2020.103660.

Viste-Ollestad, Irja (July 6, 2016), *Investigation of an incident with fatal consequences on COSLInnovator, 30 December 2015*.

Wagner, Herbrt (Jan. 1, 1932), « Über Stoß- und Gleitvorgänge an der Oberfläche von Flüssigkeiten », *in*: *ZAMM - Journal of Applied Mathematics and Mechanics / Zeitschrift für Angewandte Mathematik und Mechanik* 12.*4*, Publisher: John Wiley & Sons, Ltd, pp. 193–215, ISSN: 1521-4001.

Wei, Kai, Jie Hong, Mochen Jiang, and Wenyu Zhao (June 1, 2022), « A review of breaking wave force on the bridge pier: Experiment, simulation, calculation, and structural response », *in*: *Journal of Traffic and Transportation Engineering (English Edition)* 9.*3*, pp. 407–421, ISSN: 2095-7564, DOI: 10.1016/j.jtte.2021.03.006.

Wienke, J. (2001), « Druckschlagbelastung auf schlanke zylindrische Bauwerke durch brechende Wellen », PhD thesis.

Wienke, J. and H. Oumeraci (May 1, 2005), « Breaking wave impact force on a vertical and inclined slender pile - theoretical and large-scale model investigations », *in*: *Coastal Engineering* 52.*5*, pp. 435–462, ISSN: 0378-3839, DOI: 10.1016/j.coastaleng.2004.12.008.

Zhou, D., E. S. Chan, and W. K. Melville (Oct. 1, 1991), « Wave impact pressures on vertical cylinders », *in*: *Applied Ocean Research* 13.*5*, pp. 220–234, ISSN: 0141-1187, DOI: 10.1016/S0141-1187(05)80046-X.

Zhu, Jiahui, Yangyang Gao, Lizhong Wang, and Wei Li (Nov. 2022), « Experimental investigation of breaking regular and irregular waves slamming on an offshore monopile wind turbine », *in*: *Marine Structures* 86, p. 103270, ISSN: 09518339, DOI: 10.1016/j.marstruc.2022.103270.

Appendix A

List of the investigated impact cases

A.1 First experimental campaign

The different impact cases that were investigated during the first experimental campaign are listed in table A.1 below. Wave number refers to the number defined in table 3.2. Parameter δ_r is the distance between $x = 21$ m and the front face of the cylinder. The $_r$ stands for raw, as the breaking location has not been corrected to account for the actual location of breaking which may not be exactly at $x = 21$ m. Parameter θ corresponds to the pitch angle of the mockup (see figure 4.23 for the definition of the pitch angle). Parameter V corresponds to the horizontal velocity of the mockup at the time of impact. The velocity is positive when the mockup is moving in the wave propagation direction.

Table A.1 – Impact cases investigated during the first experimental campaign

Test number	Wave number	δ_r [m]	θ [°]	V [m/s]
70	3	0.46	0	0
71	3	0.46	0	0
72	3	0.46	0	0
73	3	0.36	0	0
74	3	0.36	0	0
75	3	0.36	0	0
76	3	0.26	0	0
77	3	0.26	0	0
78	3	0.26	0	0
79	3	0.16	0	0
80	3	0.16	0	0

Test number	Wave number	δ_r [m]	θ [°]	V [m/s]
81	3	0.26	0	0
82	3	0.16	0	0
83	3	0.06	0	0
84	3	0.06	0	0
85	3	0.06	0	0
86	9	0.30	0	0
87	9	0.30	0	0
89	9	0.30	0	0
90	3	0.30	0	0
91	3	0.30	0	0
94	3	0.30	0	0
96	3	0.21	0	0
97	3	0.21	0	0
98	3	0.21	0	0
99	3	0.185	0	0
102	3	0.185	0	0
103	3	0.185	0	0
104	3	0.1725	0	0
105	3	0.1725	0	0
106	3	0.1725	0	0
107	3	0.1725	0	0
108	3	0.185	0	0
109	3	0.1725	0	0
110	3	0.56	0	0
111	3	0.56	0	0
112	3	0.56	0	0
113	1	0.26	0	0
114	1	0.26	0	0
115	1	0.16	0	0
116	1	0.16	0	0
118	3	0.36	0	0.8
119	3	0.36	0	0.8

Test number	Wave number	δ_r [m]	θ [°]	V [m/s]
120	3	0.36	0	0.8
121	3	0.36	0	0.4
122	3	0.36	0	0.4
123	3	0.36	0	0.4
124	3	0.36	0	0
125	3	0.36	0	0
126	3	0.36	0	0
127	3	0.36	5	0
128	3	0.36	5	0
129	3	0.36	5	0
130	3	0.36	5	0
131	3	0.36	10	0
132	3	0.36	10	0
133	3	0.36	10	0
134	3	0.36	-5	0
135	3	0.36	-5	0
136	3	0.36	-5	0
137	3	0.36	-10	0
138	3	0.36	-10	0
139	3	0.36	-10	0
140	5	0.26	0	0
141	5	0.26	0	0
142	5	0.26	0	0
143	10	0.36	0	0
144	10	0.36	0	0
145	10	0.26	0	0
146	12	0.36	0	0
147	12	0.36	0	0
148	13	0.36	0	0
149	13	0.36	0	0
150	13	0.16	0	0
151	13	0.01	0	0

Test number	Wave number	δ_r [m]	θ [°]	V [m/s]
152	7	0.36	0	0
153	7	0.36	0	0
154	7	0.36	0	0
155	7	0.36	0	0
156	8	0.36	0	0
157	8	0.36	0	0
158	8	0.36	0	0
159	9	0.36	0	0
160	9	0.36	0	0
161	9	0.36	0	0
162	10	0.36	0	0
163	12	0.36	0	0
164	6	0.36	0	0
165	3	0.66	0	0
166	3	0.66	0	0
167	3	0.66	0	0
168	7	0.26	0	0
169	7	0.26	0	0
170	7	0.16	0	0
171	7	0.16	0	0
172	7	0.46	0	0

A.2 Second experimental campaign

The impact cases investigated during the second experimental campaign are listed in table A.2.

Table A.2 – Impact cases investigated during the second experimental campaign.

Test number	Wave number	δ_r [m]	θ [°]	V [m/s]
380	3	0.01	0	0
381	3	0.01	0	0
382	3	0.11	0	0

Test number	Wave number	δ_r [m]	θ [°]	V[m/s]
383	3	0.11	0	0
384	3	0.11	0	0
385	3	0.11	0	0
389	3	0.41	0	0
390	3	0.41	0	0
391	3	0.41	0	0
392	3	0.31	0	0
406	3	0.31	0	0
407	3	0.31	0	0
408	3	0.36	0	0
409	3	0.36	0	0
410	3	0.21	0	0
411	3	0.21	0	0
412	3	0.51	0	0
413	3	0.51	0	0
414	3	0.61	0	0
415	3	0.61	0	0
416	3	0.81	0	0
417	3	0.81	0	0
418	3	0.18	0	0
419	3	0.18	0	0
420	3	0.17	0	0
421	3	0.17	0	0
422	3	0.17	0	0
423	3	0.01	0	0
424	3	0.11	0	0
425	3	0.17	0	0
426	3	0.21	0	0
427	3	0.31	0	0
428	3	0.36	0	0
429	3	0.41	0	0
430	3	0.51	0	0

Test number	Wave number	δ_r [m]	θ [°]	V[m/s]
431	3	0.61	0	0
432	1	0.31	0	0
433	1	0.41	0	0
434	1	0.51	0	0
435	1	0.21	0	0
436	1	0.11	0	0
437	1	0.01	0	0
438	7	0.31	0	0
439	7	0.31	0	0
440	7	0.21	0	0
441	7	0.21	0	0
442	7	0.11	0	0
443	7	0.11	0	0
444	7	0.41	0	0
445	7	0.41	0	0
446	7	0.51	0	0
447	7	0.51	0	0
448	7	0.61	0	0
449	7	0.61	0	0
450	7	0.71	0	0
451	7	0.71	0	0
452	7	0.81	0	0
453	7	0.81	0	0
454	7	0.31	0	0
455	7	0.21	0	0
456	2	0.21	0	0
457	7	0.21	0	0
458	2	0.21	0	0
460	7	0.21	0	0
461	6	0.21	0	0
462	7	0.21	0	0
463	7	0.11	0	0

Test number	Wave number	δ_r [m]	θ [°]	V[m/s]
464	7	0.41	0	0
465	7	0.51	0	0
466	7	0.61	0	0
467	7	0.71	0	0
468	7	0.81	0	0
469	7	0.36	0	0
470	7	0.36	0	0
471	7	0.36	0	0
472	15	0.31	0	0
473	15	0.31	0	0
474	15	0.21	0	0
475	15	0.21	0	0
476	15	0.11	0	0
477	15	0.11	0	0
478	15	0.41	0	0
479	15	0.41	0	0
480	15	0.51	0	0
481	15	0.51	0	0
482	15	0.61	0	0
483	15	0.61	0	0
484	15	0.31	0	0
485	15	0.21	0	0
486	15	0.11	0	0
487	15	0.41	0	0
488	15	0.51	0	0
489	15	0.61	0	0
490	15	0.36	0	0
492	15	0.36	0	0
493	7	0.36	0	0
494	7	0.36	0	0
495	23	0.31	0	0
496	23	0.31	0	0

Test number	Wave number	δ_r [m]	θ [°]	V[m/s]
497	23	0.31	0	0
498	23	0.31	0	0
499	23	0.21	0	0
500	23	0.21	0	0
501	23	0.41	0	0
502	23	0.41	0	0
503	23	0.41	0	0
504	23	0.21	0	0
505	23	0.51	0	0
506	23	0.51	0	0
507	23	0.51	0	0
508	23	0.36	0	0
509	23	0.36	0	0
510	23	0.36	0	0
511	23	0.36	0	0
512	23	0.26	0	0
513	23	0.26	0	0
514	23	0.26	0	0
515	23	0.335	0	0
516	23	0.335	0	0
517	23	0.335	0	0
518	23	0.31	0	0
519	23	0.36	0	0
520	23	0.11	0	0
521	23	0.11	0	0
522	23	0.11	0	0
523	23	0.61	0	0
524	23	0.61	0	0
525	23	0.61	0	0
526	2	0.01	0	0
527	2	0.11	0	0
528	2	0.21	0	0

Test number	Wave number	δ_r [m]	θ [°]	V[m/s]
534	2	0.31	0	0
535	2	0.31	0	0
536	2	0.41	0	0
537	2	0.51	0	0
538	2	0.61	0	0
539	7	0.61	0	0
540	7	0.36	0	0
542	15	0.36	0	0
543	15	0.36	0	0
544	15	0.26	0	0
545	15	0.26	0	0
546	15	0.26	0	0
547	15	0.31	0	0
548	15	0.31	0	0
549	15	0.41	0	0
550	3	0.81	0	0
551	3	0.71	0	0
552	3	0.71	0	0
553	3	0.71	0	0
554	3	0.18	0	0
555	3	0.26	0	0
556	3	0.26	0	0
557	3	0.26	0	0
558	3	0.31	0	0
559	2	0.31	0	0
560	2	0.61	0	0
561	2	0.61	0	0
562	2	0.36	5	0
563	2	0.36	10	0
564	2	0.36	15	0
565	2	0.36	20	0
566	2	0.36	-5	0

Test number	Wave number	δ_r [m]	θ [°]	V[m/s]
567	2	0.36	-10	0
568	2	0.36	-15	0
569	3	0.36	-15	0
570	3	0.36	-15	0
571	3	0.36	-15	0
572	3	0.36	-10	0
573	3	0.36	-10	0
574	3	0.36	-10	0
575	3	0.36	-5	0
576	3	0.36	-5	0
577	3	0.36	-5	0
578	3	0.36	5	0
579	3	0.36	5	0
580	3	0.36	5	0
581	3	0.36	10	0
582	3	0.36	10	0
583	3	0.36	10	0
584	3	0.36	15	0
585	3	0.36	15	0
586	3	0.36	15	0
587	3	0.36	20	0
588	3	0.36	20	0
589	3	0.36	20	0
590	24	0.31	0	0
591	24	0.31	0	0
592	24	0.31	0	0
593	24	0.21	0	0
594	24	0.21	0	0
595	24	0.21	0	0
596	24	0.11	0	0
597	24	0.11	0	0
598	24	0.11	0	0

Test number	Wave number	δ_r [m]	θ [°]	V[m/s]
599	24	0.41	0	0
600	24	0.41	0	0
602	24	0.51	0	0
603	24	0.51	0	0
604	24	0.51	0	0
605	24	0.61	0	0
606	24	0.61	0	0
607	24	0.61	0	0
608	24	0.71	0	0
609	24	0.71	0	0
610	24	0.71	0	0
611	24	0.81	0	0
612	24	0.81	0	0
613	24	0.81	0	0
614	24	0.91	0	0
615	24	0.91	0	0
616	24	0.91	0	0
617	24	0.01	0	0
618	24	0.01	0	0
619	24	0.01	0	0
620	7	0.41	5	0
621	7	0.41	5	0
622	7	0.41	5	0
623	7	0.41	10	0
624	7	0.41	10	0
625	7	0.41	10	0
626	7	0.41	-5	0
629	7	0.41	-5	0
631	7	0.41	-10	0
632	7	0.41	-10	0
633	7	0.41	-10	0
634	24	0.41	0	0

Test number	Wave number	δ_r [m]	θ [°]	V[m/s]
635	24	0.41	0	0
636	23	0.81	0	0
637	23	0.81	0	0
638	23	0.81	0	0
639	23	0.01	0	0
640	23	0.01	0	0
641	23	0.01	0	0
642	2	0.71	0	0
643	2	0.71	0	0
644	2	0.81	0	0
645	4	0.36	0	0
646	4	0.36	0	0
647	4	0.36	0	0
648	5	0.36	0	0
649	5	0.36	0	0
650	5	0.36	0	0
651	8	0.41	0	0
652	8	0.41	0	0
653	8	0.41	0	0
654	9	0.41	0	0
655	9	0.41	0	0
656	9	0.41	0	0
657	10	0.41	0	0
658	10	0.41	0	0
659	10	0.41	0	0
663	2	0.36	0	0
664	3	0.36	0	0.4
665	3	0.36	0	0.4
666	3	0.36	0	0.4
667	3	0.36	0	0.2
668	3	0.36	0	0.2
669	3	0.36	0	0.2

Test number	Wave number	δ_r [m]	θ [°]	V[m/s]
670	3	0.36	0	0.6
671	3	0.36	0	0.6
672	3	0.36	0	0.6
673	3	0.36	0	0.8
674	3	0.36	0	0.8
675	3	0.36	0	0.8
680	7	0.41	0	0.4
681	7	0.41	0	0.4
682	7	0.41	0	0.4
683	7	0.41	0	0.2
684	7	0.41	0	0.2
685	7	0.41	0	0.2
686	7	0.41	0	0.6
687	7	0.41	0	0.6
688	7	0.41	0	0.6
689	7	0.41	0	0.8
691	7	0.41	0	0.8
692	12	0.41	0	0
693	12	0.41	0	0
694	12	0.41	0	0
696	14	0.36	0	0
697	20	0.36	0	0
698	3	0.91	0	0
699	3	0.91	0	0
700	3	0.91	0	0
701	7	0.41	0	0.8
704	18	0.20	0	0
705	18	0.10	0	0
706	2	0.91	0	0
707	23	0.71	0	0
708	23	0.91	0	0
709	3	0.31	0	0

Test number	Wave number	δ_r [m]	θ [°]	V[m/s]
710	3	0.31	0	0
711	3	0.31	0	0
712	3	0.31	0	0
713	3	0.31	0	0
714	3	0.31	0	0
715	24	0.41	0	0
716	7	0.41	0	0

Appendix B

DIMPACT EXPERIMENTAL DATABASE

Following the experimental campaigns, we produced a database that will be made available online one year after the end of the DIMPACT project. The database contains the measurements of the second experimental campaign.

We here describe the architecture of the database. Bold font is used for **folder** names and italic font is used for *file* names. The data of the impact experiments are stored in a folder named **impacts**. The folder **impacts** contains 300 folders corresponding to the 300 different impact cases listed in table A.2. The name of each folder corresponds to the test number given in table A.2. Within each folder, the data are organized as follows:

loads_accelerations	*time.txt*	[s] Time vector
	Fx1.txt	[N] Raw force on section S_1
	Fx2.txt	[N] Raw force on section S_2
	Fx3.txt	[N] Raw force on section S_3
	Fx4.txt	[N] Raw force on section S_4
	Fx1Compensated.txt	[N] Compensated force on section S_1
	Fx2Compensated.txt	[N] Compensated force on section S_2
	Fx3Compensated.txt	[N] Compensated force on section S_3
	Fx4Compensated.txt	[N] Compensated force on section S_4
	acc1_1.txt	[m/s] Acceleration of $A_{1.1}$
	acc1_2.txt	[m/s] Acceleration of $A_{1.2}$
	acc1_3.txt	[m/s] Acceleration of $A_{1.3}$
	acc1_4.txt	[m/s] Acceleration of $A_{1.4}$
	acc1_5.txt	[m/s] Acceleration of $A_{1.5}$
	acc1_6.txt	[m/s] Acceleration of $A_{1.6}$
	acc1_7.txt	[m/s] Acceleration of $A_{1.7}$
	acc2_2.txt	[m/s] Acceleration of $A_{2.2}$
	acc2_3.txt	[m/s] Acceleration of $A_{2.3}$
	acc2_4.txt	[m/s] Acceleration of $A_{2.4}$
	acc2_5.txt	[m/s] Acceleration of $A_{2.5}$
	acc2_6.txt	[m/s] Acceleration of $A_{2.6}$
	acc2_7.txt	[m/s] Acceleration of $A_{2.7}$
	acc3.txt	[m/s] Acceleration of A_3
	acc4.txt	[m/s] Acceleration of A_4
waveGauge_paddlePos	*time.txt*	[s] Time vector. Different from the time vector in **loads_accelerations**.
	waveGauge.txt	[m] Free-surface elevation at the wave gauge
	paddlePos.txt	[m] Position of the wave paddle

The results of the numerical simulations (see section 3.1.1) and measurements of the waves are stored in a folder named **waves**. The numerical simulation results are stored in a folder named **BEMResults**. The file *t.txt* contains the time steps of the simulation. The files *u.txt*, *w.txt*, *x.txt* and *z.txt* contain the horizontal fluid velocity, the vertical fluid velocity, the longitudinal position of the nodes and the vertical position of the nodes, respectively. These four folders are organised as follows: the different lines correspond to the different time instants given in file *t.txt*, and the different columns correspond to the

different nodes of the simulation. The position of the nodes is given in the files *x.txt* and *z.txt*.

The results of the video camera measurements (see section 3.2.4) are stored in a folder named **cameraMeasurement**. This folder contains several folders: each folder corresponds to one repeat of the wave measurement. Each measurement is composed of a time vector (file *tCamera.txt*) and of the position of the detected interface points: the longitudinal position is stored in *xCamera.txt* and the vertical position in *yCamera.txt*. Each line corresponds to a time instant and each column to a point on the interface. Note that the number of detected points is not constant (NaN values are stored in the last columns). The folder **othersensor** contains the measured free-surface elevation (file *quasar.txt*) and paddle position (file *paddlePos.txt*). File *t.txt* contains the time vector, which is different from the time vector for the free-surface measurements.

COLLEGES SCIENCES
BRETAGNE POUR L'INGENIEUR
LOIRE ET LE NUMERIQUE

ENSTA BRETAGNE

Titre : Étude expérimentale des chargements hydrodynamiques générés par les impacts de vagues déferlantes sur les éoliennes flottantes

Mot clés : Impact de vagues déferlantes, éoliennes flottantes,chargements hydrodynamiques, essais

Résumé : Les impacts de vagues déferlantes peuvent être responsables des chargements hydrodynamiques les plus importants rencontrés par une éolienne pendant son cycle de vie. Des progrès sont nécessaires pour prédire ces efforts avec précision. Nous avons cherché à identifier expérimentalement les différents paramètres des vagues et de la turbine qui influencent ces chargements. Pour cela, nous avons mesuré les efforts d'impact générés par différentes vagues focalisées sur un cylindre circulaire segmenté. Un nouveau procédé basé sur des accéléromètres a été utilisé pour compenser les oscillations des mesures d'efforts induites par les vibrations de la structure. Un effort important a été consacré à la caractérisation des vagues déferlantes. Celles-ci ont été mesurées à l'aide d'une caméra et modélisé avec un solveur potentiel entièrement non-linéaire. Nous avons étudié l'influence de l'intensité du déferlement de la vague, de la distance entre le point de déferlement et la face avant du cylindre, de l'inclinaison du cylindre et de sa vitesse horizontale pendant l'impact. L'effet de l'intensité du déferlement est quantifié.

Title: Experimental study of the hydrodynamic loads generated by breaking wave impacts on floating offshore wind turbines

Keywords: Breaking wave impacts, floating offshore wind turbines, hydrodynamic loadings, experiments

Abstract: Breaking wave impacts may be responsible for the most severe hydrodynamic loads encountered during the life time of a floating offshore wind turbine, and significant progresses are required to predict these loads with confidence. We aimed to experimentally identify the different parameters of the waves and of the turbine which influence the impact force and to quantitatively assess their importance. A segmented circular cylindrical mockup was used to measure the loads generated by focused breaking wave impacts. We used a new methodology based on a set of accelerometers to compensate for the force signal oscillations induced by the vibrations of the mockup, which are triggered by the impulsive nature of impact. An important effort was devoted to the characterisation of the impacting breaking waves in terms of geometry, crest speed and breaking strength. They were measured using a video camera and modelled with a fully non-linear potential flow solver. We investigated the influence of the breaking strength of the impacting waves, the distance between the breaking location and the front face of the cylinder, the tilt angle of the cylinder and the horizontal velocity of the cylinder during impact.